

A CONSTITUTIVE MODEL FOR SAND AND THE ANALYSIS OF THE CANLEX
EMBANKMENTS

by

HUMBERTO PUEBLA

B.Sc., National Autonomous University of Mexico, 1985
M. Eng., National Autonomous University of Mexico, 1994

A THESIS SUBMITTED IN PARTIAL FULFILLMENT OF
THE REQUIREMENTS FOR THE DEGREE OF
DOCTOR OF PHILOSOPHY
in
THE FACULTY OF GRADUATE STUDIES
Department of Civil Engineering

We accept this thesis as conforming
to the required standard

THE UNIVERSITY OF BRITISH COLUMBIA

October, 1999

© Humberto Puebla, 1999

In presenting this thesis in partial fulfilment of the requirements for an advanced degree at the University of British Columbia, I agree that the Library shall make it freely available for reference and study. I further agree that permission for extensive copying of this thesis for scholarly purposes may be granted by the head of my department or by his or her representatives. It is understood that copying or publication of this thesis for financial gain shall not be allowed without my written permission.

Department of CIVIL ENGINEERING

The University of British Columbia
Vancouver, Canada

Date December 10, 1999

ABSTRACT

A numerical analysis procedure including a constitutive model for predicting static liquefaction occurrence and liquefaction-induced displacements is presented in this dissertation. The main features of sand characteristic behaviour, as observed from laboratory element tests, are first identified to establish the most important issues regarding static liquefaction analysis. Based on physics fundamentals and elastic-plastic theory, a relatively simple constitutive model capable of capturing sand characteristic behaviour is then proposed. The model has two independent plastic components, a shear mechanism and a volumetric mechanism. The plastic shear mechanism is governed by a hyperbolic relationship between the stress ratio and plastic shear strain, and a flow rule for estimating shear-induced plastic volumetric strain from plastic shear strain. In addition, it has the ability to handle some of the effects induced by inherent anisotropy and rotation of principal stresses. The plastic volumetric mechanism responds to a power law that relates the cap pressure to the plastic volumetric strain induced by compressive loading.

The proposed constitutive model is incorporated into a commercially available computer program (FLAC). The code uses a finite differences method that satisfies dynamic equilibrium using a step-by-step time domain procedure and a groundwater flow technique, allowing coupled stress-flow analyses to be performed.

The proposed model is calibrated using data from conventional laboratory tests. The model is shown to capture reasonably well the drained and undrained characteristic

response of Syncrude sand as observed from element tests, over a range of confining stresses and relative densities.

The calibrated model is subsequently used for modelling the Canadian Liquefaction Experiment (CANLEX) embankments that included a field event in which a test embankment was built over a loose sand foundation layer, and a centrifuge test performed on a sand model of the prototype structure. Both earth-structures were planned to induce a static liquefaction failure and their responses characterized by the observed displacements and pore pressures.

The proposed constitutive model and numerical procedure used to simulate the CANLEX embankments are shown adequate for performing analysis of sand liquefaction, triggered by rapid monotonic (static) loading. The results from modelling both embankments are in reasonable agreement with the measured responses.

TABLE OF CONTENTS

ABSTRACT	ii
TABLE OF CONTENTS	iv
LIST OF TABLES.....	ix
LIST OF FIGURES	x
LIST OF SYMBOLS.....	xv
ACKNOWLEDGEMENTS.....	xix
CHAPTER 1: INTRODUCTION.....	1
1.1 Consequences of soil liquefaction: Some case histories.....	2
1.2 Liquefaction	5
1.3 Brief historical review of how analysis of soil liquefaction has been approached.....	6
1.4 Efforts made to calibrate constitutive models for numerical liquefaction analysis.....	8
1.5 Objectives and organization of the Thesis	10
1.5.1 Objectives.....	10
1.5.2 Organization of the Thesis	11
CHAPTER 2: SAND CHARACTERISTIC BEHAVIOUR	13
2.1 Characteristic shear behaviour of sand	14
2.2 Characteristic behaviour of sand under isotropic compression	24
2.3 Sand response to proportional loading.....	26
2.4 Pure rotation of principal stresses	26
2.5 Undrained response of sand	28
2.6 Characteristic sand liquefaction response	30
2.7 Summary of sand characteristic behaviour	37
CHAPTER 3: STRESS-STRAIN MODELS FOR SAND.....	41
3.1 Models based on elastic theory	41
3.2 Models based on incremental elastic-plastic theory	42

3.3 Brief description of the basic elements of incremental elastic-plastic theory	43
3.4 Sand characteristic behaviour within an incremental elastic-plastic framework	49
3.5 Different types of incremental elastic-plastic constitutive models ..	50
3.5.1 Critical State type of models.....	50
3.5.2 Mohr-Coulomb type of models.....	51
3.5.3 Multi-yield surface model.....	53
3.5.4 Other models	55
3.6 Key factors in modelling monotonic sand liquefaction	55
 CHAPTER 4: CONSTITUTIVE MODEL.....	57
4.1 Description and simplifying assumptions of the model.....	58
4.2 Elastic response.....	68
4.3 Plastic shear response.....	70
4.3.1 Failure and yield functions of the cone (shear) mechanism.....	70
4.3.2 Flow rule and plastic potential of the cone (shear) mechanism.....	72
4.3.3 Hardening rule of the cone (shear) mechanism	74
4.3.4 Hardening parameter of the cone (shear) mechanism.....	86
4.3.5 Pure rotation of principal stresses	87
4.4 Plastic volumetric response.....	90
4.4.1 Yield function of the cap (volumetric) mechanism	91
4.4.2 Flow rule and plastic potential of the cap (volumetric) mechanism.....	92
4.4.3 Hardening rule of the cap (volumetric) mechanism.....	92
4.4.4 Hardening parameter of the cap (volumetric) mechanism... ..	93
4.5 Total response	94
4.6 Undrained response.....	94
4.7 Model parameters.....	97
4.7.1 Elastic parameters	97
4.7.2 Plastic shear parameters	99
4.7.3 Plastic cap parameters	103
4.8 Summary	105
 CHAPTER 5: NUMERICAL ANALYSIS PROCEDURE.....	108
5.1 Explicit finite difference approach (FLAC).....	109
5.2 Numerical implementation of the proposed constitutive model	119
5.3 Modelling the single element behaviour	124
5.4 Fully drained analysis	131
5.5 Undrained analysis.....	131

5.6 True constant volume	132
5.7 Partially saturated analysis.....	133
5.8 Coupled stress-flow analysis.....	133
5.9 Summary	134
CHAPTER 6: CALIBRATION OF THE CONSTITUTIVE MODEL AGAINST SYNCRUDE SAND EXPERIMENTAL DATA	135
6.1 Capturing the characteristic behaviour of air pluviated samples (C-CORE and UBC tests)	139
6.1.1 Model parameters for air pluviated element tests	139
6.1.2 Discussion	143
6.2 Capturing the characteristic behaviour of water pluviated samples (UBC tests)	156
6.3 Sensitivity of predicted response to variation in the model parameters	163
6.4 Summary	165
CHAPTER 7: CENTRIFUGE MODELLING	172
7.1 Centrifuge Test 1.....	173
7.2 Sand in centrifuge model vs. sand specimens used for laboratory testing.....	180
7.3 Boundary conditions assumed for numerical analysis of centrifuge model	183
7.4 Numerical simulation of centrifuge model construction.....	183
7.5 Initial state of stress under an acceleration field of 50 g.....	184
7.5.1 Initial state of stress from assuming fully drained response	185
7.5.2 Initial state of stress from assuming partially drained response	185
7.6 Numerical procedure used to simulate loading of the centrifuge model.....	192
7.7 Undrained analyses of centrifuge model response to loading.....	195
7.7.1 Application of loading increments under undrained conditions	196
7.7.2 Application of loading increments under undrained conditions with allowance made for pore pressure dissipation after each loading increment	201
7.7.3 Simulation of non-dilative undrained response of centrifuge model to loading	204
7.7.4 Conclusions from undrained analyses.....	207
7.8 Coupled stress-flow analyses of the centrifuge model response to loading	208

7.8.1 Loading stage analysis from swing up simulation	209
7.8.2 Loading stage analysis from assuming fully drained response during self-weight compression	213
7.8.3 Influence of the initial state of stress in the computed response of the centrifuge model to loading	216
7.8.4 Effects of scaling centrifuge model from 50 g to 1 g and element size of the grid	220
7.8.5 Effects of friction on the bottom boundary of the centrifuge model.....	221
7.8.6 Conclusions from coupled stress-flow analyses	229
7.9 Summary	230
 CHAPTER 8: ANALYSIS OF CANLEX FIELD EVENT	233
8.1 Liquefaction event.....	233
8.2 Analysis of field event	237
8.2.1 Initial state of stress in the foundation layer	241
8.2.2 Numerical simulation of Clay Embankment and Compacted Sand Cell construction	242
8.2.3 Numerical simulation of CANLEX Embankment and Foundation Layer response to loading under partially drained conditions.....	242
8.2.4 Numerical simulation of CANLEX Embankment and Foundation Layer response to loading under undrained conditions	250
8.2.5 Hypothetical case in which the height of the embankment would have been 16 m.....	252
8.3 Implications of using the state-of-the-practice approach for liquefaction analysis.....	255
8.4 Conclusions from CANLEX Field Event analysis	259
 CHAPTER 9: SUMMARY, FINDINGS AND FURTHER STUDIES	261
9.1 Summary and findings	261
9.2 Further research.....	267
 BIBLIOGRAPHY	270
 APPENDIX A: DERIVATION OF SHEAR FLOW RULE.....	280

APPENDIX B: CONSTITUTIVE MODEL IMPLEMENTATION	282
B.1 Plane strain formulation	283
B.1.1 Incremental elastic law	283
B.1.2 Yield and plastic potential functions	284
B.1.3 Hardening/Softening parameters	285
B.1.4 Plastic corrections.....	287
B.1.4.1 Shear and volumetric yield conditions.....	290
B.1.4.2 Shear yield conditions only.....	291
B.1.4.3 Volumetric yield conditions only.....	292
B.1.4.4 Shear, volumetric and tensile yield conditions	292
B.1.4.5 Volumetric and tensile yield conditions	294
B.1.4.6 Tensile yield conditions only	294
B.1.4.7 Shear and tensile yield conditions	295
B.2 Axi-symmetric formulation.....	295
B.2.1 Loading with vertical compression under axi-symmetric conditions.....	297
B.2.2 Loading with vertical extension under axi-symmetric conditions	298
B.2.3 Shear hardening parameter under axi-symmetric conditions.....	300

LIST OF TABLES

Table 4.1 Typical values of A , $F(e)$ and the elastic exponent me	97
Table 4.2 Approximate values of the elastic shear modulus number k_G^e	98
Table 4.3 Approximate values of shear parameters for practical purposes	102
Table 6.1 Properties of Syncrude tailings sand.....	136
Table 6.2 Model parameters for capturing Syncrude Phase-I sand characteristic behaviour of air pluviated element tests.....	143
Table 6.3 Indices computed for comparing measured vs. predicted undrained response of air pluviated Syncrude Phase-I sand	155
Table 6.4 Model parameters for capturing Syncrude sand characteristic behaviour of water pluviated element tests	157
Table 6.5 Indices computed for comparing measured vs. predicted undrained response of water pluviated Syncrude sand.....	158
Table 6.6 Parameters derived from field test data and from calibrating the constitutive model against water pluviated Syncrude sand.....	160
Table 7.1 Parameters used for modelling the centrifuge model swing up according to the assumed relative density on each stage of the swing up process.....	188
Table 7.2 Comparison among $1/k_c = \sigma'_h / \sigma'_v$ ratios at the monitored points of the centrifuge model, as obtained under an acceleration field of 50 g by considering two different conditions for analysis: fully, and partially drained	191
Table 7.3 Measured and predicted maximum values of displacements and peak pore pressures for fully undrained analysis with gradual application of two load increments.....	196
Table 7.4 Maximum values of displacements and peak pore pressures from undrained analysis with periods of pore pressure dissipation between loading increments.....	202
Table 7.5 Measured and predicted maximum values of displacements and peak pore pressures for undrained analysis assuming non-dilative response	205
Table 7.6 Measured and predicted maximum values of displacements and peak pore pressures for coupled stress-flow analysis from swing up simulation ...	212
Table 7.7 Measured and predicted maximum values of displacements and peak pore pressures for coupled stress-flow analysis from assuming fully drained response during self-weight compression	215
Table 8.1 Typical material parameters used for the earth-structures at the field event site.....	240

LIST OF FIGURES

Figure 1.1 Cross-section through flow slide in Fort Peck dam at station 22+00.....	3
Figure 1.2 Cross-section through embankment No. 2 dyke.....	4
Figure 1.3 Cross-section of No. 2 dyke and phreatic surface movement	4
Figure 2.1 Stress-Strain behaviour of Ottawa sand in drained simple shear	15
Figure 2.2 Relationship between shear to normal stress ratio, $\eta=\tau/\sigma'$, and the strain increment ratio, $-(\Delta\epsilon_s/\Delta\gamma)$, of Ottawa sand in drained simple shear tests.....	16
Figure 2.3 Relationship between the stress ratio and the strain increment ratio in drained simple shear tests on Ottawa sand at low stress ratio levels	17
Figure 2.4 Undrained static behaviour of water-pluviated Syncrude sand in hollow cylinder torsion tests.....	18
Figure 2.5 Loading and unloading response in conventional triaxial paths.....	19
Figure 2.6 Stress-Strain and volume change behaviour of loose Santa Monica Beach sand in triaxial compression test with several unloading-reloading cycles.....	20
Figure 2.7 Orientation of strain increment vectors of irrecoverable nature.....	21
Figure 2.8 Contours of shear strain, γ , for loose samples of Fuji River sand	22
Figure 2.9 Stress-strain relation in torsional shear.....	23
Figure 2.10 Effect of cyclic shear strain amplitude and volumetric strain on drained stress-strain amplitude relationships.....	24
Figure 2.11 Isotropic compression of loose Sacramento River sand with primary loading, unloading and reloading branches	25
Figure 2.12 Effect of pure rotation of principal stresses in drained cyclic test on Toyoura sand	27
Figure 2.13 Stress-strain response of loose and medium sand under undrained monotonic compressive loading	29
Figure 2.14 Typical response of loose saturated sand under undrained static and cyclic loading.....	32
Figure 2.15 Typical response of saturated sand under cyclic loading with stress reversal.....	34
Figure 2.16 Undrained response of loose Syncrude sand to cyclic simple shear loading	35
Figure 2.17 Limited liquefaction followed by cyclic mobility	36
Figure 2.18 Idealized drained behaviour of sand.....	39
Figure 3.1 Bullet-shaped yield surface as proposed by Drucker et al. 1955 for triaxial test conditions.....	45
Figure 3.2 Essential features of CamClay model.....	51
Figure 3.3 Cone and Cap yield surfaces	53
Figure 3.4 Nested yield loci that are carried along with the stress point as this one moves.....	54

Figure 4.1 Idealized skeleton behaviour of sand under monotonic loading	60
Figure 4.2 Observed and predicted responses in a drained simple shear test on Ottawa sand	61
Figure 4.3 Elastic and plastic zones	62
Figure 4.4 Deviatoric view of the six-sided pyramid of Mohr-Coulomb, Matsuoka- Vermeer's model, and failure envelope measured by Vermeer (1982).....	67
Figure 4.5 Schematic representation of the failure and yield functions of the cone mechanism.....	71
Figure 4.6 Schematic representation of radial yield loci, plastic potentials, and plastic strain increment vectors induced by the cone mechanism	73
Figure 4.7 Relationship between developed stress ratio, η_d , and plastic shear strain γ^p ..	75
Figure 4.8 Plastic shear strain increment resulting from a mean stress reduction	78
Figure 4.9 Undrained static behaviour of water pluviated Syncrude sand	80
Figure 4.10 Expansion of elastic region with virgin loading.....	82
Figure 4.11 Kinematic hardening of elastic region.....	83
Figure 4.12 Reloading before reaching the image stress ratio η_{dmax}^I	84
Figure 4.13 Quadrants of stress ratio to define crossover points	85
Figure 4.14 Small rotation of the principal stress	88
Figure 4.15 Representation of the spherical yield cap in the s' : t plane	91
Figure 4.16 Soil element and equivalent fluid models.....	95
Figure 4.17 Effect of the failure ratio R_F on the shape of the hyperbolic stress-strain curve	101
Figure 5.1 Basic explicit calculation cycle	110
Figure 5.2 Basic grid element	111
Figure 5.3 Flow chart of the constitutive model numerical implementation	125
Figure 5.4 Boundary and loading conditions of a single element grid for modelling laboratory element tests	130
Figure 6.1 Syncrude sand grain size distribution curve	137
Figure 6.2 Effect of specimen reconstituting method on undrained simple shear response of Syncrude sand	138
Figure 6.3 Comparison between measured and predicted response of Syncrude sand tested in isotropic compression	144
Figure 6.4 Comparison between measured and predicted response of Syncrude sand tested in drained triaxial compression	145
Figure 6.5 Comparison between measured and predicted response of Syncrude sand tested in simple shear at constant volume	146
Figure 6.6 Repeatability of plane strain, anisotropically consolidated extension test on Syncrude sand.....	147
Figure 6.7 Effect of rotation of principal stresses in simple shear test	148

Figure 6.8 Comparison between measured and predicted response of air pluviated Syncrude sand tested in undrained triaxial compression.....	151
Figure 6.9 Comparison between measured and predicted response of air pluviated Syncrude sand tested in undrained triaxial extension.....	152
Figure 6.10 Measured and predicted response of Syncrude sand tested in undrained triaxial compression and extension	159
Figure 6.11 Measured and predicted response of Syncrude sand tested in simple shear at constant volume.....	159
Figure 6.12 Predicted vs. range of measured response in constant volume simple shear tests carried out on undisturbed (in-situ frozen) Syncrude sand (Phase-III) obtained from the field event site (J-Pit)	161
Figure 6.13 Predicted vs. measured undrained response in plane strain extension (PSE) and triaxial extension (TXE) tests on water pluviated samples (SyncrudePhase-III sand), anisotropically consolidated to the in-situ void ratio, and including a state of stress reversal	163
Figure 6.14 Sensitivity of predicted response to variation in model parameters.....	166
Figure 7.1 Initial centrifuge model and instrumentation configuration	174
Figure 7.2 Measured response of centrifuge model during swing up.....	176
Figure 7.3 Measured response of centrifuge model to loading.....	178
Figure 7.4 Suspended load during centrifuge test loading.....	179
Figure 7.5 Pattern of displacements observed in centrifuge model after the first load was applied	180
Figure 7.6 Element response in undrained triaxial compression under partially and fully saturated conditions.....	182
Figure 7.7 Boundary conditions used for numerical simulation of centrifuge test.....	183
Figure 7.8 Effect of initial state of stress in undrained response	184
Figure 7.9 Gradual increase of the acceleration field in the centrifuge test.....	186
Figure 7.10 Comparison between measured and predicted response of centrifuge model during swing up	189
Figure 7.11 Grid used to simulate the centrifuge model and loading plates.....	193
Figure 7.12 Undrained Analysis: Measured and predicted patterns of displacement after the first load of 60 kPa was applied	198
Figure 7.13 Comparison among the stress paths of element (32,7) in the centrifuge model and those from a single element subjected to compressive loading under plain and axial symmetric conditions	199
Figure 7.14 Undrained Analysis with allowance made for pore pressure dissipation between loading increments: Measured and predicted patterns of displacement following application of the first load (60 kPa) and after the first period of pore pressure dissipation	203
Figure 7.15 Comparison between non-dilative and dilative response of element (32,7) during simulation of the centrifuge test loading stage	206
Figure 7.16 Undrained analysis assuming non-dilative response: Measured and predicted patterns of displacement after application of the first loading increment of 60 kPa.....	206

Figure 7.17 Comparison between predicted response of centrifuge model to loading by assuming partially drained conditions during self-weight compression, and observed behaviour	210
Figure 7.18 Predicted patterns of displacement for coupled stress-flow analysis from swing up simulation	212
Figure 7.19 Comparison between predicted response of centrifuge model to loading by assuming fully drained conditions during self-weight compression, and observed behaviour	214
Figure 7.20 Predicted patterns of displacement for coupled stress-flow analysis from assuming fully drained response during self-weight compression.....	216
Figure 7.21 Comparison among stress paths of elements (32,7) and (16,7) as predicted from coupled stress-flow simulations of the centrifuge test loading stage that started from two different initial states of stress, namely <i>PD</i> and <i>FD</i>	219
Figure 7.22 Predicted response of centrifuge model to loading for the case in which the angle of friction at the bottom boundary was specified as 1°.....	222
Figure 7.23 Predicted response of centrifuge model to loading for the case in which the angle of friction at the bottom boundary was specified as 2°.....	223
Figure 7.24 Predicted response of centrifuge model to loading for the case in which the angle of friction at the bottom boundary was specified as 3°.....	224
Figure 7.25 Predicted response of centrifuge model to loading for the case in which the angle of friction at the bottom boundary was specified as 5°.....	225
Figure 7.26 Predicted response of centrifuge model to loading for the case in which the angle of friction at the bottom boundary was specified as 10°	226
Figure 7.27 Predicted response of centrifuge model to loading for the case in which the angle of friction at the bottom boundary was specified as 15°	227
Figure 7.28 Predicted response of centrifuge model to loading for the case in which the nodes at the bottom boundary were specified as fixed	228
Figure 8.1 Plan and cross-sectional views of liquefaction event site.....	234
Figure 8.2 Plan view of instrumentation lines through embankment	236
Figure 8.3 Pore pressure response to embankment loading in terms of piezometric heads along Lines 1, 2, 3 and 5	238
Figure 8.4 Configuration of the numerical system after construction of clay dyke and sand cell	243
Figure 8.5 Direction of major and minor principal stresses in the region where the clay embankment was located immediately after construction	243
Figure 8.6 Comparison between predicted and measured time-histories of excess pore pressures during and immediately after loading the test embankment.....	245
Figure 8.7 Pattern of displacements predicted under partially drained conditions	247
Figure 8.8 Contours of predicted total pore water pressure after the steady state seepage condition was reached.....	248
Figure 8.9 Orientation of principal stresses after pumping tailings sand behind the clay dyke under partially drained conditions.....	249
Figure 8.10 Pattern of displacements predicted under undrained conditions	251

Figure 8.11 Contours of predicted total pore water pressure after the state of equilibrium under undrained conditions was reached	251
Figure 8.12 Predicted response at mid depth of the foundation layer in Section D.....	253
Figure 8.13 Predicted undrained response at mid depth of the foundation layer in Section D, had the embankment height been 16 m in stead of 8 m.....	253
Figure 8.14 Predicted pattern of displacements, had the embankment height been 16 m instead of 8 m and loaded under undrained conditions	254
Figure 8.15 Predicted contours of total pore water pressure, had the embankment height been 16 m instead of 8 m and loaded under undrained conditions ..	255
Figure 8.16 Results from undrained analysis of CANLEX field event carried out assuming a s_{ur}/s_o ratio constant (independent of direction of loading) and equal to 0.06.....	257
Figure 8.17 Results from partially drained analysis of CANLEX field event carried out assuming a s_{ur}/s_o ratio constant (independent of direction of loading) and equal to 0.06	258

LIST OF SYMBOLS

C_{ijkl}	Elastic stiffness tensor
CSL	Critical state line
CSR	Critical stress ratio
EQL	Equivalent linear elastic
D_r	Relative density
H	Plastic modulus
M	Slope of CSL
$(N_I)_{60}$	Normalized standard penetration test resistance
PT	Phase transformation
W_p	Plastic work
$d\epsilon$	Infinitesimal total strain increment
$d\epsilon^e$	Infinitesimal elastic strain increment
$d\epsilon_{ij}^e$	Components of the elastic strain increment tensor
$d\epsilon^p$	Infinitesimal plastic strain increment
$d\epsilon^p$	Plastic strain increment vector
$d\epsilon_{ij}^p$	Components of the plastic strain increment tensor
$d\epsilon_v^p$	Plastic volumetric strain increment
$d\epsilon_l^p$	Major plastic principal strain increment
$d\epsilon_2^p$	Intermediate plastic principal strain increment
$d\epsilon_3^p$	Minor plastic principal strain increment
df	Differential of the function f
$d\sigma'_{ij}$	Components of the effective stress increment tensor
f	Yield function
g	Plastic potential function
p'	Mean normal effective stress
p'_c	Cap pressure in Camclay model
q	Generalized deviatoric stress
s_{ur}	Residual strength
v	Specific volume
$\Delta\epsilon$	Total strain increment
$\Delta\epsilon^e$	Elastic strain increment
$\Delta\epsilon^p$	Plastic strain increment
$\Delta\epsilon^{pc}$	Cap plastic strain increment
$\Delta\epsilon^{ps}$	Cone plastic strain increment
$\Delta\epsilon_v^p$	Plastic volumetric strain increment
$\Delta\gamma^e$	Elastic shear strain increment
$\Delta\gamma^p$	Plastic shear strain increment
α_σ	Angle formed by the major principal stress σ_l and the vertical
∂	Partial differential

ε_v^p	Plastic volumetric strain
$\underline{\varepsilon}_p$	Effective plastic strain
ϕ	Internal friction angle
ϕ_{cv}	Constant volume friction angle
ϕ_{PT}	Phase transformation angle
η	Stress ratio
κ	Hardening parameter
λ	Non-negative scalar function that determines the magnitude of the plastic strain increment
σ'	Effective normal stress
σ	Total normal stress
σ_1	Major principal stress
σ_2	Intermediate principal stress
σ_3	Minor principal stress
σ'_1	Effective major principal stress
σ'_2	Effective intermediate principal stress
σ'_3	Effective minor principal stress
σ'_{ij}	Components of the effective stress tensor
σ'_{vc}	Vertical effective confining stress
τ	Shear stress
τ_{st}	Static shear stress
v	Poisson's ratio
$\Delta\sigma'$	Effective stress increment
$\Delta\tau$	Shear stress increment
E	Young's modulus
G^e	Elastic shear modulus
x, y and z	Subscripts corresponding to the orientation of the Cartesian coordinate axes
$[C^e]$	Matrix of elastic coefficients
B^e	Elastic bulk modulus
me	Elastic exponent
k_B^e	Elastic bulk modulus number
k_G^e	Elastic shear modulus number
P_A	Atmospheric pressure
s'	Mean or confining stress = $(\sigma'_1 + \sigma'_3)/2$
t	Maximum shear stress = $(\sigma'_1 - \sigma'_3)/2$
f_f	Failure function
ϕ_f	Internal friction angle at failure
$N_{\phi f}$	N_ϕ factor at failure = $(1 + \sin\phi_f)/(1 - \sin\phi_f)$
η_f	Stress ratio at failure
γ^p	Plastic shear strain
ϕ_d	Developed friction angle

f^c	Cone yield function
$N_{\phi d}$	Developed N_ϕ factor = $(1 + \sin\phi_d)/(1 - \sin\phi_d)$
η_d	Developed stress ratio
$\Delta\varepsilon_v^{ps}$	Cone plastic volumetric strain increment
$\Delta\gamma^{ps}$	Cone plastic shear strain increment
ψ_d	Developed dilation angle
ϕ_{cv}	Constant volume friction angle
g^s	Cone plastic potential function
$N_{\psi d}$	Developed N_ψ factor = $(1 + \sin\psi_d)/(1 - \sin\psi_d)$
$\Delta\varepsilon_{ij}^{ps}$	Cone plastic strain increments
λ^s	Constant of proportionality between plastic strain increments and plastic potential function of the cone mechanism
$\Delta\eta$	Stress ratio increment
G_i^p	Initial plastic shear modulus
G^p	Plastic shear modulus
R_F	Failure ratio
η_{ult}	Ultimate stress ratio from the best fit hyperbola
k_G^p	Plastic shear modulus number
np	Plastic shear modulus exponent
G^*	Normalized tangent plastic shear modulus
$\Delta\eta_d$	Developed stress ratio increment
Δt	Shear stress increment
$\Delta s'$	Mean stress increment
α_σ	Angle between the direction of the major principal stress σ'_1 and the vertical
F	Factor of anisotropic plastic response
τ_{xy}	Shear stress in the $x : y$ plane
σ_d	Stress difference between the vertical and horizontal stresses
σ_v	Stress in the vertical direction
σ_h	Stress in the horizontal direction
κ	Hardener parameter
ΔW^{ps}	Increment of energy dissipated by the cone mechanism during a plastic strain increment
η_{xy}	Stress ratio on the $x : y$ plane
$d\eta_{rot}$	Stress ratio increment due to a small rotation of the principal stresses
f^c	Cap yield function
σ^c	Cap pressure
ε_v^{pc}	Cap plastic volumetric strain
$\Delta\varepsilon_{ij}^{pc}$	Cap plastic strain increments
λ^c	Constant of proportionality between plastic strain increments and plastic potential function of the cap mechanism
g^c	Cap plastic potential function
$\Delta\sigma^c$	Cap pressure increment
B^p	Plastic bulk modulus
k_B^p	Plastic bulk modulus number

m_p	Plastic bulk modulus exponent
$\Delta\kappa^s$	Cone hardener parameter increment
$\Delta\kappa^c$	Cap hardener parameter increment
κ^c	Cap hardener parameter
ε_1^p	Major plastic strain
ε_2^p	Intermediate plastic strain
ε_3^p	Minor plastic strain
$\Delta\varepsilon_1^p$	Major plastic strain increment
$\Delta\varepsilon_2^p$	Intermediate plastic strain increment
$\Delta\varepsilon_3^p$	Minor plastic strain increment
$[D']$	Constitutive model matrix in terms of effective stresses
Δu	Pore water pressure increment
B_f	Fluid bulk modulus
n	Porosity
$\Delta\varepsilon_v^f$	Equivalent fluid volumetric strain
$\Delta\varepsilon_v$	Volumetric strain
$[D_f]$	Equivalent fluid stiffness matrix
e	void ratio
A	Particle size and shape variable
V_s	Shear wave velocity
ρ	mass density of soil
G	Combined shear modulus
$\Delta\gamma$	Total shear strain increment
G_i	Combined initial shear modulus
γ	Total shear strain
γ_r	Reference shear strain
γ_f	Shear strain at failure
u	Pore water pressure
ε_v	Total volumetric strain
B_i^p	Initial plastic bulk modulus
B_i^e	Initial elastic bulk modulus
B_i	Initial combined bulk modulus

ACKNOWLEDGEMENTS

I have had the privilege of working under the supervision and advice of Professor Dr. Peter M. Byrne for the past five years. I want to thank Professor Byrne for his guidance and teachings, and of course, for the incredible examples and sources of encouragement that his excitement, intensity, and love for research are.

I would also like to express my gratitude to the members of my supervisory/examining committee, Professors J. A. Howie, Y. Vaid, W. D. L. Finn, D.L. Anderson, O. Hungr, D. Chan and Dr. M. K. Lee for their helpful comments and suggestions.

Financial aid provided by the Consejo Nacional de Ciencia y Tecnología (CONACYT), and the Facultad de Ingeniería, Universidad Nacional Autónoma de México (FI-UNAM), as well as the Graduate Research Assistantship granted by the University of British Columbia are greatly appreciated. Golder Associates Ltd support for printing the final version of the manuscript, is also acknowledged.

Sincere thanks to my colleagues A. Hameiri, A. Eliadorani and S. Sivathayalan for their friendship, support and helpful discussions.

To my father Humberto, my sisters Margarita and Claudia, and to my absolutely extraordinary friends in Mexico and Toronto, and Leyla in Vancouver, thanks very much for always being there for me, and putting up with five years of absence.

Special thanks to Professor Agustín Deméneghi C. for guiding me through my first steps in Engineering, and to Professor Leonardo Zeevaert W. for bringing me back on the right track and lighting up my inner flame of love for Geotechnical Engineering.

To Leigh-Ann and Stephanie, thanks very much for your patience and for all the playtime hours stolen from you.

It would be impossible to describe with words all the contributions that my lovely wife Erika has made to this work and to my life. Thank you Erika from the bottom of my heart. I love you!

Finally, I would like to dedicate this work to the memory of my mother, Ninfa Cadena Flores.

CHAPTER 1

INTRODUCTION

This thesis deals with constitutive modelling of sand and numerical analysis of static liquefaction phenomena (liquefaction triggered by rapid monotonic loading). The study is geared towards modelling the Canadian Liquefaction Experiment (CANLEX) embankments that included a *field event* in which a test embankment was built over a loose sand foundation layer, and a *centrifuge test* performed on a model of the prototype structure. The response of such earth-structures was characterized by the displacements and pore pressures observed during the experiments. In order to numerically model the CANLEX embankments and capture the observed responses, a new procedure for static liquefaction analysis capable of predicting both displacements and pore pressures was developed. This procedure required the development of a stress-strain model based on the characteristic behaviour of sand. The constitutive model was calibrated by capturing the behaviour of Syncrude sand as observed in laboratory element tests. The numerical procedure was first verified by modelling one of CANLEX centrifuge experiments and then applied to the field event. To place the study into context, this first chapter describes liquefaction phenomena and presents an overview on how liquefaction analysis has been approached. The objectives as well as the organization of the thesis are also described.

1.1 Consequences of soil liquefaction: Some case histories

Many cases of soil liquefaction have been reported in the literature, e.g. Seed (1973, 1979a, and 1984), Casagrande (1975), Ishihara (1984), O'Rourke and Hamada (1992). In this section, only two case histories will be presented in order to illustrate possible consequences of liquefaction: (i) Fort Peck dam and (ii) Mochikoshi dams.

Casagrande (1975) explained the sudden failure of a portion of Fort Peck dam in 1938, while this was almost completed, as a flow slide induced by liquefaction in the fine sand zone of the shell, and spreading into the foundation sand layer. A cross-section through the slide in two different scales, i.e. 1:1 and 1:5 (horizontal to vertical), is shown in Figure 1.1. After the slide, the mobilized mass was almost level. Movement ceased in about 3 minutes, during which time portions of the upstream toe moved about 400 meters from their original locations with the speed of a rapidly moving river, Casagrande (1975). This case is typical of a liquefaction failure induced by monotonic loading during construction, like those that have occurred in several mining facilities, e.g. Fort McMurray, Alberta.

A very well documented case history of liquefaction is the case of the Mochikoshi tailings dams failure. As a result of the Izu-Ohshima-Kinkai earthquakes of January 14 and 15, 1978, two dams, termed dyke No. 1 and dyke No. 2 (Ishihara, 1984), that contained mine waste in Japan, failed. The dams were built using the upstream construction procedure. Ishihara (1984) indicated that dyke No. 1 failed approximately 10 seconds after the main earthquake, due to liquefaction of the tailings materials.

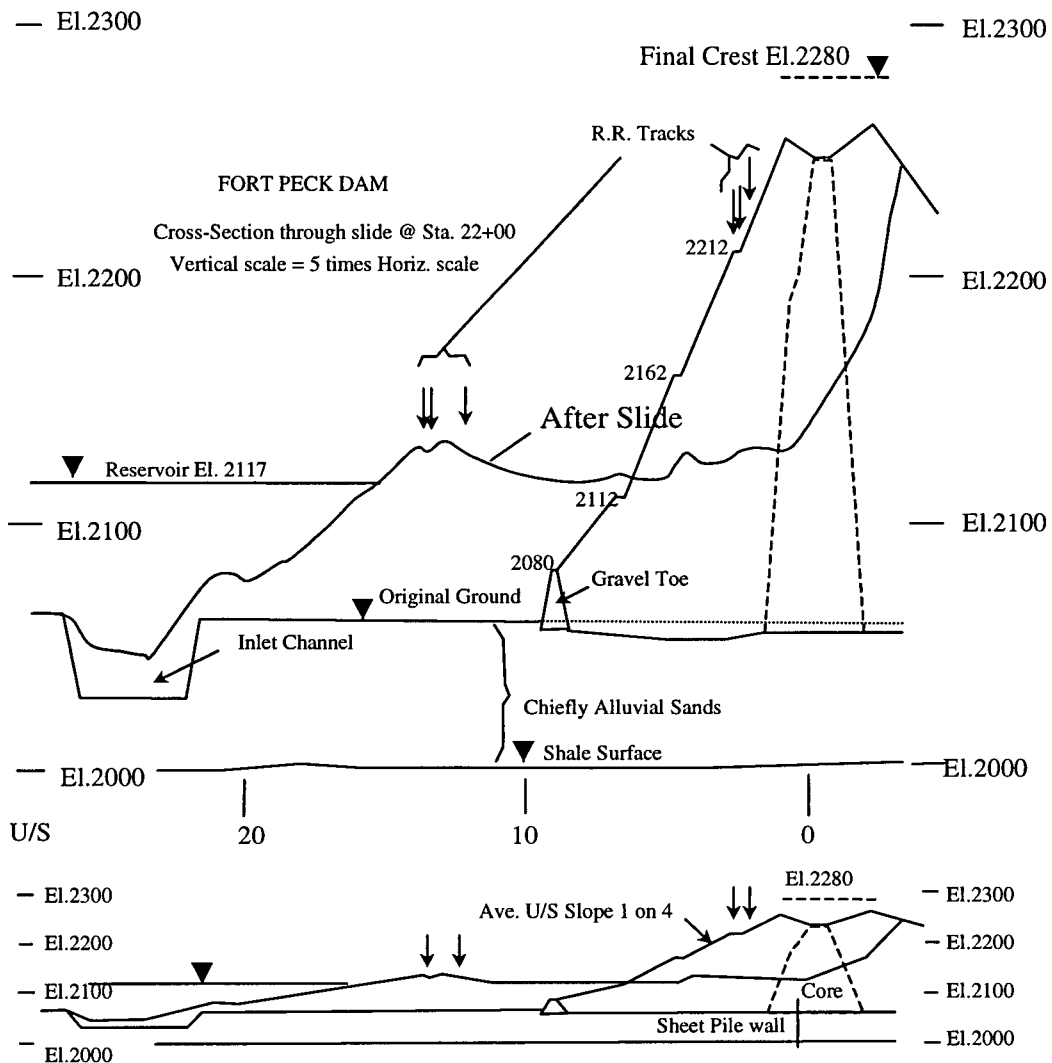


Figure 1.1 Cross-section through flow slide in Fort Peck dam at station 22+00 (after Casagrande, 1975).

Dyke No.2 (Figure 1.2) failed about 24 hours after the main earthquake and Ishihara (1984) concluded in his analysis that the delayed failure could be explained by upward movement of the groundwater level within the dyke. He explained that excess pore water pressures that developed during the earthquake caused the tailings behind the

dam to liquefy. Although this was not enough to induce failure, a hydraulic gradient was generated, causing the groundwater within the dam to move upwards (Figure 1.3), and inducing instability. After carrying out a limit equilibrium analysis, Ishihara (1984) concluded that a higher position of the phreatic surface would induce instability in the slope. When the failure took place, a huge mass of tailings flowed down the valley with catastrophic consequences. Details of this case history can be found in Ishihara (1984), and Jitno and Byrne (1995).

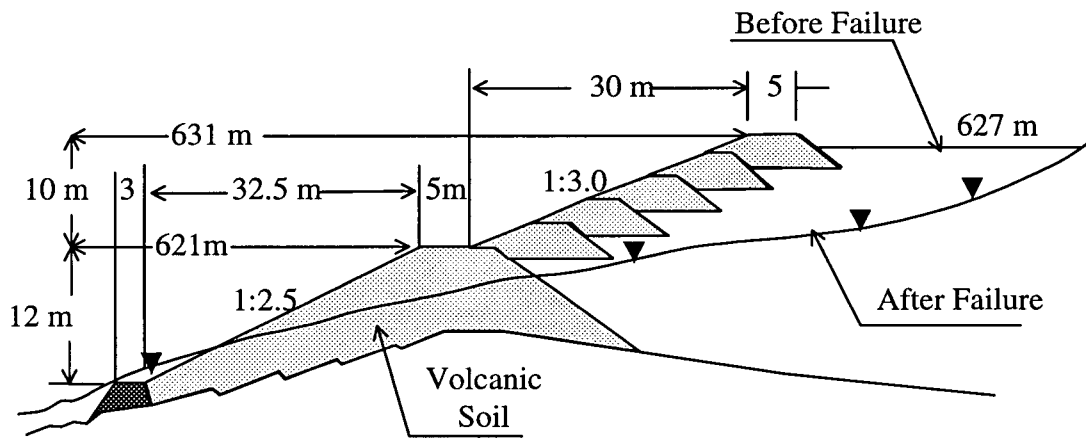


Figure 1.2 Cross-section through embankment No. 2 dyke (after Ishihara, 1984).

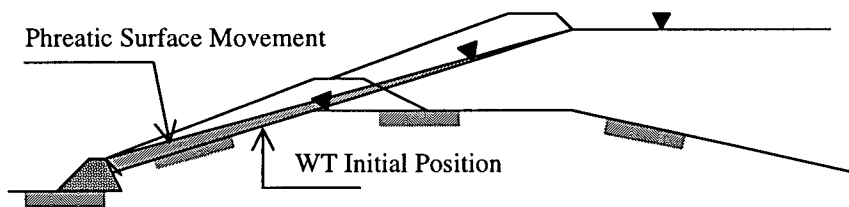


Figure 1.3 Cross-section of No. 2 dyke and phreatic surface movement (after Ishihara, 1984).

Although the liquefaction of tailings behind dyke No.2 was not triggered statically, the analysis performed by Ishihara (1984) suggests that pore water pressure redistribution can lead to a flow failure under static stresses. Thus, this phenomenon should not be disregarded in analysis.

1.2 Liquefaction

Two aspects that characterize liquefaction of saturated cohesionless soils are: (i) loss of strength and stiffness, and (ii) large deformations. A detailed discussion of sand characteristic behaviour and the conditions that lead to liquefaction will be presented in Chapter 2.

Soils in general, and sands in particular, are comprised of particles that are in contact with each other, forming several different arrangements or structures. The strength of sand is essentially controlled by friction at grain contacts arising from the contact forces among particles. Hence, in terms of stresses, the role of the effective stress σ' is a fundamental one, since it is σ' and not the total stress σ that governs the deformation response of sand.

Under shear loading, sand exhibits a tendency to change in volume. When sand is saturated, loads are transferred first to the fluid and the tendency of the soil skeleton to dilate or contract results in a change in the pore fluid pressure and a change in effective stress. If the soil skeleton tends to contract under partially drained or undrained conditions, the pore fluid pressure increases, the effective stress decreases, and therefore, the shear strength drops. Under such circumstances, if the state of stress in the soil

exceeded the reduced strength of the material, a failure would occur. Thus, a substantial loss of strength and excessive deformations of sand, i.e. *liquefaction*, can occur as a result of shear-induced pore pressure arising from shear loading under partially drained or undrained conditions. A rise in the groundwater level, which in turn would reduce the effective stress, is another factor that could lead to liquefaction.

However, liquefaction of a granular soil is closely related to the drainage conditions and an undrained scenario may not be the worst possible, as suggested by Vaid (1998). Since sand is a porous material, the pore water can flow in and out the soil. Hence, only when the rate at which the pore pressure increases is greater than the rate of pore pressure dissipation, can a substantial loss of strength take place. Therefore, the drainage condition is a key factor in determining the feasibility of liquefaction occurrence.

1.3 Brief historical review of how analysis of soil liquefaction has been approached

Comprehensive reviews of the “state-of-the-art” regarding liquefaction and the developments in this field have been presented by Yoshimi et al. (1977), Seed (1979b), Finn (1981), Ishihara (1993) and Robertson and Fear (1995). Here, only an overview is given. Since liquefaction induced by rapid monotonic loading under partially drained and undrained conditions is the focus of this dissertation, the discussion will be mainly centered in these types of problems.

After the two major earthquakes that took place in Alaska and Japan, in 1964, determining the mechanisms that trigger liquefaction and developing procedures to

predict liquefaction occurrence, became a prime objective in geotechnical engineering. Pursuing this goal, liquefaction was induced in sand specimens by Seed and Lee (1966) and Castro (1969) in the triaxial test apparatus. Seed and Lee considered triggering liquefaction, while Castro focused on the residual strength adequate to prevent a flow slide. Under the light of these tests the study of liquefaction developed rapidly.

Liquefaction resistance was later measured in different laboratory tests: cyclic simple shear (e.g. Peacock and Seed, 1968; Finn et al., 1971b), torsional cyclic simple shear tests (e.g. Ishihara and Li, 1972), large scale shaking table tests (e.g. Finn et al., 1970, 1971a; Byrne et al., 1982), and centrifuge tests (e.g. Steedman, 1986). Despite the progress achieved with these tests, empirical rules based on case histories were needed for liquefaction assessment. Thus, early laboratory studies complemented with empirical rules allowed geotechnical engineers to develop empirical methods for assessing liquefaction potential.

In a liquefaction problem, there are three aspects that have to be investigated:

- 1) Will liquefaction be triggered and to what extent?
- 2) If so, is the residual strength adequate to prevent a flow slide?
- 3) What displacements will occur?

Thus, a complete liquefaction analysis may comprise three stages: (i) triggering analysis, (ii) flow slide analysis, and (iii) displacement analysis. The three of them are usually performed separately.

Liquefaction assessment can be done based on the physics of a specific problem using a mechanics based approach. This is most commonly achieved utilizing the *total*

stress approach or *decoupled analysis* in which pore pressure effects are indirectly considered through reduced strength and stiffness. The approach is simple, but does not allow estimating pore pressures directly. In contrast, the *effective stress approach* for studying liquefaction allows predicting pore pressures but it is more complex. If computation of stresses, strains and pore pressures is carried out simultaneously, the effective stress approach is termed *coupled analysis*. If computation of pore pressures and its effects on stresses and strains is performed through a separate pore pressure model, the analysis is called *indirectly* or *loosely coupled analysis*. Both methods of analysis, the total and the effective stress approaches, use numerical procedures for solving the dynamic equations of motion and they are typically coded in computer programs.

Displacements of the deformed soil mass, whether associated with liquefaction or not, depend on the fundamental stress-strain relation of the soil. Thus, both the total and the effective stress approaches require *stress-strain laws* to simulate soil behaviour and account for strain compatibility. The two methods of analysis are usually carried out assuming undrained conditions and hence, the effects of pore water pressure dissipation and redistribution are not accounted for.

1.4 Efforts made to calibrate constitutive models for numerical liquefaction analysis

As discussed in the previous section, stress-strain laws that simulate soil behaviour are necessary for liquefaction assessment. Moreover, the effective stress approach not only requires stress-strain laws, but also *constitutive models* that simulate

sand *fundamental behaviour*. Once the element behaviour of a soil is captured by such a model, the model will predict all stress paths. Hence, the parameters of the constitutive models must be obtained for each particular soil. This is usually done by back analysis of laboratory tests, e.g. triaxial and simple shear tests. In addition, numerical procedures need to be validated under complex loading patterns that cannot be simulated in laboratory tests. Thus, centrifuge tests have been used to study liquefaction phenomena and validate models beyond the possibilities of conventional laboratory testing. Two major examples of these efforts are: the VELACS project (VERification of Liquefaction Analysis using Centrifuge Studies, Arulanandan and Scott, 1994) and the CANLEX project (CANadian Liquefaction EXperiment).

The VELACS Project involved calibration and verification of analytical methods to simulate liquefaction triggered by dynamic loading in nine different centrifuge tests. The centrifuge models were subjected to base acceleration simulating earthquake and a group of numerical modellers was asked to predict the response of the models; measured and numerically predicted values of accelerations, pore water pressures and displacements were compared. Details of the project can be found in Arulanandan and Scott (1994).

The CANLEX project was a major research effort in Canada, to study soil liquefaction. The project started in February 1993, and ended in December 1997. This project was funded through a Collaborative Research and Development Grant from the Natural Sciences and Engineering Research Council of Canada (NSERC), Syncrude Canada Ltd., Suncor Inc., Highland Valley Copper, BC Hydro, Hydro Quebec and Kennecott Corporation. The collaboration includes the geotechnical consultants, EBA

Engineering Consultants Ltd., Klohn-Crippen Consultants Ltd., AGRA Earth and Environmental Ltd., Golder Associates Ltd., and Thurber Engineering Ltd., as well as, faculty, staff and students from the Universities of Alberta, British Columbia, Laval and Carelton. The main objectives of this endeavour were as follows:

- Develop and evaluate sampling techniques for sandy soils.
- Calibrate and verify in-situ testing methods.
- Characterize sand in order to predict its liquefaction response.
- Perform four centrifuge tests on model embankments to help design a full-scale liquefaction event and validate numerical analysis procedures.
- Carry out a statically triggered, full-scale liquefaction event at the Syncrude site near Fort McMurray, Alberta.
- Calibration of numerical models to predict liquefaction phenomena.

A comprehensive list of the very large number of references with regard to the CANLEX project can be found in Robertson and Wride (1997).

1.5 Objectives and organization of the Thesis

1.5.1 Objectives

Since catastrophic consequences due to soil liquefaction have been observed on numerous occasions, the development of reliable methods for predicting these phenomena is essential for geotechnical engineering. In the previous sections, it was emphasized that from the analytical methods, the effective stress approach or coupled

stress analysis was the only one capable of closely capturing the fundamental behaviour of sand, as well as the pre and post-liquefaction response. Nonetheless, to keep the effective stress approach within reach of geotechnical engineering practice, the constitutive model has to be simple. In addition, the parameters of the model should be obtained from conventional laboratory tests. With this philosophy, the objectives of this research were as follows:

- 1) Develop a constitutive model capable of closely capturing sand characteristic behaviour and predicting liquefaction.
- 2) Calibrate the developed constitutive model against experimental data obtained from conventional laboratory tests.
- 3) Validate the constitutive model and the numerical analysis procedure. This was achieved by comparing measurements taken in one of the CANLEX centrifuge embankments in which liquefaction was triggered by rapid loading, with results of undrained and partially drained (coupled stress-flow) analyses of that test.
- 4) Apply the calibrated analysis procedure to the CANLEX full-scale static liquefaction event carried out at the Syncrude site near Fort McMurray, Alberta, and compare field measurements of pore water pressures and displacements with predicted values.

1.5.2 Organization of the thesis

This thesis deals with constitutive modelling of sand and numerical analysis of liquefaction phenomena. The work is divided into nine main chapters:

- Chapter 1 describes liquefaction phenomena, different approaches to liquefaction analysis of sand, and the objectives as well as the organization of the thesis.

- Chapter 2 discusses sand characteristic behaviour.
- Chapter 3 reviews different types of constitutive models for granular soils and its main attributes.
- Chapter 4 presents in detail the proposed constitutive model for sand liquefaction analysis and methods for determining the model parameters.
- Chapter 5 discusses the numerical analysis procedure used in this study and the different ways in which drainage conditions are incorporated into the analysis.
- Chapter 6 deals with calibration of the proposed constitutive model against experimental data and discusses the parameters of the model.
- Chapter 7 describes the centrifuge modelling of CANLEX embankments, compares the numerical simulation of one of these centrifuge tests with actual measurements, and discusses some effects of boundary conditions in centrifuge modelling.
- Chapter 8 includes the analysis of the full-scale CANLEX embankment, also called Field Event, and compares the results from undrained and coupled stress-flow numerical analyses with field measurements.
- Chapter 9 summarizes the work done in this research, the conclusions drawn from the achieved results, and points out important issues related to this study that require further attention and work.

CHAPTER 2

SAND CHARACTERISTIC BEHAVIOUR

In this chapter, sand characteristic behaviour and the mechanisms that trigger liquefaction will be discussed. Sand is a granular material and its particles are packed in states ranging from very loose to very dense. The particles are generally not bonded and under the action of loading, they tend to rearrange themselves to cope with the load. In contrast to metals, which only exhibit volumetric deformations when the mean stress is changed, sands usually change in volume when they are sheared. This phenomenon is termed *dilatancy* and it is a very important characteristic of sands. Dilatancy represents the coupling between shear and volumetric strains, termed *shear-volume coupling*, and it is the fundamental reason for the difference between drained and undrained response of sand, as will be seen later.

Because of dilatancy, sand tends to change in volume during loading. If water is present within the soil, the pore water has to flow in and out of the voids of the soil to allow rearrangement of sand particles. When the pore water drains freely during loading, volumetric changes occur and the sand exhibits a response termed *drained*. On the other hand, when drainage is prevented from occurring, sand presents a response called

undrained. Between these two extreme drainage conditions, the response is termed partially drained.

2.1 Characteristic shear behaviour of sand

Vaid et al. (1981) investigated the behaviour of Ottawa sand at different relative densities in drained simple shear tests. Results from such tests were interpreted here in terms of stress ratio (Figure 2.1) rather than shear stress only, by assuming the horizontal plane as the plane of maximum shear stress. Here, it is seen that the stress ratio vs. shear strain relation is nonlinear and depends on the material's density. A loose material contracts (negative dilatancy) as it shears, and its shear response is much softer than a dense material, which contracts at low values of the stress ratio and then dilates as it shears at higher values of stress ratio, Figures 2.1*a* and *b*. In addition, an ultimate value seems to be approached by the stress ratio curves at large strains.

Stress dilatancy of sand has been studied by several researchers, e.g. Rowe (1962, 1971), Bishop (1966), Matsuoka and Nakai (1977), and Negussey and Vaid (1990). The data from drained simple shear tests by Vaid et al. (1981) on Ottawa sand presented in Figure 2.1 was further examined here in terms of stress and strain increment ratios (Figures 2.2 and 2.3). Here, it can be observed that when the shear to normal stress ratio, $\eta = \tau/\sigma'$, is greater than approximately 0.2 to 0.3, a nearly unique relationship exists between η and the strain increment ratio, $(\Delta\varepsilon_v / \Delta\gamma)$. At stress ratios (η) less than about 0.2, the data points in these figures fall below the trend line.

However, as will be discussed later in this section, strains directly measured in the laboratory (namely *total strains*) comprise two parts: (i) a component that is recoverable

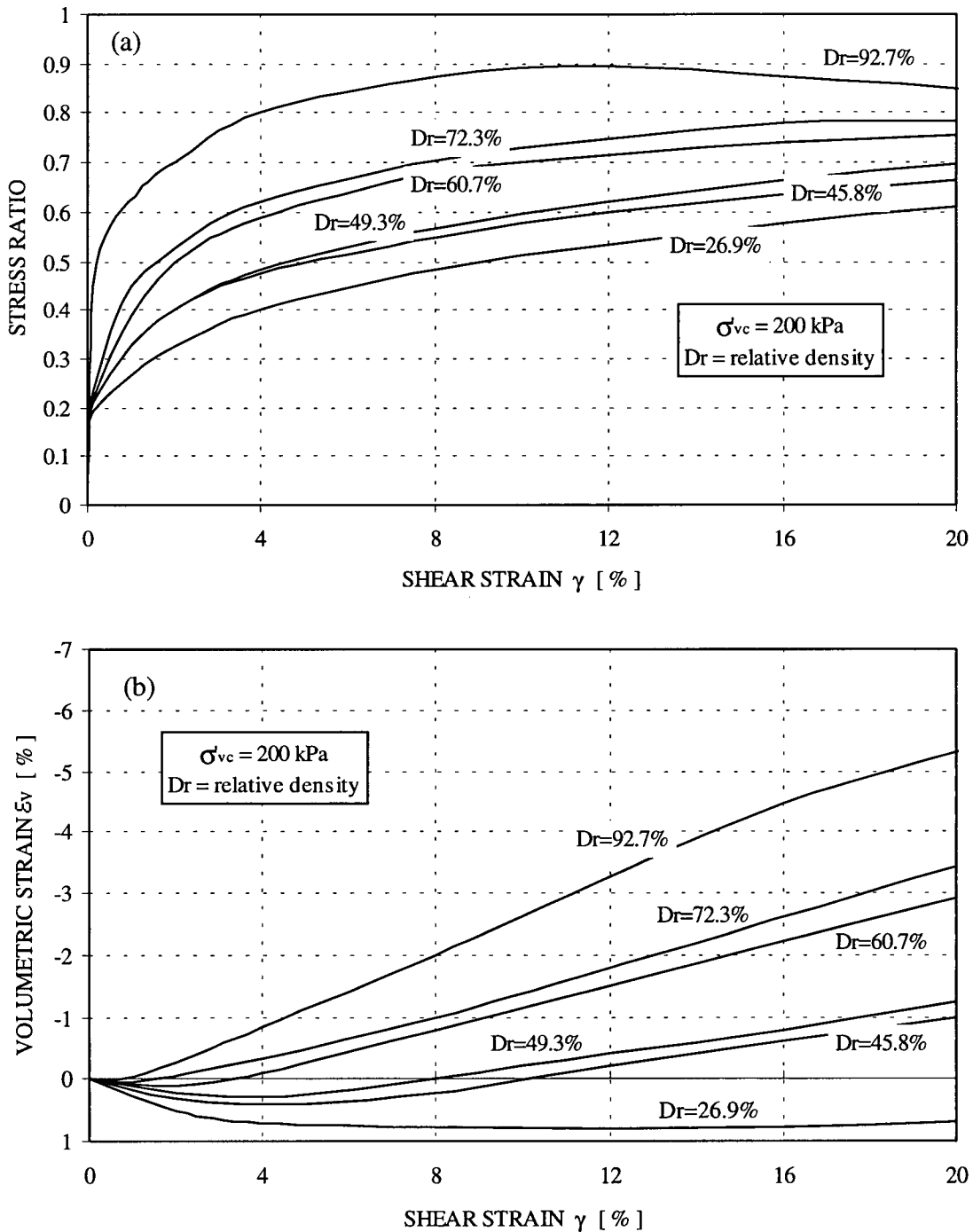


Figure 2.1 Stress-Strain behaviour of Ottawa sand in drained simple shear (modified from Vaid et al. 1981). (a) Shear behaviour. (b) Volumetric behaviour. σ'_{vc} , vertical effective confining stress.

(if the state of stress is brought back to the initial condition), and (ii) an irrecoverable component. In addition, while recoverable strains dominate the observed *total strain* response at low strain levels (10^{-4} to 10^{-2}), irrecoverable strains dominate at higher strain levels. Separating measured *total strains* into their recoverable and irrecoverable components at low stress ratio levels and hence small strains is difficult to achieve in the laboratory. Therefore, the results shown in Figures 2.2 and 2.3 in terms of *total strains* should be considered carefully. Strictly, the rate of dilatancy (Rowe, 1971) refers to the strain increment ratio in terms of *irrecoverable strains* and the results in Figures 2.2 and 2.3 should be presented in such terms to better assess the stress dilatancy relationship.

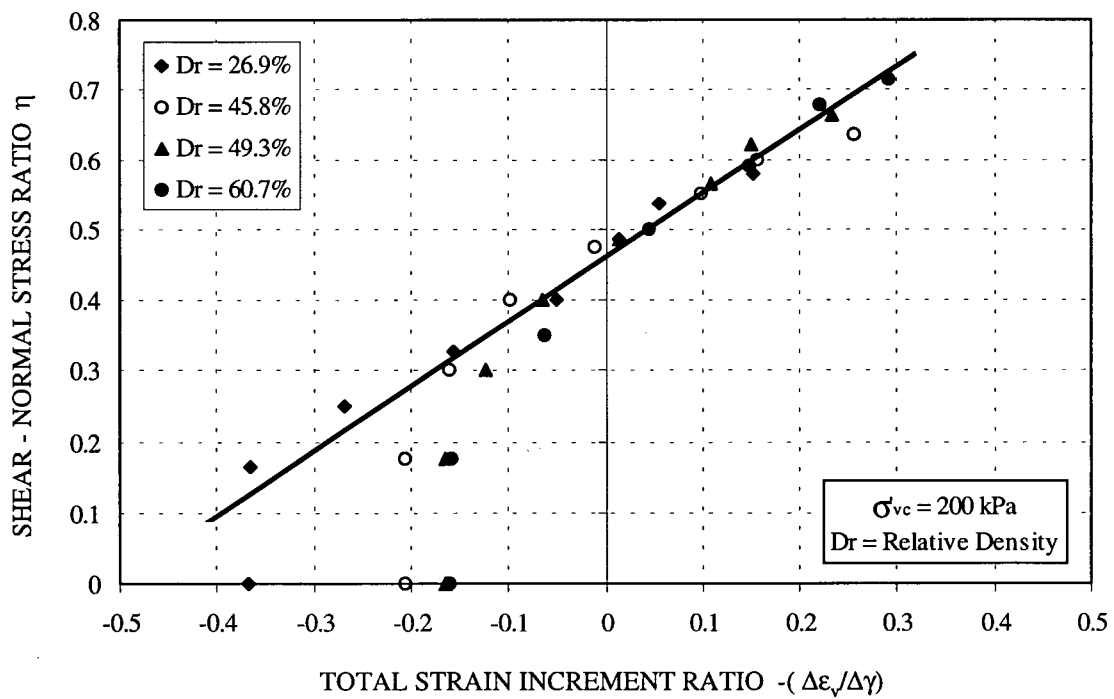


Figure 2.2 Relationship between the shear to normal stress ratio, $\eta = \tau/\sigma'$, and the strain increment ratio, $-(\Delta\epsilon/\Delta\gamma)$, of Ottawa sand in drained simple shear tests (basic data obtained from Vaid et al. 1981).

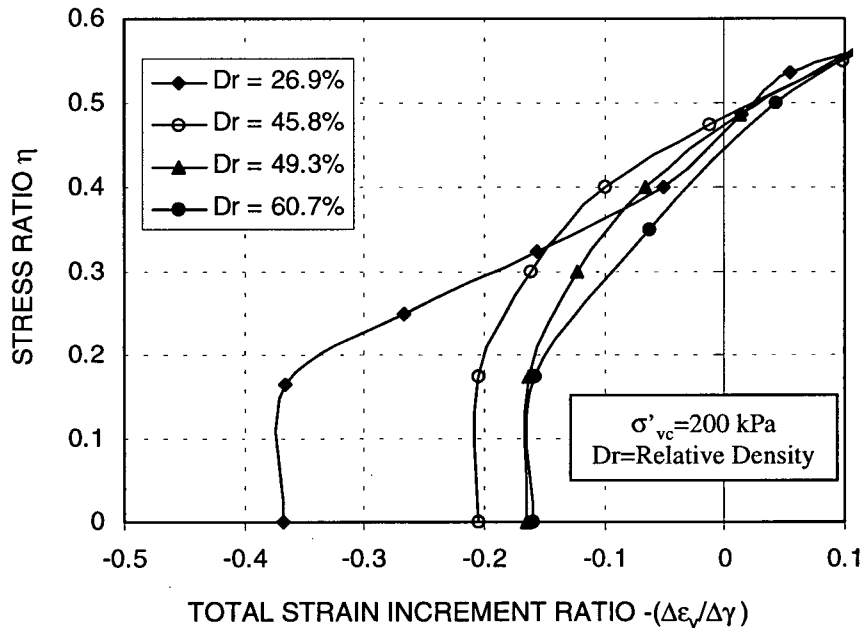


Figure 2.3 Relationship between the stress ratio and the strain increment ratio in drained simple shear tests on Ottawa sand at low stress ratio levels (basic data obtained from Vaid et al., 1981).

The fact that the data points in Figures 2.2 and 2.3 fall below the trend line at η less than about 0.2 is to be expected since recoverable rather than irrecoverable strains dominate the total strain response at small stress ratio levels. This topic will be further examined and discussed in Chapter 4, Section 4.1.

For first time monotonic loading, the direction in which sand is loaded has a very strong effect on sand behaviour and this has been studied by several researchers, e.g. Park and Tatsuoka (1994), Vaid et al. (1995a) and others. Results from Vaid et al. (1995a) are shown in Figure 2.4 to illustrate the difference in response of Syncrude sand at identical initial states. The tests were carried out in the hollow cylinder device and the angle α_σ that the major principal stress σ_1 forms with the vertical represents the direction of loading. The samples were prepared using the water pluviation technique and

hydrostatically consolidated to a confining stress of 400 kPa. Subsequently, load was applied under $b = (\sigma_2 - \sigma_3)/(\sigma_1 - \sigma_3) = 0.5$, keeping the direction of σ_1 constant during loading. The stiffer response was obtained when the direction of σ_1 coincided with the vertical, $\alpha_\sigma = 0$, i.e., σ_1 was perpendicular to the bedding plane of sand deposition. As the angle α_σ gradually increased from 0° to 90° , the response became softer. This type of anisotropy is termed *inherent anisotropy*, and is related to the structure formed by the sand grains as they are deposited.

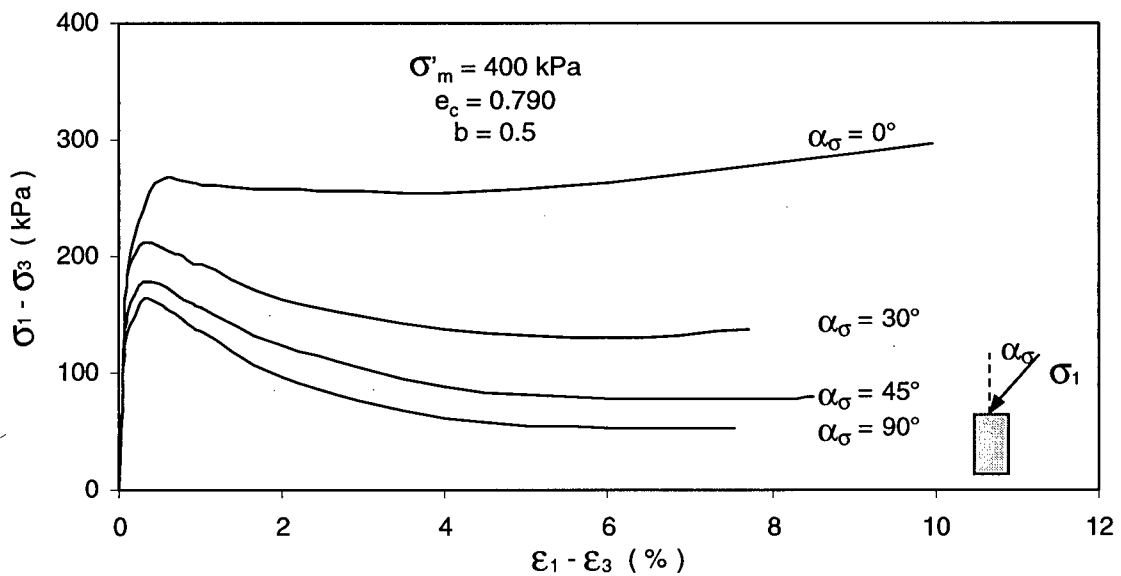


Figure 2.4 Undrained static behaviour of water-pluviated Syncrude sand in hollow cylinder torsion tests (modified from Vaid et al. 1995a). σ'_m , effective mean normal stress; $b = (\sigma_2 - \sigma_3)/(\sigma_1 - \sigma_3)$; e_c , voids ratio at σ'_m .

Results of drained triaxial compression tests on Ottawa sand conducted by Negussey (1984), including cycles of loading, unloading and reloading, but without reversing the sign of the shear stress, are shown in Figure 2.5. Several important features of the characteristic behaviour of sand can be noticed in this figure:

- 1) Sand exhibits a much stiffer response upon unloading than for primary loading.

- 2) From the total strain achieved during primary loading, part is recoverable, but a significant part of it is permanent (irrecoverable).
- 3) At strains less than 0.05%, the unload-reload loop area of the stress-strain curve is small and for practical purposes, the unload-reload curves could be reasonably approximated by a straight line (Line A). Nonetheless, as the strain level increases, the loops become larger and the difference in slope of the unload-reload curves grows (slopes of Lines B and C).
- 4) Once the reload curve reaches approximately the same stress level from where unloading was started the stress-strain curve follows the trend of the primary loading curve.

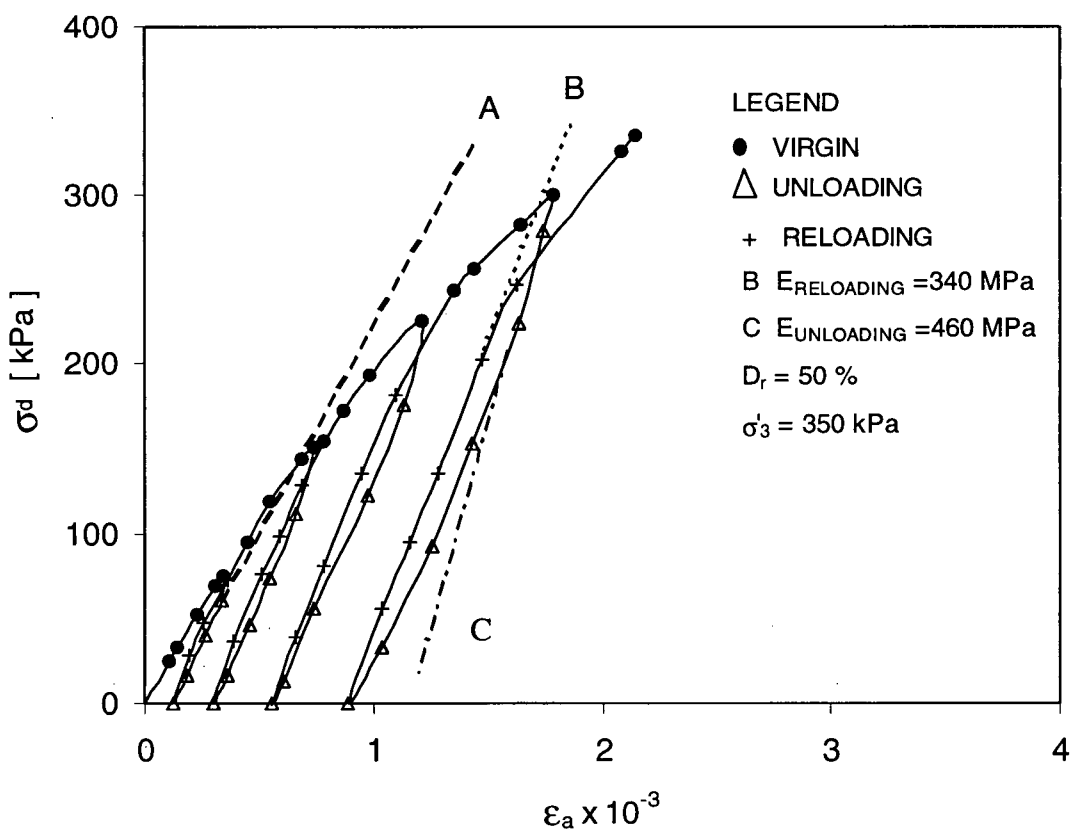


Figure 2.5 Loading and unloading response in conventional triaxial path (after Negussey, 1984).

The same observations apply to results of triaxial compression tests on loose Santa Monica Beach sand presented by Lade and Boonyachut (1982) and shown in Figure 2.6. It is interesting to see in this figure that at low strain level, the unload-reload loop of the volumetric strain curve is very small. However, at higher levels of strain, the loops in the stress-strain curve increase and the volumetric strain curve shows that some contraction occurs during the unload-reload cycle, particularly when the sand has started to dilate under primary loading (third cycle).

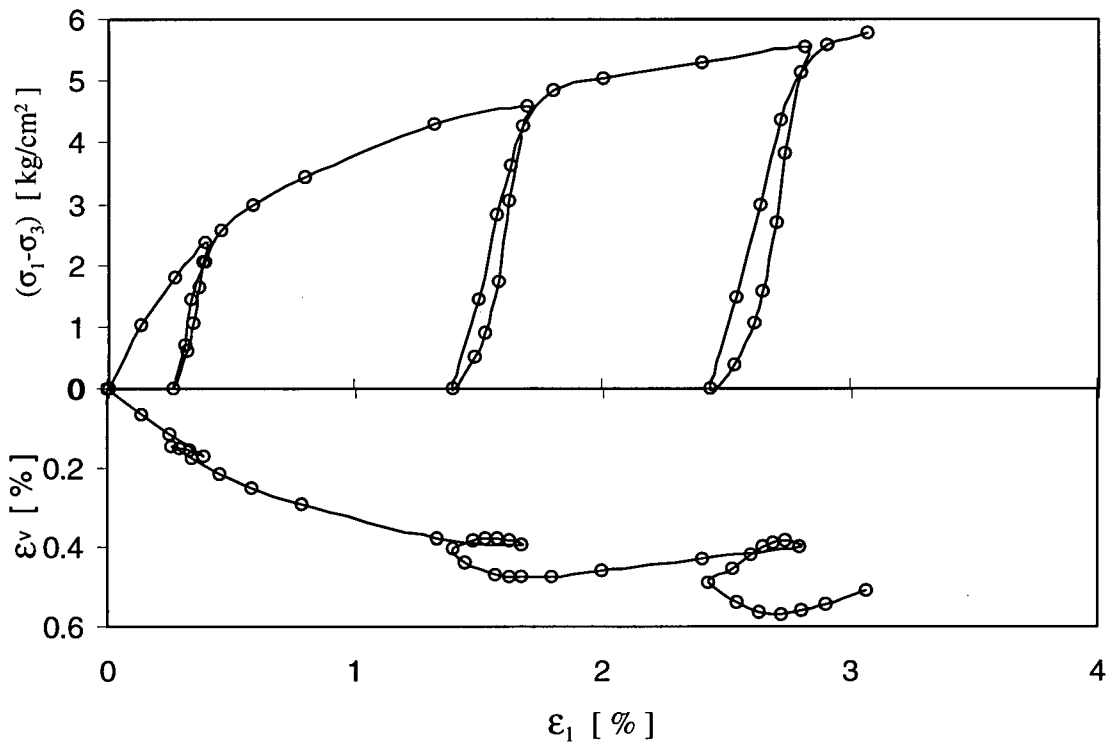


Figure 2.6 Stress-Strain and volume change behaviour of loose Santa Monica Beach sand in triaxial compression test with several unloading-reloading cycles (after Lade and Boonyachut, 1982).

Poorooshasb et al. (1966 and 1967) carried out a series of triaxial tests on Ottawa sand to study the nature of deformation of sand. In this study, sand was shown to behave as a strain hardening material. In addition, it was observed that once a certain stress ratio

was achieved in a sand sample, upon unloading and subsequent reloading, irrecoverable strains did not commence again until approximately the previous level of stress ratio was reached. Furthermore, the strain increment vectors $\Delta\epsilon$ were separated into two components: one corresponding to strains that were recoverable and another corresponding to those of irrecoverable nature. These researchers concluded that the components of the strain increment vectors that were of irrecoverable nature were perpendicular to a family of geometrically similar curves (dashed curves in Figure 2.7). However, these curves were not the lines of constant stress ratio that marked the stress level at which the nature of deformations changed upon reloading (Figure 2.7).

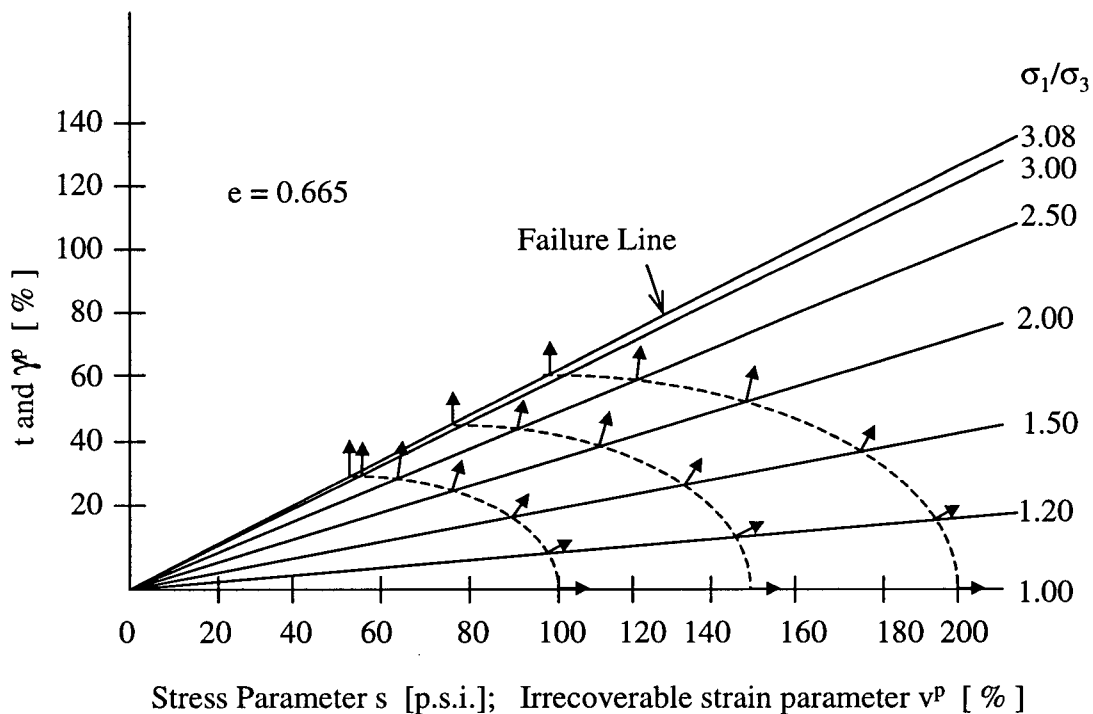


Figure 2.7 Orientation of strain increment vectors of irrecoverable nature (after Poorooshagh et al. 1966). e , void ratio; σ_1 and σ_3 , major and minor principal stresses, respectively; $s = \sqrt{1/3}(\sigma_1 + 2\sigma_3)$; $t = \sqrt{2/3}(\sigma_1 - \sigma_3)$; $v^P = \sqrt{1/3}(\epsilon_1^P + 2\epsilon_3^P)$; $\gamma^P = \sqrt{2/3}(\epsilon_1^P - \epsilon_3^P)$.

Tatsuoka and Ishihara (1974) and Ishihara et al. (1975) conducted studies on sand to determine the shape of the curves that marked the commencement of irrecoverable strains upon reloading. They used sand specimens with different densities and followed a variety of stress paths. Results of these studies showed a family of successive curves, i.e. not quite straight lines, joining points of same shear strain (Figure 2.8). Ishihara et al. (1975) suggested that these shear strain contours could be reasonable approximated by straight lines passing through the origin, at least when the effective mean stress was less than 200 kPa.

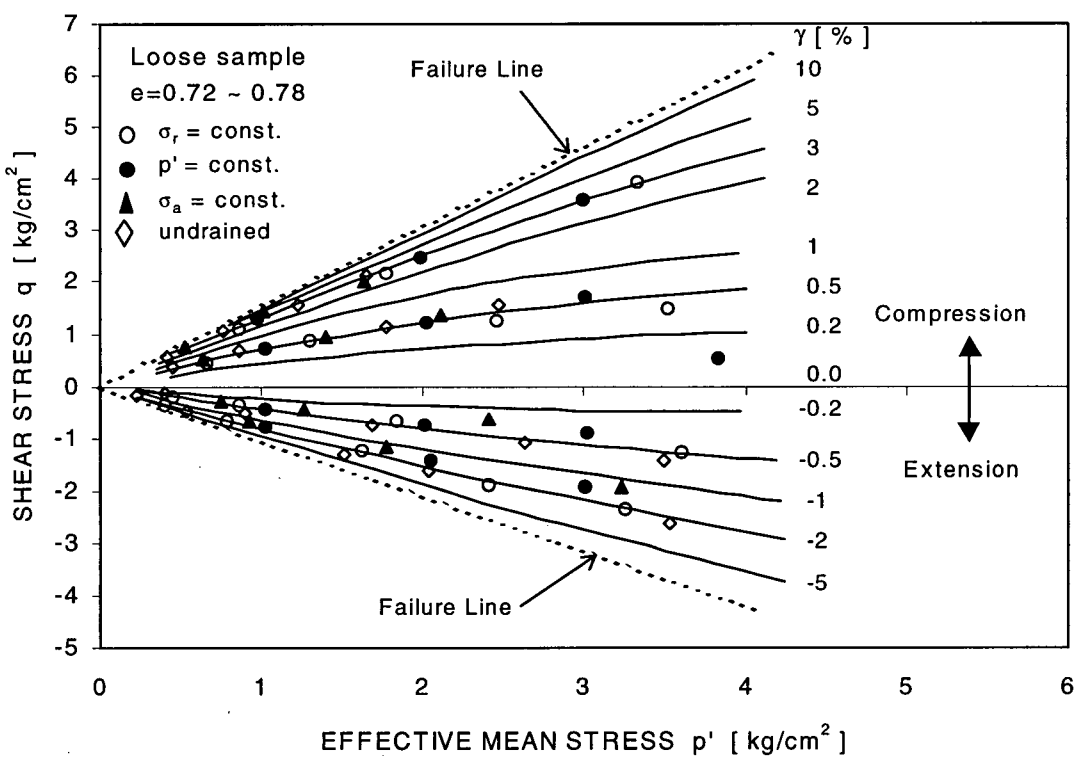


Figure 2.8 Contours of shear strain, γ , for loose samples of Fuji River sand (after Ishihara et al. 1975).

In contrast with the cases discussed above, sand can be loaded in one direction and subsequently unloaded to a point in which the shear stress becomes of the opposite sign. A change in sign of the shear stress is referred to here as *stress reversal*, Figure 2.9. When stress reversals take place, the unload-reload loops are not small. In fact, at the points in which stress reversals occur the stress-strain curve bends again and the nature of strains changes from being mainly recoverable, before stress reversal, to mainly irrecoverable, after stress reversal. Upon reloading from a point such as A (Figure 2.9), sand exhibits an even more complex behaviour. Now, the reload stress-strain curve remains stiff and the strains remain as mainly recoverable, even after stress reversal takes place. However, the stress-strain response becomes softer and the strains become mainly irrecoverable again at a lower stress level, point B in Figure 2.9, than the maximum stress level established during primary loading (point C). This suggests that such maximum level changes when stress reversals take place. Furthermore, if sand is subjected to unload-reload cycles, keeping the amplitude of shear strain constant, the response becomes stiffer as the volumetric strain accumulates, Figure 2.10 (Martin et al., 1975).

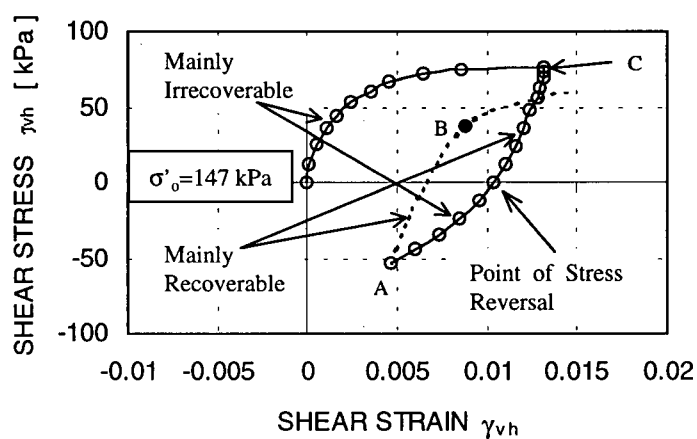


Figure 2.9 Stress-strain relation in torsional shear (modified from Ishihara et al. 1975).

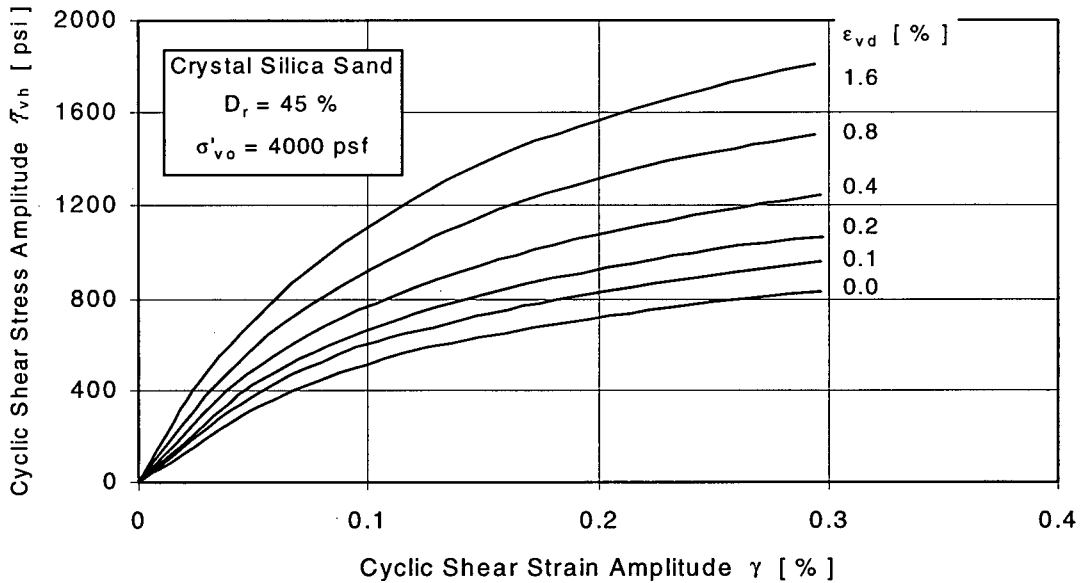


Figure 2.10 Effect of cyclic shear strain amplitude and volumetric strain on drained stress-strain amplitude relationships (after Martin et al. 1975). D_r , relative density; σ'_{vo} , initial vertical effective stress; ϵ_{vd} , volumetric strain.

2.2 Characteristic behaviour of sand under isotropic compression

Isotropic compression refers to a loading path in which the principal stresses are equal during the loading process and therefore, there are no shear stresses involved. Typical response of sand to isotropic compression is shown in Figure 2.11 (Lade and Nelson, 1987). As emphasized in the previous section, upon unloading, sand exhibits a much stiffer response than for primary loading. The total strain achieved under the original load is comprised of a part that is recoverable, and another part that is irrecoverable. At small strain levels (10^{-4} to 10^{-2}), the unload and reload curves are essentially the same, but at greater strain levels, some difference becomes apparent. While reloading, the

stress-strain curve breaks again and follows the trend of the primary loading curve, when approximately the maximum stress level previously attained is reached.

However, the stress levels at which the nature of the strains changes from being mainly recoverable to mainly irrecoverable, is related to the maximum isotropic stress attained during primary loading, rather than to the maximum stress ratio (as discussed in the previous section). In fact, under isotropic compression, the shear to normal stress ratio $(\sigma_1 - \sigma_3)/(\sigma'_1 + \sigma'_3)$ is equal to zero ($R = \sigma'_1/\sigma'_3 = 1$).

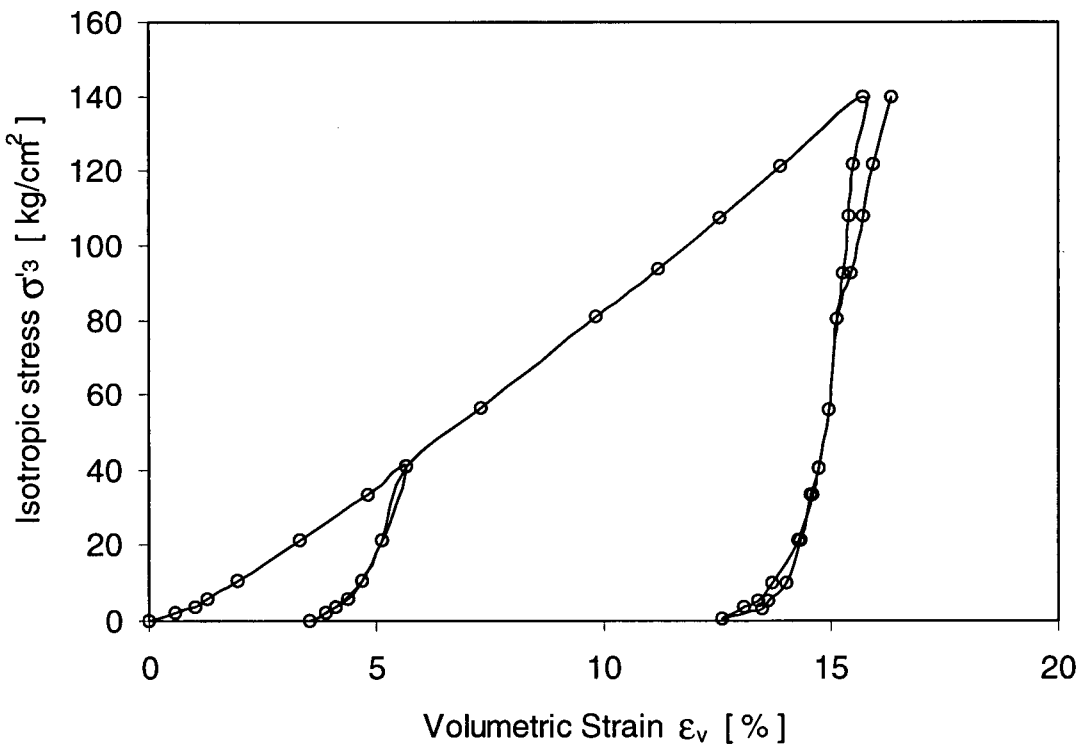


Figure 2.11 Isotropic compression of loose Sacramento River sand with primary loading, unloading and reloading branches (after Lade and Nelson, 1987).

The fact that sand behaves differently when different paths of loading are followed, i.e. sand response to loading is path dependent, is a very important

characteristic of sand. To emphasize this point further, two more loading paths will be discussed, namely proportional loading and pure rotation of principal stresses.

2.3 Sand response to proportional loading

Proportional loading refers to stress paths in which the stress ratio remains constant throughout the loading process. El-Sohby and Andrawes (1973) conducted an experimental study to examine sand anisotropy under constant stress ratio paths in the triaxial apparatus. Results of this study showed that the nature of the strains measured in sand under these loading paths was of the recoverable-irrecoverable type. The recoverable strains were related to deformations of the individual particles. In contrast, irrecoverable deformations were related to sliding of particles relative to each other. Moreover, the response in terms of the recoverable component of the strain was observed to be non-linear and isotropic, but generally anisotropic in terms of the irrecoverable component.

2.4 Pure rotation of principal stresses

A loading path in which the magnitude of the principal stresses is kept constant but their direction is continuously changed is called *pure rotation of principal stresses*. Such a stress path implies no change in the mean effective stress and maximum shear stress. Nevertheless, the stresses on planes with orientations different from the principal directions do change and induce volumetric and shear strains as result of the rotation of principal stresses. This phenomenon has been studied by Arthur et al. (1980,1981),

Ishihara and Towahata (1983), and Matsuoka and Sakakibara (1987), among others. Results of a drained cyclic test on loose Toyoura sand in which the direction of the principal stresses was rotated continuously from 0° to $\pm 45^\circ$ ($-45^\circ \leq \theta \leq +45^\circ$) following a semi-circular stress path, are shown in Figure 2.12 (Ishihara and Towahata, 1983).

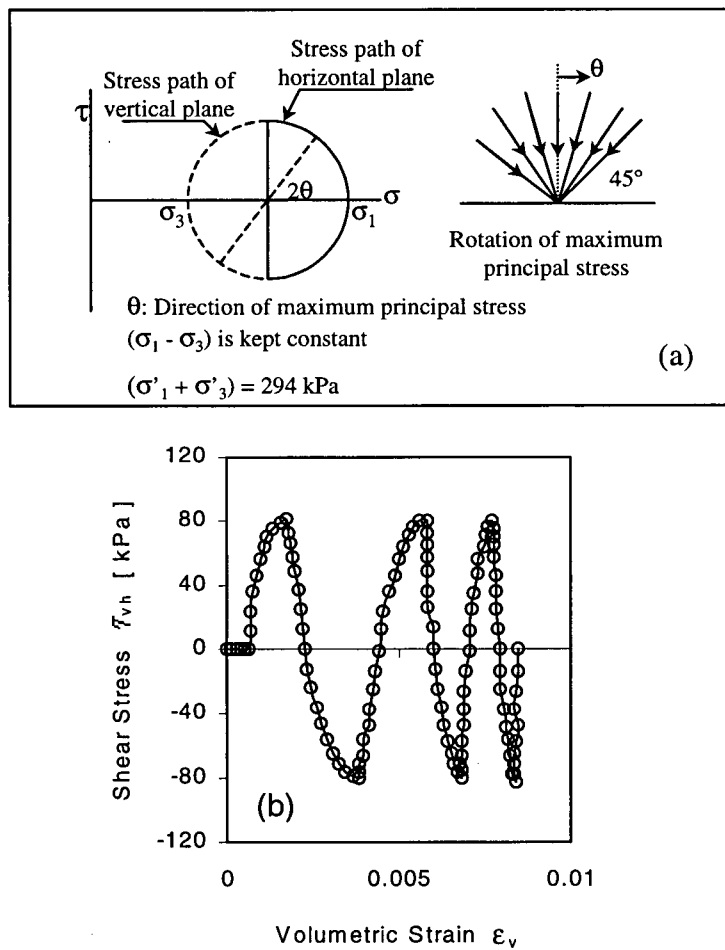


Figure 2.12 Effect of pure rotation of principal stresses in drained cyclic test on Toyoura sand (after Ishihara and Towhata, 1983). (a) Rotation of the principal stress directions following a semi-circular stress path. (b) Torsional shear stress versus volumetric strain.

It can be seen in this figure that as the cycles of rotation of principal stresses progressed, both volumetric and shear irrecoverable strains were accumulated, Figure 2.12b. On the other hand, the effect decreased as the number of cycles increased (i.e. hardening response). Upon unloading, the shear stress-volumetric strain curve became stiffer than for primary loading, until a stress reversal occurred. The accumulation of irrecoverable strains and hardening response with the number of cycles is similar to that observed in cyclic triaxial and simple shear tests. Irrecoverable strains induced by rotation of principal stresses could be an important source of pore water pressure generation if sand is loaded in an undrained manner and the stress path involves rotation of the principal axes.

2.5 Undrained response of sand

Under undrained conditions, the water contained in the soil pores cannot drain out during loading, imposing a volumetric constraint. Under this constraint, the tendency of the soil skeleton to dilate or contract results in a change in the pore water pressure and a change in the effective stress as will be explained in Section 4.6. Typical undrained response of Ottawa sand on loose and medium dense samples tested in triaxial compression (Vaid and Chern, 1983) is shown in Figure 2.13. The densest sand was stiff in shear and the pore water pressure dropped due to dilation, while the loose sand was much softer with an associated large pore water pressure rise.

The curve corresponding to the looser material ($D_r = 37.8\%$, Figure 2.13) showed a strain hardening response of sand until a peak value of shear stress was reached. Thereafter, the response of sand became strain softening and a minimum value of

strength, termed residual strength (s_{ur}), was achieved when the axial strain was about 2.5%. This behaviour is typical of loose sand that tends to contract as it is sheared.

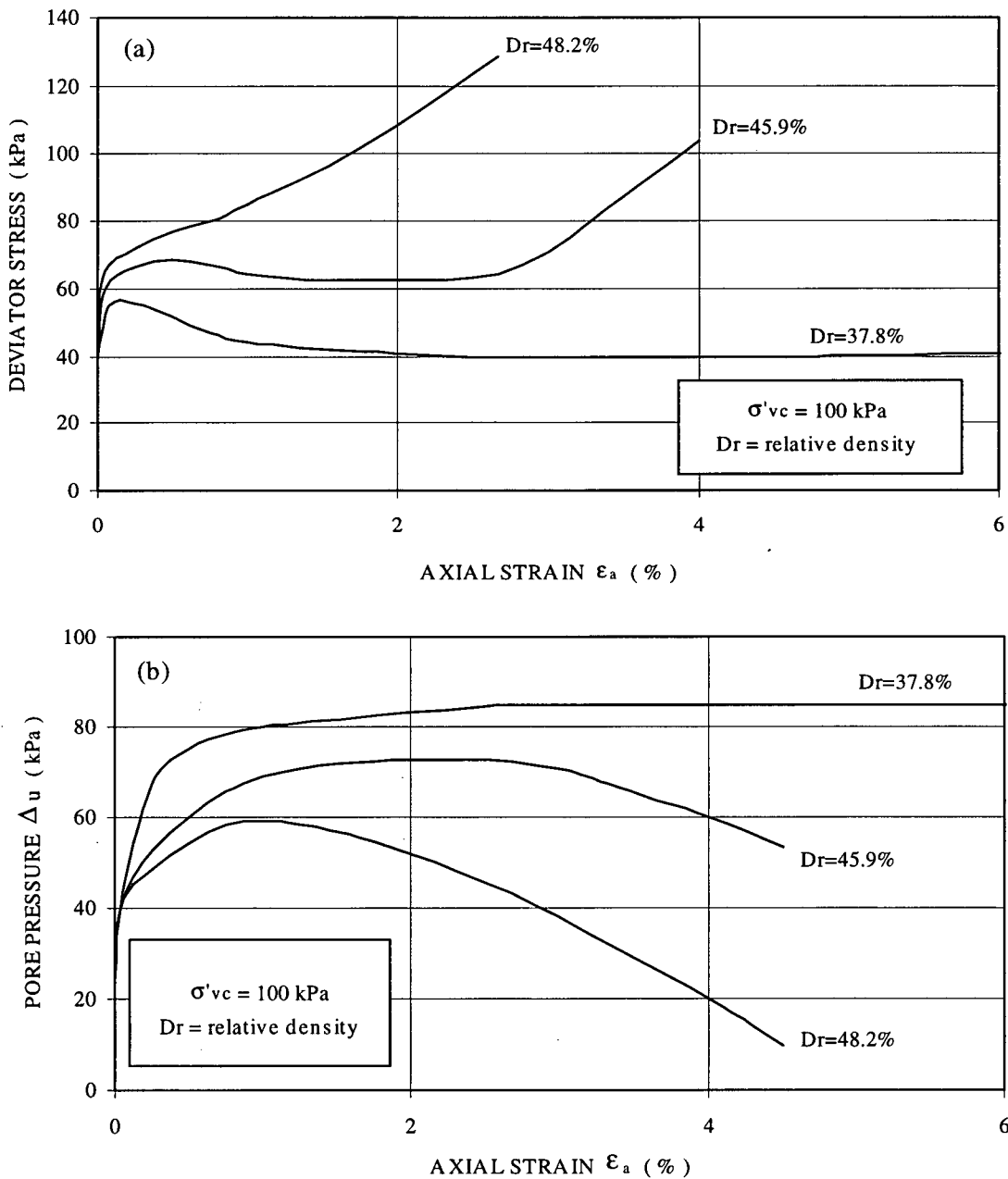


Figure 2.13 Stress-strain response of loose and medium sand under undrained monotonic compressive loading (modified from Vaid and Chern, 1983). (a) Shear response. (b) Pore pressure response. σ'_{vc} , effective confining stress.

The curve corresponding to $D_r = 45.9\%$ showed a different trend since after the shear stress reached its minimum value ($\epsilon_a \approx 2\%$, in this case), sand response became strain hardening again. Upon starting of strain hardening behaviour, the pore pressure commenced decreasing as result of the sand's tendency to dilate with further shear strain. The state at which such change in behaviour occurs is called the *phase transformation state (PT)*, Ishihara et al. (1978).

The curve corresponding to $D_r = 48.2\%$ showed a strain hardening response throughout the complete loading process. The pore pressure initially increased to a peak value due to a small initial tendency of the sand to contract. Thereafter, the pore water pressure decreased as result of the sand's tendency to dilate.

Responses of the type depicted by the curves labeled $D_r = 37.8\%$ and $D_r = 45.9\%$ in Figure 2.13 are called *Liquefaction* and *Limited Liquefaction*, respectively (Castro, 1969). A response of the type depicted by the curve labeled $D_r = 48.2\%$ in Figure 2.13 is characteristic of a *non-liquefaction* response. In the following, the characteristic liquefaction response of sand under undrained monotonic and cyclic loading will be presented.

2.6 Characteristic sand liquefaction response

A strain softening type of soil is discussed first. The typical response of loose sand to undrained monotonic and cyclic loading is illustrated in Figure 2.14. In general, an element of sand has an initial stress state that in this case is represented in Figure 2.14 by point A. Under undrained monotonic loading, the shear stress reaches a peak value (point B in Figure 2.14b), which corresponds to the maximum of the stress path curve. The line

starting at the origin and passing through point B is called *Collapse Line*. Vaid and Chern (1985) referred to this line as the *Critical Stress Ratio (CSR) Line*. As loading continues, the stress ratio (τ/σ') corresponding to the CSR line is exceeded, and the shear stress drops until it reaches its residual value s_{ur} at the *Constant Volume Line* or ϕ_{cv} *Line* (point C in Figure 2.14b). Under cyclic undrained loading, the accumulation of volumetric strains during cycling drives the pore water pressure to rise and the effective stress σ' to decrease, until the CSR line is intersected (point B' in Figure 2.14b). After this point, the shear stress drops to its residual value (point C). Since the static shear stress τ_{st} at point A in Figure 2.14a exceeds the value of the residual strength s_{ur} , once liquefaction is triggered (points B and B'), there is nothing to balance the driving stress τ_{st} and a collapse or flow failure occurs. In the field, flow failure or flow liquefaction will only occur if sufficient volume of soil liquefies and a kinematically admissible mechanism can develop.

Due to sand inherent anisotropy under first time undrained loading, as shown by Vaid et al. (1995a), sand could respond as strain hardening material when loaded in a certain direction, but as strain softening when loaded in a different direction (Figure 2.4). In a real slope, not all the soil is strain hardening; neither strain softening. Since different parts of a slope will respond to different load paths, a flow slide will only occur if the overall shear resistance in the slope is less than the driving shear force.

Sand that exhibits a strain hardening type of response could be triggered to liquefy under cyclic undrained loading. In accordance with Castro (1969), Casagrande (1975) and Seed (1979b), this kind of liquefaction is called *Cyclic Mobility*. Cyclic mobility takes place when the amplitude of the cyclic shear stress τ_{cyc} is greater than the

static shear stress τ_{st} , i.e., states of shear stress reversal occur accompanied by transient states of zero effective stress.

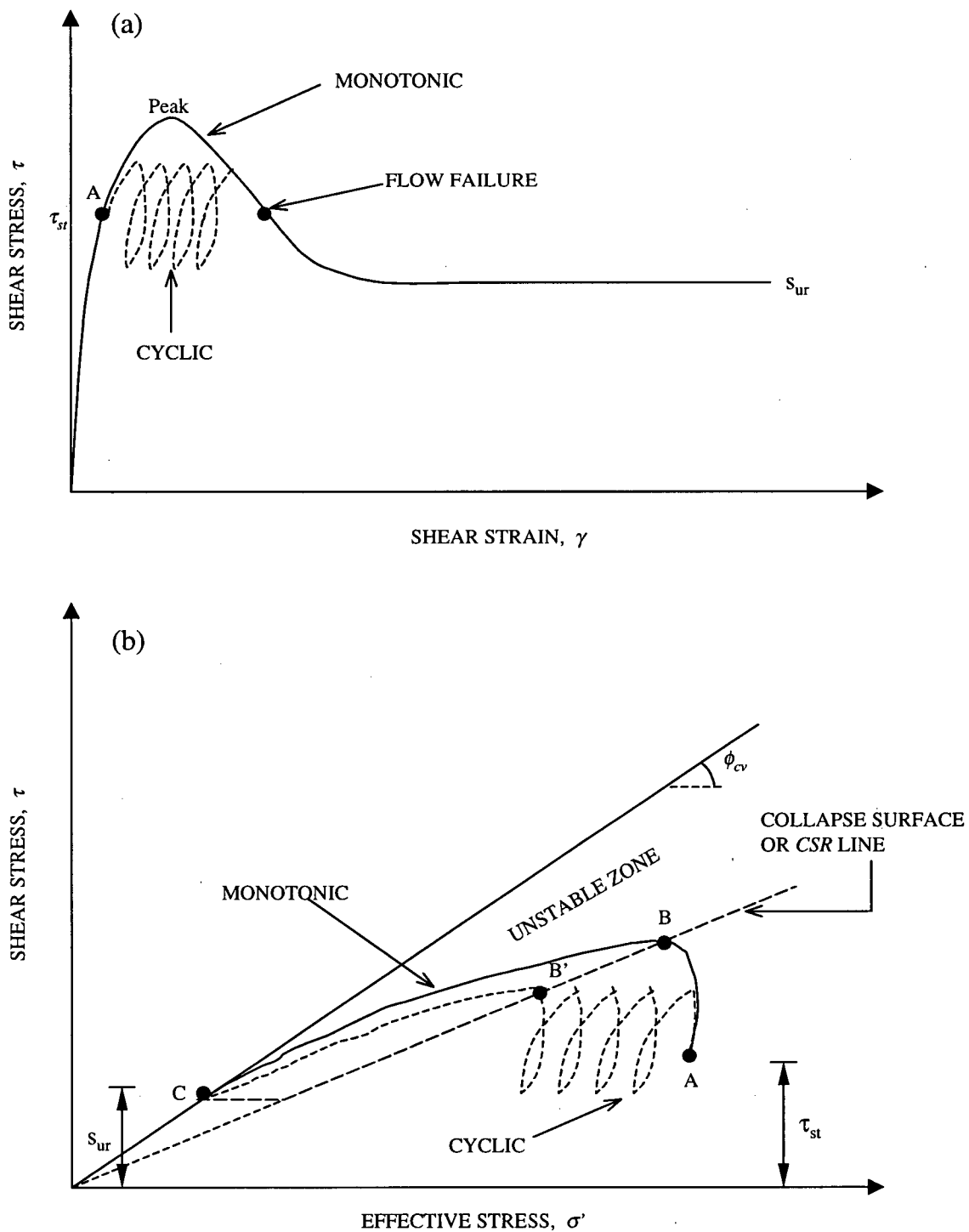


Figure 2.14 Typical response of loose saturated sand under undrained static and cyclic loading (modified from Byrne, 1996). (a) Stress-strain curves. (b) Stress paths.

Cyclic undrained loading that comprises enough number of cycles drives the effective stress σ' momentarily to zero. This is illustrated in Figure 2.15 for dense sand that starts from the initial state of stress represented by point A. As the number of cycles gets larger, small strains are accumulated until the stress path intersects the *Phase Transformation Line* or ϕ_{PT} *Line* (point B). The response between the points A and B is the pre-triggering phase or *Phase 1* (Byrne, 1996). Under further loading the stress path moves up slightly above the ϕ_{PT} Line from point B to point C (Phase 2), and large strains start to occur. Upon unloading from point C (Phase 3), the effective stress state is momentarily driven to the zero effective stress state at point D. Very large pore water pressures and deformations occur at this point since the material cannot support shearing stresses and deforms like a fluid. Byrne (1996) refers to this state as “really true liquefaction” state (Phase 4). As the loading cycle continues, the stress path moves up slightly above the ϕ_{PT} Line, and the soil dilates from point D to point E (Phase 5). The process comprised by phases 3, 4 and 5, repeats itself until the cyclic loading stops. During this process, the strain loops get larger with each cycle (Figure 2.15a), but they do not continue further once cyclic loading ceases.

Cyclic mobility is responsible for large but finite liquefaction-induced displacements and can occur even on a level ground site where there is no static driving stresses τ_{st} . Furthermore, when cyclic loading is not symmetrical, as it generally would be during an earthquake, strains accumulate in the direction of loading as shown in Figure 2.16. These type of liquefaction-induced strains can cause large lateral movements, called lateral spreading.

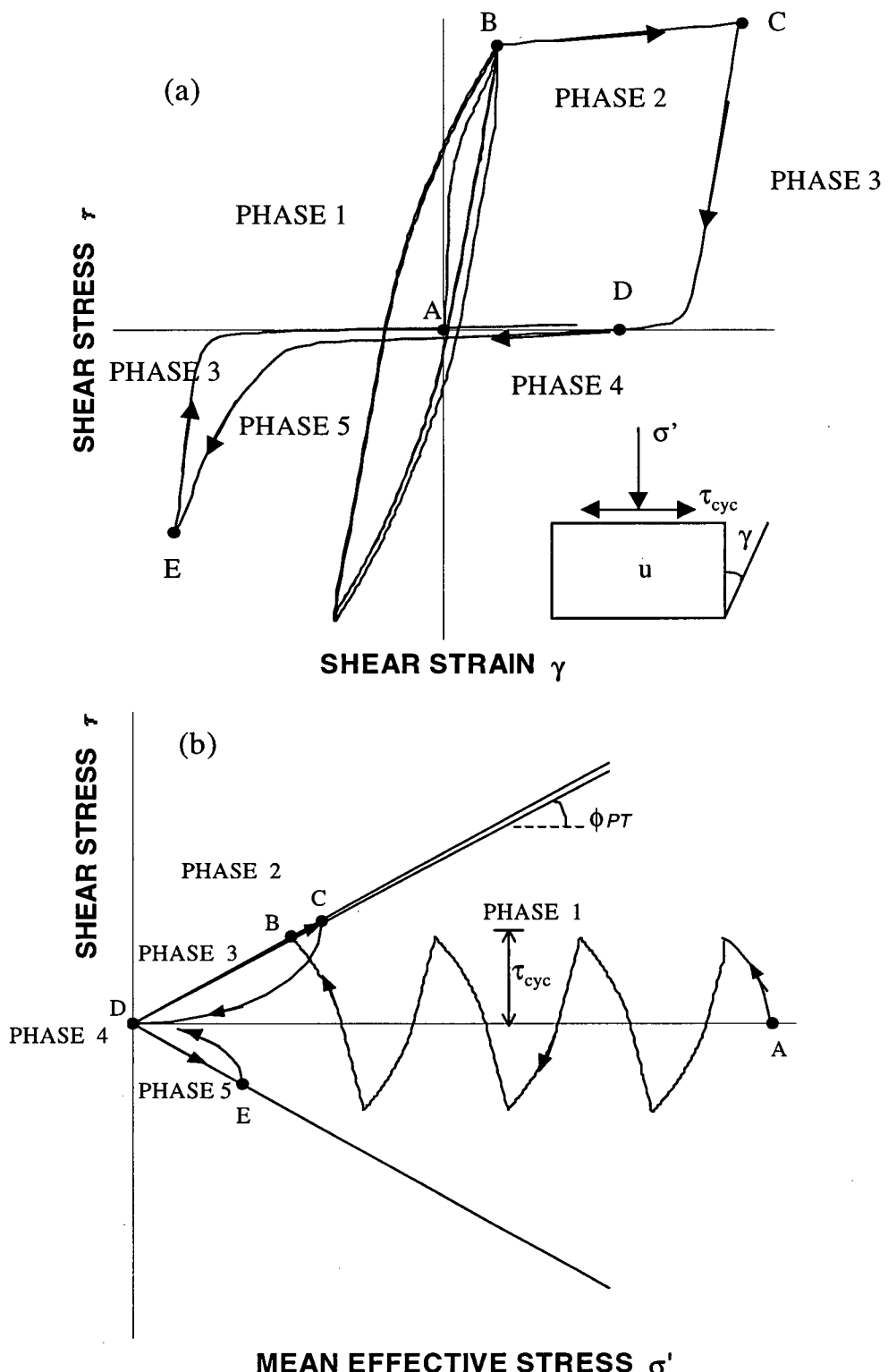


Figure 2.15 Typical response of saturated sand under cyclic loading with stress reversal (modified from Byrne, 1996). (a) Stress-strain curve. (b) Stress path.

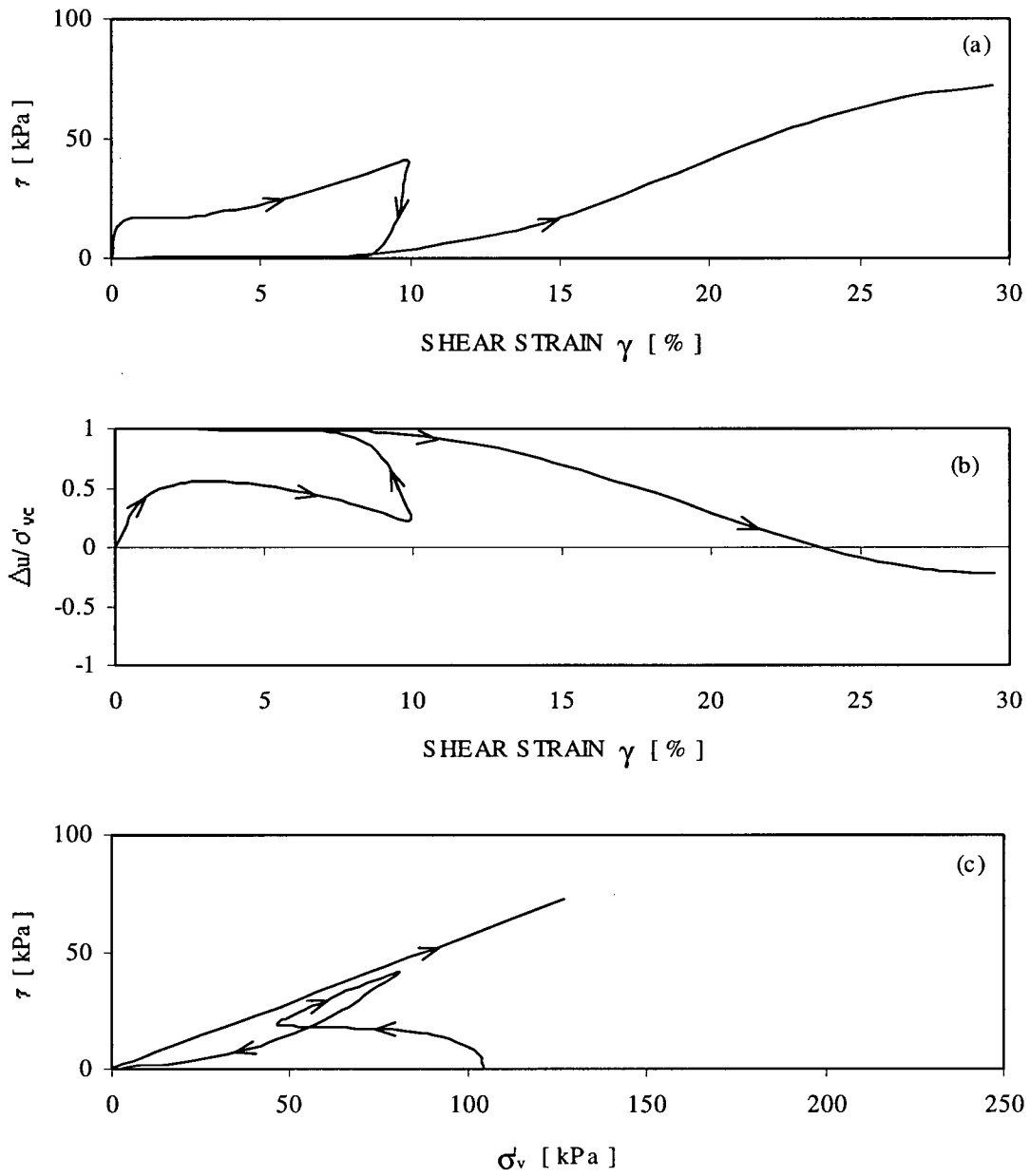


Figure 2.16 Undrained response of loose Syncrude sand to cyclic simple shear loading (after Vaid et al. 1996). (a) Stress-strain curve. (b) Pore pressure response. (c) Stress path.

Limited liquefaction and cyclic mobility can combine as shown in Figure 2.17 (Vaid and Chern, 1985). In this case, large displacements are first triggered at the onset

of liquefaction (point B'), but limited by the post-liquefaction dilative response of the soil from points PT to C. Upon unloading, large displacements are induced again due to cyclic mobility.

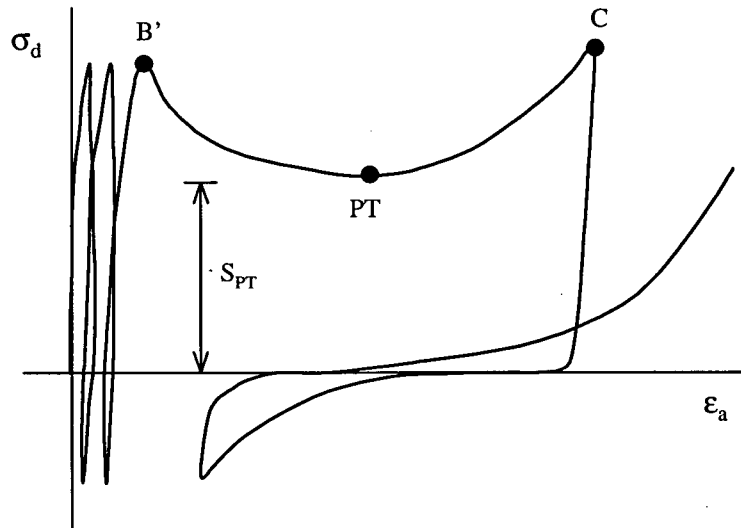


Figure 2.17 Limited liquefaction followed by cyclic mobility (modified from Vaid and Chern, 1985).

Summarizing, liquefaction can be triggered by either static (monotonic) or dynamic (cyclic) loading.

- A static trigger leads to a *Flow Slide* or to *Lateral Spreading*. A flow slide is associated with a strain softening type of response, while lateral spreading relates to strain softening followed by strain hardening type of responses. Both, flow slide and lateral spreading are typical of loose saturated sands under undrained monotonic loading. Such an undrained kind of loading can occur if the soil is saturated, or close to saturation, and subjected to a large and fast enough load, i.e., large enough to reach

the peak strength of the soil (Figure 2.14), and fast enough to generate pore water pressure at a greater rate than the rate of pore water pressure dissipation.

- A dynamic trigger leads to a *Flow Slide* if the static driving stress τ_{st} is greater than the residual strength s_{ur} , or to *Lateral Spreading*, if the ultimate undrained strength of the soil is greater than τ_{st} . A dynamic load can trigger liquefaction in sands that exhibit a strain hardening response under undrained monotonic loading, and should it do so, a lateral spread rather than a flow slide would result.

2.7 Summary of sand characteristic behaviour

The stress-strain response of a granular soil depends mainly on its density or void ratio e , the applied stresses, the stress ratio, and the volumetric constraints. The key points of the characteristic drained or *skeleton* response of granular soils are as follows:

- The stress ratio vs. shear strain relation is nonlinear and depends on the material's density.
- A loose material contracts as it shears, and its shear response is much softer than a dense material, which contracts at low values of stress ratio, and then dilates as it shears at higher values of stress ratio.
- The value of stress ratio at the state of phase transformation marks the stress level at which sand behaviour turns from being contractive to dilative. For stress states below the phase transformation value sand is contractive, while it is dilative for stress states above.
- A nearly unique relationship exists between the rate of dilatancy and the stress ratio.

The characteristic behavior of sand under monotonic loading can be idealized as presented in Figure 2.18. Here, it can be seen that the main features of the skeleton response of sand as discussed above are schematically shown.

In addition,

- Sand response is anisotropic and path dependent.
- For first time monotonic loading, sand behaviour is strongly dependent on the direction of loading.
- Rotation of principal stresses has a strong influence on sand behaviour during primary loading. However, under cycling rotation its effects decrease as the number of cycles increases.
- Once sand has been subjected to a certain stress level under loading, this stress level appears to become a threshold differentiating approximately the point at which the nature of the strains changes from being mainly recoverable to mainly irrecoverable.
- Upon unloading, sand response is much stiffer than for primary loading.
- Under cyclic loading, sand response becomes stiffer as the number of cycles increases.

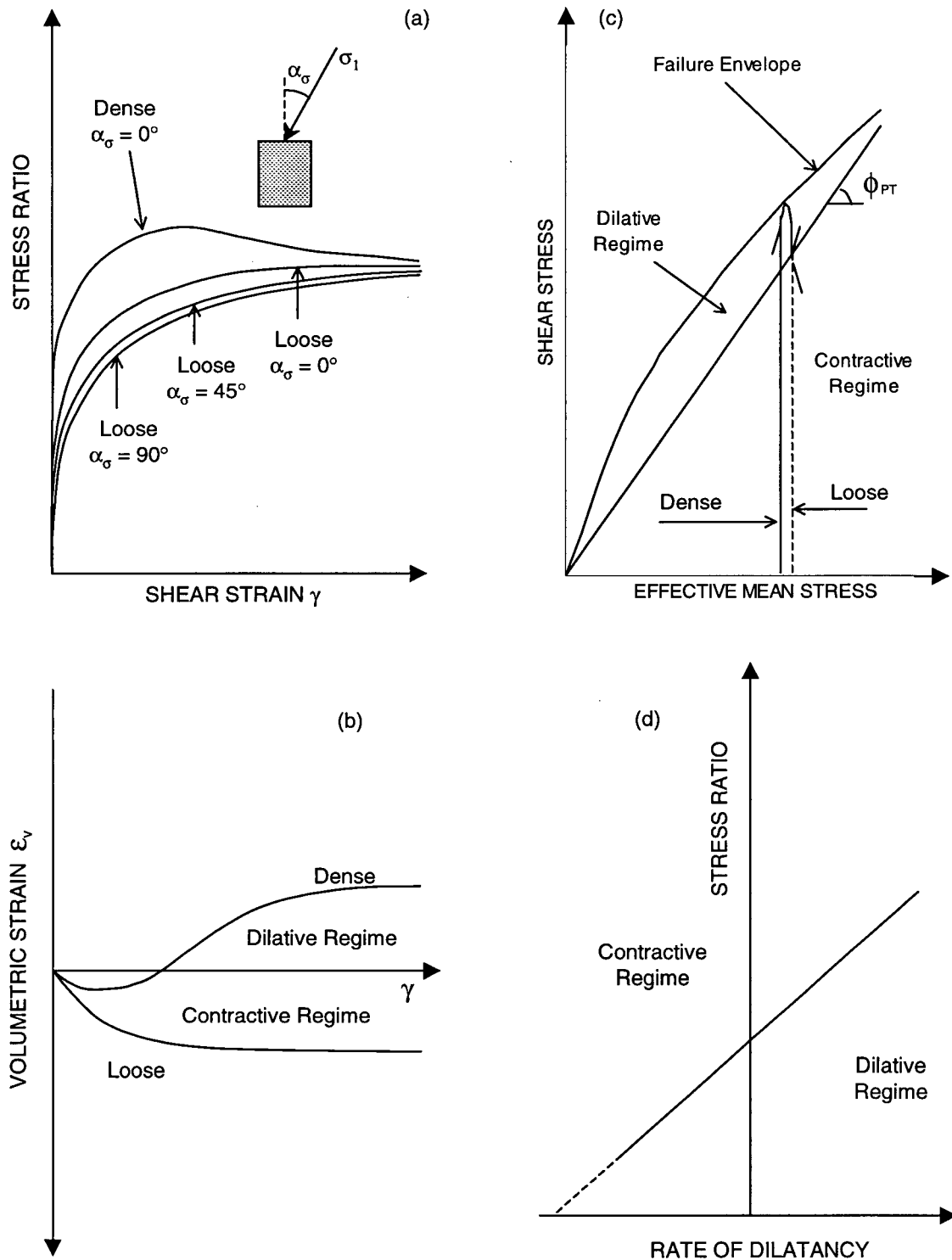


Figure 2.18 Idealized drained behaviour of sand. (a) Shear response. (b) Volumetric response. (c) Contractive and dilative states. (d) Shear-Volume coupling.

In the following chapter, different constitutive models that have been developed to capture sand behaviour will be presented and the main features that differentiate them will be discussed.

CHAPTER 3

STRESS-STRAIN MODELS FOR SAND

As discussed in Section 1.3, displacements induced by liquefaction can be estimated from the physics of the problem using a mechanics based approach, which has been calibrated with field experience. This approach requires that for a prescribed stress-strain law, equilibrium and compatibility be satisfied for the boundary and initial conditions of the problem. Numerical procedures using finite elements or finite differences techniques are routinely utilized to reasonably satisfy these conditions. All methods for stress and deformation analyses of soil structures require a *stress-strain relation* or *constitutive model* to simulate the response of soil to loading. Hence, the approach followed to model the stress-strain behaviour of soil is the main difference among these methods. Rather than a detailed review of the very large number of models that have been developed to simulate soil behaviour, the main features of different types of constitutive models will be described here, to establish a framework for analysis and discussion.

3.1 Models based on elastic theory

Models based on theory of elasticity form the basis of the total stress approach. These models do not include shear or tension limits, i.e., failure criteria limiting the maximum

attainable values of the shear stress, or of the stresses in tension, the latter usually zero for sand. The nonlinear stress-strain behaviour of soil is modelled in two different manners: (i) an incremental linear approach, or (ii) an equivalent linear approach. Since pore water pressures are not computed simultaneously with stresses and strains, the undrained response of soil is captured directly through the model parameters. Hence, the effects of pore pressure are included indirectly in the reduced strength and stiffness parameters used.

These methods are computationally simple and they constitute the state-of-the-practice techniques to estimate the undrained response of soil.

3.2 Models based on incremental elastic-plastic theory

Models based on incremental elastic-plastic theory constitute the basis of the effective stress approach. These models include shear and tension limits, and they allow capturing the characteristic stress-strain behaviour of soil, as well as the development and dissipation of pore water pressures. The generation and dissipation of pore water pressures are coupled with the incremental mechanical deformations of the soil skeleton at every step of the analysis. Therefore, they are governed and controlled by the constitutive relationship of the soil (system comprised by solids, liquid and gas). Provided that an appropriate constitutive relationship is used, this approach is in principle the most powerful and potentially accurate. However, constitutive relationships of models suitable for carrying out effective stress analyses are complex and require determining several model parameters before they can be used. This, in fact, seems to be

their major weakness. Before discussing these types of models, the basic elements of incremental elastic-plastic theory are presented in order to establish a frame of reference.

3.3 Brief description of the basic elements of incremental elastic-plastic theory

A detailed discussion of the basic elements of incremental elastic-plastic theory can be found in the literature, e.g. Hill (1950) and Desai (1984). Here, they will only be described briefly.

Models based on incremental elastic-plastic theory generally assume that the infinitesimal total strain increment $d\varepsilon$ is comprised of two infinitesimal components, the elastic strain increment $d\varepsilon^e$ and the plastic strain increment $d\varepsilon^p$. In addition, regions of elastic and plastic behaviour are assumed separated by a boundary. The zone in which only elastic response is exhibited is called *elastic region*, whereas stress states outside the boundary of the current elastic region inducing plastic deformations constitute the *plastic region*.

Hence, in the stress space defined by the principal effective stresses, the major σ'_1 , the intermediate σ'_2 and the minor σ'_3 , the locus determined by the stress points that separate elastic and plastic behaviour constitute a surface boundary. Such a surface is usually called *Yield Surface*, *Yield Locus* or *Loading surface*. Mathematically, it is described by a function f as follows:

$$[3.1] \quad f(\sigma'_{ij}) = 0$$

where σ'_{ij} represents the elements of the effective stress tensor.

Any state of stress that satisfies Equation 3.1 lies on the yield surface. If an increment of stress $d\sigma'_{ij}$ is applied and the stress state moves out of the current elastic region, a *loading* process is taking place. Since the yield surface limits the current accessible states of stress, the new stress point $\sigma'_{ij} + d\sigma'_{ij}$ can not lie outside the yield locus, requirement termed *consistency condition*, and the elastic region has to either expand, move or both (process termed *hardening*), inducing plastic strains. On the other hand, if the stress state moves into the current elastic region, an *unloading* process occurs, the elastic region remains unchanged and only elastic strains are predicted. If the new state of stress $\sigma'_{ij} + d\sigma'_{ij}$ stays on the same yield surface, a process named *neutral loading* takes place and the predicted response is solely elastic. According to these three different scenarios, the loading criteria are defined mathematically as follows:

$$\begin{aligned}
 f = 0 \text{ and } df > 0 &: \text{Loading} \\
 [3.2] \quad f = 0 \text{ and } df < 0 &: \text{Unloading} \\
 f = 0 \text{ and } df = 0 &: \text{Neutral Loading}
 \end{aligned}$$

where

$$[3.3] \quad df = \frac{\partial f}{\partial \sigma'_{ij}} d\sigma'_{ij}$$

The loading criteria defined by Equations 3.2 and 3.3 are one of the great advantages of plasticity theory, since, for isotropic material, they precisely determine the

state of loading whether it is uniaxial or multi-axial. In fact, the vector with components $\partial f/\partial \sigma'_{ij}$ is perpendicular to the yield surface and therefore, the dot product of this vector and the stress increment vector of components $d\sigma'_{ij}$, rigorously determines the nature of the loading increment.

However, the evolution of the yield surface is limited by the *failure surface*, which defines the ultimate state that soil can achieve under loading and it is determined by a failure criterion. Once the yield locus contacts the failure surface, it can not evolve anymore. Several failure criteria have been used to reflect soil strength, e.g., Mohr-Coulomb, extended Tresca, Drucker and Prager (1952), Matsuoka (1974), and Lade and Duncan (1975). Nonetheless, these criteria render yield loci that are open with respect to the hydrostatic axis ($\sigma'_1 = \sigma'_2 = \sigma'_3$) in the stress space $\sigma'_1: \sigma'_2: \sigma'_3$, and hence, fail to predict plastic volumetric strains under isotropic compression. Drucker et al. (1955) had already pointed out this limitation, and suggested a bullet-shaped yield surface to enclose part of the hydrostatic axis (Figure 3.1). In this manner, plastic volumetric strains under pure compressive loading could be accounted for. As it will be discussed later, various models have been developed following these ideas.

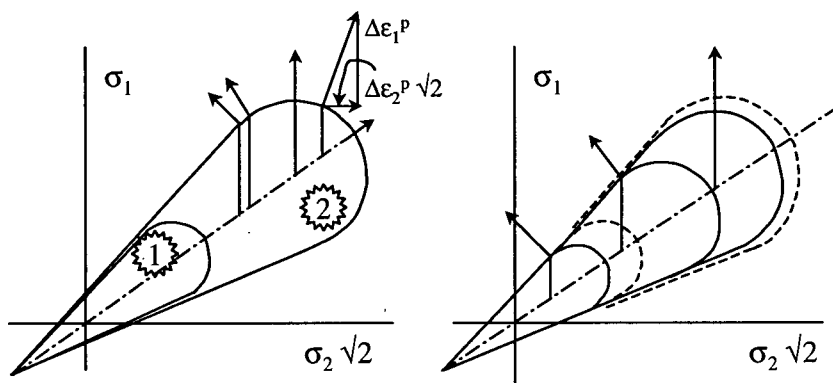


Figure 3.1 Bullet-shaped yield surface as proposed by Drucker et al. 1955 for triaxial test conditions.

In addition to the yield criteria explained above, four more elements constitute the basis of incremental elastic-plastic theory: (i) the hardening rule, (ii) the hardening parameter, (iii) the flow rule, and (iv) the incremental stress-strain relationship.

The *hardening rule* specifies the manner in which the elastic region evolves as yielding takes place. The change in the elastic region is termed *Hardening* and Prager (1955) referred to two possible hardening mechanisms: *isotropic* and *kinematic hardening*. Isotropic hardening stipulates proportional expansion of the yield surface in all directions to allocate the new plastic state. Kinematic hardening stipulates displacement of the yield surface without changes in orientation, size or shape of the elastic region. The new position of the elastic region allows the yield locus to allocate the new state of stress. Furthermore, the two extreme types of hardening can be combined in what is called *mixed hardening*.

The *hardening parameter*, κ , is a scalar quantity used to record the plastic deformation history developed during the loading process. It is usually expressed in terms of some measurement of either the cumulative plastic strain increments, e.g. Hill (1950), Mroz (1967), Roscoe and Burland (1968), Prévost and Hoeg (1975), Vermeer (1978), or the plastic work, e.g. Hill (1950), and Lade (1977). For a hardening material, the size of the yield surface f , its position, or both, depend not only on the stress state σ'_{ij} , but also on the hardening parameter κ . Thus, the yield surface is expressed as:

$$[3.4] \quad f(\sigma'_{ij}, \kappa) = 0$$

The *flow rule* defines the direction of the plastic strain increment vector, $d\boldsymbol{\varepsilon}^p$. In analogy with ideal fluid flow, a potential function at any point of the yield surface is defined in plasticity theory, and termed *plastic potential*, $g(\sigma'_{ij})$. Hence, the direction of the plastic strain increment vector, $d\boldsymbol{\varepsilon}^p$, coincides with the unit vector perpendicular to the plastic potential and therefore, the plastic strain increment components, $d\varepsilon_{ij}^p$, can be expressed as:

$$[3.5] \quad d\varepsilon_{ij}^p = \lambda \frac{\partial g}{\partial \sigma'_{ij}}$$

where λ is a non-negative scalar function that varies all through the plastic loading history. The gradient $\partial g / \partial \sigma'_{ij}$ gives the direction of the plastic strain increment while λ determines its magnitude. Equation 3.5 is termed the *Flow Rule*. If the plastic potential function g is assumed to coincide with the yield surface f , i.e., $g = f$, the flow rule is termed an *associative flow rule*, otherwise, $g \neq f$, it is called a *non-associative flow rule*.

In general, stress-strain curves describing the response of soil to loading are nonlinear but they can be approximated by piecewise linear representations of such curves. Each linear segment beyond the maximum yield stress will have a particular slope representing both elastic and plastic moduli and will be associated with a different yield surface. Mroz (1967) generalized this concept using a nest of yield surfaces in which each yield locus is associated with a corresponding linear segment of the stress-strain curve.

Since the total strain increment $d\epsilon_{ij}$ is assumed to be the sum of the elastic and plastic strain increments, $d\epsilon_{ij}^e$ and $d\epsilon_{ij}^p$, respectively, then $d\epsilon_{ij}^e$ can be written as:

$$[3.6] \quad d\epsilon_{ij}^e = d\epsilon_{ij} - d\epsilon_{ij}^p$$

The stress increment is related to the elastic strain increment by means of the generalized Hooke's law:

$$[3.7] \quad d\sigma'_{ij} = C_{ijkl} d\epsilon_{kl}^e = C_{ijkl} (d\epsilon_{kl} - d\epsilon_{kl}^p)$$

where C_{ijkl} is the elastic stiffness tensor. Since the plastic strain increment $d\epsilon_{kl}^p$ is given by Equation 3.5, the incremental stress-strain relationship can be written as follows:

$$[3.8] \quad d\sigma'_{ij} = C_{ijkl} \left(d\epsilon_{kl} - \lambda \frac{\partial g}{\partial \sigma'_{kl}} \right)$$

Hence, the key features that differentiate incremental elastic-plastic models are the assumptions made with respect to: (i) *Hardening rule*, i.e. how is the elastic region going to change? (ii) *Flow rule*, i.e. which direction will the plastic strain increment have? (iii) *Stress-strain relationship*, i.e. how are the stress and strain increments related?

3.4 Sand characteristic behaviour within an incremental elastic-plastic framework

In this section, fundamental characteristics of sand behaviour will be related to the basic elements of incremental elastic-plastic theory to establish a link between observed behaviour and elastic-plastic theory. This link will serve as a framework for the discussion to follow.

As discussed in Chapter 2, deformations in sand can be separated into those of recoverable (“elastic”) nature, and those of irrecoverable (“plastic”) nature. The nature of strains in sand is approximately bounded (“yield surface” or “yield locus”) by the maximum stress level attained during past loading. Within such a boundary (“elastic region”), strains in sand are mainly of recoverable (“elastic”) nature. Such a boundary (“yield locus”) changes with further loading beyond the maximum stress level attained (“strain hardening of the elastic region”). The irrecoverable (“plastic”) components of the strain increments are perpendicular to a family of geometrically similar curves (“plastic potentials”) that do not coincide with the boundaries (“yield loci”) of maximum stress level attained, i.e. (“non-associative flow rule”). Sand response to loading is limited by an ultimate strength value (“failure surface”).

Thus, sand behaves like a strain hardening material that hardens gradually as the yield loci expand or move with plastic shear strain, until they reach an ultimate value that can not be exceeded, namely the *failure surface*. The yield loci do not coincide with the family of plastic potentials, but they define regions in the stress space within which sand can be assumed to behave elastically. Outside these regions, the response of sand is mainly plastic. Furthermore, sand response is not isotropic and under cyclic loading, the yield surface changes its position when stress reversals take place.

3.5 Different types of incremental elastic-plastic constitutive models

Based on the fundamental concepts of incremental elastic-plastic theory outlined above, various constitutive models have been developed. The majority of these models can be grouped into two categories: Critical State type of models, and Mohr-Coulomb type of models. The main differences among them are the assumptions made regarding the yield surface, hardening rule, and flow rule. However, other types of models have been developed following very different approaches to simulate soil behaviour, e.g., bounding surface plasticity (Dafalias and Herrmann, 1980), and endochronic theory (Valanis, 1971).

3.5.1 Critical state type of models

Schofield and Wroth (1968), based on results of multiple triaxial tests on reconstituted clay, presented the Critical State theory that served as foundation for their constitutive model: the *CamClay* model. The model is based on *isotropic hardening* plasticity with an *associative flow rule*. The failure surface is determined by the critical state line *CSL* that defines stress states at which deformation takes place under constant volume and no further changes in stress. The mobile yield surface is assumed to have an elliptical shape that hardens as the void ratio or specific volume decreases. To describe soil behaviour, three state parameters were used: $p' = (\sigma'_1 + \sigma'_2 + \sigma'_3)/3$, the mean normal effective stress; $q = \{0.5[(\sigma_1 - \sigma_2)^2 + (\sigma_2 - \sigma_3)^2 + (\sigma_1 - \sigma_3)^2]\}^{0.5}$, the generalized deviatoric stress; and the specific volume, $v = (1+e)$. Essential features of the model are shown in Figure 3.2.

Several models have been developed following this type of approach and they are usually referred to as Critical State type of models. However, experimental evidence, e.g. Pooroosharb et al. (1966), has shown that an associative flow rule is not applicable to sands. In addition, the assumption of isotropic hardening does not allow capturing pore water pressures and permanent deformations induced immediately after stress reversal occurs, or by cyclic loading. In relation to these topics, Carter et al. (1982) suggested that the elastic region shrank during unloading and therefore, allowed plastic strains to occur while reloading. Jefferies (1997) proposed an internal softening cap that drags and shrinks the elliptical yield surface as unloading continues beyond a certain value of p' .

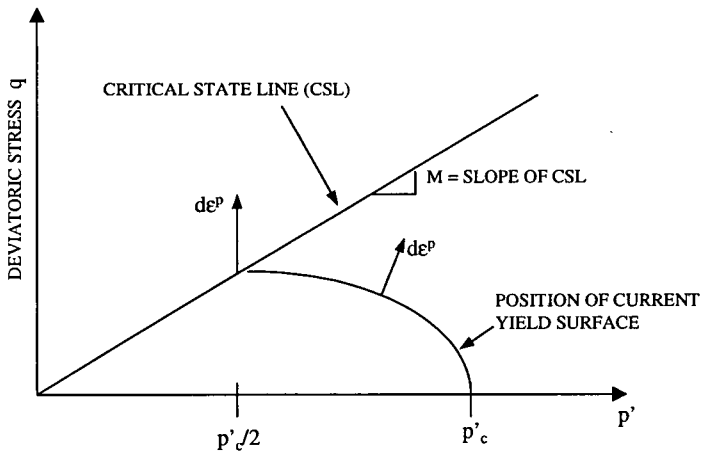


Figure 3.2 Essential features of CamClay model.

3.5.2 Mohr-Coulomb type of models

Other models for sand have been developed under the assumption that the yield loci are determined by the mobilized angle of internal friction. Vermeer (1980) referred to these models as Mohr-Coulomb type of models. Although *non-associative flow rules* have

been used, e.g. Lade and Duncan (1975), Matsuoka and Nakai (1977), and Vermeer (1978), the assumption of *isotropic hardening* implies the same limitations stated above. Puebla et al. (1996, 1997) proposed a Mohr-Coulomb type of model based on a non-associative flow rule and a concept similar to mixed hardening. The hardening rule used in this model allows prediction of elastic-plastic behaviour upon stress reversal, while only elastic strains are considered if a state of stress reversal did not occur during the loading process. This model was shown capable of capturing the observed behaviour of the CANLEX embankment reasonably well. Nevertheless, models with yield loci that do not enclose part of the hydrostatic axis (Figure 3.1) cannot predict the plastic volumetric response exhibited by sand under isotropic compression, i.e. stress paths along the hydrostatic axis.

To overcome this limitation, following Drucker's (1955) bullet-shaped yield surface idea, researchers have used a second yield surface to enclose the elastic region with respect to the hydrostatic axis and model plastic volumetric response under isotropic compression. The two yield surfaces are usually referred to as *cone* and *cap* surfaces. They are independent of each other, but they can act together to predict soil response to loading. Each of these surfaces has its own plastic potential, flow rule, hardening rule and hardening parameter. Thus, depending on where the current state of stress σ'_{ij} is located upon the elastic boundary and the direction of $d\sigma'_{ij}$, either the cone surface could be activated solely, the cap surface solely, or both simultaneously. The latter occurs when σ'_{ij} lies in the intersection of the two curves and $d\sigma'_{ij}$ points in the outward direction of the elastic region (Figure 3.3).

The intersection of the two yield surfaces, point P in Figure 3.3, is called *corner point*. At this point, the response is given by the contribution of both, cone and cap surfaces. Koiter (1953) discussed the manner in which such corner points should be treated from the elastic-plastic viewpoint. Roscoe and Burland (1968), Prévost and Hoeg (1975), Lade (1977), Vermeer (1978,1980), have suggested this kind of yield loci to model soil behaviour.

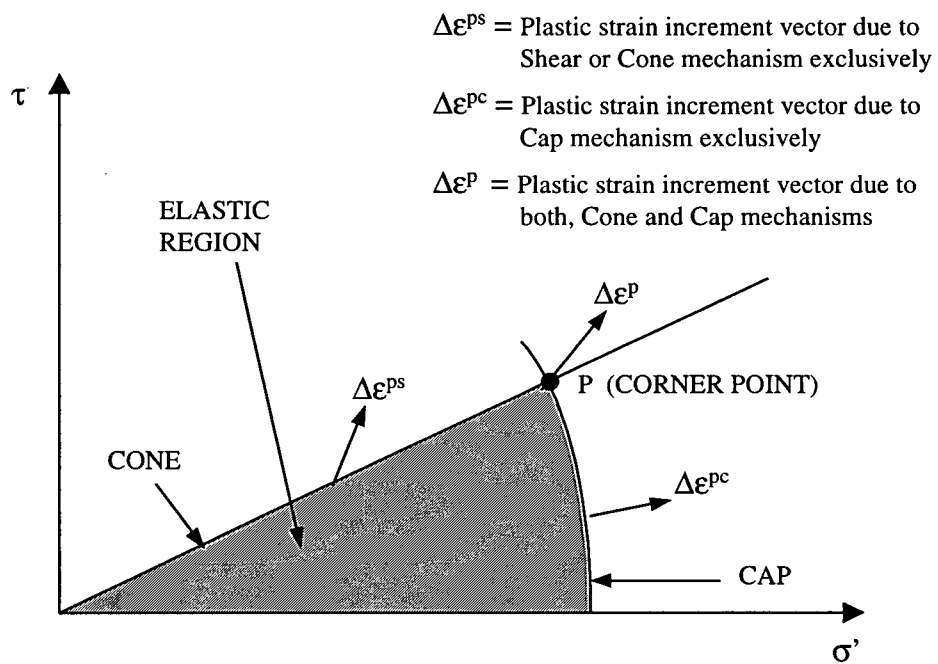


Figure 3.3 Cone and Cap yield surfaces.

3.5.3 Multi-yield surface model

As mentioned in a previous section, a multi-yield surface model was presented by Mroz (1967). In this model a nest of yield loci are used to simulate stress-strain curves. A graphical representation of such a model is illustrated in Figure 3.4 in the principal stress space. The innermost yield surface defines the elastic region that moves along as loading

occurs. Under a loading process, the elastic region translates with the stress point until the next adjacent yield locus is reached. Contact between yield loci is made in a tangential manner to ensure that the yield surfaces do not intersect. Thereafter, all yield loci that have been dragged during loading move together towards the next stage. Each yield surface defines a region of similar mechanical properties, so strains develop by increments and piecewise linear representations of stress-strain curves can be obtained.

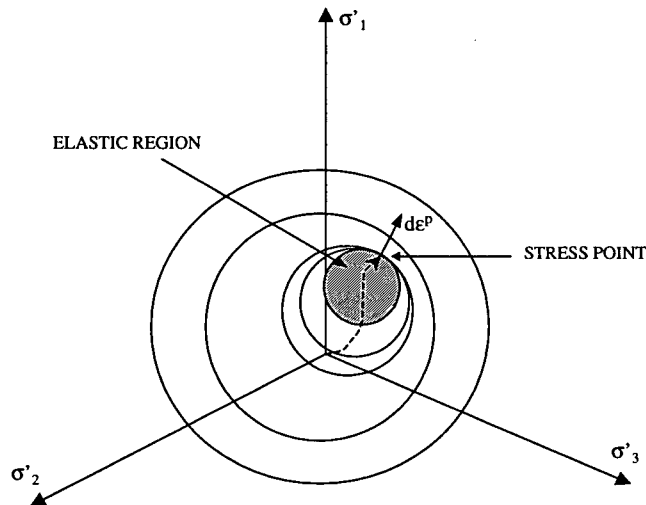


Figure 3.4 Nested yield loci that are carried along with the stress point as this one moves.

Upon unloading, the stress point moves within the elastic region until its boundary is reached again. During this process, the yield loci remain stationary and therefore, the response is purely elastic. Once loading takes place again in a different direction, the material behaves in an elastic-plastic fashion. Notice that if in a model of this type the elastic region were shrunk to a point, the entire response would be considered as elastic-plastic. However, keeping track of the position of every yield

surface, particularly when this kind of model is used with mixed hardening, could become very complex.

3.5.4 Other models

Other models have been developed to avoid the complexity of mixed hardening multi-yield surface models. A bounding surface soil plasticity model was introduced by Dafalias and Herrmann (1980), in which soil behaviour depends on the distance between a given state of stress and strain, and a boundary surface. A very different approach was followed in the endochronic theory by Valanis (1971). For details of bounding surface type of models, the reader is referred to Dafalias and Herrmann (1980,1982), and Bardet (1986). Endochronic models for soil can be found in Bazant and Krizek (1976), Valanis and Read (1982) and Bazant et al. (1982).

3.6 Key factors in modelling monotonic sand liquefaction

From the discussions presented in this chapter and Chapter 2, it follows that a constitutive stress-strain relation capable of modelling sand liquefaction must capture sand characteristic response to loading under drained, partially drained and undrained conditions. The key factors to be considered in a constitutive model adequate for monotonic liquefaction analysis in sands are then:

- Non-linearity of the stress-strain relationship and its dependence on the sand's density;
- Shear-volume coupling as well as its continuous effects on induced pore pressure under partially drained and undrained conditions;

- Path dependence and non-isotropic behaviour;
- Effects of direction of loading are particularly important; and
- Rotation of principal stresses.

Since effects of pore pressure generation and dissipation need to be accounted for continuously during liquefaction analysis, the numerical implementation of the constitutive model must be coupled with a groundwater flow technique. Coupled stress-flow analysis can then be carried out in which the hydraulic conditions and properties of the sand determine the type of response that soil would exhibit in accordance with the drainage and loading conditions.

In the following chapter, a constitutive model capable of capturing the factors stated above as key for monotonic liquefaction of sand will be presented. However, only anisotropy related to direction of loading will be considered. The numerical implementation of such model into a computer code that allows performance of coupled stress-flow analysis will be presented in Chapter 5.

CHAPTER 4

CONSTITUTIVE MODEL

A constitutive model for sand liquefaction analysis is proposed in this section. The main issues that characterize sand behaviour will be addressed along with the simplifying assumptions of the proposed stress-strain model. Simplifying assumptions are necessary to keep the model as clear as possible and at the same time, facilitate its implementation into a computer code. Although some characteristics of sand behaviour are lost in this process, the model will still be capable of capturing sand liquefaction response.

The proposed constitutive model is based on elastic-plastic theory and its plastic part is given by superposition of two mechanisms: (i) a plastic shear or cone mechanism, and (ii) a volumetric or cap mechanism. The shear mechanism is the main constituent of the plastic part of the model and is based on Byrne et al. (1995a) and Puebla et al. (1996,1997). The latter developed the cone mechanism using classical plasticity theory. This mechanism will be further improved here to account for continuous rotation of principal stresses. In addition, a volumetric or cap mechanism for capturing the plastic response induced by compressive loading will be also introduced here to complement the model.

The proposed constitutive model was developed to model liquefaction phenomena triggered by static loading. Nevertheless, the hysteretic response of sand under cyclic loading is captured in a simplified manner and due to the approach followed, the model could be extended to predict the unload-reload loops more rigorously.

4.1 Description and simplifying assumptions of the model

In the following, the main characteristics and simplifying assumptions of the proposed constitutive model together with the implications of such assumptions will be described:

- Sand is considered to behave as elastic-plastic material.

As was seen in the previous chapter, sand can be reasonably assumed to behave as an elastic-plastic material. This means that the total strains can be decomposed into elastic and plastic components ($\Delta\varepsilon = \Delta\varepsilon^e + \Delta\varepsilon^p$). Moreover, the model will be based on incremental elastic-plastic theory as outlined in Section 3.3.

- Principal axes of stress and strain increment are assumed to coincide.

This assumption is valid for isotropic material or for the special case of anisotropic material in which the principal axes of stress coincide with the axes of anisotropy (Hill, 1950). Otherwise, the principal axes of stress and strain increment do not generally coincide. However, to capture the effects induced by sand inherent anisotropy in the response of sand to first time shear loading, the material will be treated as incrementally isotropic, but the plastic shear modulus varied from increment to increment with the direction, α_σ , of the major principal stress, σ_1 . Other effects induced by sand anisotropy,

e.g. anisotropic response under constant stress ratio paths, will not be considered by the model. In addition, as suggested by Negussey and Vaid (1990), at low strain levels (10^{-4}) the strain increment directions seem related to the stress increment directions rather than to those of the stress. This is to be expected as at such low strains, elastic rather than plastic response would dominate and this will be addressed below.

- The idealized characteristic behaviour of sand discussed in Sections 2.7 and 3.4, and schematically shown in Figure 2.18, is further simplified by the model as depicted in Figure 4.1.

The behaviour illustrated in Figure 4.1 is simulated by the model assuming a unique relationship between the stress ratio and the *plastic* component of the strain increment ratio (Figure 4.1*d*), i.e. the rate of dilatancy. Negussey and Vaid (1990) found that at low stress ratio levels and hence small strains, a linear stress dilatancy relationship does not hold. However, they presented their results in terms of *total strains* as opposed to separating the strain increment ratio, $(\Delta\varepsilon_v/\Delta\gamma)$, into the *elastic* and *plastic* components. To assess the validity of the assumed relationship between the stress ratio and the *plastic* component of the strain increment ratio, $(\Delta\varepsilon_v/\Delta\gamma)^p$, the shear stress-strain and the volumetric-shear strain response observed in one of the drained simple shear tests (i.e. $D_r = 45.8\%$, Figure 2.1) on Ottawa sand by Vaid et al. (1981), was captured with the model (Figures 4.2*a* and *b*). The relationship between the shear to normal stress ratio, $\eta = \tau/\sigma'$, and $(\Delta\varepsilon_v/\Delta\gamma)$ observed in such test (Figure 2.2, $D_r = 45.8\%$) is compared in Figure 4.2*c* to the $\eta - (\Delta\varepsilon_v/\Delta\gamma)$ relationship predicted by the model. As can be seen here, the predicted

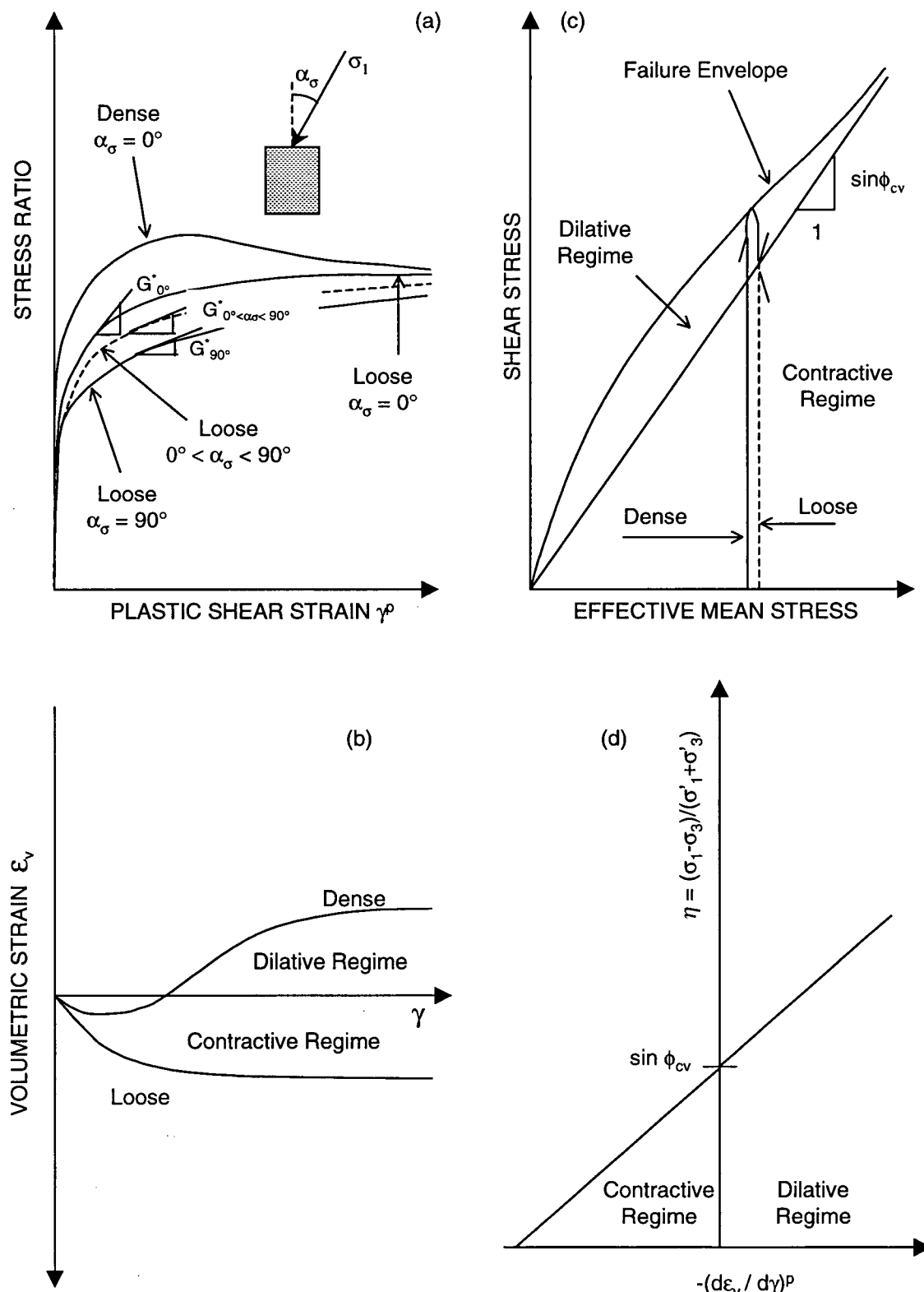


Figure 4.1 Model idealized skeleton behaviour of sand under monotonic loading. (a) Shear response. (b) Volumetric response. (c) Contractive and dilative states. (d) Shear-Volume coupling.

relationship between η and $(\Delta\varepsilon_v/\Delta\gamma)$ in terms of *total strains* is in remarkable agreement with the observed response. Therefore, assuming a unique relationship between the stress ratio and the *plastic* component of the strain increment ratio, $(\Delta\varepsilon_v/\Delta\gamma)^p$, for all strain levels is considered reasonable. In Chapter 6, the model will be shown capable of capturing laboratory test data with fair accuracy.

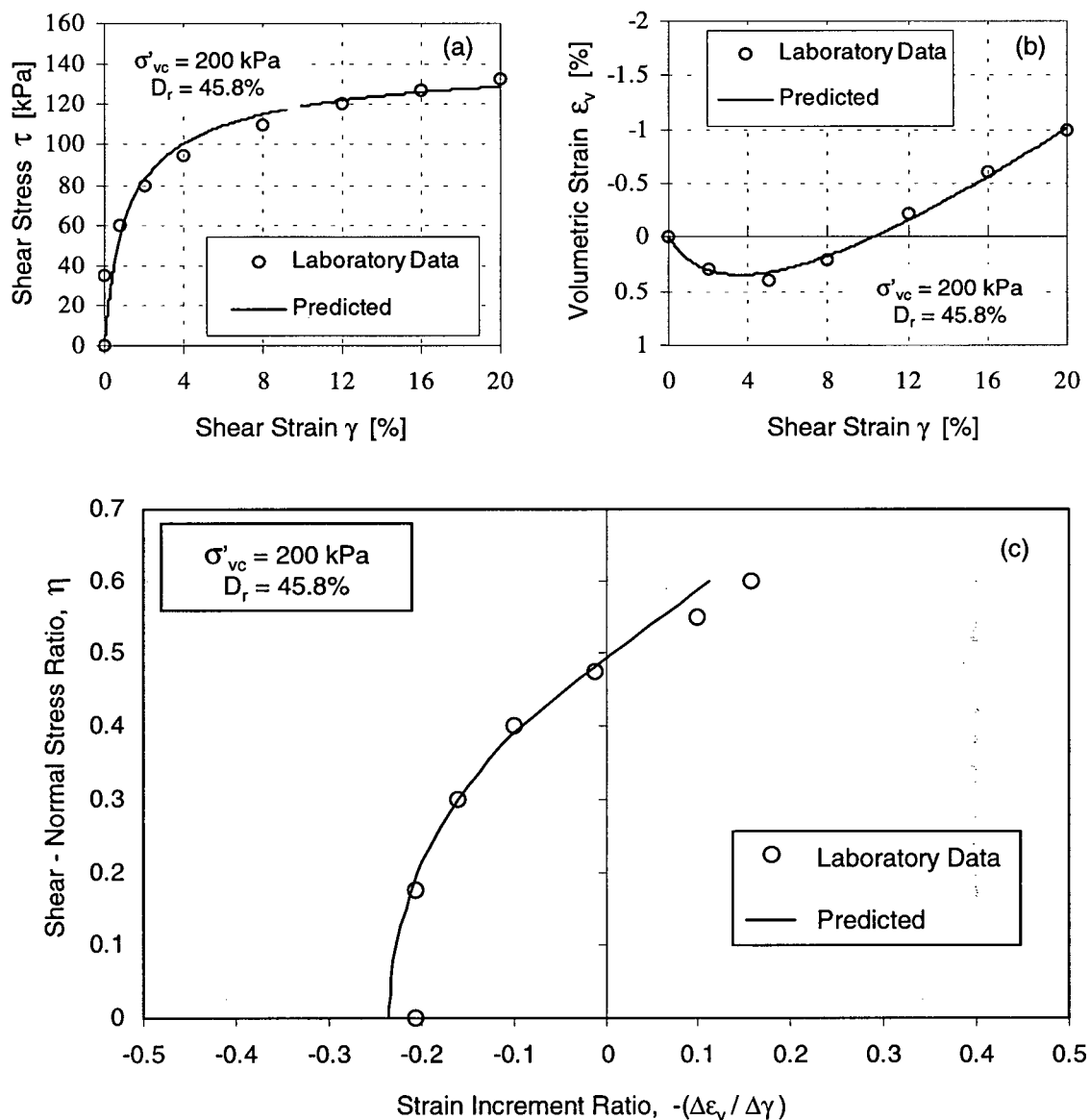


Figure 4.2 Observed and predicted responses in a drained simple shear test on Ottawa sand (basic data from Vaid et al. 1981). (a) τ vs. γ . (b) ε_v vs. γ . (c) η vs. $(\Delta\varepsilon_v/\Delta\gamma)$.

- During loading (i.e. $t/s' > \eta_d$ and/or $\{1/3[(\sigma'_1)^2 + (\sigma'_2)^2 + (\sigma'_3)^2]\}^{1/2} > \sigma^c$, see Figure 4.3) elastic and plastic strains are assumed to occur simultaneously, while only elastic strains are considered during unloading (i.e. $t/s' < \eta_d$ and $\{1/3[(\sigma'_1)^2 + (\sigma'_2)^2 + (\sigma'_3)^2]\}^{1/2} < \sigma^c$) and reloading (if the state of stress remains within the elastic region delimited by the current yield loci (Figure 4.3)).

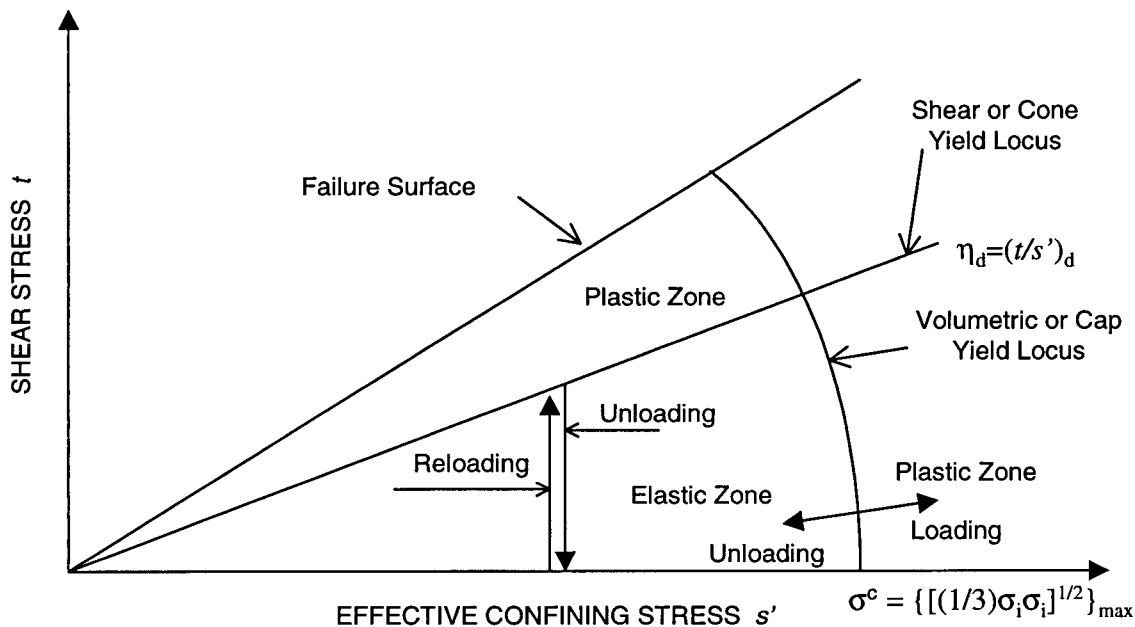


Figure 4.3 Elastic and plastic zones.

The existence of an elastic region in which only elastic response is allowed, is a realistic assumption for sand behaviour at small strain levels. It is also realistic, when sand is subjected to cyclic loading but the unload-reload excursions are not large. However, as will be explained later, the elastic region in this model is too large to allow correct prediction of large unload-reload loops. This limitation can be overcome by reducing the size of the elastic region or even more, shrinking it to a point, in which case the response would be entirely elastic-plastic during both loading and unloading.

- The incremental elastic response is considered to be linear, isotropic, stress level dependent ($f = (s')$), and specified by the generalized Hooke's law.
- The incremental plastic response is considered given by superposition of two plastic components:
 - $\Delta\varepsilon^{ps}$, yielded by a shear or cone type of mechanism (Figure 4.3) that is assumed to respond only to stress paths in which the stress ratio, η_d , increases, and
 - $\Delta\varepsilon^{pc}$, yielded by volumetric or cap type of mechanism (Figure 4.3) that is assumed to respond only to stress paths in which the consolidation pressure, referred to here as cap pressure, σ^c , increases beyond its maximum value previously attained.

The two plastic mechanisms are assumed independent of each other and the total plastic response determined by adding the contribution of each part, i.e.

$$[4.1] \quad \Delta\varepsilon^p = \Delta\varepsilon^{ps} + \Delta\varepsilon^{pc}$$

where $\Delta\varepsilon^p$ is the plastic strain increment; $\Delta\varepsilon^{ps}$ is the plastic strain increment from the shear or cone mechanism; and $\Delta\varepsilon^{pc}$ is the plastic strain increment from the cap mechanism. The total strain increment $\Delta\varepsilon$ is then given by:

$$[4.2] \quad \Delta\varepsilon = \Delta\varepsilon^e + \Delta\varepsilon^p = \Delta\varepsilon^e + \Delta\varepsilon^{ps} + \Delta\varepsilon^{pc}$$

where $\Delta\varepsilon^e$ is the elastic strain increment.

This formulation allows the model to predict different material responses under different stress paths as function of the stress ratio, the consolidation pressure and the stress increment.

- The shear plastic mechanism is considered strain hardening, its flow rule non-associative (derived from energy considerations, Appendix A), and the shear yield loci are assumed radial lines of constant stress ratio.

These assumptions are in general agreement with experimental findings and suggestions by Poorooshasb et al. (1966 and 1967), Tatsuoka and Ishihara (1974), and Ishihara et al. (1975). Tatsuoka and Ishihara (1974) determined experimentally that the shear yield surfaces are contours of same shear-strain, not quite straight lines, but suggested that they could be approximated by radial lines of constant stress ratio. However, Tatsuoka and Ishihara (1974) reported the occurrence of plastic volumetric strains under stress paths in which the maximum consolidation pressure was increased while the shear stress was kept constant. In addition, El-Sohby and Andrawes (1973) also observed the occurrence of plastic strains in sand loaded under constant stress ratio paths. Since the plastic shear or cone type of mechanism cannot predict this kind of response, the plastic volumetric or cap type of mechanism is introduced in the model.

- The volumetric plastic mechanism is considered to strain harden isotropically in accordance with an associative flow rule, and the volumetric yield surface, or cap, is assumed a sphere with center in the origin of the stress space.

Isotropic cap models of similar type have been used by Lade (1977) and Vermeer (1980) to capture the plastic volumetric compression induced by an increase in the confining pressure. Nonetheless, El-Sohby and Andrawes (1973) demonstrated that sand loaded under constant stress ratio paths exhibits plastic anisotropic response. In addition, Negussey (1984) showed that when sand is subjected to isotropic compression, the deformation field could be anisotropic due to inherent anisotropy. These issues are not addressed by the cap model.

- The evolution of the elastic region is assumed governed by the hardening rules of both shear (cone) and volumetric (cap) plastic mechanisms, i.e.,
 - a) A shear-hardening rule that assumes a hyperbolic relationship between the stress ratio and the plastic shear strain, and that combines expansion of the current shear yield locus (Figure 4.3) with kinematic hardening, as will be explained in Section 4.3.3. In addition, the current shear yield locus is assumed to soften/harden with continuous rotation of the principal stresses, as will be explained in Section 4.3.5.
 - b) A volumetric-hardening rule that considers the cap pressure and plastic volumetric strain to be related through a power law in addition to assume isotropic hardening of the current volumetric yield locus (Figure 4.3), as will be explained in Section 4.4.3.
- A Mohr-Coulomb type of failure criterion is used to determine the ultimate peak strength and state of stress.

Experimental data has shown that the shear failure surface is slightly curved as opposed to the Mohr-Coulomb pyramid, which ignores the effect of the intermediate principal stress, σ'_2 , and mean stress, $\sigma'_m = (\sigma'_1 + \sigma'_2 + \sigma'_3)/3$. Failure criteria that resemble experimental observations more closely than the Mohr-Coulomb criterion have been developed by Matsuoka (1974), and Lade and Duncan (1975), although their shapes do not deviate much from that of the Mohr-Coulomb pyramid (Figure 4.4). Nevertheless, the Mohr-Coulomb criterion has been used extensively in engineering practice with good results. The Mohr-Coulomb failure criterion was adopted for mathematical convenience and the familiarity that engineers already have with it.

The proposed constitutive model described above is considered to address most of the important characteristics of sand behaviour relevant to static liquefaction analysis, i.e.,

- Non-linearity and stress dependency of the stress-strain relationship;
- Shear-Volume coupling;
- Path dependency;
- Anisotropic response induced by direction of loading under first time shear loading;
- Strains induced by continuous rotation of principal stresses.

In terms of cyclic liquefaction, the model requires some modifications that can be implemented into the model's framework. This task can be achieved by modifying the hardening rule and defining the way in which the plastic moduli harden as cyclic plastic strains accumulate.

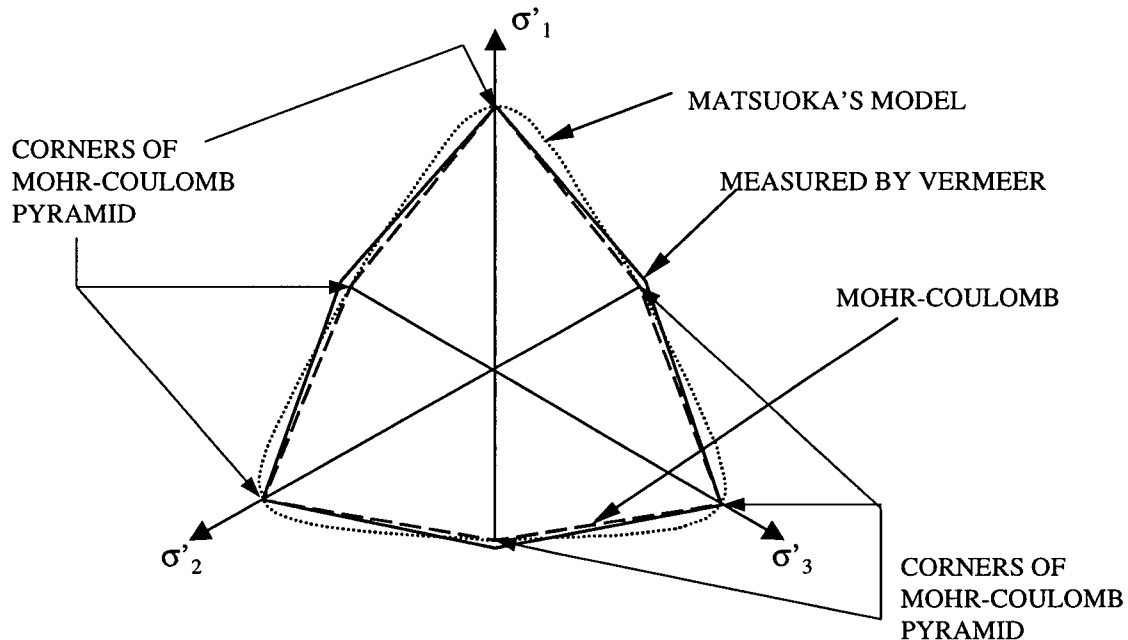


Figure 4.4 Deviatoric view of the six-sided pyramid of Mohr-Coulomb, Matsuoka-Vermeer's model, and failure envelope measured by Vermeer (1982).

In the following sections, the proposed constitutive model will be presented in detail for plane strain conditions. This is done for ease of presentation, but as will be explained when discussing the numerical implementation of the model, extension to the three-dimensional axi-symmetric case is straightforward. Since plane strain conditions require that the total out-of-plane strain, ϵ_z , be zero, two scenarios are possible: (i) both elastic and plastic components of the out-of-plane strain are zero; or (ii) elastic and plastic components of the strain in the out-of-plane direction are equal in magnitude, but of opposite sign. Here, it will be assumed that both elastic and plastic components of the out-of-plane strain, ϵ_z , are zero. This implies that, for plane strain conditions, no yielding occurs in the out of plane direction and hence, the effect of the intermediate principal stress, σ'_2 , is neglected. The model formulation is then two-dimensional and in terms of

the stress parameters s' , the effective confining stress, and t , the maximum shear stress.

The stress parameters s' and t are mathematically defined as:

$$[4.3] \quad s' = \frac{(\sigma'_1 + \sigma'_3)}{2}$$

$$[4.4] \quad t = \frac{(\sigma'_1 - \sigma'_3)}{2}$$

where σ'_1 and σ'_3 are the effective major and minor principal stresses, respectively.

4.2 Elastic response

The elastic response is assumed to be incremental linear, isotropic and specified by Hooke's law. For plane strain conditions, the incremental elastic strains are related to the stress increments by:

$$[4.5] \quad \begin{aligned} \Delta\epsilon_x^e &= \left(\frac{1-v^2}{E} \right) \Delta\sigma'_x - \left(\frac{v(1+v)}{E} \right) \Delta\sigma'_y \\ \Delta\epsilon_y^e &= - \left(\frac{v(1+v)}{E} \right) \Delta\sigma'_x + \left(\frac{1-v^2}{E} \right) \Delta\sigma'_y \\ \Delta\epsilon_{xy}^e &= \frac{\Delta\gamma_{xy}^e}{2} = \frac{\Delta\tau_{xy}}{2G^e} \end{aligned}$$

where E is the Young's modulus; v , the Poisson's ratio; G^e , the elastic shear modulus; $\Delta\sigma'$, the effective stress increment; $\Delta\epsilon^e$, elastic strain increment; $\Delta\gamma^e$, the elastic shear strain increment; $\Delta\tau$, the shear stress increment; and x and y are subscripts that correspond to the orientation of the Cartesian coordinate axes, respectively;. In matrix form, Equation 4.5 is:

$$[4.6] \quad \{\Delta\epsilon^e\} = [C^e] \{\Delta\sigma'\}$$

where $[C^e]$ is the matrix of coefficients of Equation 4.5.

The Young's modulus E and Poisson's ratio ν can be converted to elastic bulk and shear moduli as follows:

$$[4.7] \quad B^e = \frac{E}{3(1-2\nu)}$$

$$[4.8] \quad G^e = \frac{E}{2(1+\nu)}$$

where B^e is the elastic bulk modulus.

In order to account for stress level dependency of the elastic moduli, these must be formulated in such a way that no energy generation or dissipation in a closed unload-reload cycle can occur. In this respect, Molenkamp (1988) showed that to comply with energy considerations, the elastic bulk and shear moduli could be expressed as functions of the confining stress to some power ($1-P$), as long as some additional conditions were met. These supplementary conditions are: (i) the stiffness ratio G^e/B^e should be kept constant, which implies that both bulk and shear moduli depend on the same exponent ($1-P$), and (ii) the value of P should vary between 0 and 1. However, Hardin (1978) concluded that the elastic Poisson's ratio, ν , for sand varies between 0 and 0.2. In fact, he recommended a value of $\nu = 0.12$. Based on these observations, the elastic parameters B^e and G^e are assumed to be stress level dependent and characterized as follows:

$$[4.9] \quad G^e = k_G^e P_A \left(\frac{s'}{P_A} \right)^{me}$$

$$[4.10] \quad B^e = \frac{2G^e(1+\nu)}{3(1-2\nu)}$$

where k_G^e is the elastic shear modulus number; P_A , the atmospheric pressure in the chosen units; me , the elastic shear modulus exponent = $(1-P)$, where me varies between 0 and 1.0; $s' = (\sigma'_1 + \sigma'_3)/2$, the confining stress; and ν , the elastic Poisson's ratio.

4.3 Plastic Shear Response

Before presenting details of the shear plastic constituent of the model, it will be emphasized that the formulation currently under discussion relates to the plastic *shear* or *cone* mechanism only. Therefore, a superscript “*s*” will be used for conceptual clarity.

4.3.1 Failure and yield functions of the cone (shear) mechanism

A Mohr-Coulomb type of failure function is assumed to determine the ultimate strength and state of stress achievable in this model. In the $s':t$ plane, the failure function f_f is a line with slope $\sin\phi_f$ (Figure 4.5), and in terms of the effective major and minor principal stresses σ'_1 and σ'_3 , is given by:

$$[4.11] \quad f_f = \sigma'_1 - \sigma'_3 N_{\phi_f} = 0$$

where

$$[4.12] \quad N_{\phi_f} = \frac{(1 + \sin \phi_f)}{(1 - \sin \phi_f)} = \frac{(1 + \eta_f)}{(1 - \eta_f)}$$

in which ϕ_f is the internal friction angle at failure; and η_f , the stress ratio at failure = $(t/s')_f = \sin\phi_f$

In accordance with findings of Pooroosharb et al. (1966) and Ishihara et al. (1975), it is assumed that yield with strain hardening occurs when the stress ratio η increases as plastic shear strain γ^s takes place. The yield loci are then taken as lines of constant stress ratio or developed friction angle. Hence, they are mathematically defined by the yield function f^s , family of lines with slope $\sin\phi_d$ (Figure 4.5), which in terms of σ'_1 and σ'_3 , is determined by:

$$[4.13] \quad f^s = \sigma'_1 - \sigma'_3 N_{\phi_d} = 0$$

where

$$[4.14] \quad N_{\phi_d} = \frac{(1 + \sin\phi_d)}{(1 - \sin\phi_d)} = \frac{(1 + \eta_d)}{(1 - \eta_d)}$$

$$[4.15] \quad \eta_d = \left(\frac{t}{s'} \right) = \sin\phi_d$$

η_d is the developed stress ratio and ϕ_d the developed friction angle.

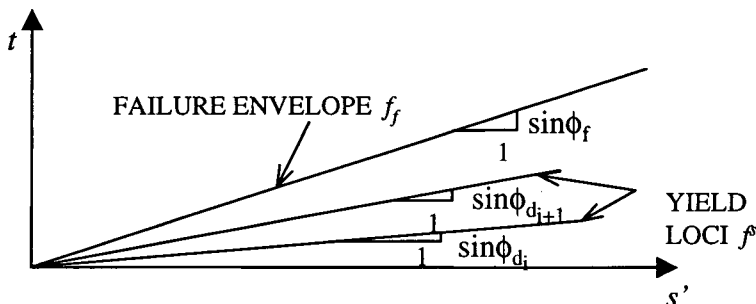


Figure 4.5 Schematic representation of the failure and yield functions of the cone mechanism.

4.3.2 Flow rule and plastic potential of the cone (shear) mechanism

The direction of the plastic strain increment vector $\Delta\boldsymbol{\varepsilon}^{ps}$ that results from the plastic shear or cone mechanism is determined by the “cone” flow rule. The flow rule used in this part of the model is non-associative and based on energy considerations. It relates the “cone” plastic volumetric and shear strain increments, $\Delta\varepsilon_v^{ps}$ and $\Delta\gamma^{ps}$ respectively, as follows:

$$[4.16] \quad \Delta\varepsilon_v^{ps} = (\sin\psi_d) \Delta\gamma^{ps}$$

where ψ_d is the developed dilation angle, which in turn is related to the constant volume friction angle ϕ_{cv} and the developed friction angle ϕ_d by:

$$[4.17] \quad \sin\psi_d = (\sin\phi_{cv} - \sin\phi_d)$$

This is a non-associative flow rule since the direction of the cone plastic strain increment vector $\Delta\boldsymbol{\varepsilon}^{ps}$ is not perpendicular to the yield loci, which are lines of constant stress ratio or developed friction angle (Figure 4.6). The derivation is presented in Appendix A and is similar to derivations by Taylor (1948), Rowe (1962), Schofield and Wroth (1968), and Matsuoka and Nakai (1977).

Equation 4.17 gives positive values for $\sin\psi_d$ (indicating contractive response) when the developed stress ratio, $\eta_d = \sin\phi_d$, is less than $\sin\phi_{cv}$, and negative values

(indicating dilative response) when η_d exceeds $\sin\phi_{cv}$. This is in agreement with the characteristic response shown in Figure 4.1d.

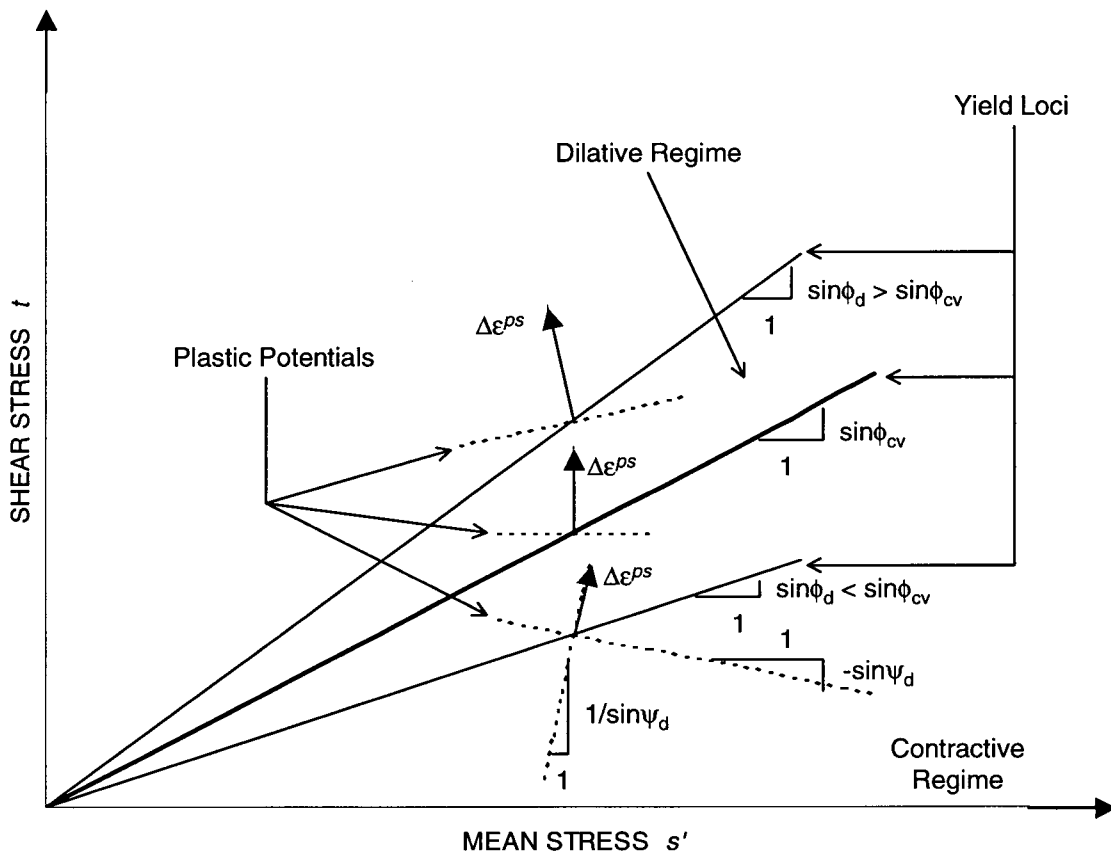


Figure 4.6 Schematic representation of radial yield loci, plastic potentials, and plastic strain increment vectors induced by the cone mechanism.

The plastic potential function that corresponds to the non-associative flow rule described above can be written as:

$$[4.18] \quad g^s = \sigma'_1 - \sigma'_3 N_{\psi_d} = 0$$

where

$$[4.19] \quad N_{\psi_d} = \frac{(1 + \sin \psi_d)}{(1 - \sin \psi_d)}$$

From plasticity theory, the plastic strain increments $\Delta\varepsilon_{ij}^{ps}$ are given by:

$$[4.20] \quad \Delta\varepsilon_{ij}^{ps} = \lambda^s \left(\frac{\partial g^s}{\partial \sigma'_{ij}} \right)$$

where λ^s is a constant of proportionality between the plastic strain increments $\Delta\varepsilon_{ij}^{ps}$ and the partial derivatives of the plastic potential g^s . The scalar λ^s is determined from plasticity theory and its derivation is presented in Appendix B.

4.3.3 Hardening rule of the cone (shear) mechanism

Plastic shear strains are assumed to be caused by an increase in stress ratio $\Delta\eta$ as shown in Figure 4.7. Hyperbolic formulations, like those by Kondner and Zelasko (1963), Duncan and Chang (1970), and Matsuoka and Nakai (1977), have been found to capture well the shear stress-strain response of most granular soils. An approach similar to Duncan and Chang (1970) is adopted here, but modified as follows: 1) only the plastic component of shear strain is assumed to follow a hyperbolic formulation; 2) the plastic shear strain is controlled by the stress ratio η rather than the shear stress only.

The developed stress ratio η_d was defined by Equation 4.15 as:

$$[4.15bis] \quad \eta_d = \left(\frac{t}{s'} \right) = \sin \phi_d$$

where t is the maximum shear stress and s' the confining stress.

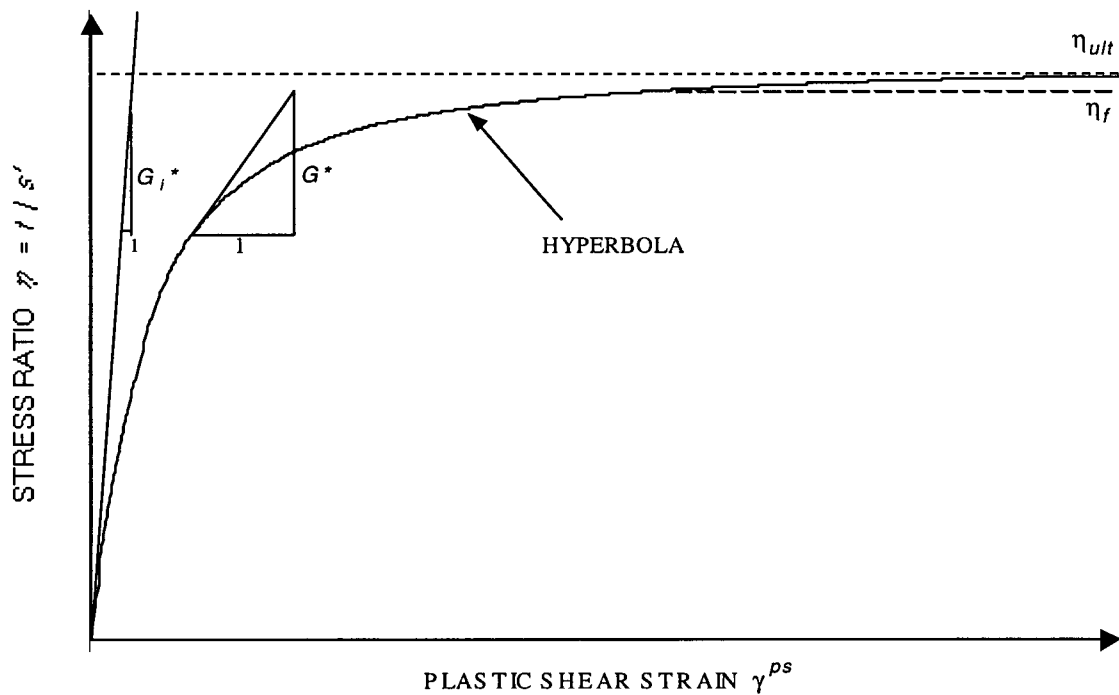


Figure 4.7 Relationship between developed stress ratio, η_d , and plastic shear strain γ^s .

The hardening law assumed for the shear or cone mechanism is given by a hyperbolic relation between the developed stress ratio η_d and the plastic shear strain γ^s as follows:

$$[4.21] \quad \eta_d = \frac{\gamma^s}{\left[\left(\frac{s'}{G_i^p} \right) + \left(\frac{\gamma^s R_F}{\eta_f} \right) \right]} = \frac{\gamma^s}{\left[\left(\frac{1}{G_i^*} \right) + \left(\frac{\gamma^s R_F}{\eta_f} \right) \right]}$$

$$[4.22] \quad G_i^p = k_G^p P_A \left(\frac{s'}{P_A} \right)^{np}$$

where G_i^P is the initial plastic shear modulus; G^* , the normalized initial plastic shear modulus = G_i^P / s' ; R_F , the failure ratio = η_f / η_{ult} , generally ranging from 0.5 to 1.0; η_f , the stress ratio at failure = $(t / s')_f = \sin\phi_f$; η_{ult} , the ultimate stress ratio from the best fit hyperbola; k_G^P , the plastic shear modulus number; and np , the plastic shear modulus exponent.

The slope of the curve η_d vs. γ^p is given by $(\Delta\eta_d / \Delta\gamma^p) = G^*$ (Figure 4.7). Therefore, the plastic shear strain increment, $\Delta\gamma^{ps}$, and developed stress ratio increment, $\Delta\eta_d$, are related through the normalized tangent plastic shear modulus G^* , as follows:

$$[4.23] \quad \Delta\gamma^{ps} = \left(\frac{1}{G^*} \right) \Delta\eta_d$$

The developed stress ratio increment $\Delta\eta_d$ in terms of shear stress t and confining stress s' is obtained by differentiating Equation 4.15, giving the following expression:

$$[4.24] \quad \Delta\eta_d = \left[\left(\frac{\Delta t}{s'} \right) - \left(\frac{t}{(s')^2} \right) \Delta s' \right]$$

where Δt is the shear stress increment and $\Delta s'$, the mean stress increment.

Thus, from Equations 4.23 and 4.24, the plastic shear strain increment $\Delta\gamma^{ps}$ can be written in incremental form as:

$$[4.25] \quad \Delta\gamma^{ps} = \left(\frac{1}{G^*} \right) \left[\frac{\Delta t}{s'} - \left(\frac{\eta_d}{s'} \right) \Delta s' \right]$$

where the normalized tangent plastic shear modulus, G^* , is given by:

$$[4.26] \quad G^* = k_G^p \left(\frac{s'}{P_A} \right)^{np-1} \left[1 - \left(\frac{\eta_d}{\eta_f} \right) R_F \right]^2$$

A negative increment in the confining stress ($\Delta s' < 0$) could cause the developed stress ratio $\eta_d = t/s'$ to increase, leading to a plastic shear strain increment $\Delta\gamma^{ps}$. In Equation 4.25, it may be seen that a stress ratio increment could be caused not only by a shear stress increment alone ($\Delta t > 0$), but also by reducing the confining stress ($\Delta s' < 0$). Consequently, a plastic shear strain increment would be induced if $\Delta s' < 0$. This is schematically shown in Figure 4.8. The concept of plastic shear strain induced by an increase in stress ratio η rather than shear stress alone is a key feature that allows the prediction of strain softening under undrained loading.

It was emphasized in Section 2.1 that the direction in which sand is loaded for the first time has a very strong effect on sand behaviour. This type of anisotropy was referred to as inherent anisotropy and was shown in Figure 2.4 (Vaid et al., 1995a). It is essential for a numerical model to capture this effect. To address this issue of inherent anisotropy, the hardening rule described above is modified by making the plastic shear modulus number, k_G^p , a function of the direction α_σ that the major principal stress σ'_1 has with respect to the vertical (normal to the bedding plane).

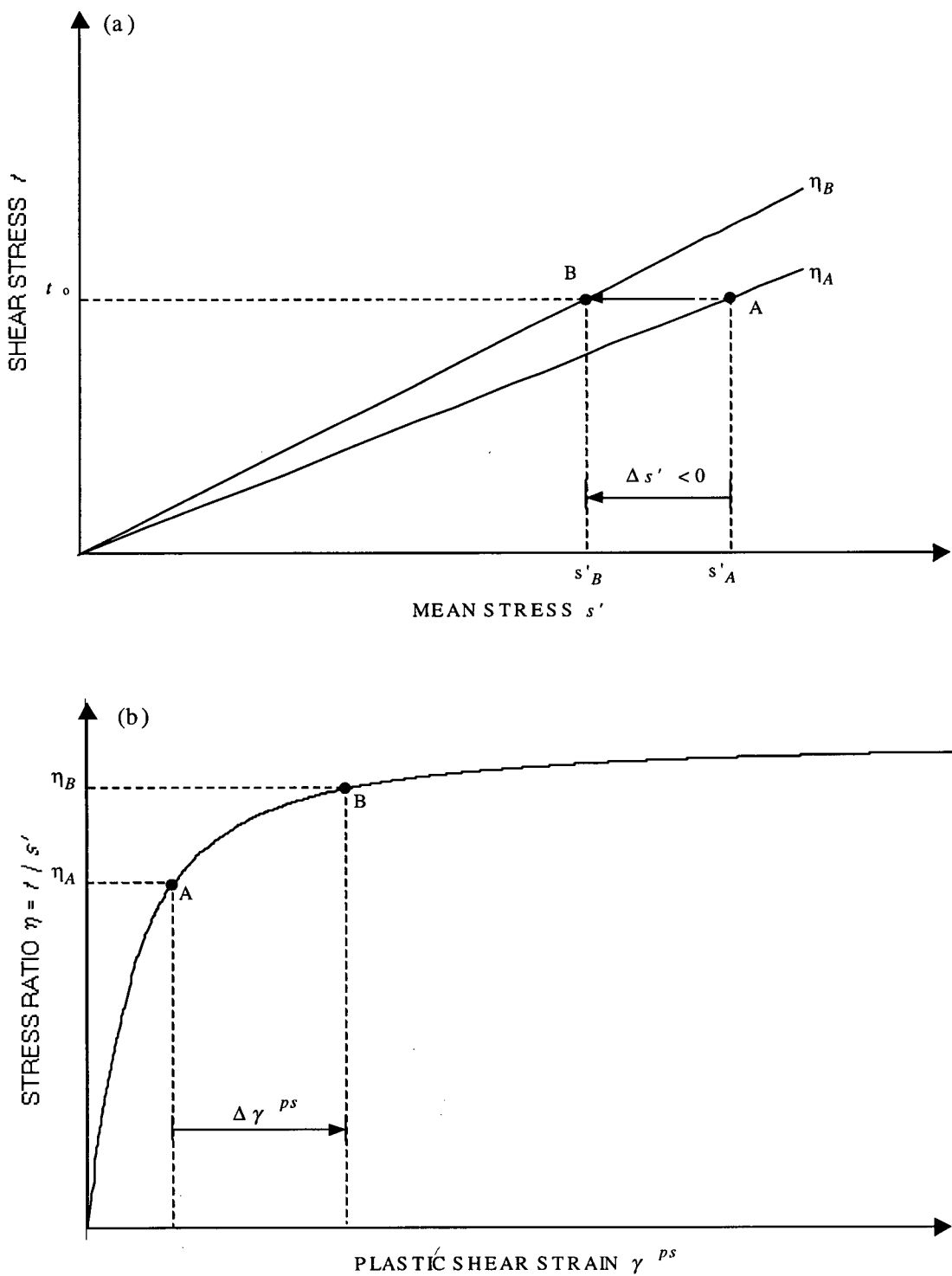


Figure 4.8 Plastic shear strain increment resulting from a mean stress reduction. (a) Stress ratio increment $\Delta\eta$ due to $\Delta s' < 0$. (b) Plastic shear strain increment $\Delta\gamma^{ps}$ induced by $\Delta\eta < 0$.

As can be seen in Figure 4.9, sand response that is strain hardening in triaxial compression, is strain softening in triaxial extension, as well as in simple shear. It may also be noted in this figure that the strongest response is exhibited in the case of vertical compression $\alpha_\sigma = 0^\circ$. The shear response becomes gradually softer as α_σ increases from 0° to its maximum value of 90° . The angle $\alpha_\sigma = 0^\circ$ corresponds to vertical compression, while $\alpha_\sigma = 90^\circ$ corresponds to vertical extension. In addition, it can be observed that the major effects of loading direction occur when α_σ varies between 0° and 45° , while only minor effects are exhibited when α_σ ranges between 45° and 90° . Based on these observations k_G^P is modified to account for anisotropy as follows:

For $0^\circ \leq \alpha_\sigma \leq 45^\circ$, k_G^P is given by:

$$[4.27] \quad k_G^P = (k_G^P)_0 [F - (F - 1)\cos 2\alpha_\sigma]$$

where $(k_G^P)_0$ is the plastic modulus number corresponding to $\alpha_\sigma = 0^\circ$ (vertical compression); F the factor of anisotropic plastic response, less than unity; α_σ the angle between the major principal stress direction and the vertical axis.

For $45^\circ < \alpha_\sigma \leq 90^\circ$, k_G^P is given by:

$$[4.28] \quad k_G^P = (k_G^P)_0 F$$

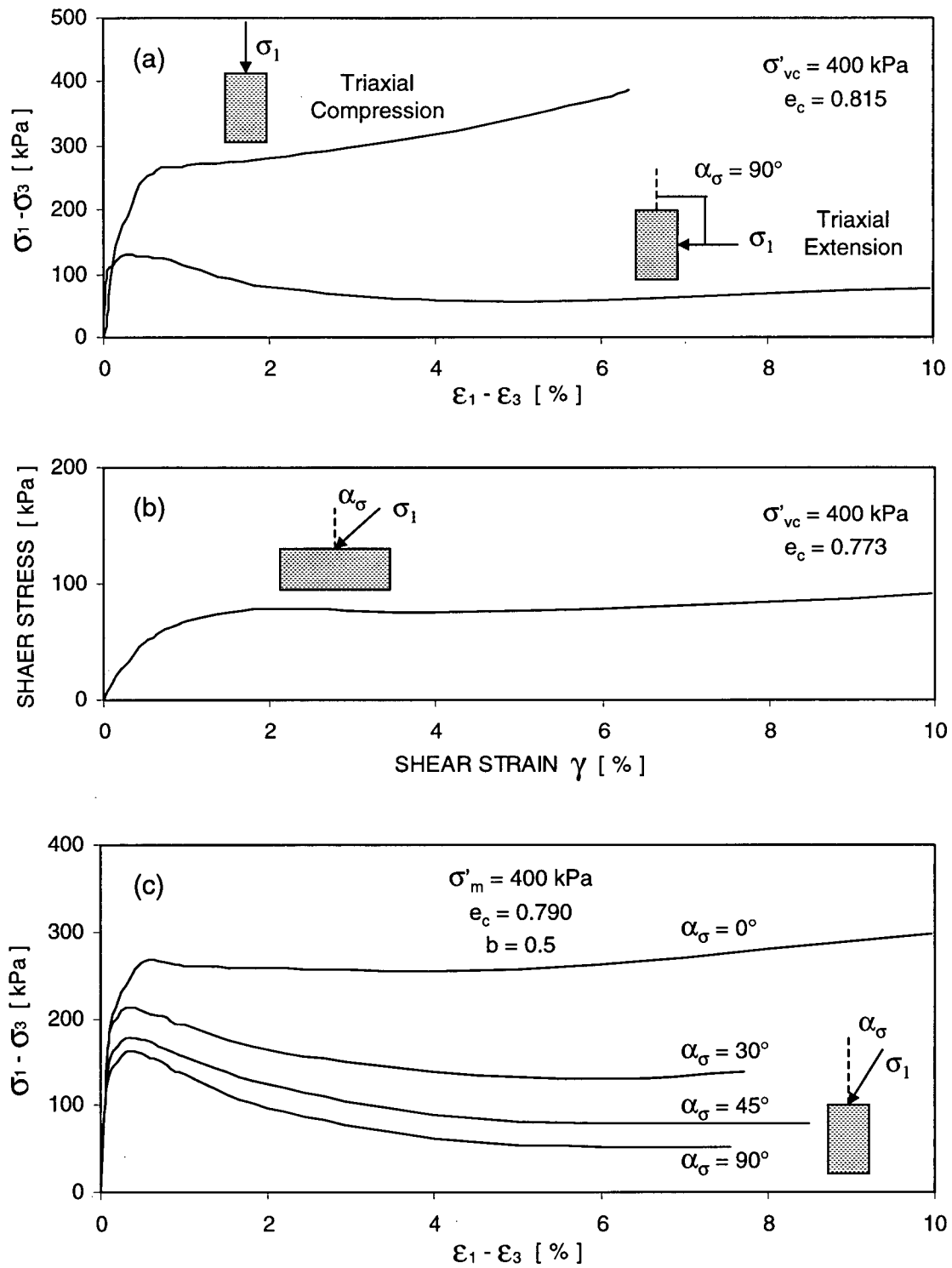


Figure 4.9 Undrained static behaviour of water pluviated Syncrude sand. (a) triaxial compression and extension, (b) simple shear, and (c) hollow cylinder torsion (modified from Vaid et al. 1995). σ'_m , effective mean normal stress; $b = (\sigma_2 - \sigma_3) / (\sigma_1 - \sigma_3)$; σ'_{vc} , effective confining stress; e_c , void ratio at σ'_{vc} .

Therefore, when $0^\circ \leq \alpha_\sigma \leq 45^\circ$, conditions ranging from vertical compression ($\alpha_\sigma = 0^\circ$) to simple shear ($\alpha_\sigma = 45^\circ$) are simulated by continuously varying the plastic modulus number, k_G^P , from its maximum to its minimum value. When $45^\circ < \alpha_\sigma \leq 90^\circ$, conditions ranging from simple shear to horizontal compression - vertical extension ($\alpha_\sigma = 90^\circ$) -, k_G^P is assumed constant.

In regard to the effect of α_σ in ϕ_f , experimental results are not conclusive. For instance, test data presented by Ishihara and Towhata (1983), and Lam and Tatsuoka (1988), suggest that ϕ_f varies with the direction of the major principal stress. In contrast, Been and Jefferies (1985) presented data indicating that ϕ_f is not significantly affected by anisotropy. Hence, a tentative relationship between ϕ_f and α_σ will be proposed here for practical purposes only, but it is left to the reader to decide whether such relationship is realistic or not.

For $0^\circ \leq \alpha_\sigma \leq 45^\circ$:

$$[4.29] \quad \phi_f = \phi_{cv} + [(\phi_f)_0 - \phi_{cv}] [F - (F - 1)\cos 2\alpha_\sigma]$$

For $45^\circ < \alpha_\sigma \leq 90^\circ$:

$$[4.30] \quad \phi_f = \phi_{cv} + [(\phi_f)_0 - \phi_{cv}] F$$

where $(\phi_f)_0$ is the friction angle at failure (maximum (σ'_1/σ'_3)).

The hardening rule presented above is used together with a hardening mechanism that combines *one-sided* expansion of the elastic region with kinematic hardening to capture the incremental elastic-plastic response. The hardening mechanism will be explained in the following by taking as an example a case in which drained compression

loading is followed by unloading and subsequent extension loading. Since the model is incremental, the procedure will be shown in an incremental fashion.

Virgin loading will be treated first. Loading starts from a condition of zero stress ratio, i.e., $\eta_d = 0$, although a state of $\eta_d \neq 0$ could be equally chosen. This state corresponds to point O in Figure 4.10. The initial elastic region is simply a line that coincides with the s' axis in Figure 4.10a. As loading takes place, an increment in γ^s causes the developed stress ratio to increase while the stress path goes from point O to A. The elastic region expands on *one side* of the s' axis *only*, and its new boundaries are the s' axis and the line of current developed stress ratio η_{dA} . Loading proceeds from point A through points B to F, and the incremental virgin loading curve in Figure 4.10b is defined. Of course, the smaller the increments are, the smoother the curve becomes.

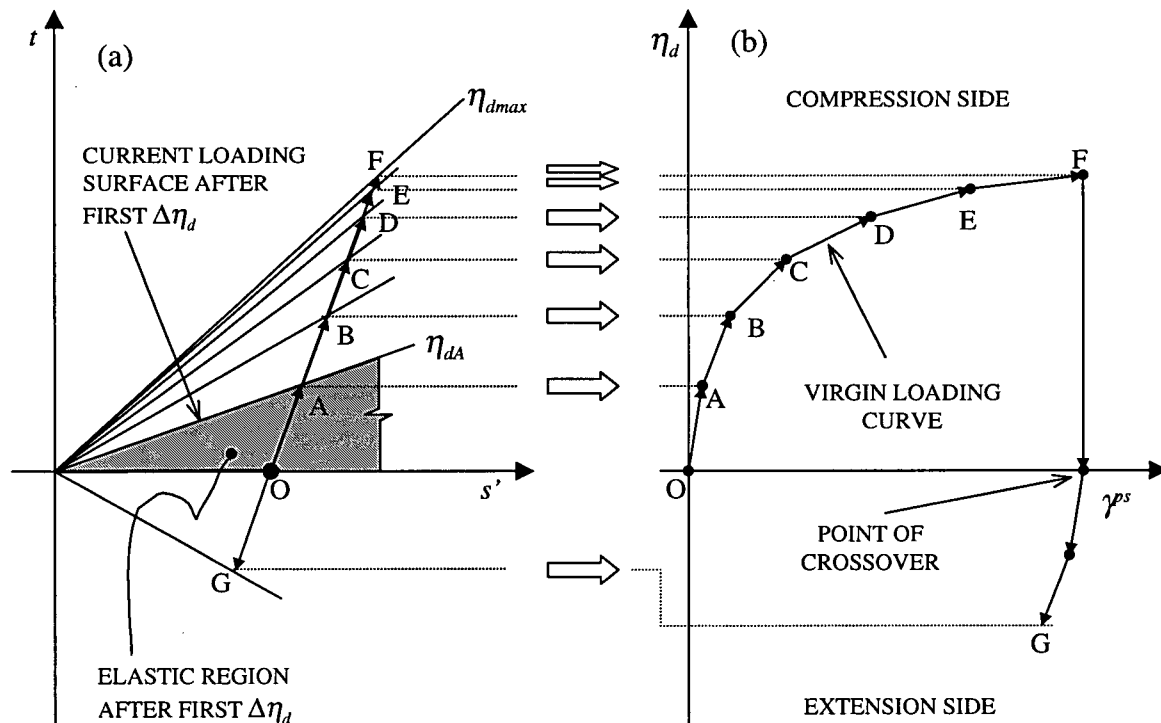


Figure 4.10 Expansion of elastic region with virgin loading. (a) Development of the elastic region. (b) Incremental stress ratio curve for virgin loading, and point of crossover upon unloading.

Upon unloading (decreasing η), the stress point transverses the elastic region from point F to O in Figure 4.10a, and a purely elastic response is predicted. If the process continues in the same direction and the s' axis is crossed over (see Figure 4.10b), loading (increasing η while $\eta > \eta_d$ on the other side of the s' axis) takes place and elastic-plastic behaviour is predicted again. The elastic domain moves now with the stress point, but does not change in size (Figure 4.11a). Kinematic hardening proceeds until the achieved state of stress in extension becomes equivalent to that defined by η_{dmax} on the compression side (Figure 4.11b). This state of stress is termed here the image stress ratio η'_{dmax} . Beyond η'_{dmax} , the elastic region stops moving as a whole and starts expanding again with γ^s , keeping one of its boundaries fixed to the s' axis while the other one strain hardens. A new value of η_{dmax} on the extension side is defined upon unloading and the process repeats as cyclic loading continues.

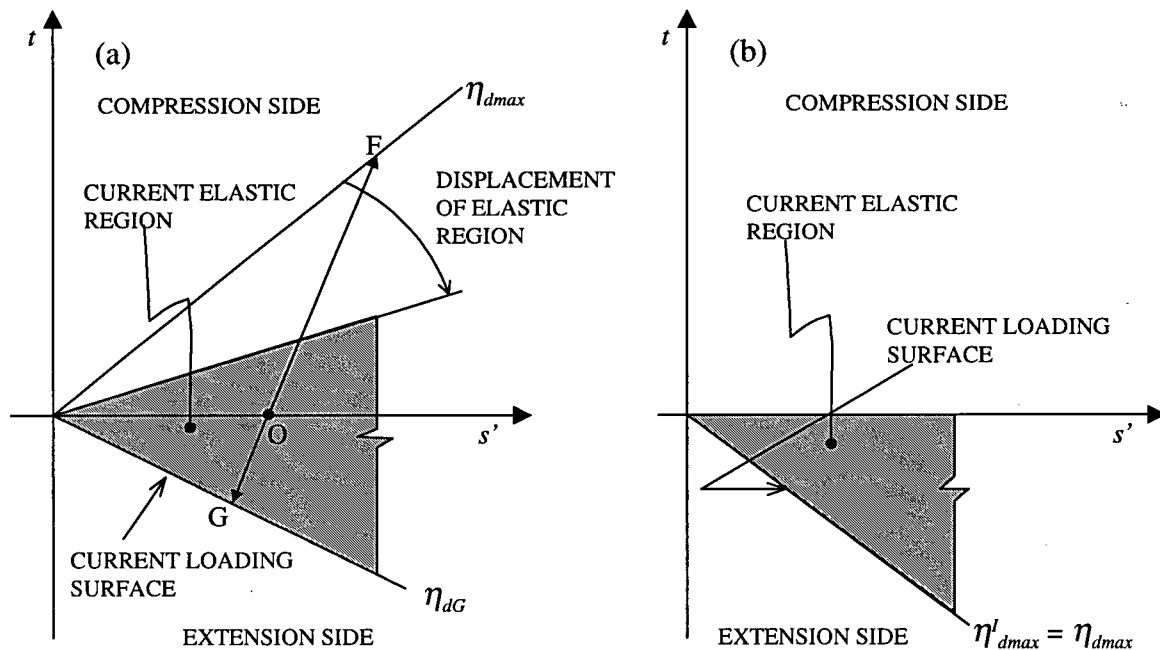


Figure 4.11 Kinematic hardening of elastic region. (a) Displacement of the elastic region without changing size or shape. (b) Image stress ratio η'_{dmax} marking the end of kinematic hardening and restarting of the elastic region expansion.

If reloading (increasing η while $\eta < \eta_{dmax}$) occurs before reaching the image stress ratio η_{dmax}^I , the predicted response is solely elastic until the opposite boundary of the elastic region is crossed (Figure 4.12). At this point, elastic-plastic response is predicted again allowing simulation of Bauschinger effect. Thereafter, strain hardening develops kinematically with no change in size of the elastic domain. Once the previously defined value of η_{dmax} on the compression side is reached, the elastic zone expands as explained before. When unloading takes place, the process of purely elastic behaviour followed by elastic-plastic response with either kinematic hardening or *one-sided* expansion of the elastic region repeats as cyclic loading goes on.

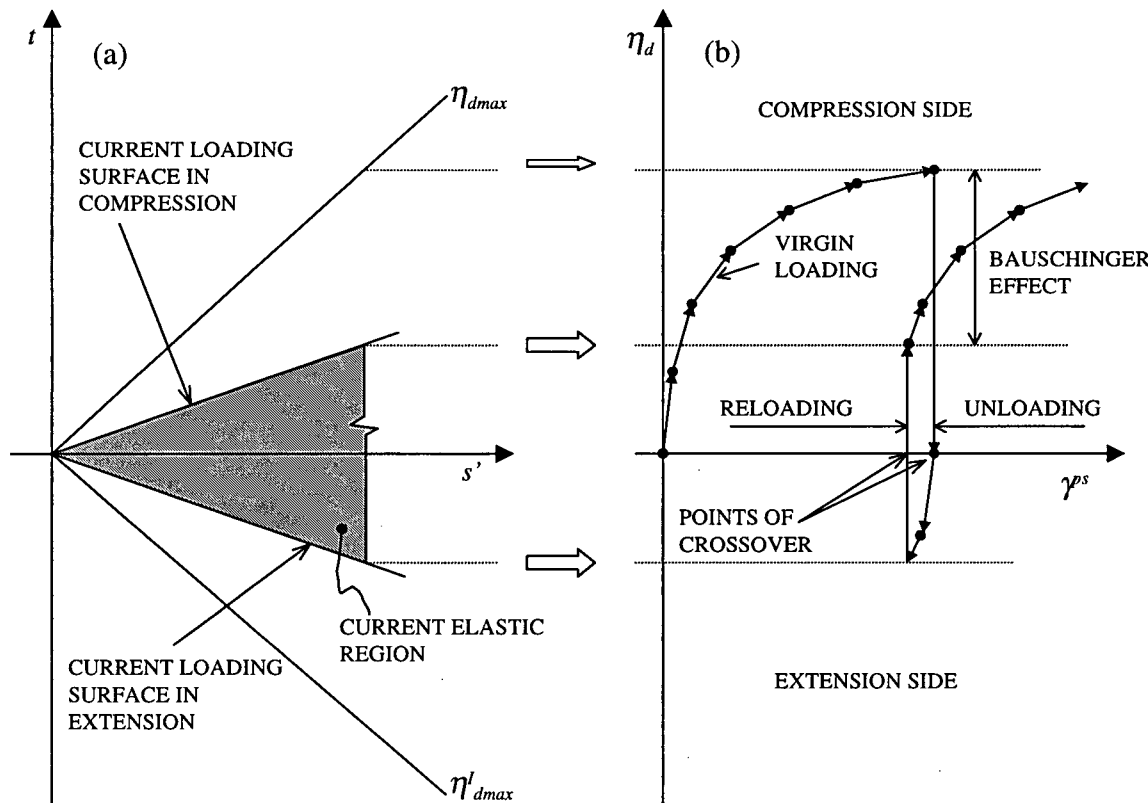


Figure 4.12 Reloading before reaching the image stress ratio η_{dmax}^I . (a) Elastic region. (b) Bauschinger effect.

The hardening mechanism as discussed so far applies strictly to compression-extension modes of loading only. To make it general, states of stress reversal, also termed here crossovers, induced by the shear stress in the x-y plane τ_{xy} , are also considered in the same fashion. The current state of stress is located in any of the four quadrants defined on the $(\sigma_x - \sigma_y)/s' : \tau_{xy}/s'$ plane (Figure 4.13). A crossover is predicted every time the state of stress passes from one quadrant to another. Depending on the yield criterion, either only elastic behaviour is anticipated if the current stress state is elastic, or elastic-plastic response is computed if the state of stress is plastic. Kinematic hardening takes place if the current stress ratio η_d is less than η_{dmax}^I , or the elastic region expands on *one of its sides* if η_d is greater than η_{dmax}^I .

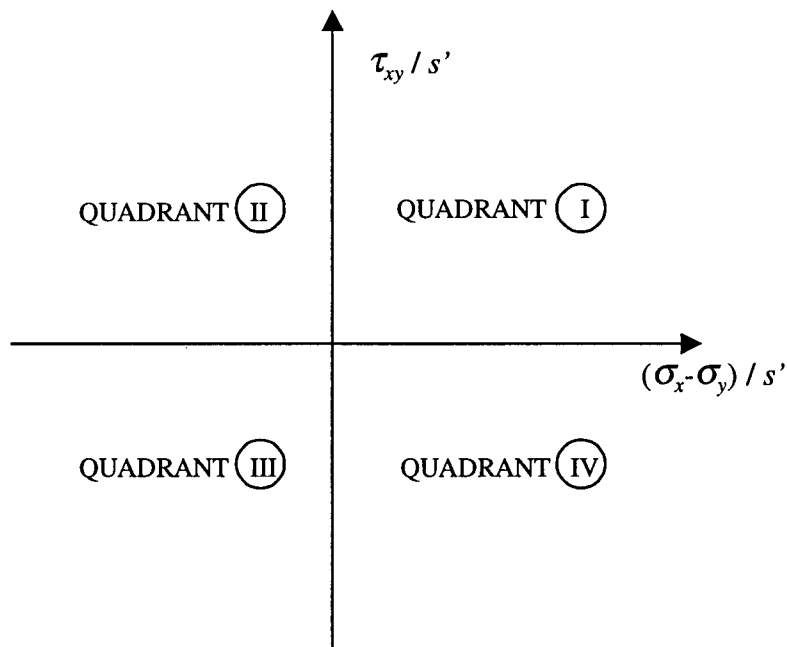


Figure 4.13 Quadrants of stress ratio to define crossover points.

Since sand does not respond as a purely elastic material when the unload-reload loops are long (see Figure 2.6), the cyclic behaviour of sand is only simulated in a simplified manner with this procedure. To overcome this limitation, the elastic region needs to be reduced. In addition, it was explained before that the unload-reload loops tend to close as cyclic plastic strains accumulate. Therefore, a hardening function that allows capturing this effect is needed to complete the model. However, this model was developed to carry out the analysis of the CANLEX static liquefaction problem in which no cyclic loading was involved. Hence, the simplified procedure discussed above was considered satisfactory from this viewpoint and a proper cyclic formulation is left for future development of the model.

4.3.4 Hardening parameter of the cone (shear) mechanism

Yield surface hardening depends on the stress history that involves plastic strains. Therefore, it is necessary to record the plastic history developed during the loading process, and this is done through the scalar quantity termed hardening parameter. The hardening parameter κ most commonly used in strain hardening models is the effective plastic strain, $\overline{\varepsilon_p}$, e.g., Hill (1950), Mroz (1967), Prévost and Hoeg (1975) and Vermeer (1978), as discussed in Section 3.3. The hardening parameter κ adopted in this model is the absolute value of the plastic shear strain increment $\Delta\gamma^{ps}$, defined as follows:

$$[4.31] \quad \Delta\kappa^s = |\Delta\gamma^{ps}| = |\Delta\varepsilon_1^{ps} - \Delta\varepsilon_3^{ps}|$$

where $\Delta\varepsilon_1^{ps}$ and $\Delta\varepsilon_3^{ps}$ are the plastic cone major and minor principal strain increments, respectively. The absolute value of $\Delta\gamma^{ps}$ is introduced to ensure that $\Delta\kappa^s > 0$, and therefore, guarantee hardening of the yield surface.

4.3.5 Pure rotation of principal stresses

Pure rotation of principal stresses refers to a stress path in which the magnitude of the principal stresses remains constant, but their directions vary continuously. Although the maximum stress ratio η_{max} does not change during this process, the stresses acting on planes with orientations different from the principal directions change with continuous rotation and induce plastic strains. In other words, the plane on which η_{max} acts is gradually changing its orientation as the principal stresses rotate.

Any state of stress can be represented on the Mohr diagram as illustrated in Figure 4.14. Here, a plane whose orientation with respect to the principal planes is defined by the angle 2θ is noted as the *a-b* plane. The effective mean normal stress s' and the shear stress τ_{ab} determine the stress ratio $\eta_{ab} = \tau_{ab} / s'$ on the *a-b* plane. Since τ_{ab} is less than the maximum shear stress t , then η_{ab} is less than the maximum stress ratio η_{max} . If the principal planes were rotated clockwise by a small angle $d2\theta$, the *a-b* plane would become the plane of maximum shear stress t and maximum stress ratio η_{max} . Thus, the *a-b* plane would experience a stress ratio increment due to a small rotation of the principal stresses, $d\eta_{rot}$, such that $\eta_{ab} + d\eta_{rot} = \eta_{max}$.

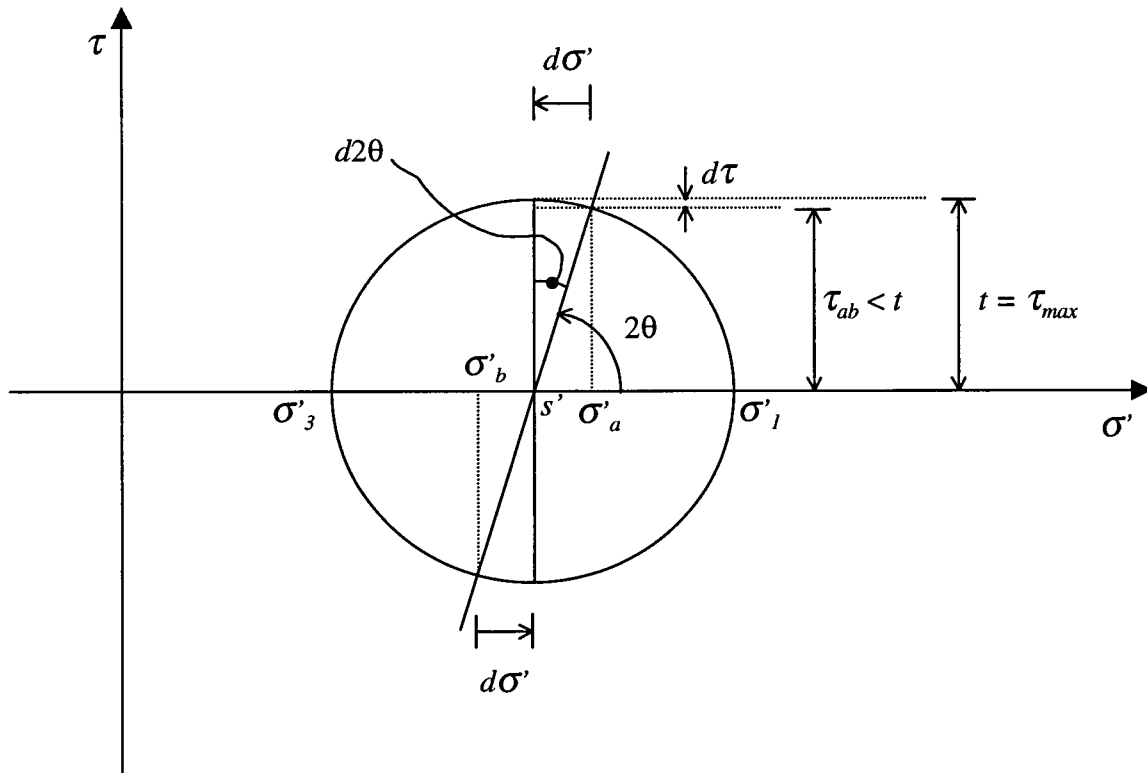


Figure 4.14 Small rotation of the principal stress.

According to the hardening rule used in this model, an increment in stress ratio $\Delta\eta$ induces an increment in shear plastic strain $\Delta\gamma^p$ (Figure 4.7). On the other hand, since the yield loci are assumed lines of maximum stress ratio η_{max} , it is straightforward to soften (contract) the current yield locus by an amount equal to $\Delta\eta_{rot}$. This would force the elastic region to expand by the same amount $\Delta\eta_{rot}$, and push the current yield locus back to its previous position defined by η_{max} . The magnitude of the principal stresses, and hence the maximum stress ratio η_{max} , would remain constant during the rotation process, but plastic behaviour would be induced in the model by softening/hardening the current yield surface in this manner.

The stress ratio increment due to a small rotation of principal stresses, $d\eta_{rot}$, will be deduced from Equation 4.24 and the aid of Figure 4.14. In this figure, it can be seen that when the a - b plane rotates an angle $d2\theta$, the normal stress σ'_a changes by an amount $d\sigma'$. From the geometry of the Mohr circle, it follows that:

$$[4.32] \quad d\sigma' = t \sin(d2\theta)$$

It can also be observed on Figure 4.14 that the shear stress τ_{ab} changes by an amount $d\tau$, but if the angle of rotation is small, i.e., $d2\theta \rightarrow 0$, $d\tau \ll d\sigma'$. During continuous rotation of principal stresses, the process could be assumed to occur in small angle increments $d2\theta$. Hence, if $d2\theta$ is small, neglecting the contribution of $d\tau$ could be considered a reasonable assumption. From Equation 4.24 and taking $dt = 0$, the stress ratio increment $d\eta$ can be expressed as:

$$[4.33] \quad d\eta = -\frac{t}{(s')^2} ds'$$

Recalling that $\eta = t / s'$, substitution of (4.32) into (4.33), renders:

$$[4.34] \quad d\eta = -\eta^2 \sin(d2\theta)$$

With this approach, gradual rotation of the principal stresses is accounted for in conjunction with the plastic shear or cone mechanism. To complete the model, the plastic cap mechanism will be presented in the following sections.

4.4 Plastic volumetric response

Yield loci like those adopted to capture plastic shear behaviour, are open with respect to the hydrostatic axis and can not account for pure volumetric compression or stress paths in which η remains constant. The plastic cap mechanism is introduced in the model to capture plastic contraction induced by both, isotropic compression and loading paths under constant stress ratio. The approach is essentially the same as that proposed by Vermeer (1980), but modified in that the elastic response is incremental, as discussed in Section 4.2, rather than obtained by a secant elastic formulation.

A superscript “c” will be used in the following sections to emphasize that the formulation currently under discussion relates to the plastic *cap* mechanism only.

4.4.1 Yield function of the cap (volumetric) mechanism

The yield cap is defined by a sphere in the effective principal stress space $\sigma'_1:\sigma'_2:\sigma'_3$,

with centre in the origin, and it is depicted in Figure 4.15 in the $s':t$ plane.

Mathematically, the yield spherical cap is given by:

$$[4.35] \quad f^c = \frac{1}{3} [(\sigma'_1)^2 + (\sigma'_2)^2 + (\sigma'_3)^2] - (\sigma^c)^2 = 0$$

where σ^c is the maximum radius attained by the sphere, termed here *cap pressure*.

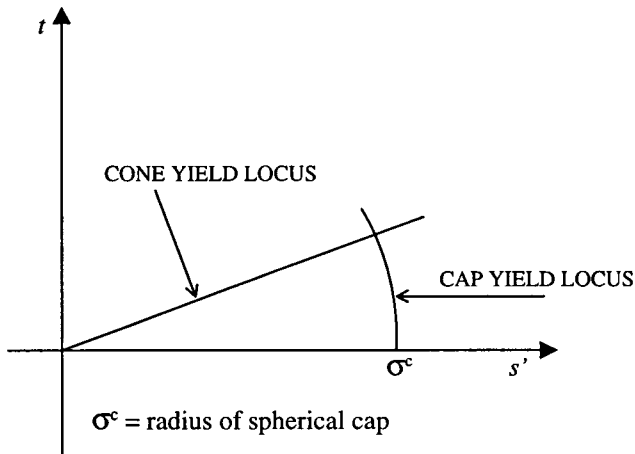


Figure 4.15 Representation of the spherical yield cap in the $s':t$ plane.

It is assumed that yield with isotropic strain hardening occurs when the cap pressure σ^c increases as plastic cap volumetric strain ε_v^{pc} takes place.

4.4.2 Flow rule and plastic potential of the cap (volumetric) mechanism

The direction of the plastic strain increment vector $\Delta\epsilon^{pc}$ that results from the plastic volumetric or cap mechanism is determined by the “cap” flow rule. The flow rule used in this part of the model is assumed associative and it is given by:

$$[4.36] \quad \Delta\epsilon_{ij}^{pc} = \lambda^c \left(\frac{\partial g^c}{\partial \sigma'_{ij}} \right)$$

where λ^c is a constant of proportionality between the cap plastic strain increments $\Delta\epsilon_{ij}^{pc}$ and the partial derivatives of the cap plastic potential g^c . λ^c is determined from plasticity theory and its derivation is presented in Appendix B.

Since the flow rule is associative, the direction of the plastic strain increment vector $\Delta\epsilon^{pc}$ is perpendicular to the yield loci and consequently the volumetric plastic potential function g^c coincides with the cap yield surface f^c . Hence,

$$[4.37] \quad g^c = f^c = \frac{1}{3} [(\sigma'_1)^2 + (\sigma'_2)^2 + (\sigma'_3)^2] - (\sigma^c)^2 = 0$$

4.4.3 Hardening rule of the cap (volumetric) mechanism

An increment in the cap pressure $\Delta\sigma^c$ is assumed to depend on the cap volumetric strain increment $\Delta\epsilon_v^{pc}$ as follows:

$$[4.38] \quad \Delta\epsilon_v^{pc} = \frac{1}{B^p} \Delta\sigma^c$$

where B^p is a stress dependent plastic bulk modulus given by:

$$[4.39] \quad B^p = k_B^p P_A \left(\frac{s'}{P_A} \right)^{mp}$$

where k_B^p is the plastic bulk modulus number and mp the plastic bulk modulus exponent.

4.4.4 Hardening parameter of the cap (volumetric) mechanism

The plastic volumetric strain ϵ_v^{pc} yielded by the cap mechanism is used to record the plastic volumetric history corresponding to this part of the model. Hence, the cap hardening parameter κ^c written in incremental form is given by:

$$[4.40] \quad \Delta\kappa^c = \Delta\epsilon_v^{pc} = (\Delta\epsilon_1^{pc} + \Delta\epsilon_2^{pc} + \Delta\epsilon_3^{pc})$$

where $\Delta\epsilon_1^{pc}$, $\Delta\epsilon_2^{pc}$ and $\Delta\epsilon_3^{pc}$ are the plastic cap major, intermediate and minor principal strains increments, respectively.

4.5 Total response

The final response is the sum of the elastic and plastic components and is given by:

$$[4.41] \quad \{\Delta\sigma'\} = [[D'^e] + [D'^p]]\{\Delta\varepsilon\} = [D']\{\Delta\varepsilon\}$$

where $\{\Delta\sigma'\}$ is the vector of effective stress increments $\Delta\sigma_x'$, $\Delta\sigma_y'$ and $\Delta\tau_{xy}$; $[D']$ is the constitutive elastic-plastic model matrix in terms of effective stresses; $[D'^e]$ and $[D'^p]$ are the constitutive elastic and plastic matrices, respectively, in terms of effective stresses, and which sum gives $[D']$, i.e. $[D'] = [D'^e] + [D'^p]$; $\{\Delta\varepsilon\}$ is the vector of total strain increments $= \{\Delta\varepsilon^e\} + \{\Delta\varepsilon^p\} = \{\Delta\varepsilon^e\} + \{\Delta\varepsilon^{ps}\} + \{\Delta\varepsilon^{pc}\}$, in which $\{\Delta\varepsilon^{ps}\}$ and $\{\Delta\varepsilon^{pc}\}$ have been transformed to the reference Cartesian coordinates by direction cosines.

4.6 Undrained response

Undrained behaviour is captured by imposing the volumetric constraint caused by the stiffness (B_f) of the fluid occupying the pores within the soil. In Figure 4.16, two elements subjected to a vertical stress increment $\Delta\sigma$ can be seen. The one on the left side represents a soil element and its volumetric stiffness is characterized by the skeleton's bulk modulus B' . The element on the right side represents an equivalent fluid that occupies the total volume of the element rather than just the volume of the soil pores. Its volumetric stiffness is characterized by the equivalent fluid stiffness (B_f / n), where n is the porosity of the soil.

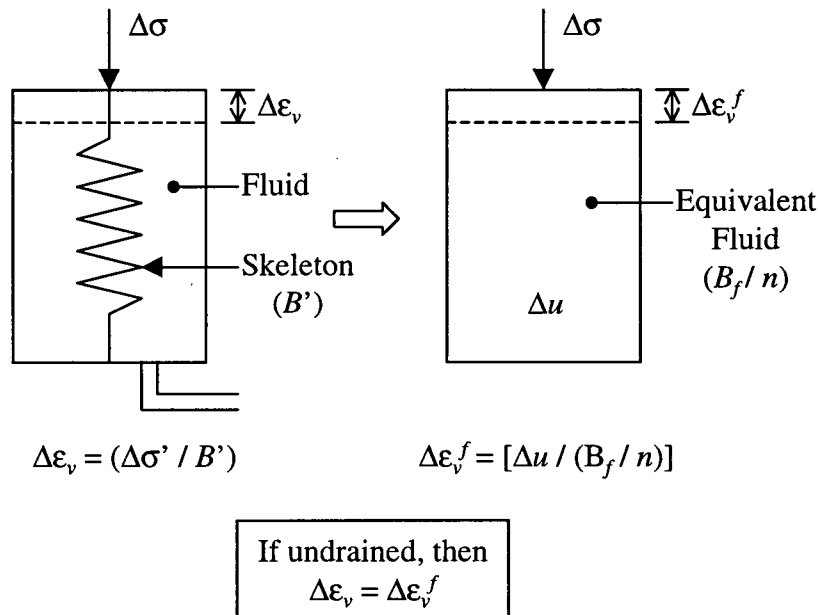


Figure 4.16 Soil element and equivalent fluid models.

Volumetric compatibility under undrained conditions requires that the equivalent fluid volumetric strain increment, $\Delta\epsilon_v^f$, must be equal to the volumetric strain of the soil skeleton, $\Delta\epsilon_v$. Hence, for a plane strain case under undrained conditions, the volumetric strain increment can be written as:

$$[4.42] \quad \Delta\epsilon_v = \Delta\epsilon_x + \Delta\epsilon_y = \Delta\epsilon_v^f$$

Therefore, the increment of pore fluid pressure due to a change in volume $\Delta\epsilon_v$ is given by:

$$[4.43] \quad \Delta u = \left(\frac{B_f}{n} \right) \Delta \varepsilon_v$$

and can be computed at the same time as the stress increment, since the strain increments $\Delta \varepsilon_x$ and $\Delta \varepsilon_y$ are known.

In matrix form:

$$[4.44] \quad \{\Delta u\} = [D_f] \{\Delta \varepsilon\}$$

where $[D_f]$ is the equivalent fluid stiffness matrix; $\{\Delta u\} = \{\Delta u, \Delta u, 0\}^T$; $\{\Delta \varepsilon\} = \{\Delta \varepsilon_x, \Delta \varepsilon_y, \Delta \varepsilon_{xy}\}^T$ and the superscript “ T ” is used to indicate the transpose vector.

By adding the stiffness contribution of the skeleton and the water, the stress-strain relationship can be formulated in terms of total stresses as follows:

$$[4.45] \quad \{\Delta \sigma\} = [[D'] + [D_f]] \{\Delta \varepsilon\}$$

Thus, for undrained conditions the stress-strain model can be obtained in terms of total stresses. Since the increment of pore fluid pressure is computed at each step of the analysis, the stress-strain model is therefore a fully coupled effective stress model. By adding the contribution of the fluid stiffness in this manner, strain softening behaviour of loose sand can be predicted.

4.7 Model parameters

The proposed constitutive model discussed in the previous sections requires determining eleven constants. Three of them are related to the elastic response and the other eight to the plastic cone and cap mechanisms. Determination of the elastic constants k_G^e , ν and me will be discussed first.

4.7.1 Elastic parameters.

Hardin (1978) found that the elastic shear modulus number k_G^e is a function of void ratio, $F(e)$, and a variable, A , related to the size and shape of the sand particles, as follows:

$$[4.46] \quad k_G^e = A \cdot F(e)$$

Values for A , $F(e)$ and the elastic exponent me suggested by various authors are listed in Table 4.1, where it can be seen that for sand, the elastic exponent me varies between 0.38 and 0.5.

Table 4.1. Typical values of A , $F(e)$ and the elastic exponent me .

Material	A	$F(e)$	me	Reference
Clean rounded sand	700	$(2.17-e)^2/(1+e)$	0.5	Yu & Richart, 1984
Clean angular sand	326	$(2.97-e)^2/(1+e)$	0.5	Yu & Richart, 1984
Clean sand	320	$(2.97-e)^2/(1+e)$	0.5	Hardin & Drnevich, 1972
Clean sand	625	$0.3+0.7e^2$	0.5	Hardin, 1978
Clean sand	900	$(2.17-e)^2/(1+e)$	0.38	Iwasaki & Tatsuoka, 1977

Note: A is a particle size and shape variable; $F(e)$ is a void ratio function.

The elastic shear modulus number k_G^e can also be approximated from normalized standard penetration values (Byrne et al., 1987), or from cone penetration test (Robertson et al., 1983). Approximate values of k_G^e in terms of relative density, D_r , or normalized standard penetration resistance, $(N_I)_{60}$, are listed in Table 4.2.

Table 4.2. Approximate values of the elastic shear modulus number k_G^e
(after Byrne et al., 1987).

State	D_r [%]	$(N_I)_{60}$	k_G^e
Very loose	0-15	0-3	300
Loose	15-35	3-8	300-900
Medium	35-65	8-25	900-2000
Dense	65-85	25-42	1500-2500
Very dense	85-100	>42	>2000

Note: The elastic exponent can be taken as 0.5.

Hardin (1978) concluded that the elastic Poisson's ratio, ν , for sand varies between 0 and 0.2, recommending a value of 0.12. A Poisson's ratio of 0.12 renders values of the elastic bulk modulus B^e that are almost equal to the elastic shear modulus G^e . In absence of specific data, the elastic bulk and shear moduli can be assumed equal. Values of the elastic bulk modulus, B^e , can also be found in Duncan et al. (1980), or derived from G^e by assuming ν .

The elastic shear modulus number k_G^e can be measured directly from laboratory tests using bender elements or a resonant column apparatus. The slope of unload-reload curves from drained triaxial tests carried out under constant confining stress can also be used to estimate k_G^e if ν is known or can be reasonably assumed. In the field, the elastic parameters G^e and k_G^e can be obtained from shear wave velocity, V_s . The shear modulus G^e is related to V_s by:

$$[4.47] \quad G^e = \rho V_s^2$$

where ρ is the mass density of the soil.

The elastic bulk modulus B^e can be directly obtained in the laboratory from the slope of unload-reload curves in isotropic compression tests or assuming a constant v .

4.7.2 Plastic shear parameters.

The plastic shear parameters can be divided in two groups: those related to stiffness and those related to strength. Plastic stiffness is associated with the shear modulus number and exponent, k_G^p and np , respectively, and the factor of anisotropic plastic response F . The plastic shear parameters connected to strength are the internal friction angle at failure ϕ_f , the failure ratio R_f and the constant volume friction angle ϕ_{cv} . Plastic stiffness parameters will be discussed first.

Duncan et al. (1980) and Byrne et al. (1987) examined shear response of granular soils. Although they did not separate the strains into elastic and plastic components as is done here, they considered a hyperbolic relation between the shear stress and total shear strain. By subtracting the elastic component from the total shear strain, the plastic component can be derived from their formulation since the combined shear modulus, G , is related to the elastic and plastic shear moduli, G^e and G^p , respectively, as follows:

$$[4.48] \quad \Delta\gamma = \Delta\gamma^e + \Delta\gamma^p = \Delta t \left(\frac{1}{G^e} + \frac{1}{G^p} \right) = \frac{\Delta t}{G}$$

where $\Delta\gamma$, $\Delta\gamma^e$ and $\Delta\gamma^p$ are the total, elastic and plastic shear strain increments, respectively. Thus, after some manipulation Equation 4.48 yields:

$$[4.49] \quad G^p = \left(\frac{GG^e}{G^e - G} \right)$$

At low strain, i.e., $\gamma < 10^{-4}$ (10^{-2} %), G is equal to the initial combined shear modulus G_i and G^p equal to the initial plastic shear modulus G_i^p . Therefore, k_G^p can be estimated from G_i^p , by using Equation 4.22, i.e., $G_i^p = k_G^p \cdot P_A (s' / P_A)^{np}$. Byrne et al. (1987) found that the initial combined shear modulus G was about $\frac{1}{2}$ to $\frac{1}{4}$ of the elastic modulus G^e . These values of G in combination with Equation 4.49 yield values of G_i ranging from about $\frac{1}{3}$ to 1.0 times G^e . Therefore, in the absence of specific data, k_G^p could be estimated within the range $\frac{1}{3} k_G^e$ to $1.0 k_G^e$.

The plastic exponent, np , can be taken equal to the elastic exponent, me , as suggested by Vermeer (1980). The factor of anisotropic plastic response F is obtained by comparison between triaxial compression and extension tests, e.g., $F = (k_G^p)_{ext} / (k_G^p)_{comp}$.

The plastic shear parameters related to the ultimate strength of sand are the internal friction angle at failure ϕ_f , the failure ratio R_F and the constant volume friction angle ϕ_{cv} . There is considerable experience on determining ϕ_f (Byrne et al., 1987). Its value is related to the stress ratio at failure $\eta_f = \sin \phi_f = (t / s')_f$, where t_f is the strength on the plane of maximum shear and s'_f the corresponding effective mean stress.

The failure ratio R_F relates the stress ratio at failure η_f and the ultimate stress ratio η_{ult} from the best fit hyperbola to laboratory data, and was defined as $R_F = \eta_f / \eta_{ult}$ in

Section 4.3.3. Thus, R_F can be seen as a measure of the strain at which the full strength η_f is reached. Since the shear stress-strain relation is hyperbolic, the stress ratio curve approaches the ultimate value η_{ult} asymptotically. Hence, if $R_F = 1$, η_f occurs at infinite shear strain, while if $R_F = 0$, then η_f is reached at $\gamma_r = (t / G_i^P)_f$, as shown in Figure 4.17.

For intermediate cases, R_F can be expressed as follows:

$$[4.50] \quad R_F = 1 - \frac{t_f}{\gamma_f G_i^P}$$

In general, based on data by Byrne et al. (1987) and Duncan et al. (1980), R_F could be taken as ranging from 0.5 to 0.98.

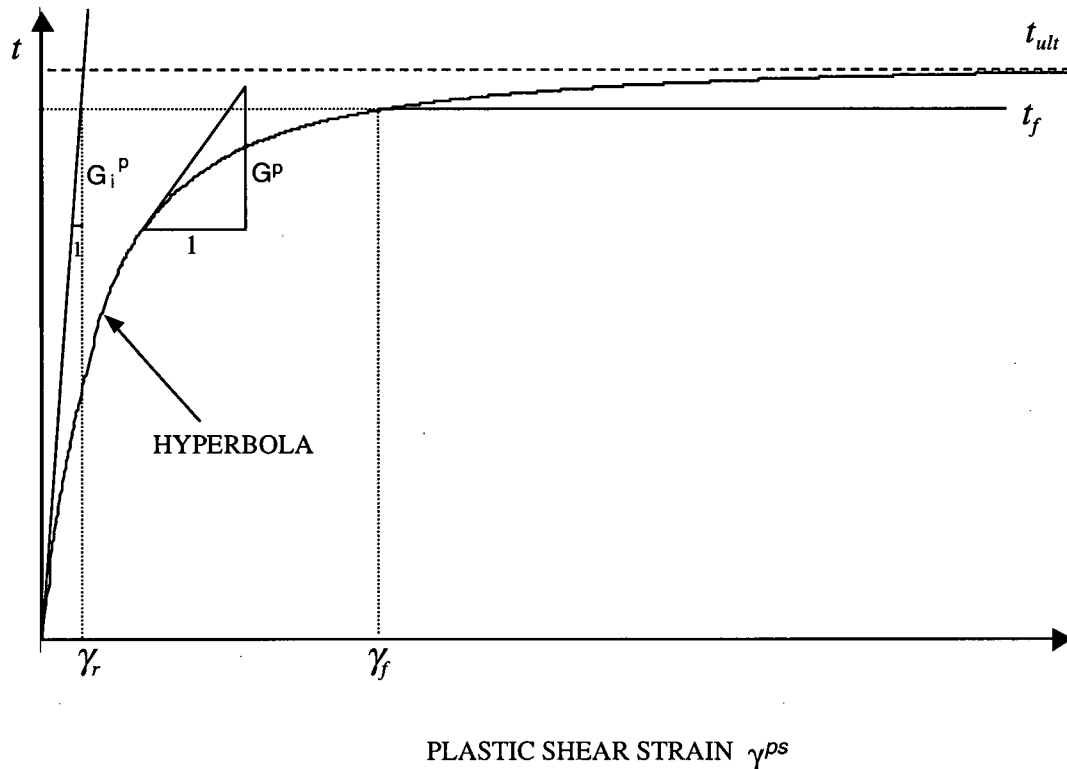


Figure 4.17 Effect of the failure ratio R_F on the shape of the hyperbolic stress-strain curve.

The constant volume friction angle ϕ_{cv} depends mainly on mineralogy, but Byrne et al. (1987) suggested that in the absence of data and for practical purposes, ϕ_{cv} could be generally considered equal to 33° (typical value for quartz sand). However, Roy (1997) summarized data from several authors indicating that ϕ_{cv} could vary between 27.5 to 35.0° . A summary relating approximate values of the shear parameters with D_r and $(N_I)_{60}$, for practical purposes, is presented in Table 4.3.

Table 4.3. Approximate values of shear parameters for practical purposes (after Byrne et al., 1987).

State	D_r	$(N_I)_{60}$	Elastic		Plastic	
			k_G^e	k_G^P*	ϕ_f	ϕ_{cv}
Very loose	0-15	0-3	300	50-300	33	33
Loose	15-35	3-8	300-900	100-900	35	33
Medium	35-65	8-25	900-2000	300-2000	38	33
Dense	65-85	25-42	1500-2000	1000-2500	43	33
Very dense	85-100	>42	>2000	>2000	50	33

Note: The relationship between $(N_I)_{60}$ and D_r is based on Skempton (1986). * Derived from Byrne et al. (1987) and Equation 4.49.

The plastic shear parameters can be directly obtained from drained shear tests in which shear and volumetric strains are measured, or from undrained tests in which pore pressures are measured in place of volumetric strains. Nevertheless, in the case of loose sands, the friction angle at failure ϕ_f obtained from undrained conditions would be slightly less than if obtained from drained tests. The procedure to obtain the plastic shear parameters from laboratory tests is essentially the same as that explained by Duncan and Chang (1970), and will be described in the following.

Equation 4.21 can be rearranged and expressed as:

$$[4.51] \quad \frac{\gamma}{\eta} = \frac{1}{G^*} + \frac{\gamma}{\eta_{ult}}$$

In the (γ / η) vs. γ plane, Equation 4.51 is a straight line with intercept to the origin $1/G^*$.

Therefore, the combined shear modulus G_i can be readily obtained from such a plot and with the aid of Equation 4.49, G_i^P is determined. At least two values of G_i^P , derived from two tests at different confining stress levels, are needed to determine k_G^P and np . By plotting G_i^P vs. (s' / P_A) in log-log scales, a straight line is obtained. The shear plastic exponent np is given by the slope of this line and $(k_G^P \cdot P_A)$ is given by the value of G_i^P at $(s' / P_A) = 1$. The stress ratio at failure η_f defines ϕ_f , as emphasized above, and R_f can be obtained with the aid of Equation 4.50. Determination of the factor of anisotropic plastic response is achieved by computing the ratio of k_G^P in extension to k_G^P in compression, i.e., $F = (k_G^P)_{ext} / (k_G^P)_{comp}$. Finally, the constant volume friction angle ϕ_{cv} can be estimated by evaluating the stress ratio η that corresponds to the point in which the slope of the curve ε_v^P vs. γ' , or pore pressure u vs. γ' , becomes zero. Strictly, the curves ε_v^P vs. γ' , or u vs. γ' , should be used to evaluate ϕ_{cv} . However, since at this strain level the elastic component of the strains is much smaller than the plastic, the error incurred by using total strains, i.e., ε_v and γ , may not be significant.

4.7.3 Plastic cap parameters

Two plastic volumetric parameters are needed by the cap mechanism, the plastic bulk modulus number and exponent, k_B^P and mp , respectively. These parameters should be

derived from back analysis of isotropic compression tests since in this type of test the volumetric response is isolated from shear effects. The value of the initial bulk modulus B_i^P can be obtained in a similar manner as G_i^P . The initial combined bulk modulus B_i is determined first from the slope of the curve ε_v vs. s' at its starting point. With B_i , B_i^e and Equation 4.49 written in terms of bulk moduli, B_i^P can be computed from:

$$[4.52] \quad B^P = \left(\frac{BB^e}{B^e - B} \right)$$

Based on experimental observations with respect to strain and stress paths in tests performed at constant stress ratio, Vermeer (1980) suggested using the same elastic and plastic exponents. He emphasized that proportional stressing induces proportional straining and vice versa, if the stress ratio, η , is not greater than the stress ratio at the k_0 condition, η_{k_0} , i.e., $\eta_{k_0} \geq \eta$. These experimental observations can only be captured by the model if all elastic and plastic exponents are equal. Hence, by assuming the plastic volumetric exponent mp equal to the elastic exponent me , as suggested by Vermeer (1980), k_B^P can be obtained from Equation 4.39, i.e., $B_i^P = k_B^P \cdot P_A (s' / P_A)^{mp}$.

The latter assumption would simplify the model by reducing the number of parameters from eleven to nine. Nevertheless, the restriction does not necessarily apply to the plastic shear mechanism used in this model since the cone mechanism does not contribute to the plastic response for paths of constant stress ratio. It is left to the user whether to use the same elastic and plastic exponents or not.

4.8 Summary

A double hardening constitutive model has been presented in this Chapter. The model addresses most of the characteristics of sand behaviour relevant to static liquefaction of sand, i.e., non-linearity and stress dependency of the stress-strain relationship; shear-volume coupling; path dependency; effects of direction of loading; and strains induced by continuous rotation of principal stresses. It is based on incremental elastic-plastic theory and has two independent yield mechanisms: (i) a shear or cone mechanism, and (ii) a volumetric or cap mechanism.

The elastic response is assumed to be incremental linear, isotropic and specified by Hooke's law. The elastic moduli are considered stress level dependent and hence, the total elastic response is non-linear.

The plastic shear mechanism assumes: (i) the ultimate strength and state of stress limited by the Mohr-Coulomb failure criterion; (ii) radial lines of constant stress ratio to be the shear yield loci; (iii) a non-associative flow rule derived from energy considerations; and (iv) a mixed hardening rule in which the relationship between the stress ratio, η , and plastic shear strain, γ^p , is assumed hyperbolic and dependent on the direction, α_σ , of the principal stress, σ_1 . In addition, the hardening rule approximates the effects of continuous rotation of principal stresses by softening/hardening the shear yield surface as a function of the rotation angle increment.

The volumetric mechanism assumes a sphere with center in the origin of the stress space as yield surface, which strain-hardens isotropically as the cap pressure, σ^c , increases beyond its maximum level. The volumetric flow rule is associative and the cap pressure is related to the plastic volumetric strain through a power law.

The total plastic response is assumed given by superposition of the two independent plastic mechanisms, and the final incremental response by adding the elastic and plastic contributions.

The major deviations of the model from observed sand behaviour are: (i) the shape of the failure surface (given by the Mohr-Coulomb pyramid), which is not curved and neglects the effect of the intermediate principal stress, σ'_2 , and mean stress, $\sigma'_m = (\sigma'_1 + \sigma'_2 + \sigma'_3)/3$; (ii) the inability to capture the observed anisotropic response under decreasing or constant stress ratio paths in which the confining stress, s' , increases beyond the preconsolidation pressure, s'_{max} ; and (iii) the size of the elastic region, which is too large to allow correct prediction of large unload-reload loops under cyclic loading.

The advantages of this model over other formulations are:

- The mixed shear hardening rule that allows prediction of elastic-plastic response upon stress reversal (cross-over), overcoming the restriction imposed by isotropic hardening rules affecting most of the simple elastic-plastic models;
- The ability to approximate the effect of principal stress direction in sand response to first time shear loading (effects induced by inherent anisotropy); and
- The capability to approximately account for the strains induced by pure and continuous rotation of principal stresses.

In the following chapter, the numerical analysis procedure used to solve the stress-deformation problem (i.e. equilibrium, compatibility and boundary conditions for the

proposed stress-strain relationship), as well as the numerical implementation of the constitutive model will be discussed.

CHAPTER 5

NUMERICAL ANALYSIS PROCEDURE

The solution of a stress-deformation problem requires that equilibrium and compatibility be satisfied for the boundary and initial conditions of the problem, using an appropriate stress-strain relationship. Finite elements or finite difference techniques are routinely used to reasonably satisfy these conditions.

In this study, analyses were carried out using the computer code FLAC -Fast Lagrangian Analysis of Continua-, version 3.3 (Cundall, 1995). The program uses the finite difference method and satisfies dynamic equilibrium using a step-by-step explicit time domain procedure. The geometric domain is discretized into a quadrilateral grid in which each zone comprises four triangles. The stiffness contribution of each zone is essentially the same as if it were represented by four constant strain triangular elements. This code allows the user to input a specific constitutive stress-strain model. Large displacements and strains are approximated by updating the nodal coordinates of the grid.

The dynamic approach used in FLAC has the advantages of achieving a numerically stable solution even when the problem is not statically stable, allowing examination of large strains and displacements prior to failure. The stress-strain model

described in Chapter 4 was implemented in FLAC and used in the analyses that will be presented in the chapters to follow.

5.1 Explicit finite difference approach (FLAC)

The numerical procedure applied in FLAC is such that for each element in the geometric domain, stresses and forces are used in the equations of motion to obtain new velocities and displacements. With these new values, the constitutive equation or stress-strain relation is then employed to predict new stresses, and in this manner, a basic explicit calculation cycle is completed. The procedure is depicted in Figure 5.1. While computing a new set of stresses, the input velocities are assumed unaffected by the new stresses. A very small time-step is used in order to comply with this assumption, so information can not physically pass from one element to another during that period. By keeping the computational front ahead of the physical front, stresses can be computed from strains in an element without requiring an iteration process even for nonlinear constitutive laws (Cundall, 1995). After several calculation cycles, changes in stresses and strains propagate across elements in a similar way as they would propagate physically.

The formulation can be used in two strain modes: “Eulerian,” termed *small-strain*, or “Lagrangian,” termed *large-strain*. In the small-strain mode, movements and deformations are relative to a fixed grid. In contrast, when using the large-strain mode, the nodal coordinates of the elements are updated at each time-step by simply adding the corresponding incremental displacements. Hence, the grid moves and deforms with the material it represents.

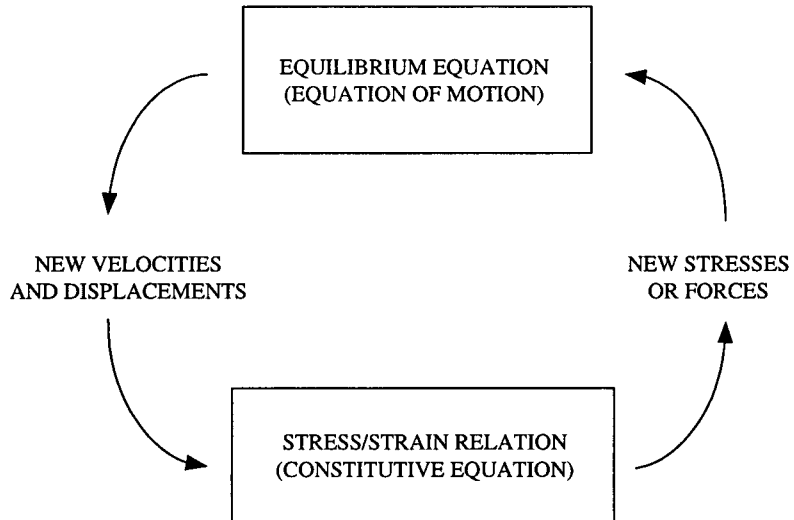


Figure 5.1 Basic explicit calculation cycle (after Cundall. 1995).

Since the geometric domain is divided into a quadrilateral grid in which each zone comprises four triangular elements (see Figure 5.2), the finite difference equations used in FLAC are derived for triangular elements from Gauss divergence theorem (Cundall, 1995). The finite difference equations are:

$$[5.1] \quad \langle \frac{\partial f}{\partial x_i} \rangle = \frac{1}{A} \sum_s \langle f \rangle n_i \Delta s$$

where f represents a scalar, vector or tensor; n_i , the unit normal vector to the surface S ; x_i are position vectors; A is the area; Δs , the length of a side of the triangle; and the summation is done over the three sides of the triangular element. The value of $\langle f \rangle$ is considered the average over a side.

For the case of a continuous solid body, Newton's law of motion can be written as follows (Cundall, 1995):

$$[5.2] \quad \rho \frac{\partial \overset{\circ}{u}_i}{\partial t} = \frac{\partial \sigma_{ij}}{\partial x_j} + \rho g_i$$

where ρ is the mass density; t , the time; $\overset{\circ}{u}_i$, velocity components; x_j , components of the coordinate vector; g_i , components of the gravitational acceleration; and σ_{ij} , the components of the stress tensor. A dot on top of a variable indicates its derivative respect to time and the indices i, j and k , denote components in a Cartesian coordinate frame.

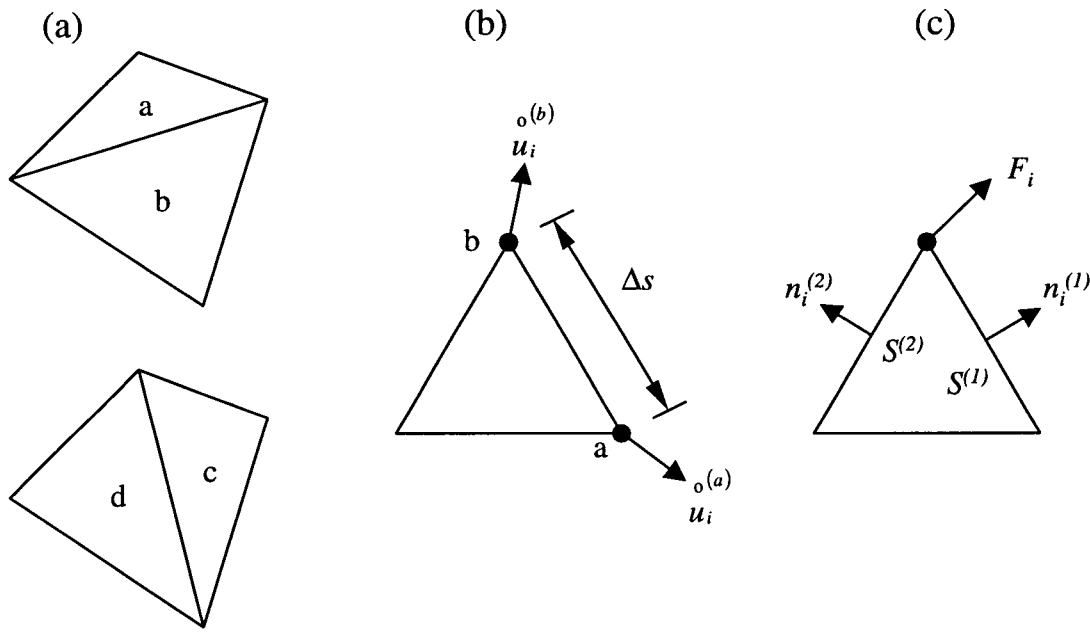


Figure 5.2 Basic grid element (after Cundall, 1995). (a) Overlaid quadrilateral elements used in FLAC. (b) Typical triangular element with velocity vectors. (c) Nodal force vector.

The nodal velocities $\overset{\circ}{u}_i$ for an element are derived from Equation 5.2. Thus, by making $\langle f \rangle$ in Equation 5.1, equal to the average velocity vector in two consecutive nodes, the nodal velocities for an element are (Cundall, 1995):

$$[5.3] \quad \frac{\partial \overset{\circ}{u}_i}{\partial x_j} \equiv \frac{1}{2A} \sum_s \left(\overset{\circ}{u}_i^{(a)} + \overset{\circ}{u}_i^{(b)} \right) n_j \Delta s$$

where the superscripts ^(a) and ^(b) indicate two consecutive nodes on the triangle boundary (Figure 5.2b).

The strain rates $\overset{\circ}{\epsilon}_{ij}$ are then computed as (Cundall, 1995):

$$[5.4] \quad \overset{\circ}{\epsilon}_{ij} = \frac{1}{2} \left[\frac{\partial \overset{\circ}{u}_i}{\partial x_j} + \frac{\partial \overset{\circ}{u}_j}{\partial x_i} \right]$$

In the large-strain mode, the stress components σ_{ij} of the stress tensor are modified due to the finite rotation of an element during one time-step in the following manner (Cundall, 1995):

$$[5.5] \quad \sigma_{ij} := \sigma_{ij} + (\omega_{ik} \sigma_{kj} - \sigma_{ik} \omega_{kj}) \Delta t$$

where $:=$ means “replaced by”; Δt is the time-step and ω_{ij} given by:

$$[5.6] \quad \omega_{ij} = \frac{1}{2} \left[\frac{\partial u_i^0}{\partial x_j} - \frac{\partial u_j^0}{\partial x_i} \right]$$

Therefore, either the stress tensor components σ_{ij} remain unchanged in small-strain mode, or they are adjusted in large-strain mode due to the finite rotation of the element during one time-step. The components σ_{ij} comprise the previous or old values of the stress tensor components, termed σ_{ij}^{old} .

The components of a stress increment $\Delta\sigma_{ij}$ are obtained from the corresponding strain rates $\overset{\circ}{\varepsilon}_{ij}$ by invoking the constitutive law. A new set of values σ_{ij}^{new} of the stress tensor components, is computed as follows:

$$[5.7] \quad \sigma_{ij}^{new} = \sigma_{ij}^{old} + \Delta\sigma_{ij} = \sigma_{ij}^{old} + D_{ij} \overset{\circ}{\varepsilon}_{ij} \Delta t$$

where D_{ij} are the coefficients of the constitutive stiffness matrix.

The new components σ_{ij}^{new} of the stress tensor are converted to equivalent nodal forces acting at the ends of the corresponding triangle side. Since each triangle vertex has two adjacent sides, the equivalent nodal forces F_i (Figure 5.2c) are (Cundall, 1995):

$$[5.8] \quad F_i = \frac{1}{2} \sigma_{ij} \left(n_j^{(1)} S^{(1)} + n_j^{(2)} S^{(2)} \right)$$

where the superscripts ⁽¹⁾ and ⁽²⁾ are used to distinguish the two adjacent sides of the triangular element.

Equation 5.8 does not account for body forces due to gravity $F^{(g)}$ or forces due to boundary conditions $F^{(BC)}$. Thus, all these forces are summed at each node to give the net nodal force ΣF_i (Cundall, 1995):

$$[5.9] \quad \sum F_i = F_i + F_i^{(g)} + F_i^{(BC)}$$

If the body is either at static equilibrium or in a state of plastic flow, ΣF_i on node “i” is zero. However, under different conditions, node “i” will be accelerated in accordance with Newton’s second law of motion, which in its finite difference form reads (Cundall, 1995):

$$[5.10] \quad \overset{\circ}{u}_i^{\left(t+\frac{\Delta t}{2}\right)} = \overset{\circ}{u}_i^{\left(t-\frac{\Delta t}{2}\right)} + \sum F_i^{(t)} \frac{\Delta t}{m}$$

where the superscripts indicate the time at which the corresponding variable is evaluated, and m is the mass.

The calculation cycle depicted in Figure 5.1 is completed in this manner and only if the problem under analysis is formulated in the large-strain mode, new nodal coordinates are determined (Cundall, 1995):

$$[5.11] \quad x_i^{(t+\Delta t)} = x_i^{(t)} + \overset{\circ}{u}_i^{\left(t+\frac{\Delta t}{2}\right)} \Delta t$$

In order to solve static problems, static or quasi-static solutions are attained in FLAC by introducing damping forces in the equations of motion. This task is achieved by adding nodal damping forces that are proportional to the magnitude of the unbalanced force $\Sigma F_i^{(t)}$, and hence, Equation 5.10 is modified as follows (Cundall, 1995):

$$[5.12] \quad u_i^{\left(t+\frac{\Delta t}{2}\right)} = u_i^{\left(t-\frac{\Delta t}{2}\right)} + \left\{ \sum F_i^{(t)} - \alpha \left| \sum F_i^{(t)} \right| \operatorname{sgn} \left(u_i^{\left(t-\frac{\Delta t}{2}\right)} \right) \right\} \frac{\Delta t}{m_n}$$

where α is a constant; “sgn” stands for sign of the nodal velocity $u_i^{\left(t-\Delta t/2\right)}$, and is used to guarantee that the direction of the nodal damping force ensures energy dissipation; and m_n is a fictitious nodal mass such that the time-step Δt is equal to unity to simplify and speed up the computational process.

FLAC is capable of simulating groundwater flow and the consolidation process in a soil when the program is configured to carry out this kind of analysis. Two mechanical effects related to the pore fluid pressure are considered: changes in pore pressures induced by volume changes, and changes in effective stresses caused by pore pressure changes. The first effect is captured through the fluid reaction to volume variations of the grid elements. Cundall (1995) refers to it as the effect of mechanical volume changes. The second effect reflects the fact that the effective stresses change when the pore pressures are modified either by mechanical effects or by the groundwater flow process.

The groundwater formulation of the program follows the same general scheme of finite differences and discretization of the grid discussed before. FLAC assumes that

pressure and saturation values are located at grid nodes. Furthermore, the groundwater equations are expressed in terms of pressures rather than hydraulic head, and hence, Darcy's law for anisotropic porous medium is written as (Cundall, 1995):

$$[5.13] \quad V_i = K_{ij} \frac{\partial P}{\partial x_j}$$

where V_i is the specific discharge vector; P the pressure; and K_{ij} is the "permeability" tensor defined as (Cundall, 1995):

$$[5.14] \quad K_{ij} = \frac{k_{ij}}{g\rho_w}$$

in which k_{ij} is the hydraulic conductivity used as a constant of proportionality in the usual form of Darcy's law: ($v = k dh/dx$); g is the gravitational acceleration; and ρ_w , the mass density of the fluid.

By making $\langle f \rangle$ in Equation 5.1 equal to P , $(\partial P / \partial x_j)$ can be evaluated and substituted into Equation 5.13, allowing evaluation of the specific discharge vector V_i (Cundall, 1995):

$$[5.15] \quad V_i \equiv \frac{K_{ij}}{A} \sum P n_j \Delta s$$

where Σ is the summation over the three sides of the triangle.

V_i is then converted to scalar volumetric flow rates, Q , at the nodes by performing the dot products with the unit vectors normal to the three sides of the triangular element, giving the following expression (Cundall, 1995):

$$[5.16] \quad Q = V_i n_i \Delta s$$

In matrix form, Equation 5.16 can be written for the whole quadrilateral element in terms of the four nodal pressures P and the four nodal flow rates Q as (Cundall, 1995):

$$[5.17] \quad \{Q\} = [M] \{P\}$$

where $[M]$ is the “permeability stiffness” matrix.

At a saturated node, the pore pressures due to the flow imbalance ΣQ are given by (Cundall, 1995):

$$[5.18] \quad \frac{\partial P}{\partial t} = -\frac{B_f}{nV} \sum Q$$

in which B_f is the fluid bulk modulus; n , the material porosity; and V , the total volume. In finite difference form, Equation 5.18 transforms into (Cundall, 1995):

$$[5.19] \quad P^{new} = P^{old} - \frac{B_f (\sum Q \Delta t + \Delta V_{mech})}{nV}$$

where P^{new} and P^{old} are the updated and old values of pore pressure, respectively; Δt is the time-step; and ΔV_{mech} is the equivalent nodal volume increase induced by mechanical deformations of the grid.

In Equation 5.19, the first term in the brackets accounts for pore pressure changes induced by groundwater flow, while the second term accounts for changes in the pore fluid pressure induced by volumetric deformations of the grid elements (“soil”). For details on these procedures, the reader is referred to Cundall (1995).

FLAC allows the user to decide whether gravitational forces, flow effects, or both, should be taken into consideration. An on/off switch instruction is used for this purpose. Turning *gravity on* implies that body forces will be accounted for in the analysis. The gravitational acceleration g is treated as a vector in FLAC’s formulation, so different vertical and horizontal components of g can be applied to a grid. In addition, the magnitude of g can be set equal to a value different from the actual Earth gravitational acceleration of 9.81 m/sec². Therefore, variations on the magnitude of g , like those in centrifuge tests, can be simulated.

Turning *flow on* implies that the fluid within a grid is allowed to move among the elements. Depending on the boundary conditions with regard to the flow, the grid will be either an opened or a closed system. In an opened system, fluid will enter or leave the grid, while in a closed system, there will not be communication with the outside. In both cases, flow will occur within the geometric domain of the problem. Turning *flow off* implies that the fluid will not enter or leave any of the elements comprising the grid, and thus, the fluid will not move at all.

5.2 Numerical implementation of the proposed constitutive model

The proposed constitutive model discussed in Chapter 4 was implemented in FLAC following the same numerical procedure used for FLAC's built-in Mohr-Coulomb model (Cundall, 1995). Although the formulation is based on plane strain conditions, the out-of-plane stress is taken into consideration by expressing the stress-strain relation in three-dimensional terms. A state of material yielding and/or a state of failure is decided in the model by a Mohr-Coulomb type of criterion, which in turn depends on the major and minor principal stresses, σ'_1 and σ'_3 , respectively. Since the out-of-plane stress, σ'_{zz} , is not forced to be the intermediate principal stress, σ'_2 , the plane defined by σ'_1 and σ'_3 , could change. Hence, if σ'_{zz} becomes the minor or major principal stress, failure and/or yielding is declared in the $\sigma'_1: \sigma'_{zz}$, or $\sigma'_{zz}: \sigma'_3$ plane, accordingly. By switching the plane in which yielding takes place in agreement with σ'_1 and σ'_3 , the numerical procedure is conformed to modelling axi-symmetric conditions. This numerical approach allows extending the plane strain formulation to 3-D axi-symmetric conditions in a straightforward manner and with minimal computational effort, if the strain increments are small (Cundall, 1995).

Many problems of interest to geotechnical engineering can be modelled assuming plane strain conditions. However, the axi-symmetric case is important since it resembles typical conditions of some laboratory tests, e.g., triaxial and uniaxial consolidation tests. In addition, for the great majority of cases in practical engineering, plane strain data are not available, and thus, constitutive models have to be calibrated with data obtained from conventional triaxial tests. In such tests, two of the principal stresses are equal and, during yielding, the stress point moves along a "corner" of the Mohr-Coulomb pyramid

(Figure 4.4). Hence, it was considered important to numerically implement the proposed constitutive model for both, plane strain and axi-symmetric conditions.

The numerical implementation of the proposed constitutive model is discussed in this section. Derivations of the expressions implemented into the computer code are presented in Appendix B. As mentioned earlier, the incremental stress-strain relation is formulated in three-dimensional terms and is expressed using the $x : y : z$ axes as reference. The out-of-plane stress, σ'_z , is considered one of the principal stresses. Both, elastic and plastic strain increments in the out-of-plane direction are assumed to be zero.

Since the components of the total strain increment, $\Delta\epsilon_i$, are considered equal to the sum of the elastic and plastic strain increment components ($\Delta\epsilon_i = \Delta\epsilon_i^e + \Delta\epsilon_i^p$), the stress increment components, $\Delta\sigma'_i$, are given by:

$$[3.8bis] \quad \{\Delta\sigma'_i\} = [D^e]\{\Delta\epsilon_i - \Delta\epsilon_i^p\}$$

where

$$[3.5bis] \quad \Delta\epsilon_i^p = \lambda \frac{\partial g}{\partial \sigma_i}$$

as described in Section 3.3.

However, the plastic strain increments $\Delta\epsilon_i^p$ are not known a priori and must be determined from plasticity theory. The occurrence of plastic strain increments depends

on whether the yield criteria are violated or not, and this is determined with the following procedure.

The total strain increments $\Delta\varepsilon_i$ obtained from Equation 5.4 are used in Hooke's law to derive the corresponding stress increments $\Delta\sigma'_i^I$ for which a purely elastic response is assumed, i.e.

$$[5.20] \quad \{\Delta\sigma'_i^I\} = [D^\varepsilon]\{\Delta\varepsilon_i\}$$

As can be seen from comparing Equations 3.8bis and 5.20, the stress increments $\Delta\sigma'_i^I$ may or may not be equal to $\Delta\sigma'_i$ depending on whether the plastic strain increments $\Delta\varepsilon_i^P$ are equal to zero (purely elastic response), or not (elastic-plastic response).

The stress increments $\Delta\sigma'_i^I$ are added to the old values of the stresses σ'_i^{old} . The new values obtained in this manner are transformed into principal stresses σ'_i^I . These principal stresses are called elastic guesses since they were derived from Hooke's law assuming a purely elastic response, and they are distinguished with the superscript “I”.

The sign convention followed in FLAC considers compressive stresses as negative, and so, the elastic guesses, σ'_i^I , are ordered in the following manner:

$$[5.21] \quad \sigma'_1^I \leq \sigma'_2^I \leq \sigma'_3^I$$

where major, intermediate and minor principal stresses are indicated by the subscripts 1, 2 and 3, respectively.

These elastic guesses are then used to evaluate the current yield functions f_j . Two different scenarios are possible:

- 1) $f_j(\sigma'_i^I) \geq 0$ (Recall that FLAC considers compressive stresses as negative). This case corresponds to a state of stress that lies within or on the boundaries of the elastic region defined by the current positions of the yield loci, and therefore, the response is purely elastic. In this case, the plastic strain increments, $\Delta\epsilon_i^P$, are equal to zero. Thus, $\Delta\sigma'_i = \Delta\sigma'_i^I$, and the new stresses, σ'_i^{new} , are equal to σ'_i^I .
- 2) $f_j(\sigma'_i^I) < 0$. This case corresponds to a state of stress that violates the yield criteria and hence, plastic strains occur. The stress increments, $\Delta\sigma'_i^I$, guessed by means of Hooke's law must be corrected in accordance with plasticity theory since only the elastic components, $\Delta\epsilon_i^E$, of the total strain increments, $\Delta\epsilon_i$, can contribute to the stress increments, $\Delta\sigma'_i$. Depending on whether one or more yield criteria have been violated, seven different yielding cases can occur (see Appendix B). In any of these cases, the stresses must be corrected using the corresponding flow rules as follows:

$$[5.22] \quad \{(\sigma')_i^{new}\} = \{\sigma'_i^I\} - [D^E] \left\{ \lambda \frac{\partial g}{\partial \sigma'_i} \right\}$$

However, in order to evaluate σ'_i^{new} , λ must be known. By definition of the consistency condition, the scalar λ is such that σ'_i^{new} lies on the current yield locus. Hence, σ'_i^{new} must satisfy the yield functions f_j , i.e. $f_j(\sigma'_i^{new}) = 0$. Since all terms except λ in the right hand side of Equation 5.22 are known, solving $f_j(\sigma'_i^{new}) = 0$ in

such terms yields the scalar λ . Therefore, λ is obtained by solving the system of simultaneous equations defined by:

$$[5.23] \quad f_j((\sigma')_i^{new}) = f_j \left(\{\sigma'^I_i\} - [D^e] \left\{ \lambda_j \frac{\partial g_j}{\partial \sigma_i} \right\} \right) = 0$$

Substitution of λ in Equations 5.22 and 3.5bis allows computation of σ'^{new}_i , and the plastic strain increments $\Delta \varepsilon_i^P$. This procedure ensures that the new state of stress, represented by σ'^{new}_i , lies on the current yield locus or loci, if more than one yield criteria were simultaneously violated. The plastic strain increments, $\Delta \varepsilon_i^P$, derived in the process are used to evaluate the hardening parameters and with these, the elastic region evolves according to the hardening rules as explained in Sections 4.3.3 (shear hardening rule), and 4.4.3 (volumetric hardening rule).

Once the new stresses σ'^{new}_i and location of the yield loci have been determined, the elastic region is updated to account for rotation of principal stresses as explained in Section 4.3.5.

Finally, the process ends examining the occurrence of stress reversal conditions. If stress reversal occurred, the yield loci are reset as explained in Section 4.3.3. A new elastic region is defined in this manner and its evolution will depend on subsequent loading.

The procedure is illustrated in Figure 5.3 in flow chart form. Here, it can be noted that in addition to the shear and volumetric yield criteria, a tension failure criterion (f^t) is

also considered. This latter criterion is defined by a constant value of tension σ^t that sand could withstand (usually zero), and mathematically, it is expressed as:

$$[5.24] \quad f^t = \sigma^t$$

The tension yield surface does not harden or soften and its numerical implementation is identical to that one used in FLAC's built-in Mohr-Coulomb model (Cundall, 1995). For details on the tension yield criterion, the reader is referred to Cundall (1995), or to Appendix B of this thesis.

5.3 Modelling the single element behaviour

One of the first steps for modelling the behaviour of a specific structure is to discretize the geometric domain into a grid of elements. The overall response of the system will depend on the boundary conditions, loading characteristics and mechanical properties of each element comprising the grid. It is therefore essential to capture the element behaviour first, since the whole system will be modelled as a collection of such elements. The element response is usually captured through laboratory testing. To this end, triaxial and simple shear tests, drained and undrained, are commonly used as element tests to characterize the material's behaviour under loading conditions representative of those in the field.

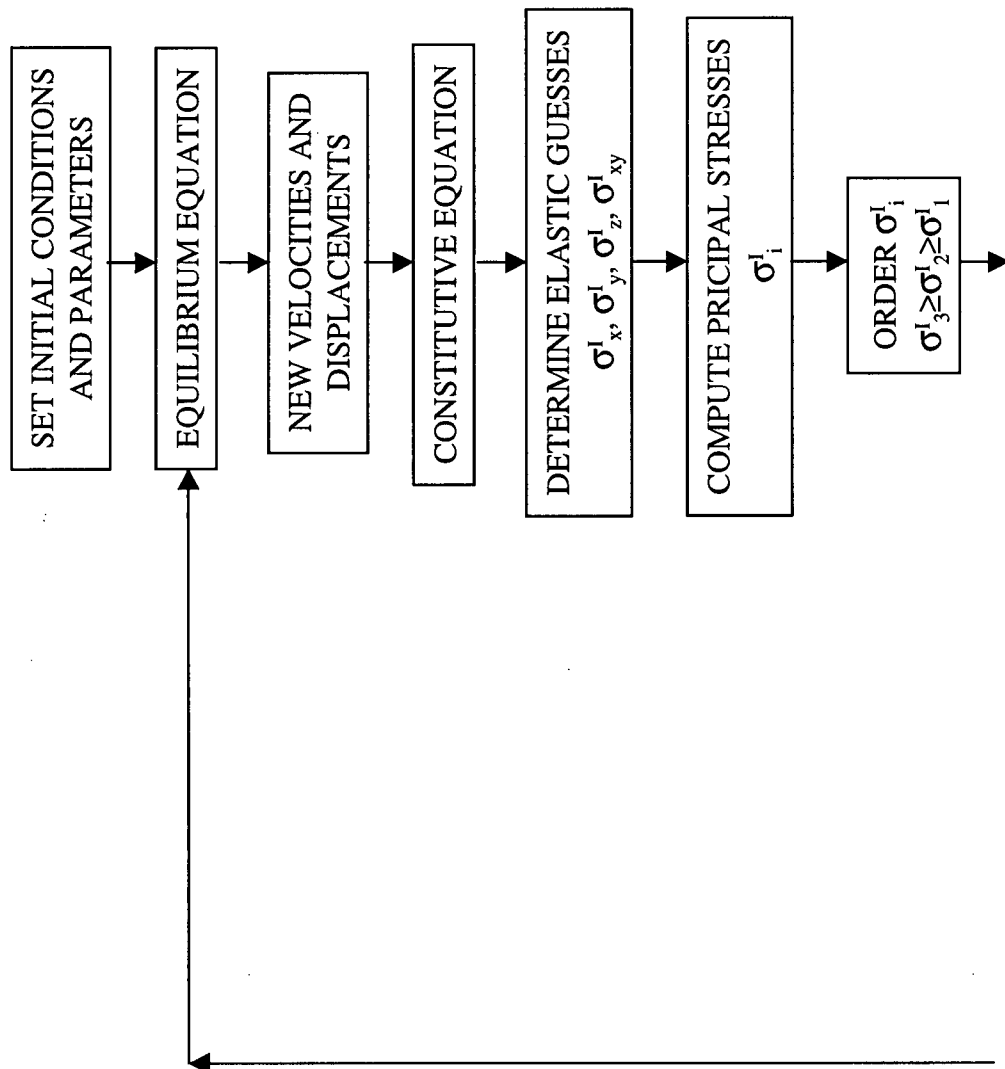


Figure 5.3 Flow chart of the constitutive model numerical implementation.

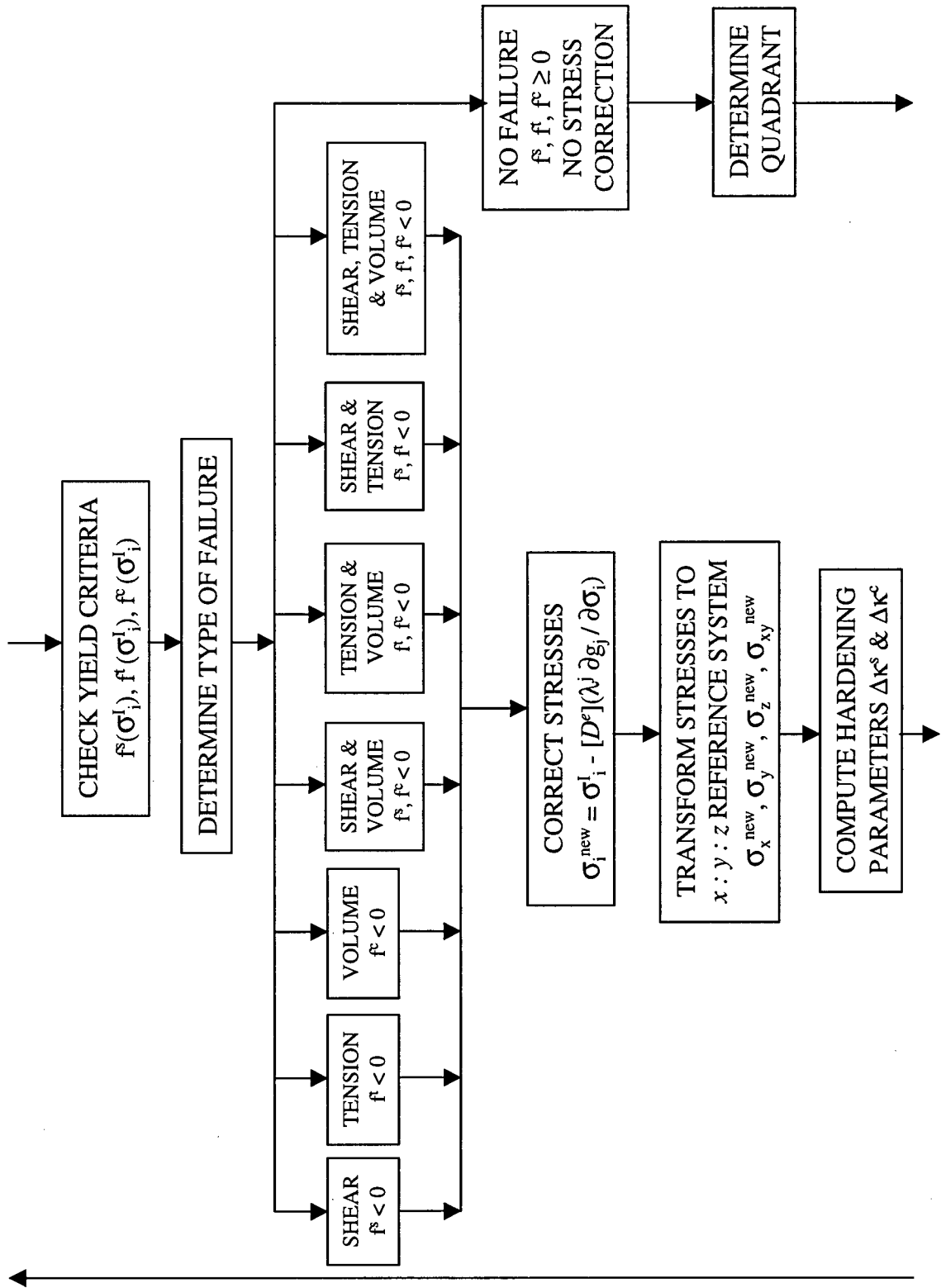


Figure 5.3 Continued

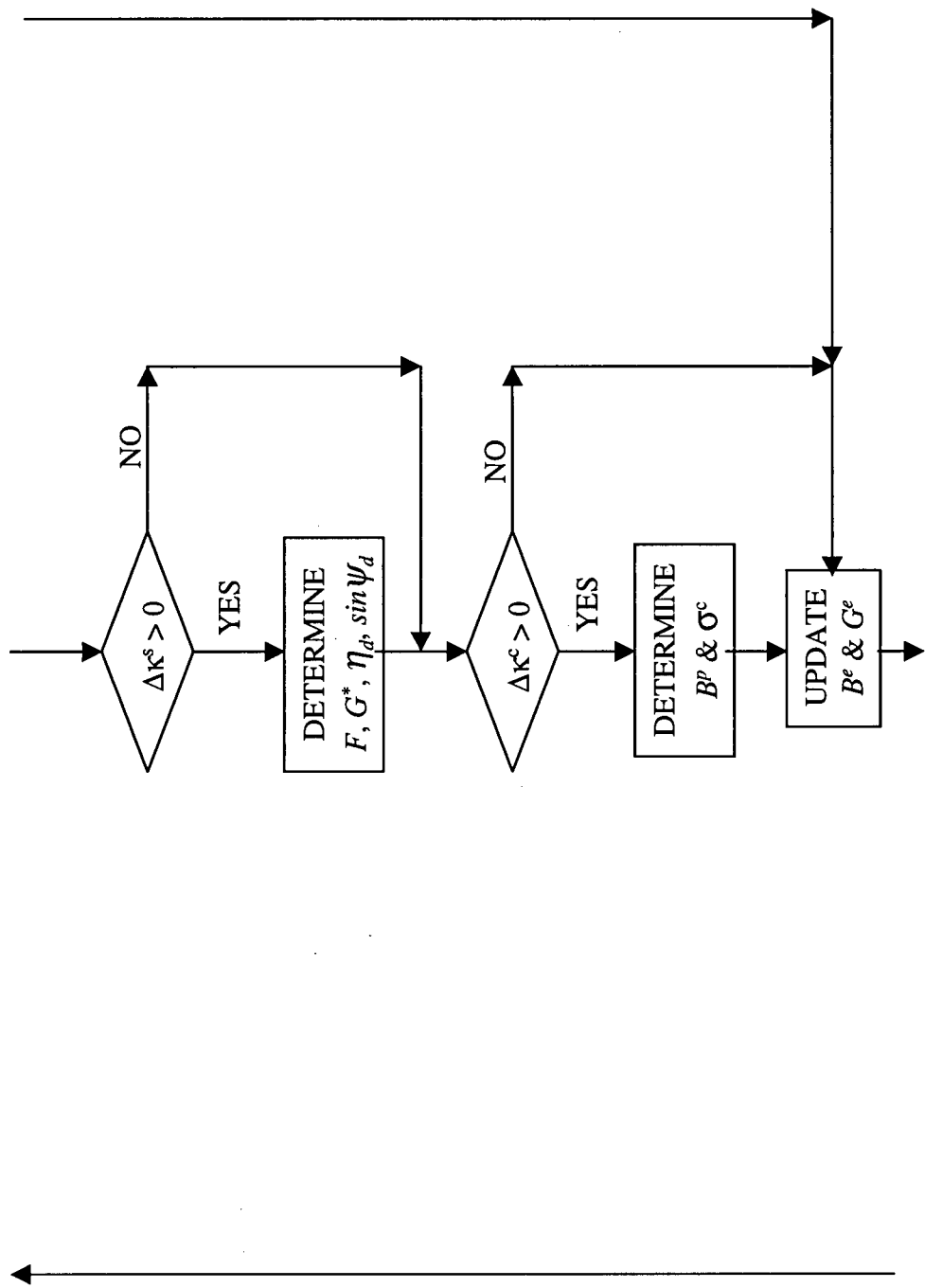


Figure 5.3 Continued

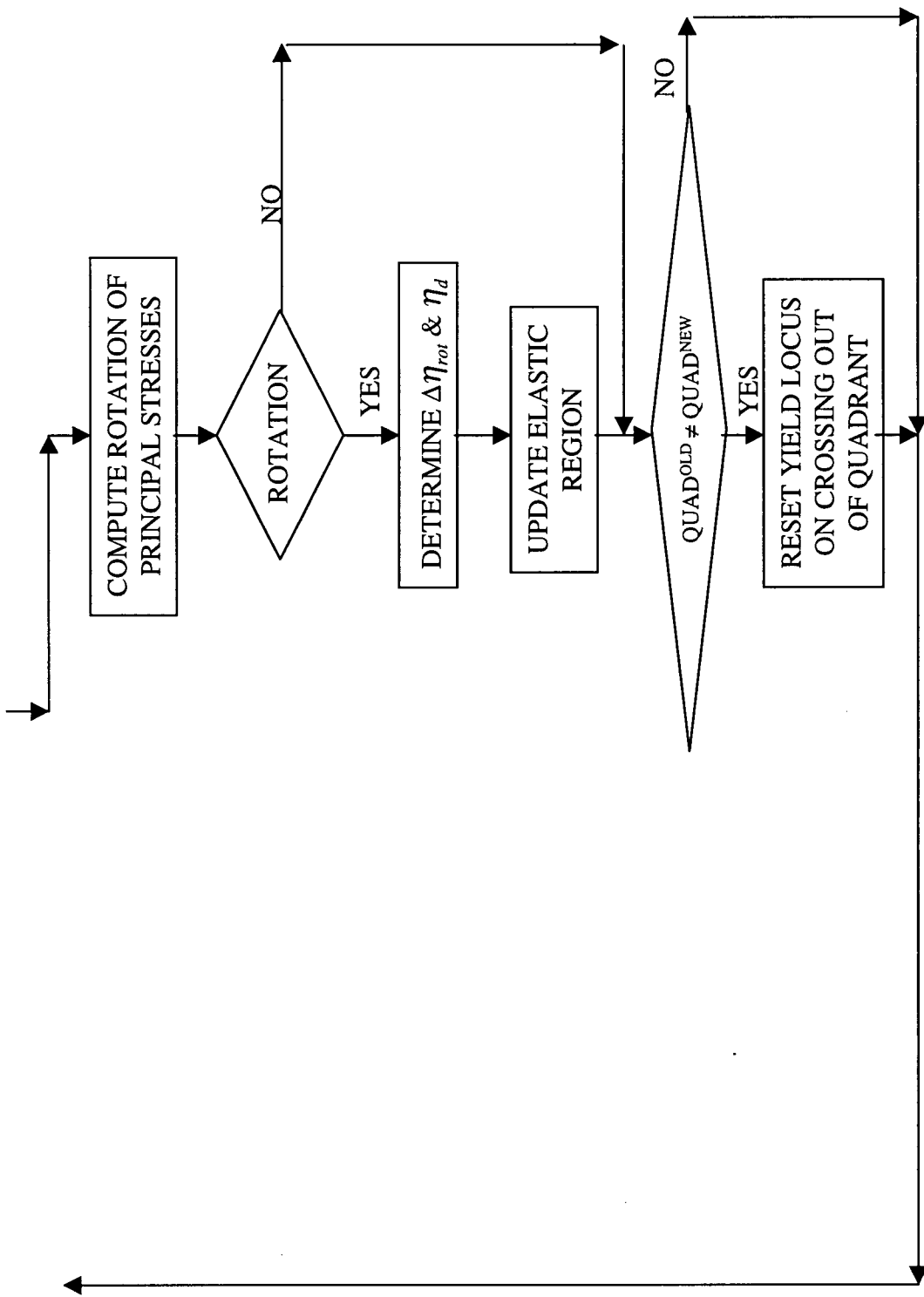


Figure 5.3 Continued

Element tests are numerically simulated by a single element grid and the different types of tests are modelled by specifying appropriate boundary and loading conditions. The element response in compression or extension tests, for example, is simulated with the boundary conditions depicted in Figure 5.4a. For plane strain conditions, no deformations are allowed in the out-of-plane direction, i.e., $\varepsilon_z = 0$, while the stress acting perpendicular to the plane of strain, i.e., σ'_z , is considered one of the principal stresses. For triaxial conditions, the axially symmetric configuration is used and hence, stresses and strains in the “z-axis” direction, i.e., σ'_z and ε_z , respectively, are considered equal to those in the “x-axis” direction, i.e., σ'_x and ε_x , respectively.

The element is first brought to equilibrium under the consolidation state of stress, although the consolidation process itself could also be simulated. Conventional constant strain rate types of tests are modelled by applying constant and equal nodal velocities at the top nodes of the grid. For compression, these velocities are applied in the negative direction of the “y-axis”, while for extension, they are applied in the opposite direction. It is clear that stress paths different from those of conventional tests could be simulated. For example, stress paths involving vertical compression or vertical extension could be modelled by applying nodal velocities at the right hand side nodes of the grid in the horizontal direction, as opposed to vertical velocities at the top nodes. Constant volume conditions could be represented by forcing the top and right hand side boundaries of the grid to move in such a way that no volume change would occur in the element.

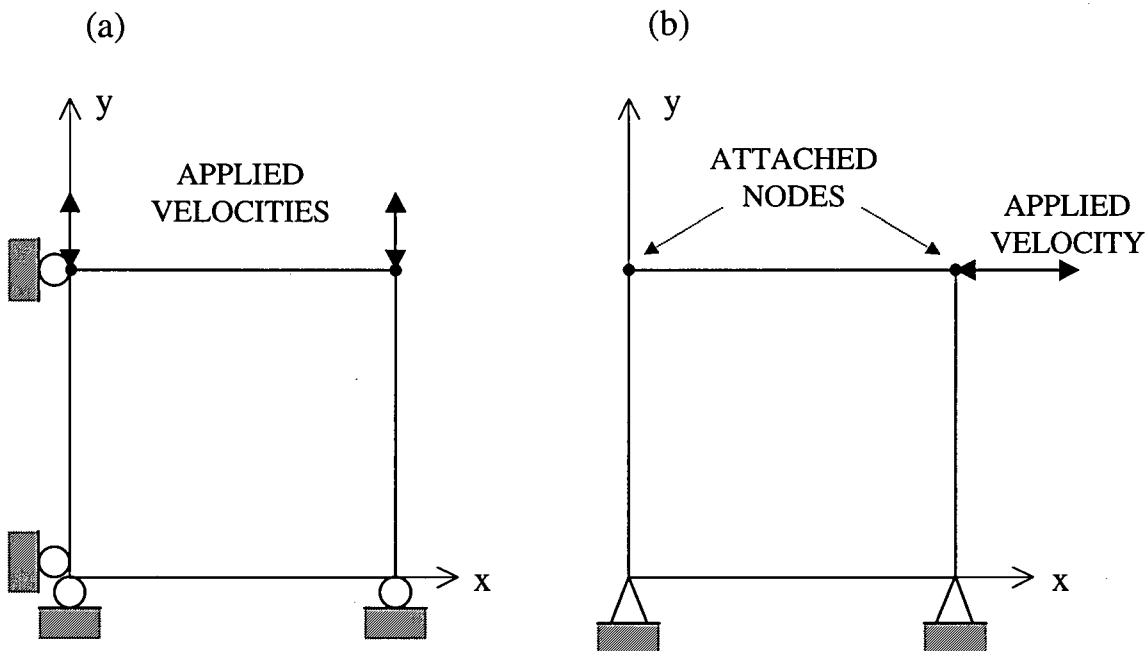


Figure 5.4 Boundary and loading conditions of a single element grid for modelling laboratory element tests. (a) Compression or extension. (b) Simple shear.

In contrast, conventional constant stress rate types of tests are modelled by applying constant stress increments at either the top horizontal or the right vertical boundaries of the grid.

Simple shear tests require different boundary conditions, as shown in Figure 5.4b. For this case, the top nodes are attached to each other in order to force them to move uniformly in the horizontal direction. Nodal velocities parallel to the “x-axis” are then applied at the top nodes. Constant volume conditions could be enforced by fixing the top nodes in the vertical direction, so no displacements in the “y-axis” direction would be allowed; forcing the volume of the element to remain constant.

From Equations 5.9 and 5.19, it is easy to note that by choosing different boundary conditions and fluid parameters, various types of analyses can be performed:

Fully Drained, Undrained, True Constant Volume, Partially Saturated and Coupled Stress-Flow.

5.4 Fully drained analysis

A fully drained response is simulated by considering the fluid stiffness to be zero, in which case the response is governed solely by the stiffness of the soil skeleton. If the bulk modulus of the fluid B_f is assumed equal to zero in Equation 5.19, the value of the pore pressure P^{new} remains constant. This is equivalent to the case in which the fluid within the soil pores can drain freely and no excess pore pressure is generated during the loading process. Therefore, a fully drained condition can be simulated in FLAC by simply assuming $B_f = 0$. The initial values of pore pressure, P^{old} , remain unchanged during the analysis whether P^{old} reflects the hydrostatic conditions, there is no water present within the soil pores ($P^{old} = 0$), or P^{old} is due to a specific groundwater pressure distribution.

5.5 Undrained analysis

When undrained conditions prevail, the fluid contained in the soil pores imposes a volumetric constraint through its stiffness B_f . An undrained response is thus simulated by considering a realistic value of the fluid stiffness and adding its contribution to the stiffness of the soil skeleton.

As pointed out before, FLAC requires the user to discretize the geometric domain of a given problem into a quadrilateral grid. If the boundaries of such a grid were

assumed impermeable, there would not be exchange of fluid between the grid and the outside. Impermeable boundaries in conjunction with a realistic value of the fluid bulk modulus B_f are used to perform *undrained* type of analyses. From Equation 5.19 two different undrained conditions can be modelled. A *truly undrained* condition could be simulated by turning the flow off, and hence, no fluid exchange among the elements would be allowed. The term $\Sigma Q\Delta t$ in Equation 5.19 would be equal to zero for this case, but changes in pore pressure would arise from the fluid reaction to volumetric changes of the grid elements, i.e., ΔV_{mech} .

When the flow is not *turned off* but the boundaries are kept impermeable, fluid exchange among the elements occurs and allows pore pressure redistribution within the grid to take place. Both terms inside the brackets of Equation 5.19 contribute to change the pore pressure P^{new} in this case. This condition is termed *undrained with pore pressure redistribution* and is considered a more realistic undrained condition since soil permeability is never really zero.

5.6 True constant volume

True constant volume can be simulated by specifying boundary conditions that force the element or elements in a grid to strain without any changes in volume. This condition can be achieved by prescribing velocities at the grid nodes in such a way that no volumetric strains take place. As discussed in Section 5.1, nodal velocities are converted into strain rates and these in turn, to stresses and nodal forces. The predicted stresses at the boundaries are equivalent to the pore pressures that would develop in an undrained

condition. Hence, true constant volume conditions, like those imposed in laboratory testing, can be easily simulated.

5.7 Partially saturated analysis

Partially saturated analysis refers to both undrained and drained conditions in soils that are not fully saturated, i.e., their degree of saturation is less than 100%. Undrained conditions on partially saturated soils can be simulated by reducing the fluid bulk modulus B_f . As discussed in Section 4.6, (B_f/n) represents the stiffness of an equivalent fluid that occupies the total volume of the element rather than just the volume of the pores. Thus, Equation 5.19 will render appropriate values of pore pressure P^{new} , by using values of B_f that are representative of the degree of saturation in the soil. The bulk fluid modulus B_f can be related to the Skempton pore pressure parameter B_{skem} , and hence, it is a simple matter to derive a value of B_f in agreement with the degree of saturation. This will be discussed in Chapter 6. Drained conditions in partially saturated soils will be addressed in the following section.

5.8 Coupled stress-flow analysis

The coupled stress-flow response is simulated by taking into account the gradual dissipation of pore pressure that occurs with time and its associated displacements. Two mechanical effects are considered in this case: changes in pore pressure induced by volume changes, and changes in effective stress caused by pore pressure changes. Both terms inside the brackets of Equation 5.19 contribute to update the values of pore

pressure P^{new} in this case. The effects induced by the consolidation process and loading conditions are accounted for at every step of calculation, capturing the so-called *coupled stress-flow* response.

Unsaturated flow is simulated in FLAC by means of an empirical function that depends on the degree of saturation, modifying the flow rates given by Equation 5.17. The reader is referred to Cundall (1995) for details on the procedure. However, when modelling a coupled stress-flow problem where a small portion of air is trapped within the fluid, the problem can be simulated by assuming full saturation of the elements but a reduced value of B_f , as discussed in the previous section.

5.9 Summary

The numerical analysis procedure and implementation of the proposed constitutive model were discussed in the previous sections. The procedure allows performing fully drained, partially drained, undrained, and constant volume type of analysis under plane strain and axi-symmetric conditions. In addition, material partial saturation can also be accounted for in analysis. In the following chapter, the proposed constitutive model will be calibrated against Syncrude sand experimental data and the model performance, will be discussed.

CHAPTER 6

CALIBRATION OF THE CONSTITUTIVE MODEL AGAINST SYNCRUDE SAND EXPERIMENTAL DATA

In the following sections, the proposed constitutive model will be calibrated against Syncrude sand experimental data; i.e. can the model capture the element behaviour of Syncrude sand? The database comprised information obtained from laboratory element tests on sand samples reconstituted by air and water pluviation, as well as undisturbed frozen samples. Two types of triaxial tests on air pluviated samples were carried out in the Centre for Cold Ocean Resources Engineering (C-CORE): Drained compression and undrained compression and extension (Phillips and Byrne, 1993). These tests were carried out to characterize the sand used in building the centrifuge model and will be referred to here as C-CORE element tests or simply C-CORE tests. Laboratory tests performed at the University of British Columbia (UBC) were mainly carried out on water pluviated samples. They comprised undrained triaxial compression and extension, constant volume simple shear and hollow cylinder tests (Vaid et al., 1995*a* and *b*). In addition, the UBC database included results from constant volume simple shear tests on air pluviated samples, as well as undrained triaxial compression, undrained triaxial extension and constant volume simple shear tests on undisturbed frozen specimens (Vaid

et al., 1996). Tests carried out at the University of British Columbia will be referred to here as UBC element tests or simply UBC tests.

Four phases of site characterization were undertaken as part of the CANLEX Project. However, only Phase-I and Phase-III are directly related to the research carried out in this thesis. Syncrude Phase-I sand was used for building the centrifuge model by air pluviation, while Syncrude Phase-III sand was utilized in the CANLEX field event to form the foundation layer by hydraulic deposition. Syncrude sand emanated as waste from the oil sand mining industry in Alberta and its key properties regarding undrained behaviour are presented in Table 6.1 together with other properties of relevance to this study. The grain size distribution curve is shown in Figure 6.1.

Table 6.1 Properties of Syncrude tailings sand (after Phillips and Byrne, 1993, Vaid et al. 1996 and Vaid et al. 1998).

Property	Phase-I (Centrifuge Model)	Phase-III (Field Event)
Specific gravity (G_s)	2.64 ^(a)	2.63 ^(b)
Maximum dry density, kg/m ³	1720 ^(a)	-
Minimum dry density, kg/m ³	1350 ^(a)	-
Maximum void ratio, e_{max}	0.960 ^(a)	0.901 ^(c)
Minimum void ratio, e_{min}	0.530 ^(a) *	0.579 ^{(c)*}
D_{60} , mm	0.195 ^(a)	0.20 ^(c)
D_{50} , mm	0.17 ^(a)	-
D_{10} , mm	0.092 ^(a)	0.091 ^(c)
C_u	2.12 ^(a)	2.2 ^(c)
% Fines	8 ^(a)	2-8 ^(c)
Permeability (m/s) to oil @ 21°C, at $D_f = 40\%$	3.25E-07 ^(a)	-
% Quartz	90 ^(c)	90 ^(c)
Grain shapes	Sub-angular to sub-rounded ^(a)	Rounded ^(c)

Note: ^(a) Phillips and Byrne, 1993. ^(b) Vaid et al., 1996. ^(c) Vaid et al., 1998. * ASTM wet method.

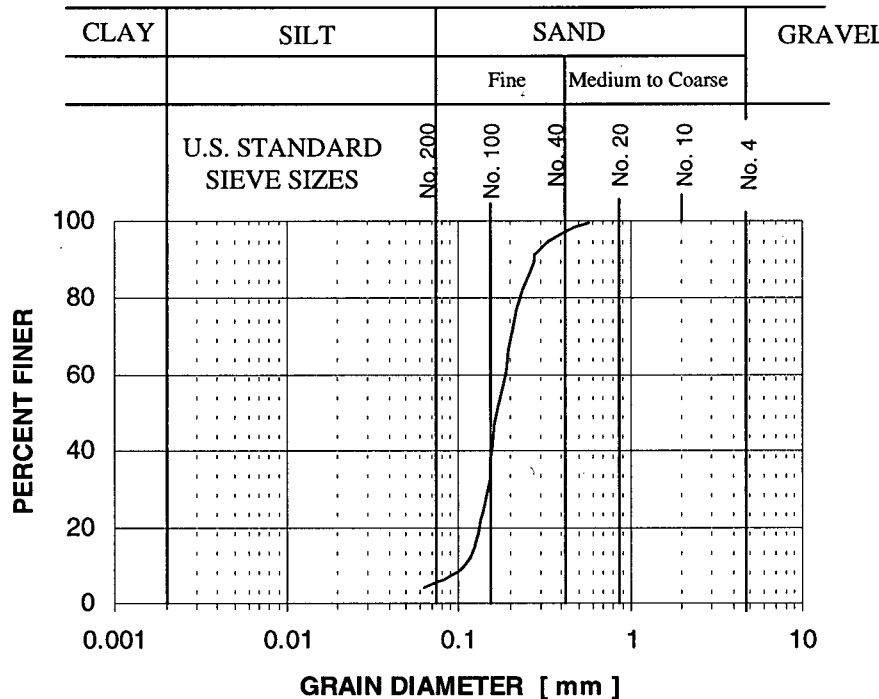


Figure 6.1 Syncrude sand grain size distribution curve (after Phillips and Byrne, 1993).

Vaid et al. (1995a) showed that the method used to reconstitute sand samples in the laboratory had a significant effect on the response of Syncrude sand to first time undrained shear loading as can be seen in Figure 6.2. The most contractive or strain softening response was exhibited by the moist tamped specimen compared to a much smaller degree of strain softening in the case of the air pluviated sample. On the other hand, the water pluviated specimen exhibited a dilative response. Vaid et al. (1995a) attributed the difference in behaviour of air and water pluviated specimens to the ensuing fabric that developed under each deposition technique. This is an important point to consider when analyzing the CANLEX embankments since the centrifuge models were prepared by air pluviation, while the layer that served as foundation for the field event was hydraulically placed. Details on both, centrifuge models and CANLEX field event

will be given in Chapters 7 and 8, respectively. Here, the constitutive model will be calibrated considering the difference in monotonic undrained behaviour of Syncrude sand as result of the method of placement used.

Hence, from the large database (Vaid et al., 1996, and Phillips and Byrne, 1993), two sets of data were of particular interest for modelling the CANLEX embankments:

- (i) Data from air pluviated specimens, since the centrifuge model was built using this pluviation technique, and
- (ii) Data from water pluviated specimens and from undisturbed frozen samples obtained at the test embankment site, since the foundation layer of the field event was hydraulically placed.

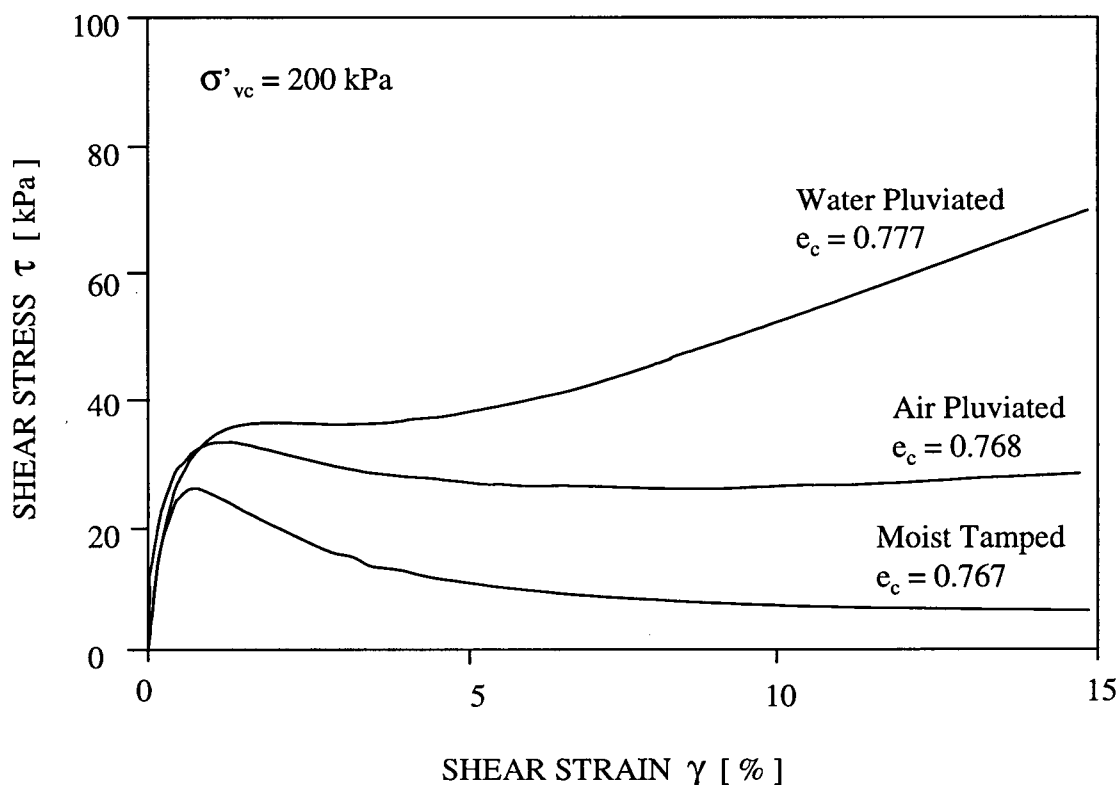


Figure 6.2 Effect of specimen reconstituting method on undrained simple shear response of Syncrude sand (after Vaid et al. 1995a).

6.1 Capturing the characteristic behaviour of air pluviated samples (C-CORE and UBC tests)

Calibration of the constitutive model following the procedure discussed in Section 4.7 requires very detailed information not readily available from typical laboratory testing programs. Hence, an alternative procedure involving direct determination of only readily available parameters, e.g. ϕ_f , $\phi_{PT/cv}$, strain at failure, initial slope of shear and/or volumetric stress-strain curves, will be used. Although the unknown parameters will be initially estimated from typical values, e.g. Table 4.3, this does not mean that the characteristics of the site-specific material will be disregarded. On the contrary, the unknown (estimated) parameters must be adjusted by successive approximations to fit the observed response, e.g. strain-stress curves, of site-specific material.

6.1.1 Model parameters for air pluviated element tests

The C-CORE database included information from the following tests on air pluviated samples (Phillips and Byrne, 1993):

- Three drained triaxial compression tests conducted on water saturated samples, although measurements of volumetric strains were not available for this particular set of tests. The tests were carried out at initial isotropic confining stresses of 50, 100 and 200 kPa, with relative densities of 38.1, 36.7 and 36.5%, respectively.
- One drained isotropic compression test performed on a water saturated triaxial sample, at an initial relative density of 39.6%.
- Four undrained triaxial extension tests on water saturated specimens, with pore pressure measurements. The tests were carried out at initial isotropic confining

stresses of 50, 100, 200 and 400 kPa, with relative densities of 37.7, 35.1, 43.7, 42.6%, and Skempton B values of 0.95, 0.97, 0.92 and 0.98, respectively.

- Three undrained triaxial compression tests on water saturated samples, with pore pressure measurements. The tests were performed at initial isotropic confining stresses of 100, 200 and 400 kPa, with relative densities of 39.6, 40.5 and 43.0%, and Skempton B values of 0.91, 0.93 and 0.93, respectively.

As can be noted from the Skempton B values, full saturation of the specimens tested on undrained triaxial compression and extension, was not achieved. Although the use of such tests for calibrating the model would have been possible by simply accounting for the specific Skempton B values, this approach was not followed in order to avoid complexity. Instead, calibration of the model was based on drained data from triaxial compression tests (C-CORE tests) and constant volume simple shear tests on air pluviated samples performed at UBC (Vaid et al., 1995b). The latter database included information from four simple shear tests in which the initial vertical confining stresses were 50, 100, 200 and 400 kPa, and the initial relative densities were 28.5, 32.7, 34.5 and 43.5%, respectively. The consolidation stages of such simple shear tests were not carried out isotropically and hence the horizontal stresses corresponded to the k_0 condition. This implies that upon shear loading the principal stress directions rotated gradually, inducing volumetric and shear strains of the type discussed in Section 2.4. Thus, results from simple shear tests that start from a k_0 condition include the effect of principal stress rotation and such effect must be accounted for in modelling simple shear tests.

From drained triaxial compression data, a friction angle at failure of approximately 34° was determined ($\phi_f \approx 34^\circ$). In addition, crude approximations of the initial combined shear modulus G_i and strain at failure were made from the stress-strain curves; values of $G_i \approx 25000$ kPa and $\epsilon_f \approx 20\%$ were estimated. With the aid of Equation 4.50, the failure ratio R_F was calculated as 0.97. The friction angle at phase transformation was obtained from the stress paths of constant volume simple shear tests ($\phi_{PT/cv} \approx 32.1^\circ$). Assuming the Poisson's ratio $\nu = 0.125$, the elastic shear modulus number as well as plastic shear and elastic moduli exponents, were obtained from Tables 4.2 and 4.3, i.e., $k_G^e = 300$ and $me = np = 0.5$. Four more parameters were required: the plastic shear and volumetric moduli numbers, k_G^p and k_B^p , respectively, the plastic volumetric exponent mp , and the plastic anisotropy factor, F .

To this end, the isotropic compression curve from the laboratory was fitted first to determine k_B^p and mp by successive approximations since the volumetric response is known in this test. Following the guidelines on modelling the element behaviour discussed in Section 5.3, the numerical simulation was carried out using the axisymmetric configuration. Once a reasonable match on volumetric response was achieved, the shear parameter k_G^p was obtained by back analyzing the drained triaxial compression test carried out at an initial isotropic confining stress of 100 kPa.

Finally, the plastic anisotropy factor, F , was evaluated from fitting the constant volume simple shear test performed at a vertical confining stress of 100 kPa. Simple shear tests were simulated by using plane strain configuration and by assuming two different initial confining stress conditions: (i) $\sigma'_h = k_0 \cdot \sigma'_v$, where $k_0 = 1 - \sin \phi_f$; and (ii) $\sigma'_v = \sigma'_h$ and hence $1/k_c = 1$. In the first case, the continuous rotation of principal

stresses that occurs during the test was accounted for by using the procedure discussed in Section 4.3.5. Although no simple shear test was carried out under a $1/k_c = 1$ condition, this assumption allows isolating the shear response from the effects induced by the continuous rotation of the principal stresses that occurs during of this type of test when $1/k_c = k_0$. It was considered important to simulate such condition since the proposed procedure to account for continuous rotation of principal stresses had not been used before and Syncrude sand was not tested under pure rotation of principal stresses. Thus, Syncrude sand experimental data was not available for direct validation of the aforementioned procedure. The model predictions for the two initial confining stress conditions that were assumed will be presented and discussed in Section 6.1.2.

The elastic shear modulus number had to be adjusted in order to match the simple shear response. This in turn led to a modified k_B^P and another cycle of successive approximations was necessary to reassess k_G^P and F . The value of k_G^P does not change much with k_B^P since the cap mechanism has little influence in stress paths like those from conventional drained triaxial compression tests, i.e., σ_3 constant. Hence, a second round of approximations is usually enough to finish calibrating the model. The final parameters used to capture the characteristic behaviour of air pluviated specimens of Syncrude Phase-I sand are presented in Table 6.2.

The predicted and observed responses in isotropic compression, drained triaxial compression and constant volume simple shear tests at initial confining stresses of 50, 100 and 200 kPa, are compared in Figure 6.3 to 6.5. A reasonable agreement between the observed *characteristic behaviour* and the predicted response can be appreciated in these

figures. The model fit to experimental data will be examined quantitatively in Section 6.1.2.

Table 6.2 Model parameters for capturing Syncrude Phase-I sand characteristic behaviour of air pluviated element tests.

Parameter	Value
Poisson's ratio, ν	0.125 ^(a)
Elastic shear modulus number, k_G^e	210.0 ^(b)
Elastic moduli exponent, me	0.5 ^(b)
Plastic shear modulus number, k_G^p	280.0 ^(b)
Plastic shear modulus exponent, np	0.5 ^(b)
Friction angle at failure, ϕ_f [°]	34.0 ^(d/ad)
Constant volume friction angle, ϕ_{cv} [°]	32.1 ^(d/ad)
Failure ratio, R_F	0.97 ^(d/ad)
Factor of anisotropic plastic shear response, F	0.24 ^(b)
Plastic bulk modulus number, k_B^p	200.0 ^(b)
Plastic bulk modulus exponent, mp	1.0 ^(b)

Note: ^(a) Indicates the parameter was assumed. ^(b) Indicates the parameter was back analyzed from experimental data. ^(d/ad) Indicates the parameter was derived from experimental data/adjusted for best fit.

6.1.2 Discussion

It is important to notice the difference between capturing *characteristic behaviour* and matching “almost perfectly” the measured response at different stress levels and under different stress paths. The issue is emphasized because the constitutive model is based on physical concepts as opposed to curve-fitting techniques. Once the constitutive parameters of the model are determined for a given sand, the model should be capable of capturing the *characteristic response* of that sand at different stress levels and under different stress paths. As long as the database used for calibrating the model reflects

measured behaviour in some of those stress paths, the physical properties of the model should not need further adjustment.

No model would render perfect agreement over a range of stress paths and levels since soil is not a perfect material. In fact, if laboratory tests were to be repeated, slight differences in the achieved void ratio, i.e. not identical void ratio, would influence the soil response as can be seen in Figure 6.6. Nonetheless, the characteristic behaviour would be the same. Therefore, some discrepancy among experimental data and predicted values over a range of stress levels and paths should be expected.

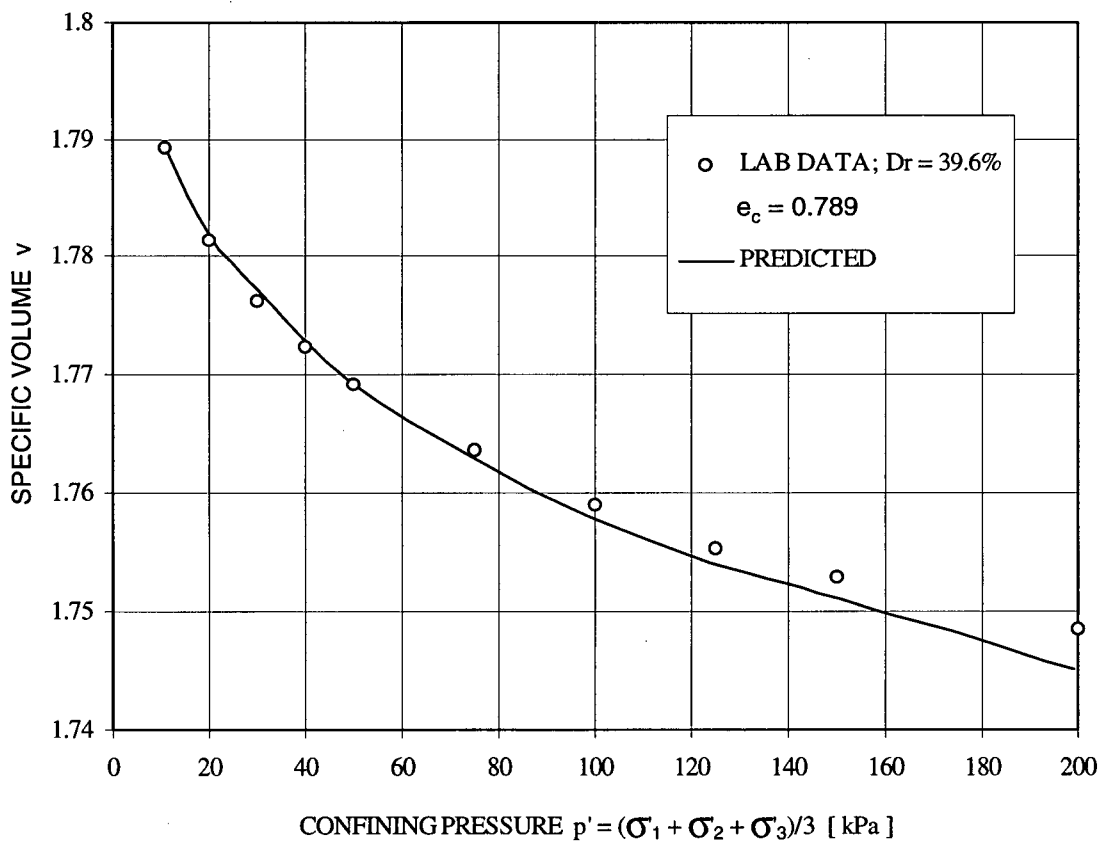


Figure 6.3 Comparison between measured and predicted response of Syncrude sand tested in isotropic compression. Data from C-CORE (Phillips and Byrne, 1993).

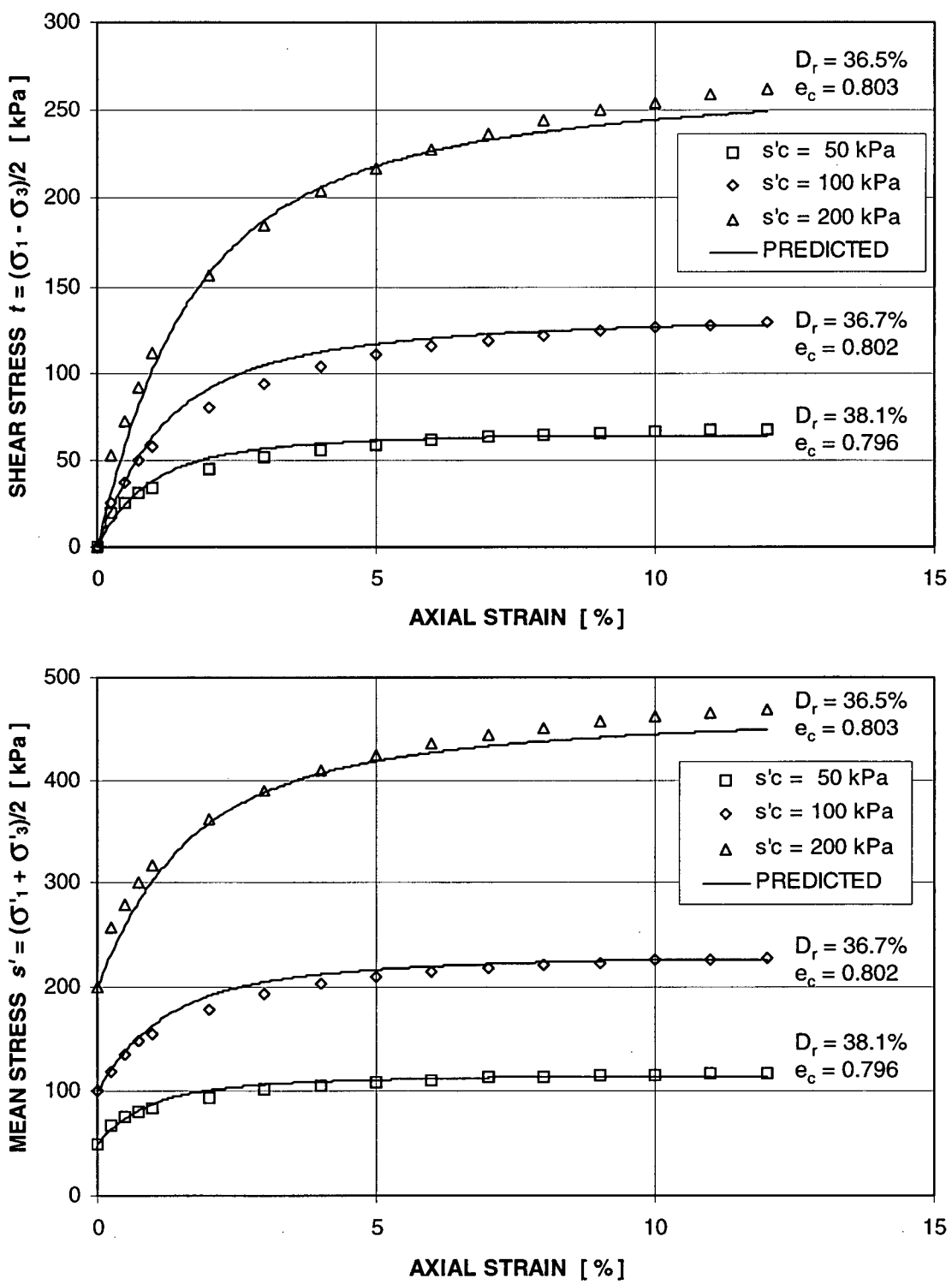


Figure 6.4 Comparison between measured and predicted response of Syncrude sand tested in drained triaxial compression. Data from C-CORE (Phillips and Byrne, 1993).
 (a) Shear stress. (b) Mean stress.

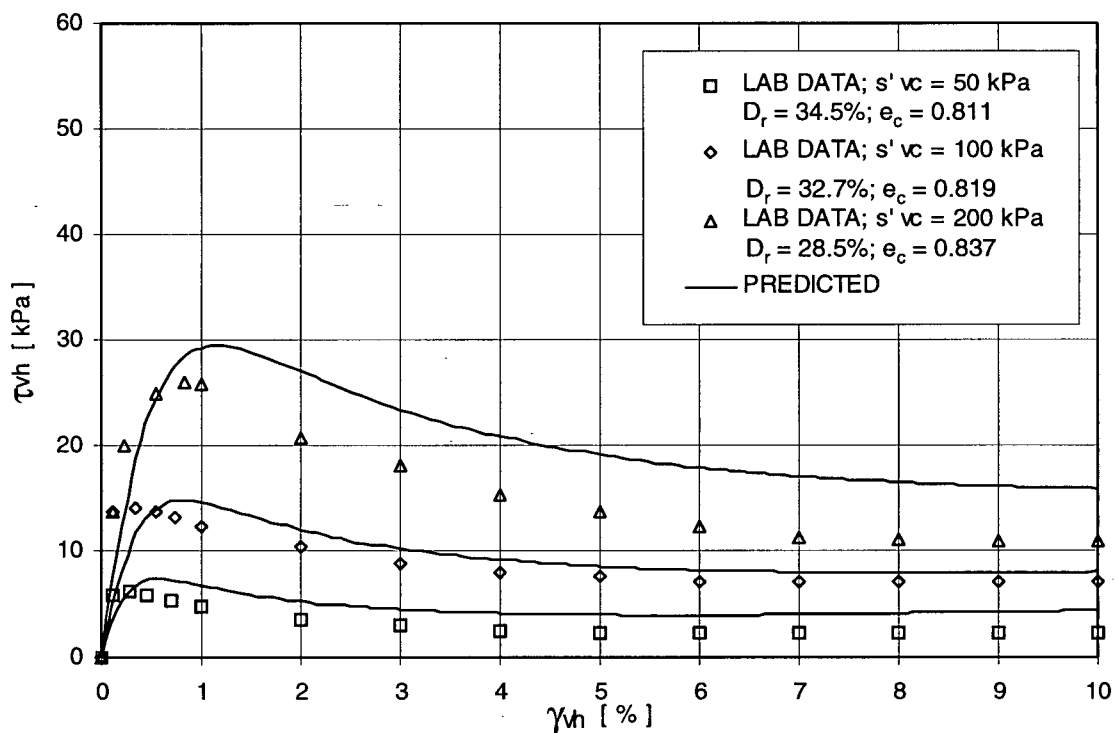


Figure 6.5 Comparison between measured and predicted response of Syncrude sand tested in simple shear at constant volume. Data from UBC air pluviated specimens (Vaid et al. 1995b).

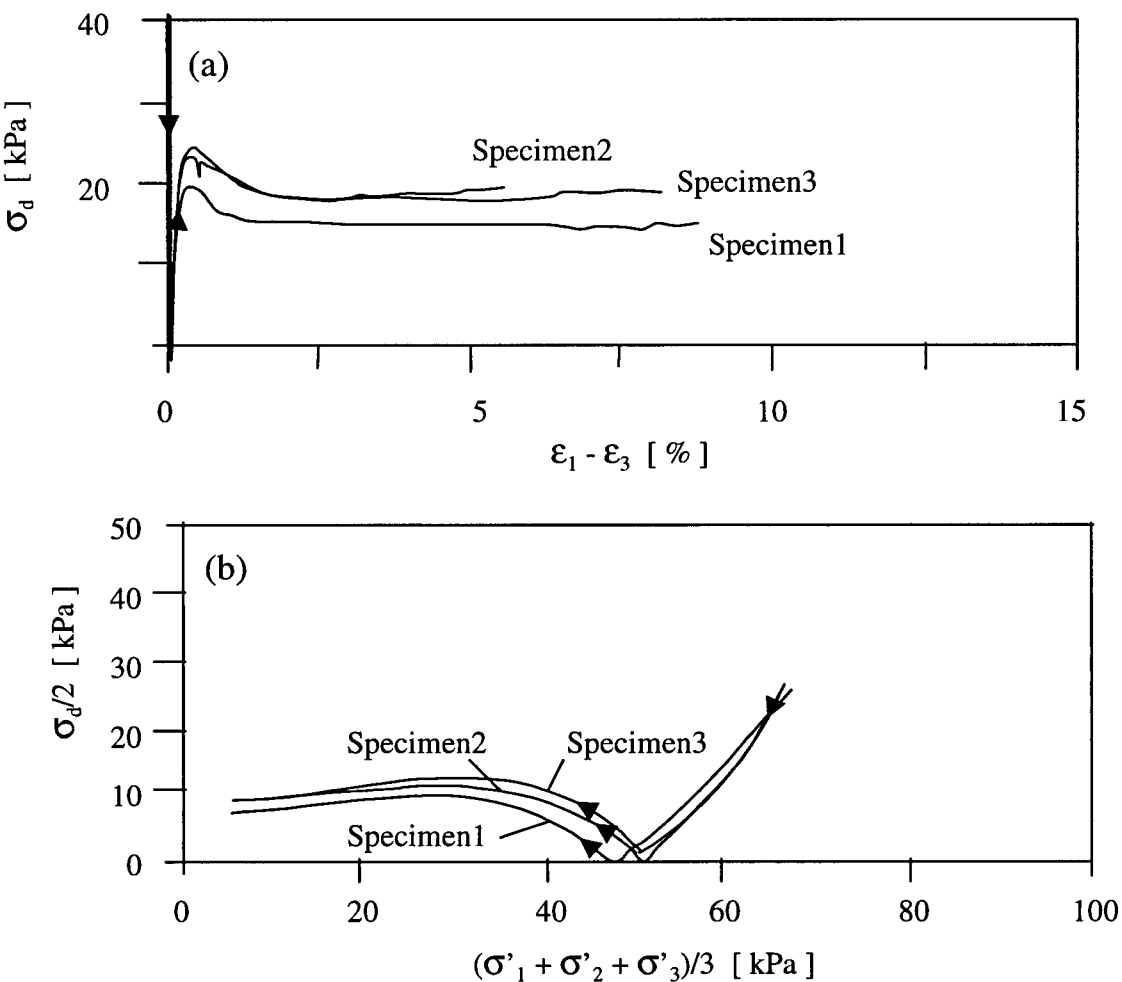


Figure 6.6 Repeatability of plane strain, anisotropically consolidated extension test on Syncrude sand (after Vaid et al. 1996). (a) Stress-strain response. (b) Stress paths.

As can be noted in Figure 6.5, the predicted responses in simple shear by assuming $1/k_c = 1$ conditions are softer than those observed in the pre-peak region in the laboratory tests. A closer view is presented in Figure 6.7, where a comparison is made among the measured response in simple shear at a vertical confining stress, σ'_v , of 100 kPa and different model predictions, i.e. assuming consolidation states in which $1/k_c = \sigma'_h / \sigma'_v = 1$, and $1/k_c = k_0$, with and without accounting for continuous rotation of principal stresses. The horizontal stress, σ'_h , in the actual test was unknown, but assumed

related to σ'_v through k_0 , where $k_0 = 1 - \sin\phi_f$ and $\sigma'_h = k_0 \cdot \sigma'_v$. At the beginning of the test, the plane of maximum shear was oriented 45° respect to the vertical. As the test progressed, the shear stress on the horizontal plane gradually increased and the principal stresses rotated continuously until the plane of maximum shear coincided with the horizontal, point A in Figure 6.7.

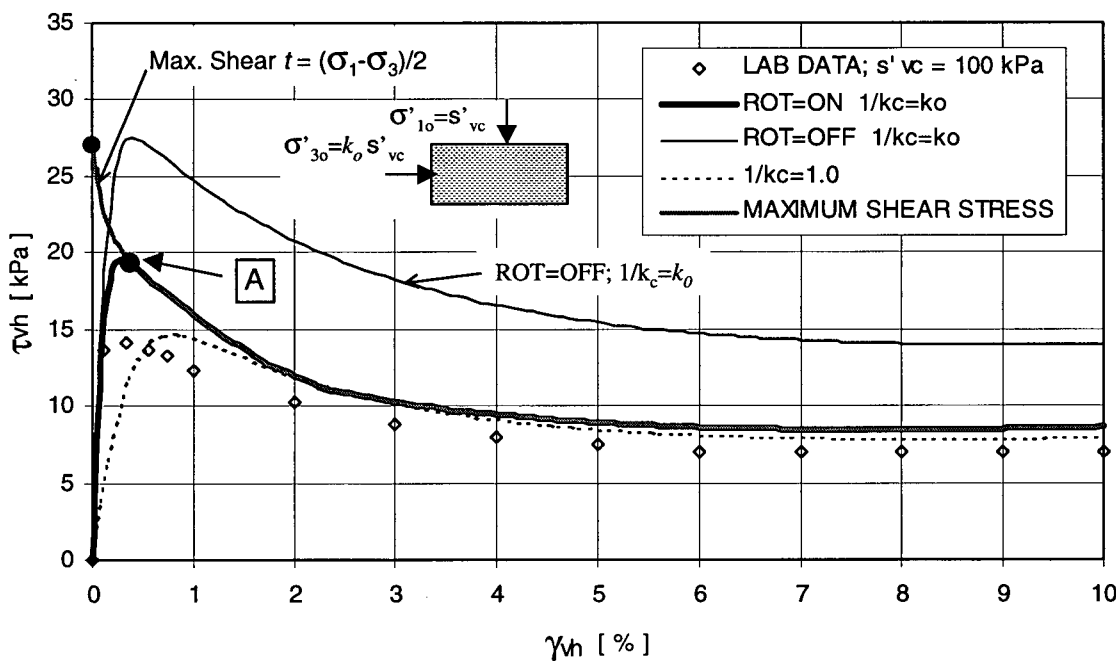


Figure 6.7 Effect of rotation of principal stresses in simple shear test.

In Figure 6.7, the model's prediction in which rotation of principal stresses is accounted for is labeled ROT=ON, ($1/k_c = k_0$), and it is indicated with the thickest line. The curve labeled ($1/k_c = 1$), dashed curve, shows the model prediction if the shear response were isolated from the effects of continuous rotation of principal stresses by starting the test from an isotropic consolidation state. For the ($1/k_c = 1$) case, the consolidation stresses σ'_v and σ'_h are assumed equal and at the commencement of

shearing, the plane of maximum shear abruptly becomes the plane of shear stress application. Although curve ($1/k_c = 1$), dashed curve, seems to resemble the trace of experimental data better than curve ROT=ON ($1/k_c = k_0$), thickest line, the predicted response for ($1/k_c = 1$) is less stiff than measured in the pre-peak region. In contrast, the strain at which the peak strength was measured is better captured by curve ROT=ON ($1/k_c = k_0$), but the peak strength is overestimated.

The curve labeled ROT=OFF, ($1/k_c = k_0$), indicated with the thinnest line, shows the model's prediction if the effects of continuous rotation of principal stresses were not accounted for at all by the model, while such rotation actually occurs since $\sigma'_v \neq \sigma'_h$ at the beginning of the test. As can be seen in Figure 6.7, the measured shear stress-strain response is, in the case ROT=OFF ($1/k_c = k_0$), overestimated by the model approximately by a factor of 2; evidence of the importance of accounting for principal stress rotation in modelling. However, the peak in the predicted stress-strain curve when principal stress rotation is accounted for by the model, ROT=ON ($1/k_c = k_0$), thickest line, appears to suggest that the effects of such rotation are not captured fully, leading to overestimate the peak strength. Further improvement of the model regarding this topic might be necessary, but overall, the present formulation is considered adequate.

To test the suitability of the model to predict undrained response from capturing the skeleton behaviour as observed in drained tests, the undrained response in triaxial compression and extension tests were predicted. Predicting the undrained response in such tests required accounting for the Skempton B value in each test. This was done by computing an equivalent fluid stiffness B_f as follows:

$$[6.1] \quad B_f = \frac{nB^e}{\frac{1}{B_{Skem}} - 1}$$

where n is the porosity; B^e , the elastic bulk modulus; and B_{Skem} , the Skempton B value.

In addition, a small difference between the friction angle at failure for drained and undrained conditions was considered. For loose sand the ratio $(\eta_f - \eta_{cv})_{\text{Undrained}}$ to $(\eta_f - \eta_{cv})_{\text{Drained}}$ is close to 1, Vaid (1999). In this study, a value of $\phi_f = 33.7^\circ$ for undrained conditions, corresponding to a $(\eta_f - \eta_{cv})$ undrained to drained ratio of approximately 0.84, was found adequate to fit Syncrude sand experimental data from loose air pluviated samples.

A comparison between the predicted and observed shear stress and pore pressure vs. axial strain responses in undrained triaxial tests is shown in Figures 6.8 and 6.9. Again, a reasonable agreement in terms of characteristic behaviour can be noted. However, the initial predicted stress-strain responses in both, compression and extension tests are less stiff than the actual data.

A fair comparison between measured and predicted responses should be made using tests performed on clean sand at different confining stresses, but same relative densities (D_r), or vice versa. In fact, the present formulation of the constitutive model does not account explicitly for changes in void ratio only, but assumes that the stress level effect accounts for density change to some extent. Hence, the elastic and plastic parameters of the model need to be modified directly to reflect changes in D_r exclusively.

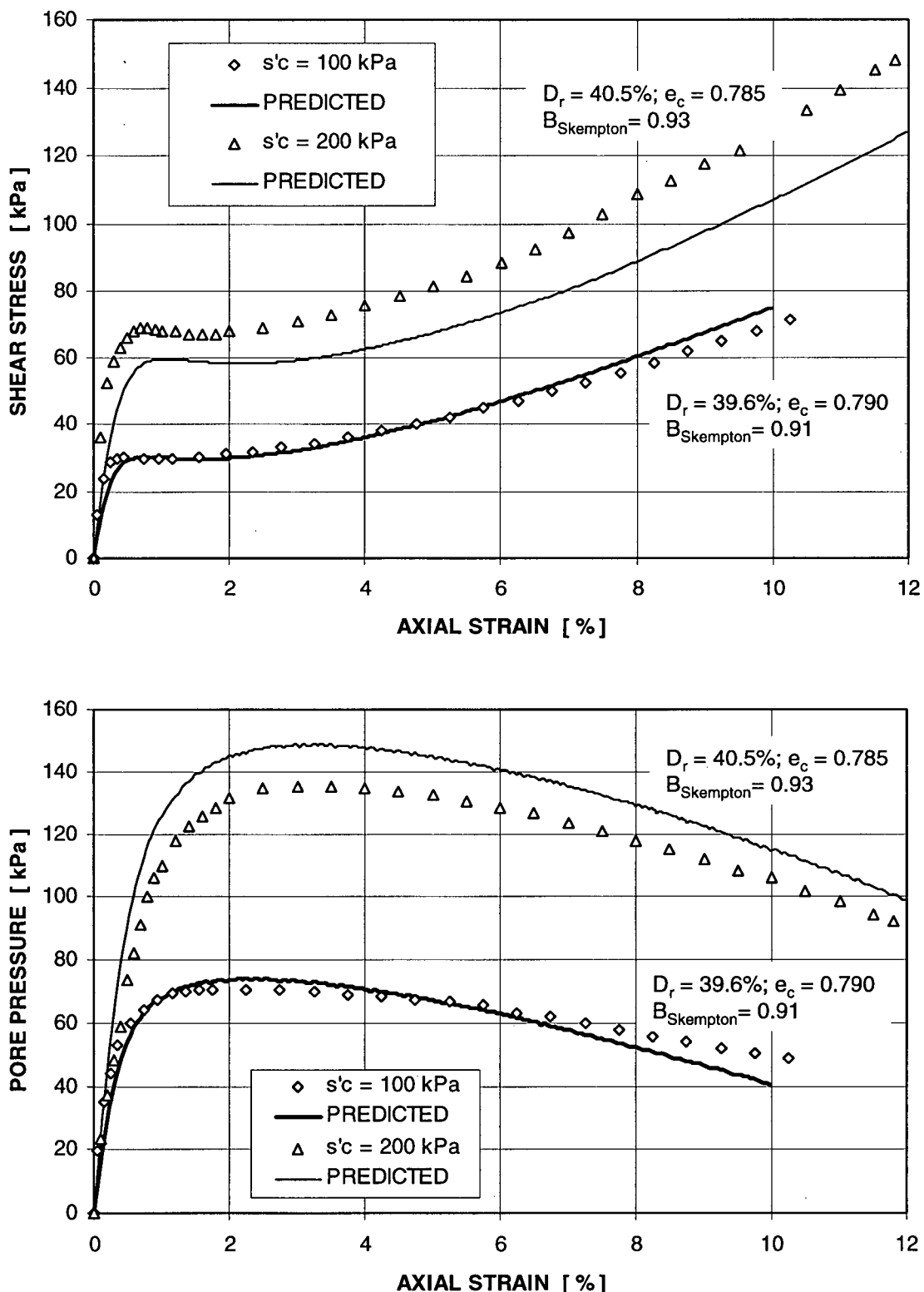


Figure 6.8 Comparison between measured and predicted response of air pluviated Syncrude sand tested in undrained triaxial compression. Data from C-CORE (Phillips and Byrne, 1993). (a) Stress-strain response. (b) Pore pressure response.

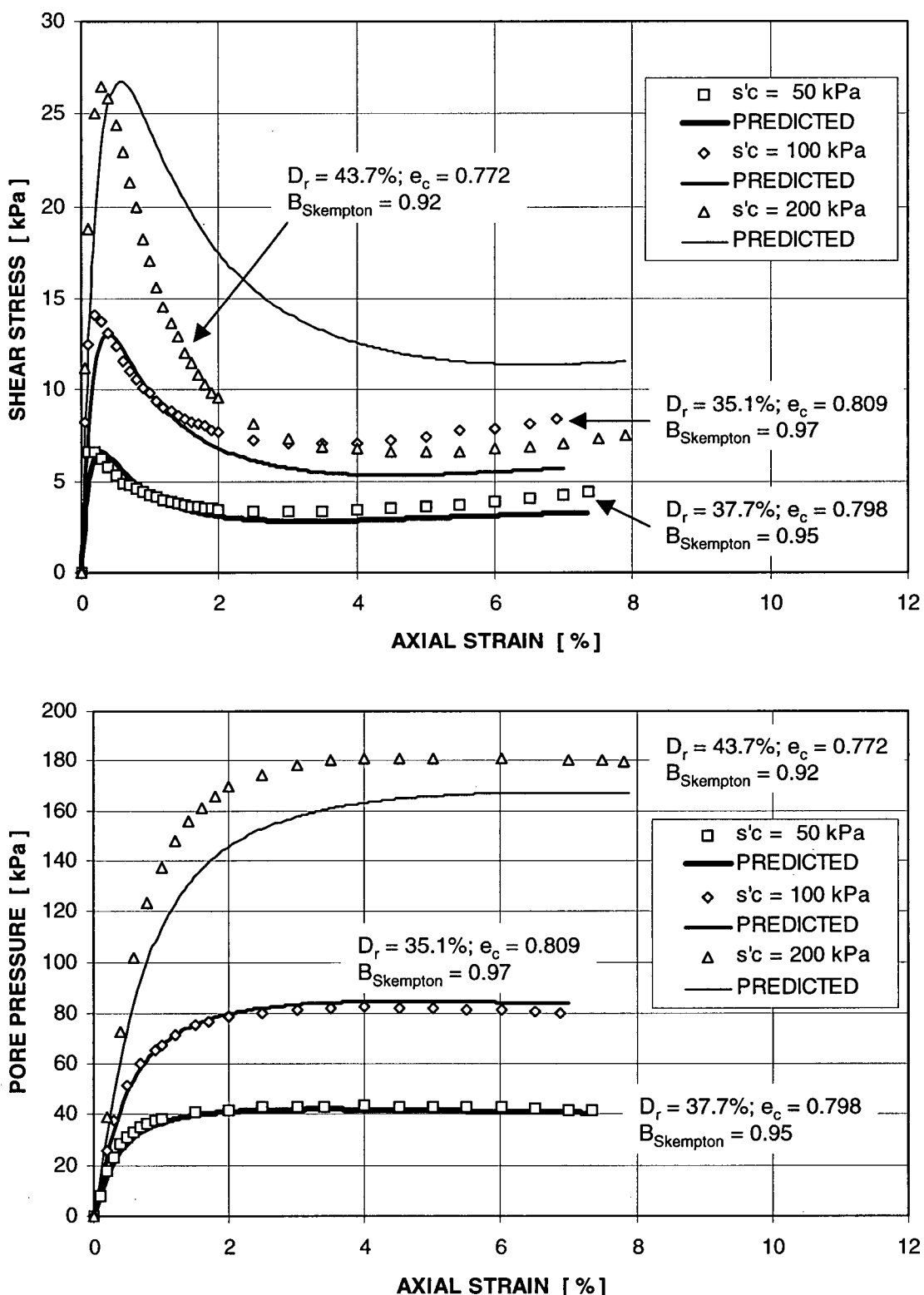


Figure 6.9 Comparison between measured and predicted response of air pluviated Syncrude sand tested in undrained triaxial extension. Data from C-CORE (Phillips and Byrne, 1993). (a) Stress-strain response. (b) Pore pressure response.

The laboratory tests presented in this section were carried out over a range of relative densities, i.e., 28.5 to 43.7%. However, the model parameters were kept the same regardless of D_r , since focus was placed on testing the ability of the model for capturing the characteristic behaviour of air pluviated Syncrude sand and predicting different stress paths, rather than a specific test. The effect of relative density in the stress-strain model response could be considered explicitly by making the model stiffness moduli dependent on void ratio. Although several relationships between elastic moduli and void ratio can be found in the literature, there is little knowledge regarding plastic parameters. Further study is necessary in order to improve the constitutive model in this area.

Since some scatter in measured response is likely to be observed from one laboratory test to another, the model fit to laboratory data will be judged in terms of key aspects for liquefaction analysis. Hence, the undrained response will be characterized here by the following indices: the normalized undrained strength ratio at the critical stress ratio, $(s_u/s'_o)_{CSR}$, and the strain developed at this point, $(\varepsilon)_{CSR}$; the normalized undrained strength ratio at the state of phase transformation, $(s_u/s'_o)_{PT}$, and the strain developed at this point, $(\varepsilon)_{PT}$; and the brittleness index (Bishop, 1971), $I_B = [(s_u)_{peak/CSR} - (s_u)_{PT}] / (s_u)_{peak/CSR}$. To account for scatter in the data these indices will be averaged to characterize the mean undrained response on each type of test. Subsequently, the ratio of the predicted average index to the measured average index, $RATIO_{pred/meas}$, will be computed as a measurement of the model fit to the observed response. Table 6.3 shows

such indices as computed from each measured and predicted undrained test on air pluviated Syncrude Phase-I sand. As can be noted, with exception of $(\varepsilon)_{CSR}$, which was overestimated by the model on all cases, the rest of the average index ratios, $RATIO_{pred/meas}$, as well as the average ratios over all triaxial tests, $(RATIO_{pred/meas})_{ave}$, show that the mean measured response is captured by the model within a 10% difference. Overestimating $(\varepsilon)_{CSR}$ implies that if $(s_u)_{peak/CSR}$ is not reached, i.e. liquefaction is not triggered, the model overestimates the strains. This could be related to the tendency of the model to overestimate the rate of dilatancy at small stress ratios, as discussed in Section 4.3. However, since strains in the pre-CSR region are small compared to those after liquefaction is triggered (post-CSR region), the error induced on post-liquefaction displacements by overestimating $(\varepsilon)_{CSR}$ may be regarded as not significant. Based on these comparison criteria and the results shown in Table 6.3, agreement between predicted and measured response of air pluviated Syncrude Phase-I sand was considered reasonable.

The fit to any one curve could be improved by accounting for a specific stress path and relative density, but when simulating the centrifuge model this would not be of much help. In the centrifuge model, the loading pattern is much more complicated than in an element test and both the degree of saturation as well as the D_r , could be variable through out the model. Therefore, refining the fit to any single curve is not as important as capturing the fundamental characteristics of the problem. The parameters listed in Table 6.2 will be used in Chapter 7 for analyzing the CANLEX centrifuge model.

Table 6.3 Indices computed for comparing measured vs. predicted undrained response of air pluviated Syncrude Phase-I sand.

<i>TCU</i>					
<i>MEASURED</i>					
<i>s'₀</i> [kPa]	(ε) _{CSR} [%]	($s_u/s'₀$) _{CSR} [-]	($s_u/s'₀$) _{PT} [-]	(ε) _{PT} [%]	I_B [-]
100	0.450	0.299	0.294	1.50	0.0164
200	0.800	0.343	0.333	1.80	0.0285
AVERAGE	0.625	0.321	0.313	1.65	0.0225
<i>TCU</i>					
<i>PREDICTED</i>					
<i>s'₀</i> [kPa]	(ε) _{CSR} [%]	($s_u/s'₀$) _{CSR} [-]	($s_u/s'₀$) _{PT} [-]	(ε) _{PT} [%]	I_B [-]
100	0.700	0.301	0.296	1.50	0.0183
200	1.100	0.297	0.291	2.14	0.0225
AVERAGE	0.900	0.299	0.293	1.82	0.0204
(RATIO_{pred/meas})	1.44	0.932	0.934	1.103	1.044
<i>TEU</i>					
<i>MEASURED</i>					
<i>s'₀</i> [kPa]	(ε) _{CSR} [%]	($s_u/s'₀$) _{CSR} [-]	($s_u/s'₀$) _{PT} [-]	(ε) _{PT} [%]	I_B [-]
50	0.300	0.124	0.067	3.000	0.464
100	0.200	0.141	0.071	4.000	0.500
200	0.300	0.132	0.033	5.500	0.750
AVERAGE	0.267	0.133	0.056	4.167	.572
<i>TEU</i>					
<i>PREDICTED</i>					
<i>s'₀</i> [kPa]	(ε) _{CSR} [%]	($s_u/s'₀$) _{CSR} [-]	($s_u/s'₀$) _{PT} [-]	(ε) _{PT} [%]	I_B [-]
50	0.299	0.132	0.056	3.247	0.576
100	0.399	0.130	0.053	4.795	0.589
200	0.549	0.134	0.056	6.342	0.574
AVERAGE	0.416	0.132	0.055	4.974	0.580
(RATIO_{pred/meas})	1.55	0.99	0.97	1.15	1.01
(RATIO_{pred/meas})_{ave}	1.50	0.96	0.95	1.12	0.96

Note: I_B = Brittleness Index = $[(s_u)_{peak/CSR} - (s_u)_{PT}] / (s_u)_{peak/CSR}$.

6.2 Capturing the characteristic behaviour of water pluviated samples (UBC tests)

It was mentioned before that the fabric or structure attained by sand depends significantly on the way sand is deposited. The difference in response of water and air pluviated specimens of Syncrude sand was illustrated in Figure 6.2. Since one of the objectives of the present study is to analyze the CANLEX field event, characteristic behaviour of Syncrude sand deposited in a water environment was considered important in order to simulate the field conditions as closely as possible. For this reason, undrained triaxial and simple shear data from UBC element tests on water pluviated specimens was used to recalibrate the model according to this condition.

The parameters utilized for capturing the response in triaxial compression and extension, as well as simple shear tests on water pluviated specimens are presented in Table 6.4. According to the laboratory report (Vaid et al. 1996), full saturation of the specimens was achieved before proceeding with the loading stage of the testing program. In contrast with air pluviated samples, in which an equivalent fluid stiffness B_f had to be estimated before simulating the laboratory tests, in this case all the numerical simulations were carried out under constant volume conditions. Hence, the fluid stiffness was not involved at all for predicting the element response since the volumetric constraint was imposed through the boundary conditions as explained in Section 5.6.

As can be noted from the values of the model parameters that are shown in Tables 6.2 and 6.4, the main difference in capturing the response of air and water pluviated samples is not due to strength, but to stiffness. The stiffness of the curve η vs. γ in the proposed constitutive model depends on the elastic and plastic moduli, and the failure

ratio R_F . These are precisely the parameters that needed modification in order to capture the shear response of water pluviated specimens.

Table 6.4 Model parameters for capturing Syncrude sand characteristic behaviour of water pluviated element tests.

Parameter	Value
Poisson's ratio, ν	0.125 ^(a)
Elastic shear modulus number, k_G^e	300.0 ^(b)
Elastic moduli exponent, me	0.5 ^(b)
Plastic shear modulus number, k_G^p	405.0 ^(b)
Plastic shear modulus exponent, np	0.5 ^(b)
Friction angle at failure, ϕ_f [°]	34.0 ^(d/ad)
Constant volume friction angle, ϕ_{cv} [°]	32.1 ^(d/ad)
Failure ratio, R_F	0.93 ^(b)
Factor of anisotropic plastic shear response, F	0.300 ^(b)
Plastic bulk modulus number, k_B^p	200.0 ^(b)
Plastic bulk modulus exponent, mp	1.0 ^(b)

Note: ^(a) Indicates the parameter was assumed. ^(b) Indicates the parameter was back analyzed from experimental data. ^(d/ad) Indicates the parameter was derived from experimental data/adjusted for best fit.

The predicted and observed undrained responses in terms of stress vs. strain difference in triaxial compression and extension tests are shown in Figure 6.10, at confining stresses of 50, 100, 200 and 400 kPa. Results from constant volume simple shear tests performed at vertical confining stresses of 50, 100, 200 and 400 kPa, in terms of shear stress vs. shear strain, are presented in Figure 6.11. Although the predicted initial response is less stiff than the one observed in triaxial tests, the characteristic behaviour at confining stresses of 50, 100 and 200 kPa was reasonably well captured by the model at least up to shear strains in the order of 6%. At higher shear strain levels, the dilative response was underestimated. On the other hand, at $s'_c = 400$ kPa, the predicted response, in terms of magnitude, deviates significantly from the laboratory tests in both,

compression and extension. The writer did not find a clear-cut explanation for this. Triaxial predictions could have been improved greatly and to a very reasonable degree by simply modifying the elastic and plastic shear moduli numbers, k_G^e and k_G^p , respectively, as well as the failure ratio R_F . However, improving triaxial predictions led to worse simple shear predictions in this case.

The same was true for simple shear predictions. Parameters that allowed the model a better simulation of these simple shear tests did not yield a very good agreement in terms of triaxial tests. Note in Figure 6.11 that the simple shear response observed in laboratory tests on water pluviated samples was of dilative type, as opposed to the contractive response observed on air pluviated specimens (Figure 6.5). Although the CANLEX field event to be analyzed is a typical plane strain problem, neglecting triaxial tests results completely was not considered appropriate. Hence, the parameters shown in Table 6.4 are a compromise between triaxial and simple shear conditions.

The undrained response of water pluviated Syncrude sand as observed in triaxial compression, extension and constant volume simple shear tests was characterized using the average indices discussed in Section 6.1.2. The computed overall average indices are presented in Table 6.5. Reasonable agreement (within a 10% difference) between predicted and measured overall average response can be noted.

Table 6.5 Indices computed for comparing measured vs. predicted undrained response of water pluviated Syncrude sand.

AVERAGE CHARACTERISTIC RESPONSE IN TCU, TEU AND CONSTANT VOLUME SS				
$(\varepsilon)_{CSR}$ [%]	$(s_u/s'_o)_{CSR}$ [-]	$(s_u/s'_o)_{PT}$ [-]	$(\varepsilon)_{PT}$ [%]	I_B [-]
(RATIO_{pred/meas})_{ave}	1.61	0.97	1.05	1.06

Note: $I_B = [(s_u)_{peak/CSR} - (s_u)_{PT}] / (s_u)_{peak/CSR}$.

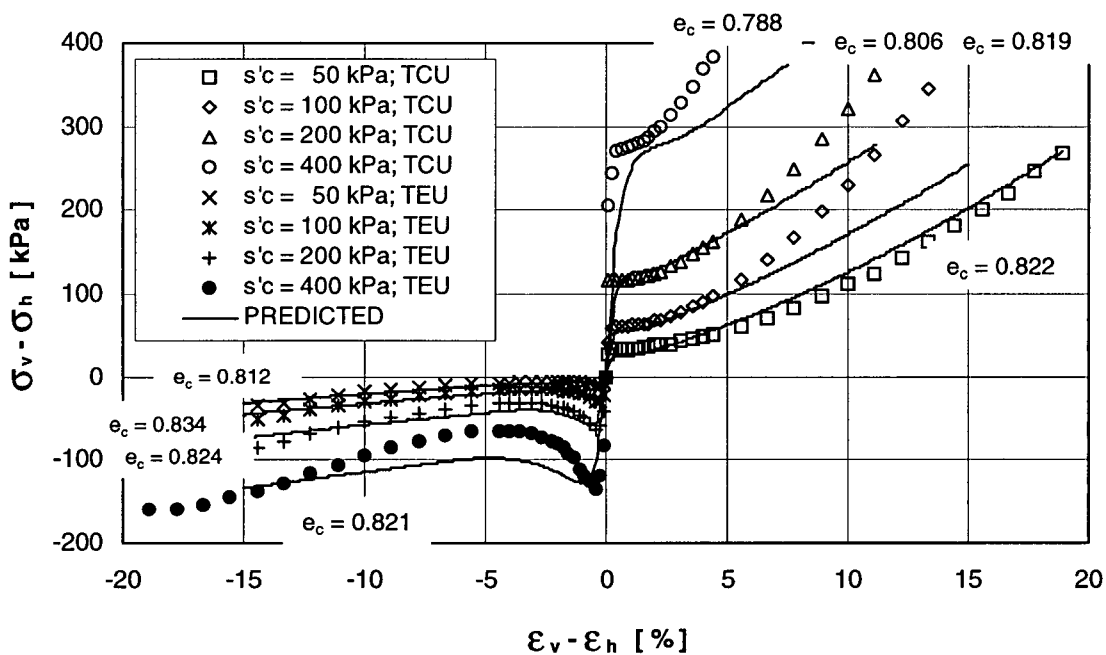


Figure 6.10 Measured and predicted response of Syncrude sand tested in undrained triaxial compression and extension. Data from UBC water pluviated specimens (Vaid et al. 1995b).

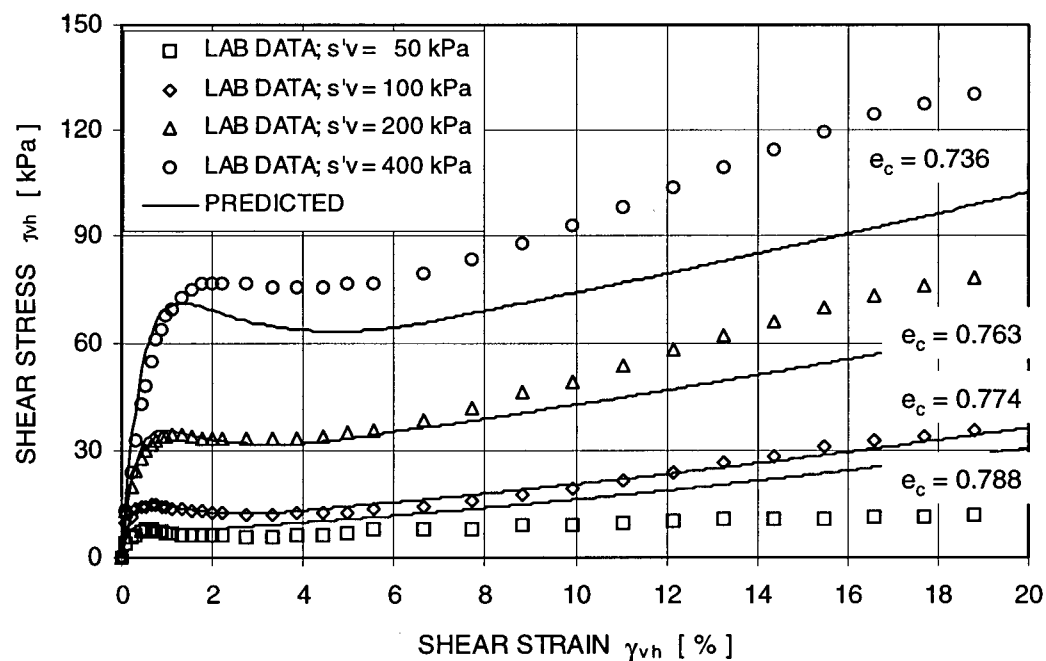


Figure 6.11 Measured and predicted response of Syncrude sand tested in simple shear at constant volume. Data from UBC water pluviated specimens (Vaid et al. 1995b).

To verify that the parameters derived from calibrating the model against water pluviated Syncrude sand behaviour were representative of the soil in the field, a comparison was made between some of these parameters and parameters derived from field test data obtained at the field event site. Three independent field measurements were taken into consideration: (i) Normalized Standard Penetration Test (SPT) blow count (N_1)₆₀, (ii) Normalized Cone Penetration Test (CPT) tip resistance (q_{c1}), and (iii) Normalized Shear Wave Velocity (V_{s1}). Hoffman et al. (1996) reported the following average values in the foundation layer: $(N_1)_{60\text{ave}} = 3.4$; $(q_{c1})_{\text{ave}} = 2350 \text{ kPa}$; and $(V_{s1})_{\text{ave}} = 127 \text{ m/s}$. The different parameters derived from field test data and the corresponding parameters obtained from calibrating the constitutive model are compared in Table 6.6 where good agreement can be noted.

Table 6.6 Parameters derived from field test data and from calibrating the constitutive model against water pluviated Syncrude sand.

Parameter	$(q_{c1})_{\text{ave}} = 2350 \text{ kPa}$	$(N_1)_{60\text{ave}} = 3.4$	$(V_{s1})_{\text{ave}} = 127 \text{ m/s}$	MODEL'S CALIBRATION
G_{\max}, kPa	30300 ^(a)	30000 ^(b)	30645 ^(c)	30000
B^e, kPa	-	30000 ^(b)	-	30000
$\phi, {}^\circ$	32.0 ^(a)	33-35 ^(b)	-	34.0

Note: ^(a) from Robertson and Campanella, 1986; ^(b) from Byrne et al. 1987; ^(c) computed from Equation 4.49 and for $\rho = 1.9 \text{ T/m}^3$ obtained from e_{\max} and e_{\min} (Table 6.1), and e_{Field} ; and ϕ , the friction angle.

To further validate the model parameters chosen for modelling water pluviated Syncrude sand, the model prediction in simple shear was directly compared to the observed response in simple shear tests performed on undisturbed in-situ frozen samples (Figure 6.12). The frozen samples were obtained from the Syncrude site where the field event was carried out. Large variation in measured response with very small differences

in void ratio may be noted in Figure 6.12. However, the predicted response is closer to the lower bound of measured response (hence, on the conservative side), but well within the observed range.

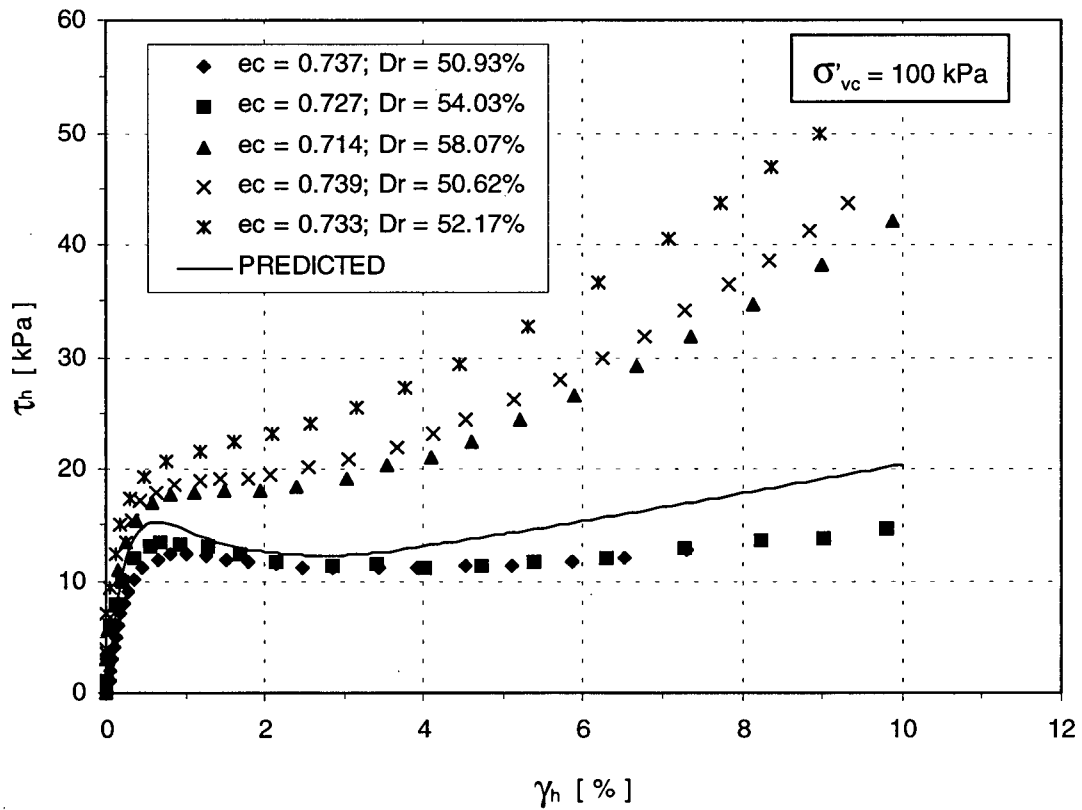


Figure 6.12 Predicted vs. range of measured response in constant volume simple shear tests carried out on undisturbed (in-situ frozen) Syncrude sand (Phase-III) obtained from the field event site (J-Pit). Data from UBC (Vaid et al. 1996).

In addition, the predicted and measured responses in undrained triaxial and plane strain extension tests performed in the hollow cylinder (HCT) device were also compared (Figure 6.13). These HCT tests were carried out on water pluviated reconstituted samples that were anisotropically consolidated to the in-situ void ratio. Furthermore, the stress paths followed in these HCT tests included a state of stress reversal for each

extension test. This characteristic of the stress paths was considered particularly interesting since it provided means to verify the model performance under such loading paths. As can be seen in Figure 6.13, the predicted and measured response compare reasonably well, although the peaks of strength were overestimated in both tests. The differences between measured and predicted responses may be related to the size of the assumed elastic region in the constitutive model. Upon unloading from the consolidation state, the constitutive model assumes elastic behaviour until the state of stress reversal takes place and hence, the model does not account for shear-induced contraction (which leads to shear-induced pore pressure) during this stage. On the other hand, real sand does exhibit some shear-induced contraction before the occurrence of a stress reversal as discussed in Section 2.1, and shown in Figure 2.6. Thus, the mean effective stresses predicted at the states of stress reversal in the modelled tests were greater than the ones in the actual tests and this might have led to overestimate the peaks of strength. However, it is evident that the proposed constitutive model overcomes the drawback of other elastic-plastic models in which isotropic hardening of the elastic region is assumed. In such models, the response after a state of stress reversal is predicted as elastic until the stress level on the other side of the hydrostatic axis reaches the same level as that from where the unloading process started. This is clearly not the observed behaviour of real sand. In contrast, the presently proposed constitutive model is consistent for the most part with the characteristic behaviour observed after the state of stress reversal.

Based on the results shown and discussed above, the model parameters listed in Table 6.4 were considered adequate for representing the soil in the field event site. Such parameters will be used in Chapter 8 for analyzing the CANLEX field embankment.

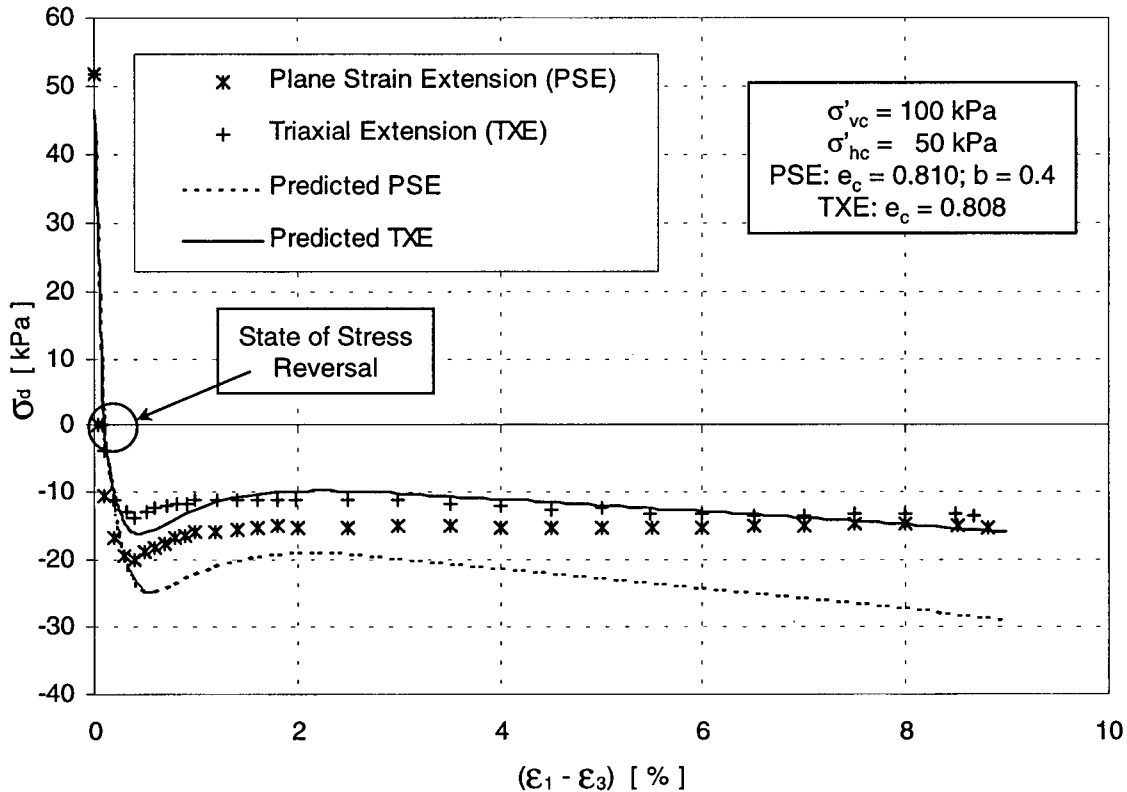


Figure 6.13 Predicted vs. measured undrained response in plane strain extension (PSE) and triaxial extension (TXE) tests on water pluviated reconstituted samples (Syncrude Phase-III sand), anisotropically consolidated to the in-situ void ratio, and including a state of stress reversal; $b = (\sigma_2 - \sigma_3)/(\sigma_1 - \sigma_3)$; σ'_vc and σ'_hc are the effective vertical and horizontal consolidation stresses, respectively; and e_c is the void ratio at consolidation. Data from UBC (Vaid et al. 1996).

6.3 Sensitivity of predicted response to variation in the model parameters

To illustrate the influence of model parameters variation on the model's predicted response, a brief sensitivity study regarding this topic was carried out. This study provides information on how the response predicted by the model in a drained triaxial extension test varies with $\pm 10\%$ variation on the model parameters. The triaxial extension test was modelled by increasing the horizontal stress rather than decreasing the vertical stress. This loading condition was chosen since all the model parameters are

involved in predicting such a stress path. It must be recognized that under different stress paths the influence of each parameter on predicted response may vary slightly. It should also be recognized that a $\pm 10\%$ variation on ϕ_f and ϕ_{cv} significantly covers the range in which such parameters usually vary for loose sands and hence, such a range imposes an extreme condition on predicted response.

The whole range in which each parameter may vary is not the same for all the model parameters; e.g., k_G^P could vary between 50 and 2500 (Table 4.3), while the value of ϕ_{cv} depends on the sand's mineralogy and for a given sand is essentially constant. Consequently, a $\pm 10\%$ variation on the model parameters does not represent the same proportion of the entire variation range of each parameter. Such a percentage of parameter variation cannot be used to establish, in general terms, the relative importance of a single parameter on the model response. Therefore, the study carried out here should only be regarded as indicative of the influence that a $\pm 10\%$ misjudgment on a specific parameter would induce in the predicted response under the studied loading condition.

The parameters used to predict the benchmark drained triaxial extension response under an isotropic consolidation stress of 100 kPa were essentially those used for capturing air pluviated Syncrude sand response. However, ϕ_f , R_F , and mp were slightly modified to allow a $\pm 10\%$ variation; e.g., R_F can only vary between 0 and 1, but since $R_F = 0.97$ (see Table 6.2), then $1.1 \cdot R_F = 1.067 > 1$! The values of the chosen parameters are $k_G^e = 210$; $v = 0.15$; $me = 0.5$; $k_G^P = 280$; $np = 0.5$; $\phi_{cv} = 32.1$; $\phi_f = 36$; $R_F = 0.9$; $F = 0.24$; $k_B^P = 200$; and $mp = 0.9$. The benchmark response is indicated in Figures 6.14a to l with a solid line for both maximum shear stress and volumetric strain vs. axial strain curves. The parameters were independently varied by $\pm 10\%$ in order to isolate the effect

in predicted response of each parameter. The thickest discontinuous line corresponds to the prediction made by using the benchmark parameters plus 10% (+10%) of the parameter indicated on Figures 6.14*a* to *k*. Similarly, the thinnest discontinuous line corresponds to the -10% prediction. The responses shown in Figure 6.14*l* correspond to the model's prediction when ϕ_f and ϕ_{cv} are simultaneously varied by $\pm 10\%$. As can be seen in Figure 6.14, the parameters that most significantly affect the predicted response under the chosen stress path and range of parameter variation are ϕ_f , ϕ_{cv} , R_F , and k_G^P . However, since ϕ_f and ϕ_{cv} can usually be derived from laboratory tests with a good degree of accuracy, k_G^P and R_F can then be confidently obtained from fitting the laboratory curves by successive approximations.

6.4 Summary

Calibration of the proposed constitutive model against Syncrude sand experimental data has been presented in this chapter. Two sets of model parameters were used to account for the difference in sand fabric ensued by the two methods (air and water pluviation) utilized for Syncrude sand deposition. The model was shown capable of capturing the effects induced by direction of loading as observed in triaxial compression, extension and simple shear tests. The model was found to somewhat overestimate the strains measured under undrained conditions at small stress ratios, i.e., before the critical stress ratio (CSR) is reached. However, since strains in the pre-CSR region are small compared to those after liquefaction is triggered (post-CSR region), the error induced on post-liquefaction displacements by overestimating strains in the pre-CSR region may be regarded as not significant for liquefaction analysis.

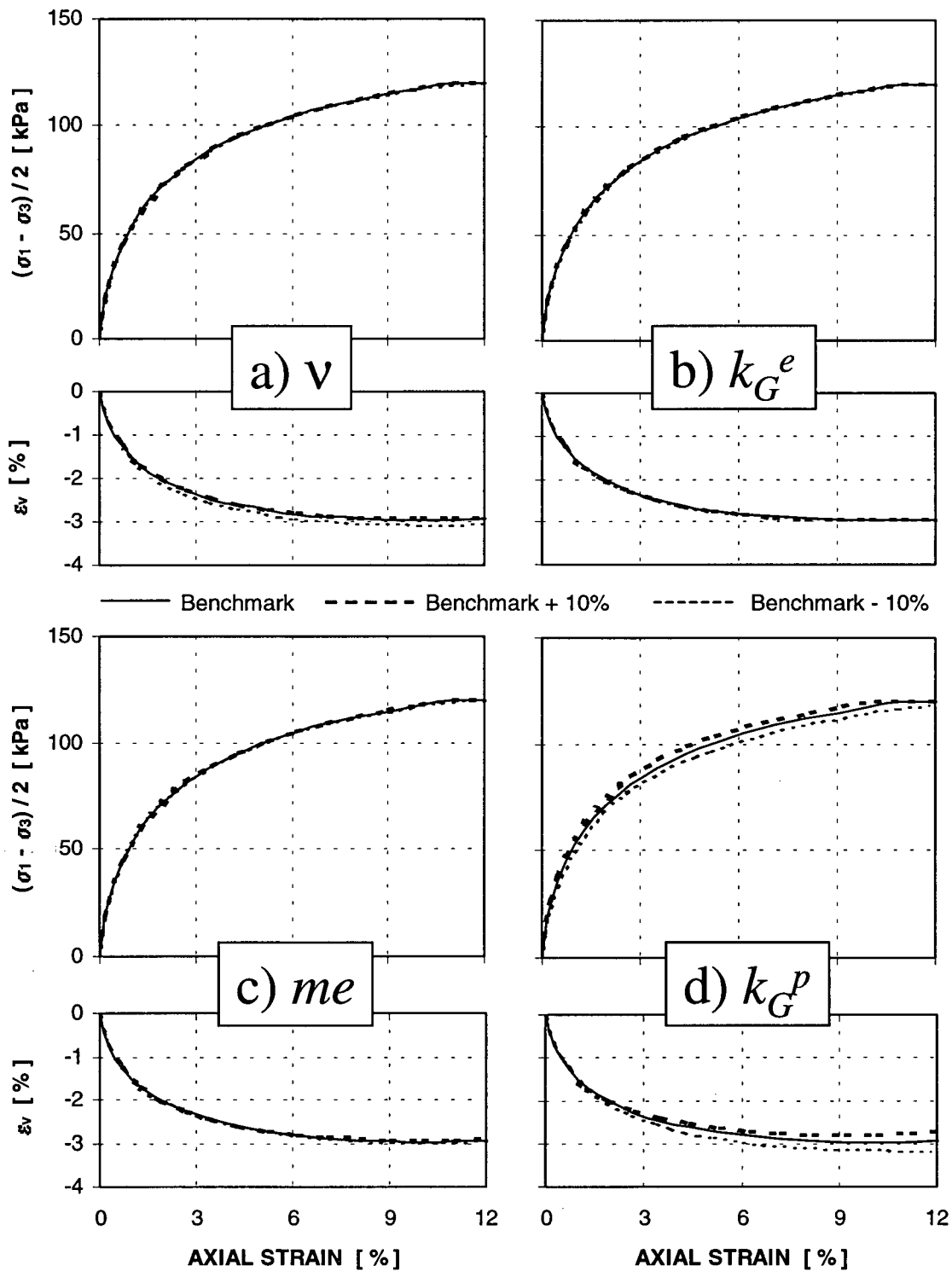


Figure 6.14 Sensitivity of predicted response to variation in the model parameters.

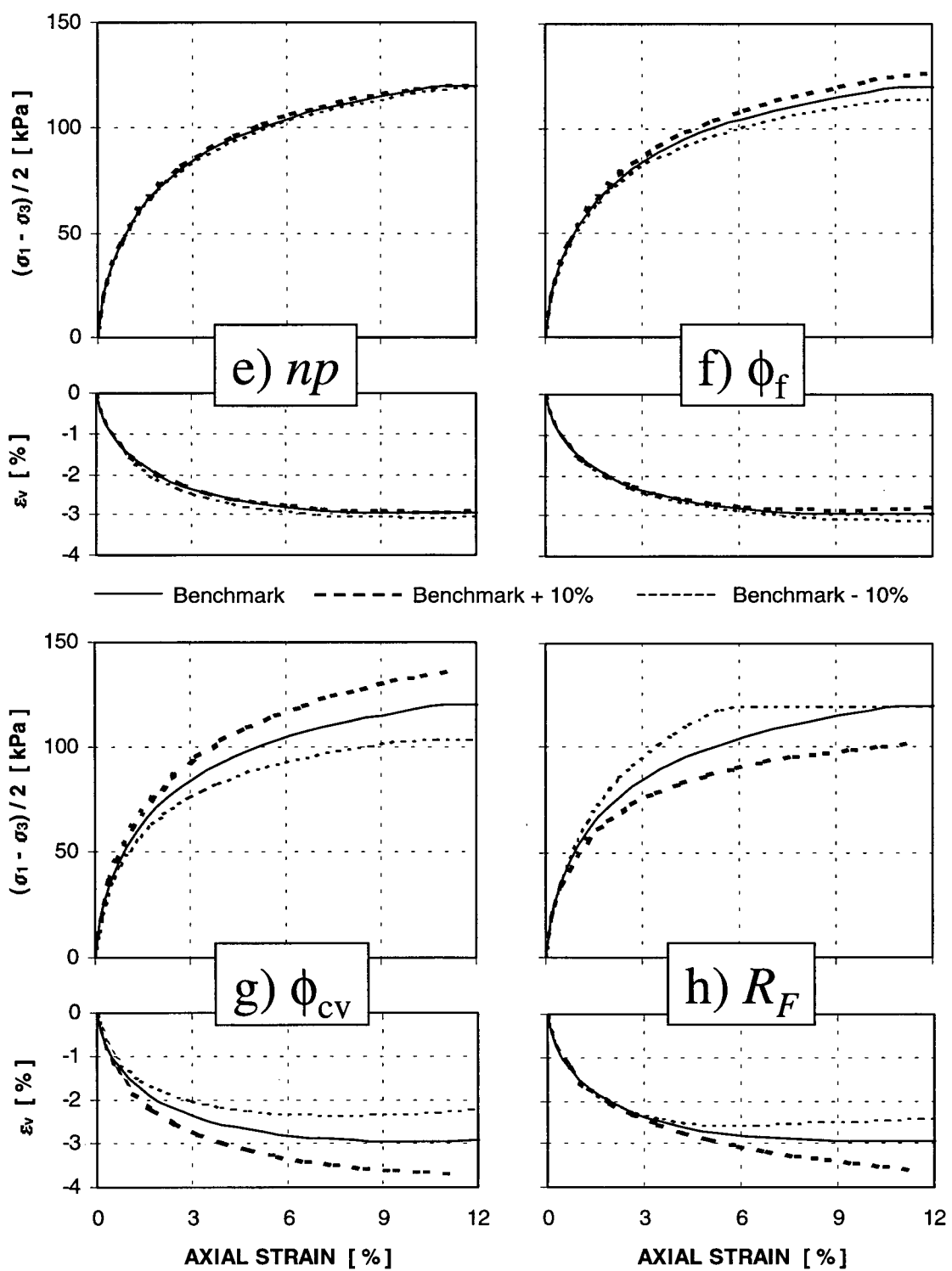


Figure 6.14 Continued.

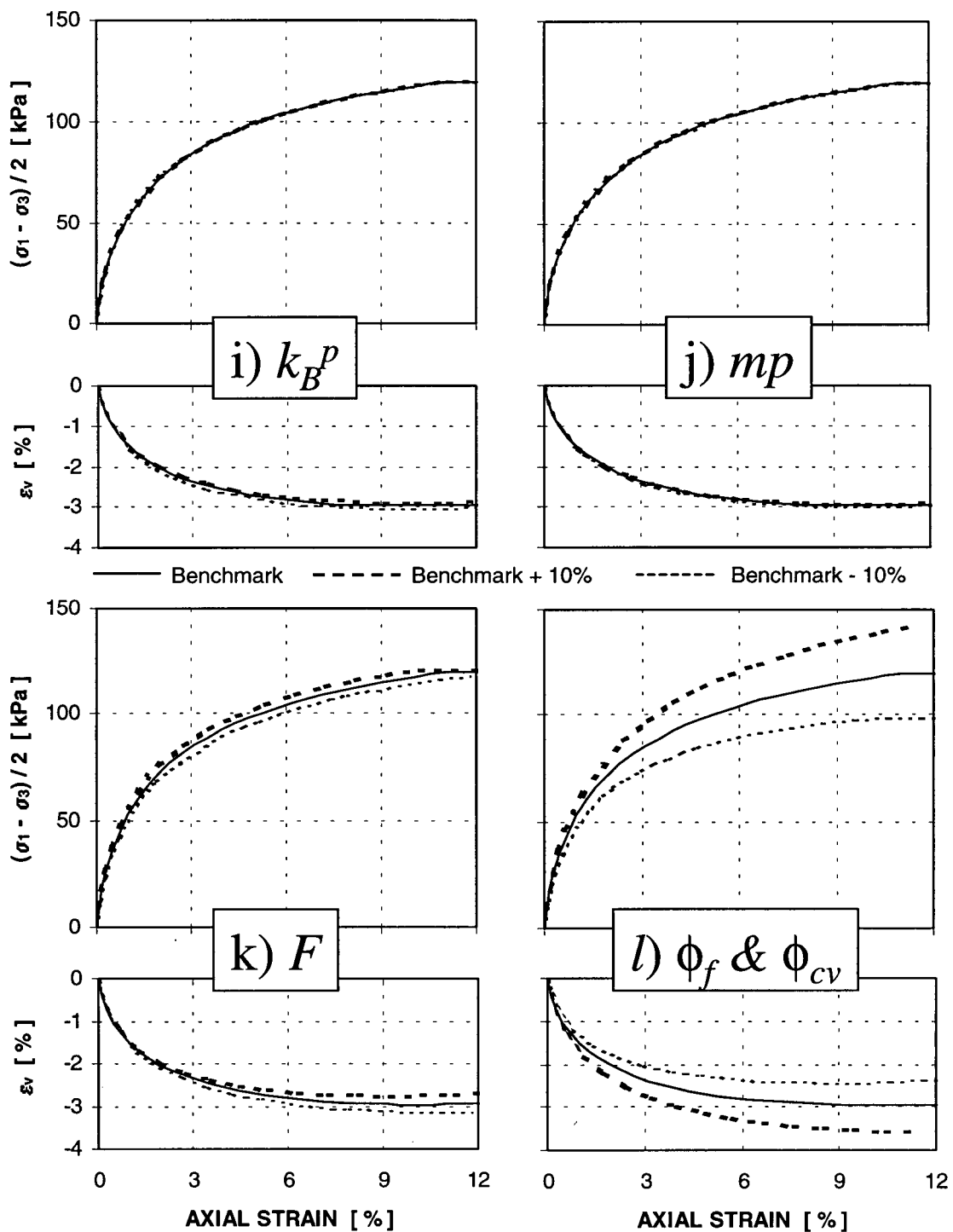


Figure 6.14 Continued.

The measured responses on air pluviated samples subjected to drained triaxial compression and constant volume simple shear tests were used for calibrating the model in order to capture air pluviated Syncrude sand (Phase-I) skeleton behaviour. The model parameters obtained from such calibration were then used for predicting undrained triaxial compression and extension tests carried out on air pluviated samples of Phase-I sand, isotropically consolidated to 50, 100 and 200 kPa. The model was shown capable of predicting the undrained characteristic behaviour observed in the tests. However, the procedure used for capturing the effects of continuous rotation of principal stresses did not fully account for such effects as they were observed in simple shear tests on anisotropically consolidated samples. Further improvement of the model in this area may be necessary.

Since the CANLEX centrifuge models were built with Syncrude sand (Phase-I) and by air pluviation, the constitutive model parameters obtained from this calibration are considered adequate for analysis of the CANLEX centrifuge test. This analysis will be presented in Chapter 7.

It must be noted that the constitutive model was calibrated against air pluviated Syncrude sand for stress levels ranging from 50 to 200 kPa. Such stress levels are considered representative of those in the centrifuge test once the physical model is under an acceleration field equivalent to 50 g. For instance, at mid-depth of the foundation layer the vertical effective stress, σ'_v , due to material self-weight ranges approximately from 45 to 140 kPa under 50 g. In contrast, σ'_v ranges from 0.9 to 2.8 kPa at 1 g (50 times less). Experimental data of Syncrude sand at such low levels of stress was not

available for calibrating the constitutive model. Hence, predicting the response of the centrifuge model during the swing up stage (increase in acceleration field from 1 g to 50 g) of the centrifuge test may be considered as out of the range for which the stress-strain model was calibrated. However, the swing up stage of the centrifuge test will be numerically modelled following a simplified approach to account for the circumstances mentioned above. Results of this analysis together with the numerical simulation of all other stages of the centrifuge test will be discussed in Chapter 7.

The behaviour of water pluviated Syncrude sand was captured by calibrating the constitutive model against undrained triaxial compression and extension tests carried out on water pluviated samples, isotropically consolidated to 50, 100, 200 and 400 kPa. The model parameters obtained from such calibration compared well with estimations of the elastic shear and bulk moduli, G^e and B^e , respectively, derived by using available field test data from the CANLEX field event site. To further verify the validity of the model parameters, the model response predicted in simple shear was directly compared with the range of measured response in simple shear on undisturbed (in-situ frozen) samples of Syncrude sand (Phase-III) obtained from the field event site. The predicted response was closer to the lower bound of measured response, but well within the measured range. In addition, undrained triaxial and plane strain extension tests carried out in the HCT device on water pluviated samples that were anisotropically consolidated to the in-situ (field event site) void ratio, were modelled. Reasonable agreement was found between measured and predicted response in these tests. Hence, the parameters obtained from calibrating the constitutive model against water pluviated Syncrude sand experimental

data are considered adequate for carrying out the analysis of the CANLEX field event.

This analysis will be presented in Chapter 8.

CHAPTER 7

CENTRIFUGE MODELLING

As part of the CANLEX project, a number of centrifuge tests were carried out to investigate the static liquefaction potential of embankments on very loose saturated sand layers. These tests were performed to serve as models to help design the CANLEX field event and to provide a database from which numerical models could be calibrated. The tests are described in detail by Phillips and Byrne (1993 and 1994).

Centrifuge modelling fundamentals were presented and discussed in detail by Schofield (1980). The basic assumption made is that the stress field acting on an earth-structure is essentially due to self-weight of the materials comprising such a structure. Hence, the stress field on a real problem can be reasonably reproduced on a scaled model of the prototype by increasing the gravity acceleration in the same proportion as the geometric ratio, n_g , between model and prototype. If the boundary and loading conditions of a given problem were known, a centrifuge model could be designed according to those conditions. Such a model would be capable of simulating the behaviour of a corresponding prototype structure with good degree of accuracy. In terms of flow, the consolidation time in the scaled model is $(n_g)^2$ times less than in the

prototype structure. To delay the rate of pore pressure dissipation in the scaled model it is common practice in centrifuge modelling to use oil as fluid instead of water.

The CANLEX field event will be described in Chapter 8, but in order to explain the CANLEX centrifuge models a few characteristics of the field test will be mentioned here. The event is described in detail by Byrne et al. (1995b) and Robertson et al. (1996). The purpose of the full-scale event was to statically trigger a liquefaction flow slide by rapidly loading a loose saturated sand deposit. The loose and saturated sand deposit, 10 m deep, served as a foundation for an 8 m high clay dyke that was built slowly to ensure drainage of the sand during the construction process. Subsequent rapid loading was accomplished by pumping tailings behind the clay dyke.

The idea of rapidly loading an embankment that is resting on a 10 m loose saturated sand layer was replicated in the centrifuge model. However, the manner in which load was brought about differed from the procedure that was used in the field. Instead of pumping tailings behind the scaled dyke in the centrifuge tests, loading was accomplished by gently placing two steel plates on the crest of the model embankment (see profile of centrifuge model in Figure 7.1). In the following, details of Test 1 (Phillips and Byrne, 1994) will be given.

7.1 Centrifuge Test 1

Test 1 (Phillips and Byrne, 1994) was chosen for detailed description and analysis because it resembled the proposed field event most closely. A profile of the model test embankment is shown in Figure 7.1. The sand model was first built in a strongbox by air pluviating Syncrude Phase-I sand. Thus, during construction, the model in the laboratory

was only under the gravity acceleration field. The model was instrumented with five pore pressure transducers, PPT1 to PPT5, and two displacement transducers, LDT18 and LDT19, as shown in Figure 7.1. Subsequently, vacuum was applied to the model and saturation was attempted by allowing Canola oil to flow into the base of the strongbox that contained the sand model. Canola oil was chosen as pore fluid to delay the rate of pore pressure dissipation, which in turn was necessary to promote an undrained type of response during the loading stage (Phillips and Byrne, 1993). After the saturation period, Phillips and Byrne (1994) estimated from the average settlements of the crest and toe plane of the slope that the average relative density of the model was 13%.

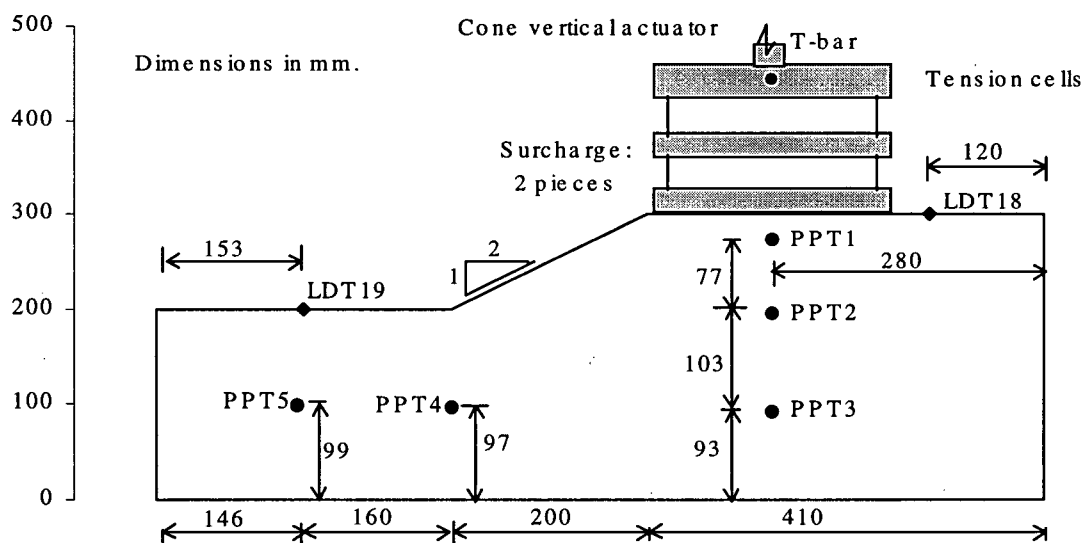


Figure 7.1 Initial centrifuge model and instrumentation configuration (after Phillips and Byrne, 1994). All dimensions and vertical scale in mm. PPT, pore pressure transducer; LDT, longitudinal displacement transducer.

During a first stage termed *swing up*, the strongbox was lifted and spun by the centrifuge device, causing the acceleration field to increase from 1 g to 50 g. The acceleration field was brought about in five gradual increments of 10 g each with allowance made for pore pressure dissipation by staging the increments at three minutes

intervals. During each 3-min period, the excess pore pressures induced by the increase in the acceleration field were dissipated to avoid premature failure of the system during self-weight compression. The average relative density in the sand model changed during the swing up stage from 13% to 29% (Phillips and Byrne, 1994), indicating large volumetric changes. These were expected since the effective stresses were increased by about a factor of 50 as a result of increasing the acceleration field from 1 g to 50 g. Under an acceleration field of 50 g the model structure corresponds to a 10 m depth of target layer supporting a 5 m high embankment.

While in flight and under an acceleration field of 50 g, a steel plate was gently placed on the crest of the slope. The weight of the steel plate subjected the embankment to a pressure of 60 kPa, which in turn corresponded to a loading of about 3.5 m of Syncrude sand tailings. Shortly after application of the first load, a second steel plate was gently placed, adding another 60 kPa to the load applied on the crest. Thus, the loading was equivalent to the rapid application of 7 m of soil over a 10 m target layer and hence had similarity with the field event.

The response of the centrifuge model to self-weight compression in terms of both, pore pressure and displacements is shown in Figure 7.2. During the swing up process, PPT1 became desaturated and PPT5 broke (Phillips and Byrne, 1994). The pore pressure time-histories as registered by the remaining transducers, i.e., PPT2 to PPT4, are presented in Figure 7.2a. Displacements of about 12 and 4 mm were measured by LDT18 and LDT19, respectively, and the displacement time-histories are shown in Figure 7.2b. A consistent pattern between pore pressures and displacements at each acceleration increment can be observed in these figures.

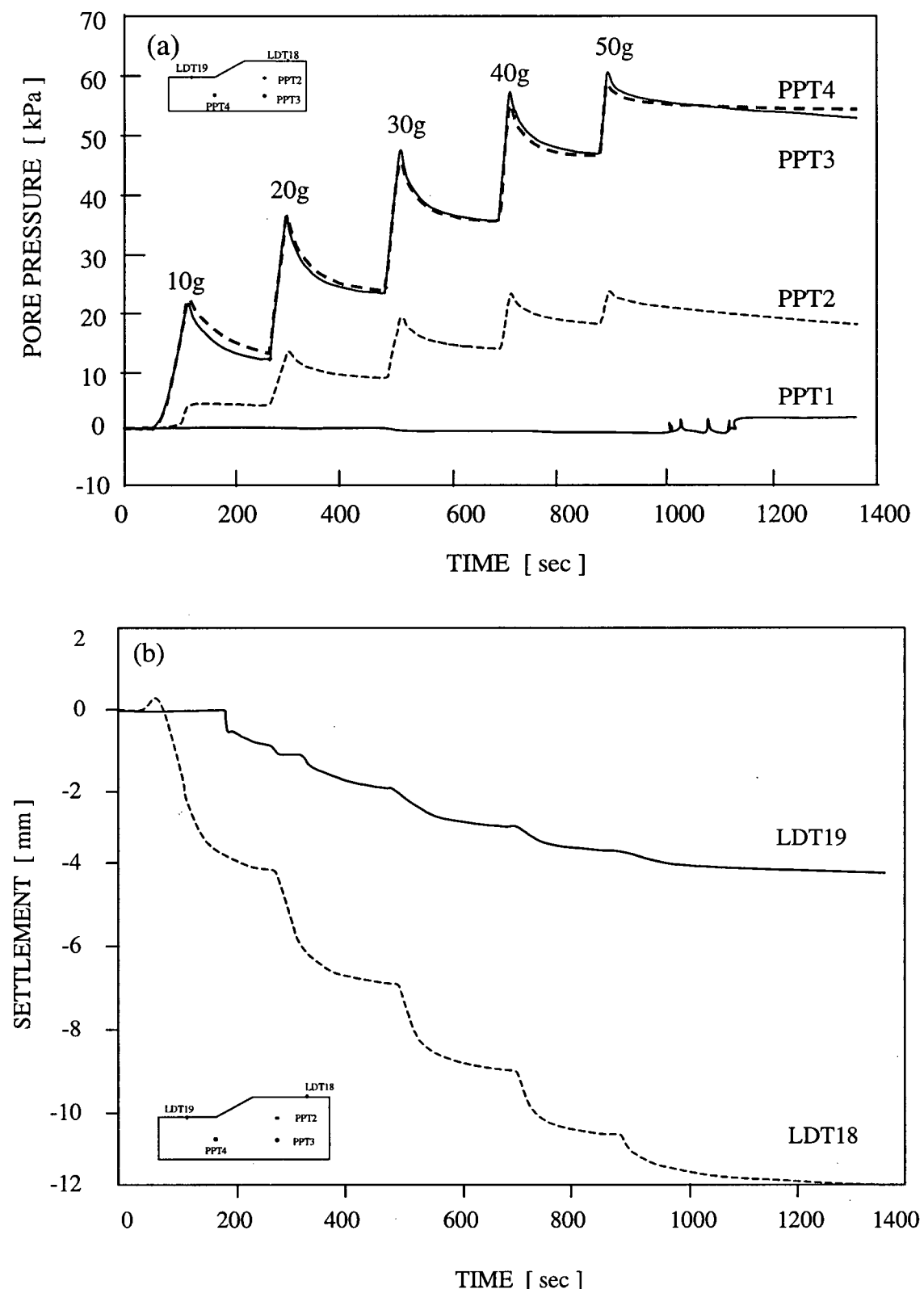


Figure 7.2 Measured response of centrifuge model during swing up (after Phillips and Byrne, 1994). (a) Pore pressures. (b) Surface settlement at monitored points.

Figure 7.3 shows the response of the centrifuge model to loading. It may be seen that pore pressure transducers PPT2 and PPT3, which were located directly beneath the load, registered sharp increases in pore pressure followed by rapid drops under each of the loading increments (Figure 7.3a). However, a very different pore pressure response can be noted below the toe of the slope, as registered by PPT4. Here, the pore pressure rose rapidly but remained almost unchanged with application of the second load increment.

The vertical movements recorded by LDT18 (on the crest) and LDT19 (in the toe area) are shown in Figure 7.3b. LDT18 indicated that the crest settled 4.3 mm under the first load and continued to deform upon the second load up to 6.7 mm. Scaled to 50 g, these settlements correspond to 0.215 m and 0.335 m, respectively. In contrast, LDT19 showed upward movement of about 3 mm, or 0.15 m scaled to 50 g. Nevertheless, Phillips and Byrne (1994) pointed out that from the video filmed while the centrifuge test was being carried out, further heave of the toe was observed. In fact, once the test had finished, the pad under LDT19 was found 5 to 10 mm below the sand surface. Phillips and Byrne (1994) concluded that the additional heave might have been compensated by penetration of this LDT pad into the sand.

The Toe displacement was determined by comparing the initial profile of the model with the profile that the embankment attained at the end of the test. The comparison showed that the Toe moved a distance of 40.7 mm in the horizontal direction as result of loading (Phillips and Byrne, 1994).

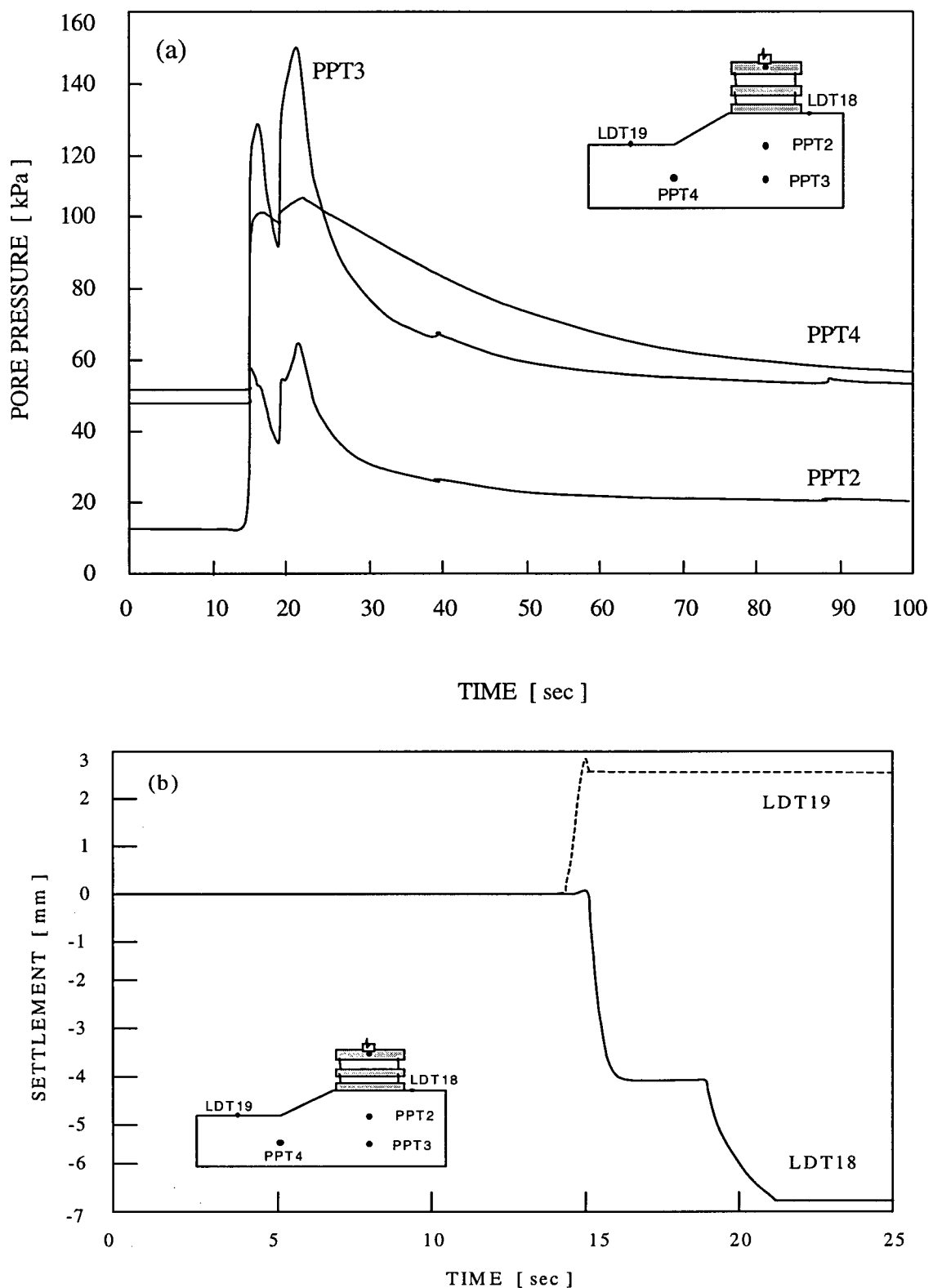


Figure 7.3 Measured response of centrifuge model to loading (after Phillips and Byrne, 1994). (a) Pore pressures. (b) Surface displacements at monitored points.

As illustrated in Figure 7.1, the two steel plates that comprised the loading were suspended from four cables. The rate at which the tension in the cables changed as the loading process took place is shown in Figure 7.4. From this figure, the first loading increment was estimated to last between 1.0 to 1.91 sec, while the second increment lasted approximately 1.94 sec. The period elapsed between the two loading increments was estimated to be 2.6 sec. These periods were considered essential information for analyzing the centrifuge test since the response to loading of the system greatly depended on the relationship between the rates of loading and pore pressure dissipation.

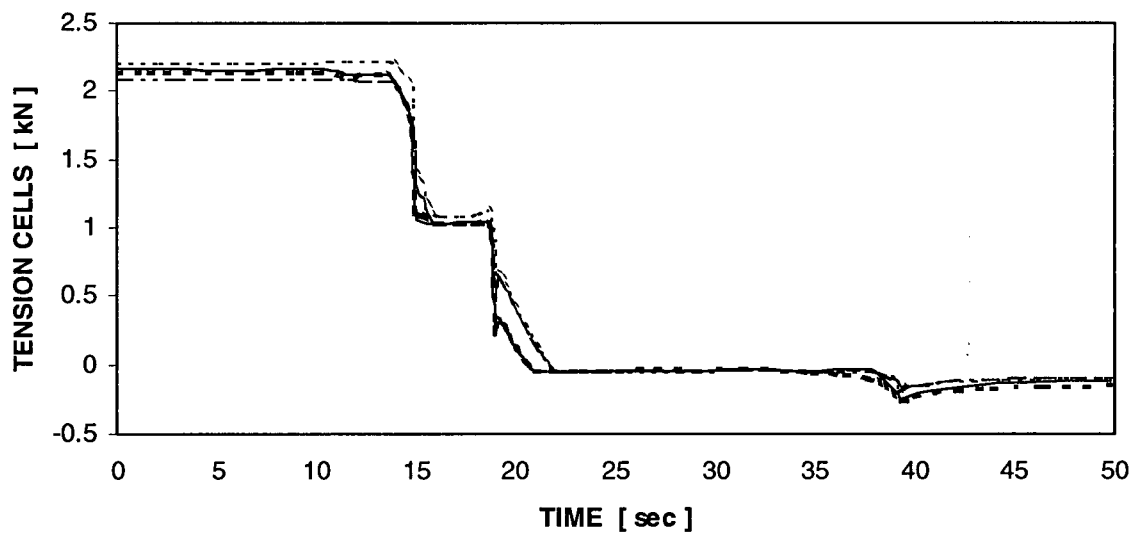


Figure 7.4 Suspended load during centrifuge test loading (after Phillips and Byrne, 1994).

The pattern of displacements observed after the first load was applied but prior to application of the second load is shown in Figure 7.5. The pattern is deep seated.

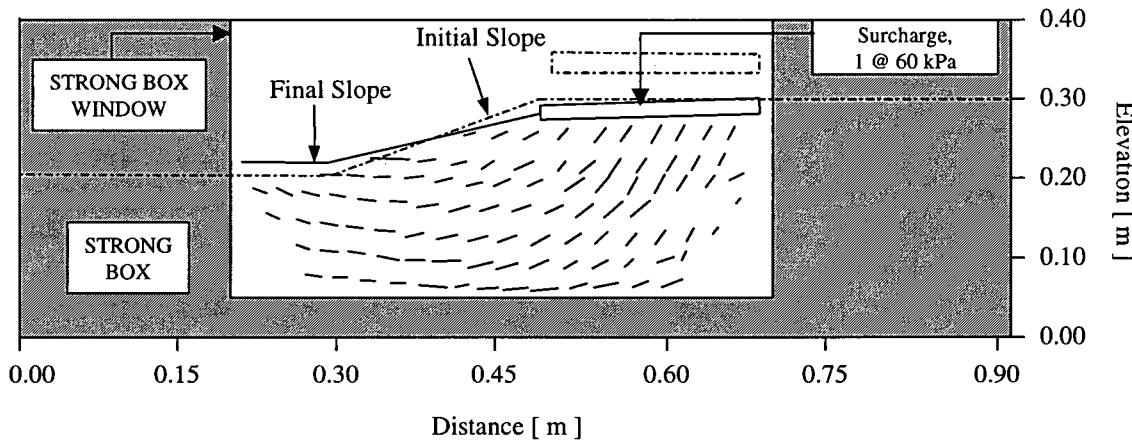


Figure 7.5 Pattern of displacements observed in centrifuge model after the first load was applied (modified from Phillips and Byrne, 1994).

7.2 Sand in centrifuge model vs. sand specimens used for laboratory testing

As discussed in Section 6.2, to carry out the numerical analysis of the centrifuge test the constitutive model was calibrated against Syncrude Phase-I sand data from tests performed on air pluviated specimens. Although the same soil and pluviation techniques were used in building the centrifuge model, the fluid in the laboratory specimens and in the centrifuge model was not the same. Furthermore, before discussing the numerical analysis it is important to point out that:

- The centrifuge model had a relative density of about 13% before the swing up process took place, and of about 29% at the end of it (Phillips and Byrne, 1994).
- The element tests that served as basis for calibrating the constitutive model were performed at relative densities significantly greater, i.e., 37% on average, and confining stresses ranging from 50 to 200 kPa.
- The stress levels in the centrifuge model under an acceleration field of 1 g were very low, although they gradually increased as the swing up process advanced.

- Laboratory data at such low levels of stress was not available, and hence, there was no direct way for calibrating or even testing the constitutive model performance under those conditions.
- The permeability of Syncrude sand to Canola oil as determined in the laboratory was $k = 3.25 \times 10^{-7}$ m/sec, at a relative density of 40% (Phillips and Byrne, 1993). Assuming this value as independent of void ratio would not be realistic.

To account for these differences a very simplified approach was followed and it will be explained in a later section, when discussing the initial state of stress (Section 7.5.2).

In addition to the points mentioned above, the degrees of saturation in the centrifuge model before and after the swing up process were not determined but simply assumed based on visual observation of the phreatic oil surface position. From the analysis viewpoint, this is an important piece of information since the response of the system to be analyzed could be entirely different depending on whether full or partial saturation is considered. Assuming full saturation of material below the phreatic surface is not necessarily accurate, particularly when the sand was initially placed dry and the fluid used to later flood the system was oil rather than water. In fact, sand specimens tested in the triaxial chamber at C-CORE were not fully saturated, but no explanation was given in the C-CORE report (Phillips and Byrne, 1993) to this matter. Nevertheless, if full saturation of triaxial specimens was not achieved, it is not likely that the centrifuge model would have been saturated either.

As can be seen in Figure 7.6, the degree of saturation has a strong influence in the undrained response to loading. In this figure, the undrained response observed in a triaxial compression test at a confining stress of 100 kPa is compared with two different predictions of the model. The thick line corresponds to the model's prediction in which partial saturation of the specimen was considered according to the Skempton B value reported in the laboratory test ($B_{skem} = 0.91$). The thin line corresponds to the predicted response at constant volume ($B_{skem} = 1.0$).

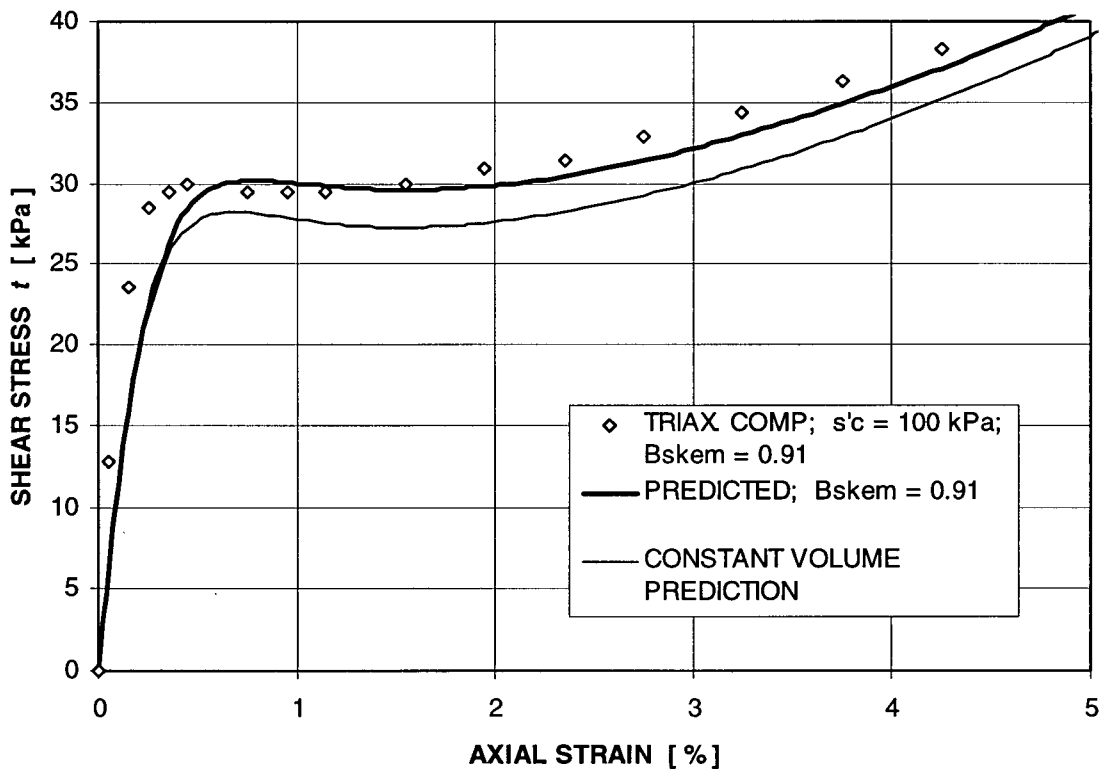


Figure 7.6 Element response in undrained triaxial compression under partially and fully saturated conditions.

In this respect, the centrifuge model was assumed to have the same degree of saturation as the sand samples tested in the laboratory.

7.3 Boundary conditions assumed for numerical analysis of centrifuge model

The boundary conditions on the model were assumed as follows: zero horizontal displacements on the vertical boundaries and zero vertical displacements on the bottom horizontal boundary, as shown in Figure 7.7. The oil table was assumed horizontal and coinciding with the surface of the target layer.

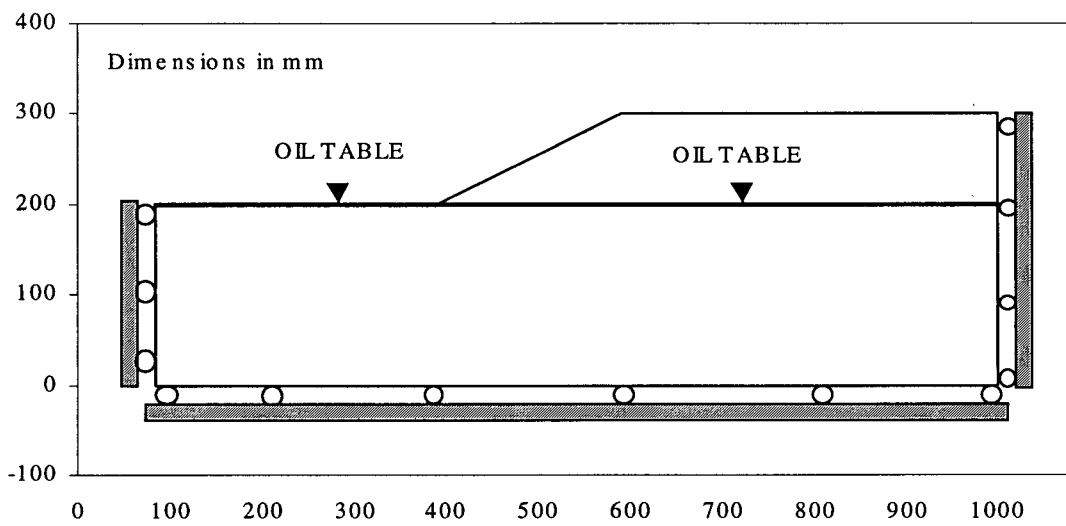


Figure 7.7 Boundary conditions used for numerical simulation of centrifuge test. Scales in mm.

7.4 Numerical simulation of centrifuge model construction

The numerical model was first brought to equilibrium under an acceleration field of 1 g and dry conditions, just as in the actual centrifuge test. Then, the effect of raising the oil table to the surface of the target layer was accounted for by prescribing a hydrostatic distribution of pore pressures and using different densities of the sand above and below the oil table. In accordance with laboratory data (Phillips and Byrne, 1993), the total and dry densities of Syncrude sand were taken as 1.87 T/m^3 and 1.45 T/m^3 , respectively. The fluid density was taken as 0.91 T/m^3 . The constitutive model parameters used for this

part of the analysis were those obtained from the model's calibration against element tests on air pluviated specimens and were listed in Table 6.2.

7.5 Initial state of stress under an acceleration field of 50 g

The initial state of stress is a very important factor in determining the response to loading of a system, particularly under undrained conditions. For instance, two states of stress in which the major principal stresses are the same, but the minor different, are represented by k_{c1} and k_{c2} in Figure 7.8. Undrained loading from these two conditions would induce different amounts of pore pressures, Δu_1 and Δu_2 . In addition, the increases in deviator stress, $\Delta \sigma_{d1}$ and $\Delta \sigma_{d2}$, required to reach the undrained peak strength are also different. In terms of liquefaction, this could be a decisive factor in predicting liquefaction occurrence and the correct magnitude of pore pressures. For this reason, the initial state of stress due to self-weight under an acceleration field of 50 g was obtained considering two drainage conditions: 1) fully drained, and 2) partially drained. Their effects in predicting the response of the centrifuge model to loading will be discussed in Section 7.8.3.

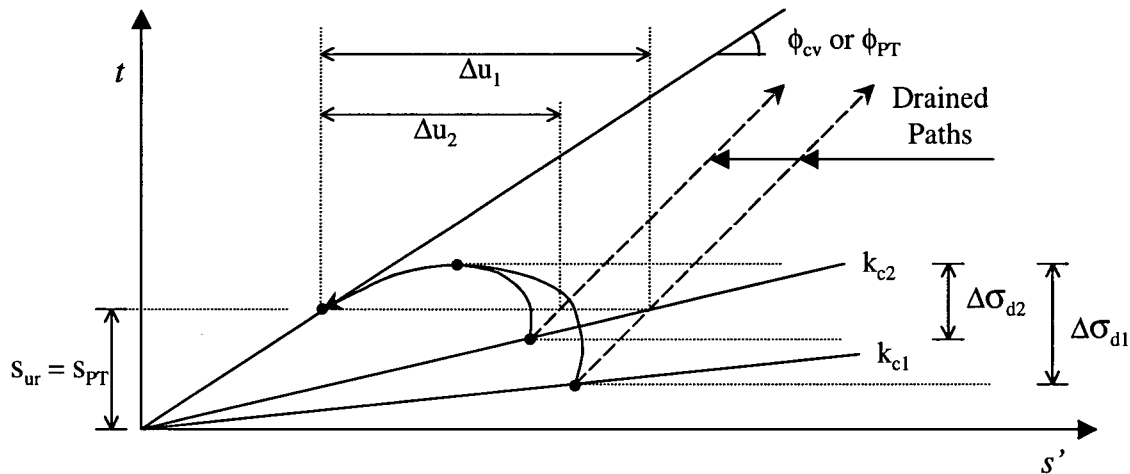


Figure 7.8 Effect of initial state of stress in undrained response.

7.5.1 Initial state of stress from assuming fully drained response

In this first case, rather than modelling the gradual building up of stress during swing up, effective stresses were computed by assuming a fully drained response while the acceleration field was changed from 1 g to 50 g. Once the construction of the centrifuge model was simulated as explained in Section 7.4, the fluid stiffness was prescribed as zero. This in turn, allowed computation of the state of stress under an acceleration field of 50 g without generating excess pore pressure as the equilibrium state of the system was reached. This is equivalent to a fully drained condition.

The aim of this analysis was to obtain the initial state of stress without giving importance to the accurate prediction of displacements since the effect of induced pore pressure was not accounted for by assuming fully drained conditions. Hence, the constitutive model parameters used in the analysis were those obtained from the model's calibration and listed in Table 6.2. The initial state of stress obtained through this numerical procedure was characterized by the ratio $1/k_c = \sigma'_h / \sigma'_v$ attained at the three monitored points corresponding to the location of the pore pressure transducers PPT2, PPT3, and PPT4. The $1/k_c$ ratios were termed k_{c2} , k_{c3} , and k_{c4} , and their computed values were 0.55, 0.56, and 1.42, respectively. These values will be used for comparison and discussion in the following section.

7.5.2 Initial state of stress from assuming partially drained response

In this second case, the gradual building up of stress during swing up was modelled using a coupled stress-flow approach of analysis together with the following procedure:

- 1) The state achieved under an acceleration field of 1 g and oil table at the surface of the target layer was previously explained and will not be repeated here.
- 2) The process of increasing the acceleration field from 1g to 50 g in the centrifuge experiment was numerically followed with a small variation. In the actual test, each increment of 10 g was applied gradually. For ease of analysis, in the numerical simulation each 10 g increment was subdivided into ten smaller increments of 1 g each. The numerical procedure was tied to the time elapsed in the centrifuge experiment during each 10 g acceleration increment and it is schematically shown in Figure 7.9. Coupled stress-flow computations were carried out during the whole process of gravity acceleration increase. Hence, the computed response of the system accounted for the effects of both the excess pore pressure induced by increasing the acceleration field, and the capacity of the system to dissipate pore pressure.
- 3) In accordance with the periods for pore pressure dissipation in the centrifuge test, coupled stress-flow analysis was continued under a constant acceleration field during the same intervals as in the actual test (see Figure 7.9).

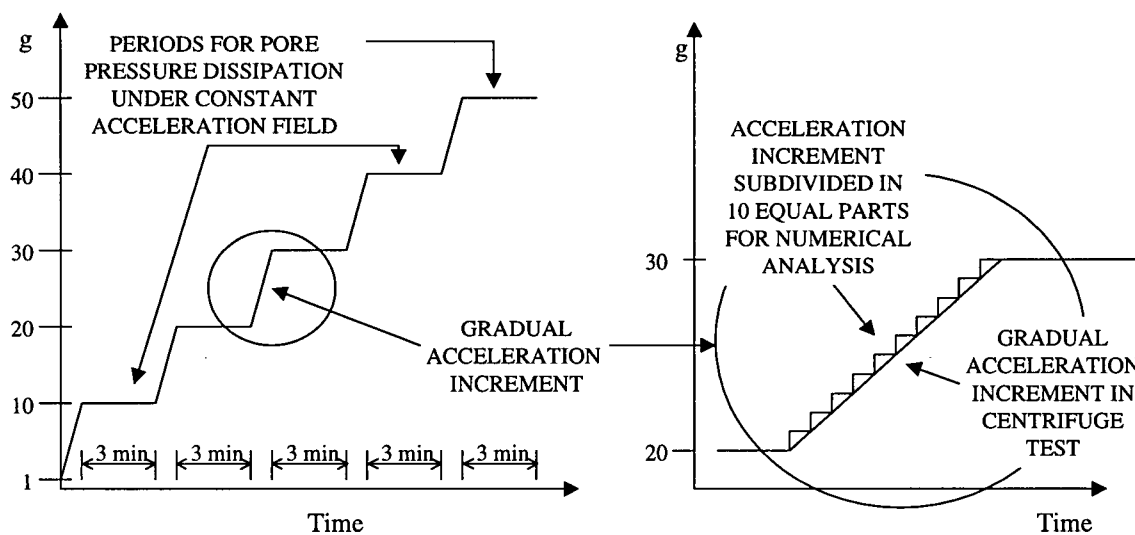


Figure 7.9 Gradual increase of the acceleration field in the centrifuge test.

The aim of this analysis was not only to obtain the initial state of stress but also to accurately predict pore pressures and displacements during the swing up stage of the centrifuge experiment. For this reason, the characteristics of the sand comprised in the centrifuge model had to be accounted for by adjusting the model parameters in accordance to the conditions discussed in Section 7.2. A very simplified approach was followed to accomplish this task and it will be explained in the following paragraphs.

In the C-CORE laboratory report by Phillips and Byrne (1993), they indicated that the permeability of Syncrude sand to Canola oil could be normalized to a relative density of 40% as follows:

$$[7.1] \quad k \propto \frac{e^3}{1+e}$$

where e is the void ratio.

On the other hand, it is commonly assumed that the elastic moduli vary in proportion with $(2.17-e)^2/(1+e)$, Yu and Richart (1984), and Iwasaki and Tatsuoka (1977).

The relative density at each stage of the swing up process was unknown. However, making a crude assumption, it was considered to vary linearly from 13% at 1g, to 29% at 50 g. Under this crude assumption, estimations of the void ratio e at the beginning of each stage of the swing up process were made. The values of permeability and moduli numbers were then adjusted accordingly with the relationships discussed above, although it is recognized that there is no evidence to assume the plastic and elastic moduli varying with density in the same proportion. The adjusted values of such parameters are shown in Table 7.1. The rest of the model parameters were listed in Table 6.2.

Table 7.1 Parameters used for modelling the centrifuge model swing up according to the assumed relative density on each stage of the swing up process.

Gravity [m/s ²]	1g	10g	20g	30g	40g	50g
D_r [%]	13	15.9	19.2	22.5	25.7	29
k_B^p	189	194	200	206	212	218
k_G^e	165	170	175	180	185	191
k_G^p	223	229	236	243	250	258
k [m/s]	4.61E-07	4.45E-07	4.27E-07	4.10E-07	3.93E-07	3.77E-07

Results obtained from the coupled stress-flow analysis of the swing up stage, in terms of pore pressures and displacements are compared in Figure 7.10 with measurements taken during the test at the monitored points. As can be seen in this figure there is resemblance among the traces of predicted and measured pore pressure time-histories, as well as displacement time-histories. However, the measured displacements were larger and the observed rates of pore pressure dissipation were slower. A more detailed discussion in terms of pore pressures will be presented in the following. For ease of discussion, an increment in the acceleration field will be referred to in this particular section simply as *increment*, unless otherwise indicated, and it will be written in *Italics* to avoid confusion.

In Figure 7.10a, it can be observed that the peak pore pressure values at PPT3 and PPT4 were reasonably well predicted with the exception of the last *increment*, in which the peak value at PPT3 was overestimated. At PPT2, the peak pore pressure was overpredicted for the first *increment*, very well captured in the second one and underestimated for the rest of the *increments*. It is considered fair to say that prediction of pore pressures at PPT2 was a difficult task since this point was located right below the fluid boundary (oil table). Nevertheless, the rate of predicted pore pressure dissipation was greater than the one observed in the test for practically all cases.

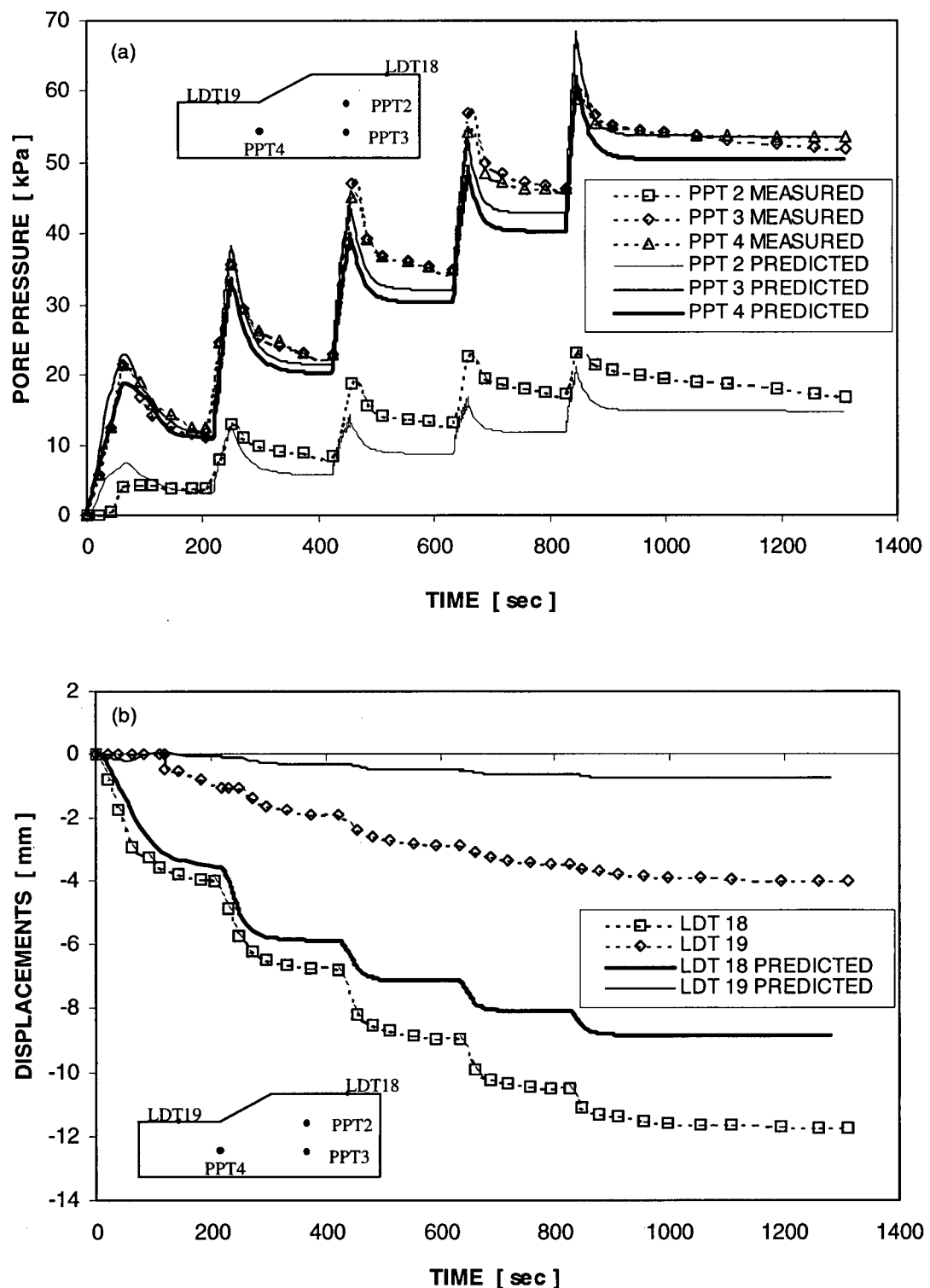


Figure 7.10 Comparison between measured and predicted response of centrifuge model during swing up. (a) Pore pressures. (b) Surface settlement at monitored points.

As can also be noted in Figure 7.10a, the measured excess pore pressures did not completely dissipate during the 3-min periods given in the test between *increments*. However, the minimum values measured after each 3-min period were consistently greater than the hydrostatic pressures that would correspond to the initial positions of the pore pressure transducers (PPT's). This indicated that the PPT's settled during the swing up process. Settlement of the PPT's might explain why the predicted equilibrium values of pore pressure under constant acceleration fields were consistently lower than the minimum values measured after each 3-min period. In fact, the predicted equilibrium pore pressures coincide for practical purposes with the hydrostatic values that correspond to the original position of the PPT's.

Good agreement between predicted and measured values was not really expected in this case since critical parameters, i.e., permeability and both elastic and plastic moduli were based on simplistic assumptions. Results from the analysis show that the assumptions made were rather crude. In the absence of more specific data, the analysis could only be refined by a tedious trial and error procedure.

Considering the limitations faced in modelling the swing up process, it is the author's opinion that both, constitutive model and analysis procedure, appeared appropriate for capturing the essence of the problem. Lack of accuracy was rather due to insufficient data for properly calibrating the model than inadequacy of the numerical implementation. Further study on this type of problem is necessary and recommended in order to verify the suitability of the constitutive model and numerical procedure for this kind of analysis.

The initial state of stress obtained by this numerical simulation of the swing up stage was also characterized by the ratio $1/k_c = \sigma'_h / \sigma'_v$. As in the case in which fully drained response of the target layer was assumed, the three monitored points chosen for comparison between both states of stress were those corresponding to the location of the pore pressure transducers PPT2, PPT3, and PPT4. A comparison among the computed $1/k_c$ ratios from both analyses and the value of $1/k_c$ at failure is presented in Table 7.2.

Table 7.2. Comparison among $1/k_c = \sigma'_h / \sigma'_v = k_{ci}$ ratios at the monitored points of the centrifuge model, as obtained under an acceleration field of 50 g by considering two different conditions for analysis: fully, and partially drained.

TYPE OF ANALYSIS	k_{c2}	k_{c3}	k_{c4}	$(k_c)_{FAILURE}$
FULLY DRAINED CONDITIONS	0.551	0.556	1.418	0.285
PARTIALLY DRAINED CONDITIONS	0.321	0.320	0.813	0.285

As can be seen in Table 7.2 the states of stress rendered by both analyses are significantly different. The analysis in which fully drained conditions were assumed yielded greater horizontal stresses than those predicted by accounting for partial drainage. Furthermore, the horizontal stress predicted under the toe of the slope for fully drained conditions was greater than the vertical stress ($k_{c4} > 1$). In contrast, the coupled stress-flow analysis predicted a state of stress under the toe of the slope in which the vertical stress was greater than the horizontal ($k_{c4} < 1$). Moreover, the k_{ci} values presented in Table 7.2 indicate that the states of stress predicted under partially drained conditions are closer to the failure condition ($k_c)_{FAILURE}$ than the states of stress predicted assuming a fully drained response. It is commonly assumed in engineering practice that the initial

state of stress in the field corresponds to that of the 1-D consolidation condition, the $k_0 = 1 - \sin\phi$ (Jaky, 1944) condition. For this case, Jaky's condition yields $k_0 = 0.44$, but such condition is not applicable to the centrifuge model due to the presence of the slope.

To avoid failure of the centrifuge model during swing up, 3-min periods for excess pore pressure dissipation were allowed after each increment in the acceleration field (see Figure 7.2a). Thus, the state of stress that was actually achieved in the centrifuge model after the swing up stage took place was not considered to be close to the failure condition. Furthermore, the state of stress obtained through numerical analysis by assuming partially drained conditions during the swing up stage was achieved basing the model parameters on simplistic assumptions. Hence, it was concluded that the stress state yielded by assuming fully drained response during the consolidation stage was more realistic. As mentioned previously, the state of stress from which the response of the centrifuge model to subsequent loading is predicted could strongly influence the predicted response. A discussion in this respect will be presented when analyzing the loading stage under partially drained conditions (Section 7.8.3).

7.6 Numerical procedure used to simulate loading of the centrifuge model

As explained at the beginning of this chapter, the loading stage in the centrifuge test was accomplished by gently placing two steel plates on the crest of the model embankment (see profile of centrifuge model in Figure 7.1). Placement of the steel plates comprising the loading in the centrifuge test was simulated by adding a row of elements on the crest of the slope, as shown in Figure 7.11. Modelling the steel plates in this manner allows consideration of their stiffness and hence, the soil-structure interaction between sand and

steel. Since the time-step used by FLAC depends on the stiffness of the elements, using the actual stiffness of steel causes FLAC to converge very slowly. For this reason, an investigation was carried out to determine a stiffness ratio between “sand” and “steel” elements that would properly capture the soil-structure interaction and at the same time would allow converging rapidly. It was found that a stiffness ratio of 10 gave reasonable results, i.e., stiffness ratios > 10 took longer to converge, but render the same response.

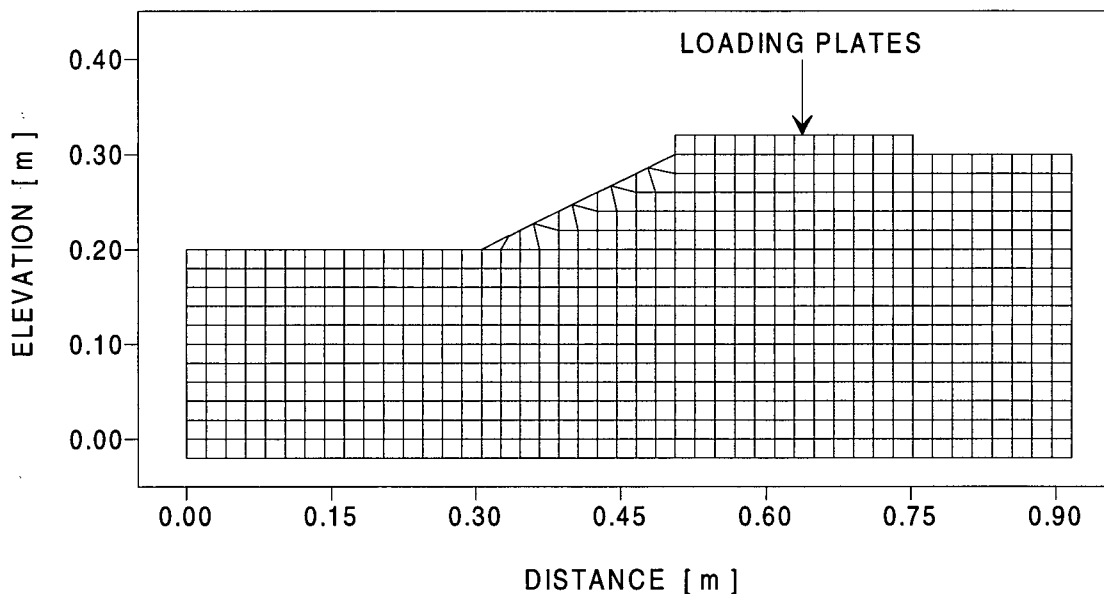


Figure 7.11 Grid used to simulate the centrifuge model and loading plates.

In addition, by modelling the steel plates in this manner the load can be applied instantaneously or gradually by modifying the density of the elements in the top row. This is a fundamental factor in modelling the loading stage because of two reasons:

- From the physics viewpoint, it is not the same to suddenly apply a large load than to apply it monotonically. Sudden application of a large load could induce inertia effects into the system that would not necessarily be present in the real structure.

- From the liquefaction perspective, the rate of loading is an essential element for predicting the response of a system to such load. If the rate of loading were slower than the rate of pore pressure dissipation, a drained type of response would be predicted and liquefaction would not be anticipated. In contrast, if the rate of loading were higher than the rate at which pore pressure could dissipate an undrained type of response would be expected and liquefaction could be triggered.

Two different types of numerical analyses were carried out to simulate the loading stage of the centrifuge test: 1) undrained, and 2) coupled stress-flow. For the case of undrained analysis, the loading process and the response of the system do not take place in real time, but computational time. However, gradual application of loading is important to avoid shocking the system. Furthermore, in modelling coupled stress-flow problems, a procedure to apply gradual loading is essential to replicate the rate of loading that occurs in the modelled system.

The modelling procedure used for simulating loading was as follows:

- 1) Given that the loading plates were suspended from four cables, the rates at which the tension in the cables changed were used as an indication of the loading rates and the time it took each plate to come to rest (see Figure 7.4). Changing the density of the elements representing the steel plates in accordance with these rates numerically simulated loading.
- 2) Since for the case of undrained analysis real time was not involved, the load was applied by increments of 0.08 kPa each. The program was run for 100 steps between every load increment in order to approach the quasi-static solution as the load was applied. After simulating the first surcharge of 60 kPa, some more

computational steps were executed to ensure that no further movement would occur before the application of the second surcharge (see Figure 7.3b). The second load of 60 kPa was applied in the same manner.

- 3) For the case of coupled stress-flow analysis, real flow-time was involved. Hence, the prescribed rates of density change were the same as the loading rates. Approximate estimations of these rates were made from Figure 7.4, where the tension on the cables supporting the steel plates is shown against time. The first loading increment was estimated to last 1.91 sec and the second one 2.47 sec. Coupled stress-flow calculations were made during each loading process by alternating 100 mechanical-steps with 1 flow-step to approach the quasi-static solution as the loads were applied. The period between application of each surcharge was estimated to last 2.6 sec and coupled stress-flow calculations were made during this interval under a constant load of 60 kPa by alternating mechanical and flow steps in a one to one proportion. After full application of the second surcharge, coupled stress-flow computations were carried out for 80 sec more under a constant load of 120 kPa. At this point, the analysis was considered finished in accordance with the response measured during the actual centrifuge test.

7.7 Undrained analyses of centrifuge model response to loading

The case of undrained conditions could be seen as excessively conservative since both, redistribution and dissipation of pore pressures are prevented. However, predicting the response of the model under these conditions should provide important insights of the

problem. Furthermore, as shown by Eliadorani (1999) and Vaid (1998), partially drained conditions could be more severe than truly undrained conditions.

The initial state of stress prior to application of the loading was based on the fully drained analysis described previously in Section 7.5.1.

7.7.1 Application of loading increments under undrained conditions

The response of the system to rapid loading was modelled here as undrained. A first analysis was carried out assuming full saturation of the elements below the oil table, i.e., $B_f \equiv 1.8 \times 10^6$ kPa (Phillips and Byrne, 1993). A catastrophic failure of the system was predicted and it was concluded that the assumption of full saturation below the oil table was not realistic. Therefore, it was assumed that the degree of saturation below the phreatic surface was equivalent to the average Skempton B value obtained in triaxial tests on air pluviated specimens, yielding a $B_f \equiv 1.0 \times 10^5$ kPa. Under this assumption, the analysis was performed again. A comparison between the measured and predicted pore pressures and displacements at the monitored points in the centrifuge test is presented in Table 7.3.

Table 7.3. Measured and predicted maximum values of displacements and peak pore pressures for fully undrained analysis with gradual application of two load increments.

	LDT18 [mm]		LDT19 [mm]		TOE [mm]		PPT2 [kPa]		PPT3 [kPa]		PPT4 [kPa]	
LOAD INC.	Δq_1	Δq_2	Δq_1	Δq_2	Δq_2	Δq_1	Δq_2	Δq_1	Δq_2	Δq_1	Δq_2	
MEASURED	-4.3	-6.7	+2.7	+7.7	-40.7	60.0	66.4	128.0	149.3	103.7	107.2	
PREDICTED	-3.7	-8.6	+4.8	+14.1	-18.7	30.0	32.0	108.0	104.0	100.0	108.0	

Note: Displacements at LDT18 and LDT19 are vertical (positive upwards), and at the Toe, horizontal (positive towards the right). Δq_1 and Δq_2 indicate first and second loading increments, respectively.

As can be noted in Table 7.3, agreement between measured and predicted peak pore pressures at PPT4 was excellent, while peak pore pressures at PPT2 and PPT3 were underpredicted by about 50% and 30%, respectively. Since PPT2 and PPT3 were located in a region of the model in which dilative type of response was expected, dilation might have been the reason for underpredicting pore pressures at these locations. In contrast, PPT4 was located in a region of the model in which contractive response was expected, and agreement between measured and predicted values was excellent. It seemed then as if dilation in the elements of the numerical model, which were subjected to compression type of loading, was being overpredicted.

In terms of displacements, these were underpredicted at LDT18 for the first loading increment but overpredicted after the second load. At LDT19, displacements were overestimated, and at the Toe, underestimated. Although the predicted displacements did not differ greatly from the measured values, they were not consistent in terms of always being under or overestimated. The predicted and measured patterns of displacement after the first load was applied are compared in Figure 7.12. The predicted pattern is deep seated and consistent with the measured one.

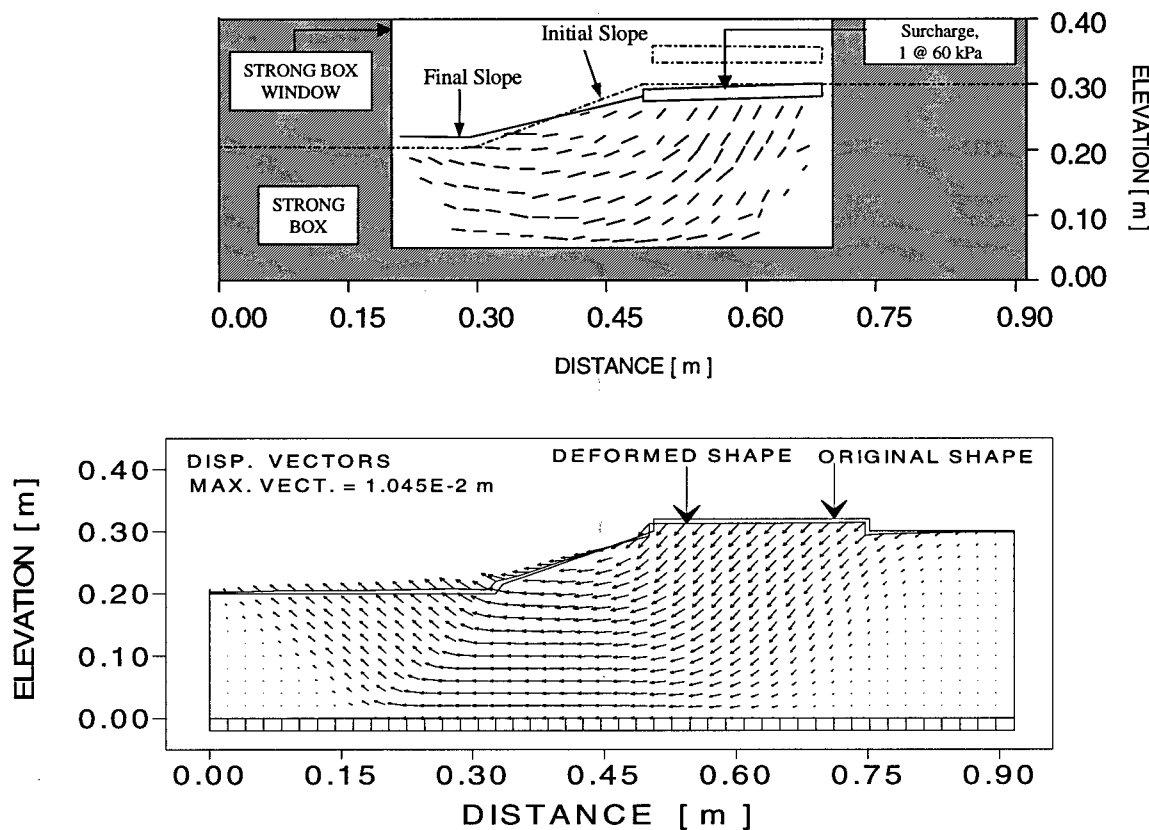


Figure 7.12 Undrained Analysis: Measured and predicted patterns of displacement after the first load of 60 kPa was applied.

To further investigate the issue of dilation, the response of the element corresponding to PPT3 in the centrifuge test simulation was compared to the undrained response of a single element under the same conditions. The single element was subjected to the same initial state of stress as that in the centrifuge simulation and subsequently loaded with the same procedure used to simulate the loading stage of the test. To avoid confusion, the evolution of pore pressures with computational time will not be presented. Instead, the stress path in element (32,7), which corresponds to the location of PPT3, is compared against the stress path predicted for a single element in Figure 7.13. In fact, three stress paths are presented in this figure. Element (32,7) is indicated with a regular line. The response of a single element under *plane strain* conditions is represented by the thickest line and the response of a single element under *axi-symmetric* conditions is delineated by the thinnest line.

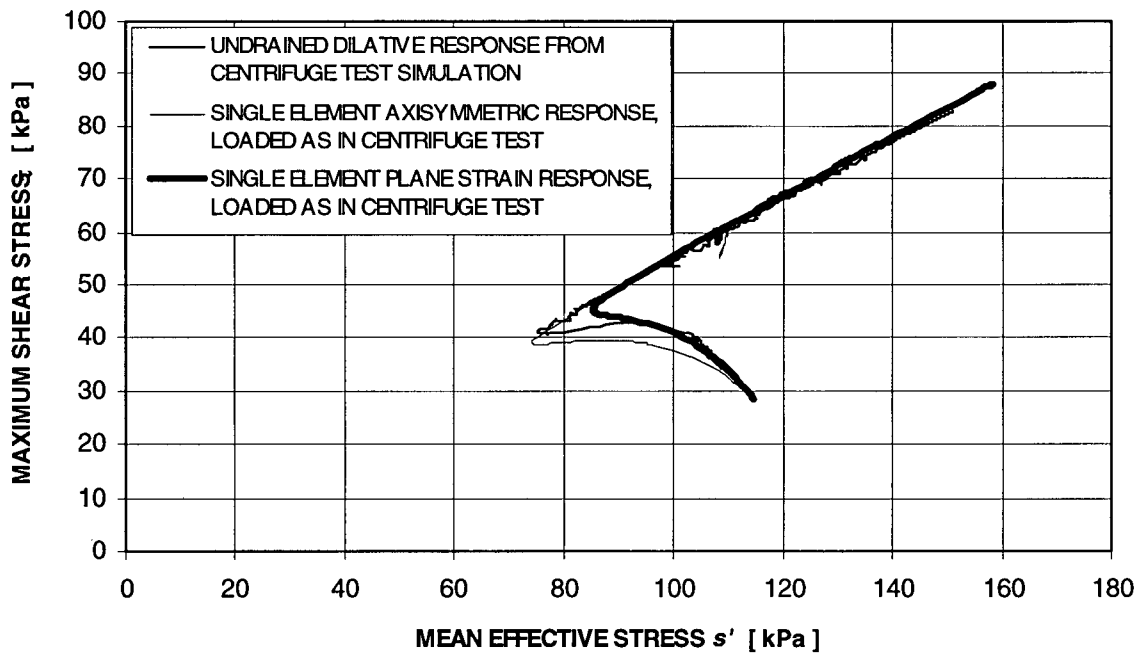


Figure 7.13 Comparison among the stress paths of element (32,7) in the centrifuge model and those from a single element subjected to compressive loading under plain and axial symmetric conditions.

As can be seen in Figure 7.13, the three stress paths were very similar and the response of element (32,7) was enclosed by the responses of a single element under plane strain and axi-symmetric conditions. The response for plane strain was stiffer and stronger than the one for axi-symmetric conditions, as should be expected. The stress path in element (32,7) progressed essentially together with that of the single element in plane strain until almost the point at which the peak strength was reached. Afterwards, element (32,7) exhibited a mildly contractive behaviour while the single element strain hardened through out all the loading process. Of course, the single element responded to an ideal condition in which the load came on strictly in compression. In contrast, element (32,7) had to comply with strain compatibility and the load did not come on as pure compression. However, the accord among the three stress paths is remarkable and demonstrates agreement between the response of element (32,7) and the behaviour observed in the laboratory element tests used to calibrate the stress-strain model.

From the discussion above it can be concluded that there was nothing apparently wrong with the constitutive model, the parameters used or the numerical procedure utilized to simulate the centrifuge test. It is also clear that pore pressures development in the “compression” region of the model were curtailed by dilation and that this was not observed to occur, at least to such an extent, in the actual test. The reason for this is not obvious, but three speculations will be presented. The first one relates to the state of density. The relative density of the element test specimens, on which calibration of the model was based, varied between 28.5% and 43.7%, but on average $D_r \approx 37\%$. On the other hand, the relative density of the centrifuge model prior to the loading stage was

reported as 29% (Phillips and Byrne, 1994). A difference of 8% in relative density clearly shows that the sand comprising the centrifuge model was significantly looser than the sand in the specimens tested in the laboratory. In addition, the value of $D_r = 29\%$ was estimated from the profile of the model after swing up (self-weight compression under 50 g) and evidently could have not been uniform across the whole model.

The second possibility relates to the fluid in the pores. Laboratory tests were carried out on specimens in which water was used as pore fluid. In the centrifuge model, Canola oil was used. It could be possible that a thin coat of oil would have been formed around the sand particles in the model causing the friction angle at failure to decrease. This in turn would translate into a lesser tendency of the sand to dilate.

A third hypothesis regarding flow into the elements that tend to dilate, preventing or reducing pore pressure drop, can be suggested. This type of phenomenon has been observed by Eliadorani (1999) and Vaid (1998) in laboratory tests.

Rather than speculating over the difference in predicted and observed pore pressure response, the effects of flow and dilation will be directly investigated through numerical analysis in the subsequent sections.

7.7.2 Application of loading increments under undrained conditions with allowance made for pore pressure dissipation after each loading increment

Before investigating the effect of dilation in the response of the system, drainage between first and second load increments, and after completing the loading stage, will be considered. The numerical procedure used here was essentially the same as that used in the previous case, but the flow was “turned on” once the system reached equilibrium after

completion of each loading increment. Since the vertical and bottom boundaries of the model were naturally impermeable, fluid could not flow across them. However, the surfaces of the target layer, as well as the slope and crest of the model embankment were considered fluid boundaries subjected to the atmospheric pressure.

After the first 60 kPa was placed under fully undrained conditions, the flow was “turned on” and both mechanical and flow computational steps were executed. In accordance with the elapsed time between full application of the first loading increment and initiation of the second loading increment in the actual test, the first dissipation period lasted about 2.6 sec. Thereafter, the flow was “turned off” again to predict the undrained response of the system to the second loading increment. Once the undrained response to 120 kPa was determined, the flow was “turned on” again and the mechanical-flow response of the system was computed for about 80 sec of flow-time. For this analysis, a comparison between the measured and predicted pore pressures and displacements at the monitored points in the centrifuge test is presented in Table 7.4.

Table 7.4. Maximum values of displacements and peak pore pressures from undrained analysis with periods of pore pressure dissipation between loading increments.

	LDT18 [mm]		LDT19 [mm]		TOE [mm]		PPT2 [kPa]		PPT3 [kPa]		PPT4 [kPa]	
LOAD INC.	Δq_1	Δq_2	Δq_1	Δq_2	Δq_2		Δq_1	Δq_2	Δq_1	Δq_2	Δq_1	Δq_2
MEASURED	-4.3	-6.7	+2.7	+7.7		-40.7	60.0	66.4	128.0	149.3	103.7	107.2
PREDICTED	-3.7	-6.3	+4.8	+9.9	+12.7	-14.7	30.0	45.0	108.0	95.0	100.0	92.0

Note: Displacements at LDT18 and LDT19 are vertical (positive upwards), and at the Toe, horizontal (positive towards the right). Δq_1 and Δq_2 indicate first and second loading increments, respectively.

In Table 7.4, it can be noted that results from this analysis were in essence the same as those of the previous case for which no dissipation of pore pressure was

considered at all. To avoid redundant discussion, only some points regarding flow effects will be mentioned: (i) Dissipation of pore pressures led to predicted smaller final displacements; (ii) Measured and predicted displacements at LDT18 and LDT19 were in very good agreement, while at the Toe, they were underestimated by about a factor of 3; (iii) In terms of pore pressures, the same inconsistencies discussed before about peak values are valid, although the predicted peak values under the second load were smaller than before at PPT3 and PPT4, and greater at PPT2. The predicted and measured patterns of displacements after the first load was applied but prior to application of the second load are compared in Figure 7.14. Again, the predicted pattern is deep seated and consistent with the measured one.

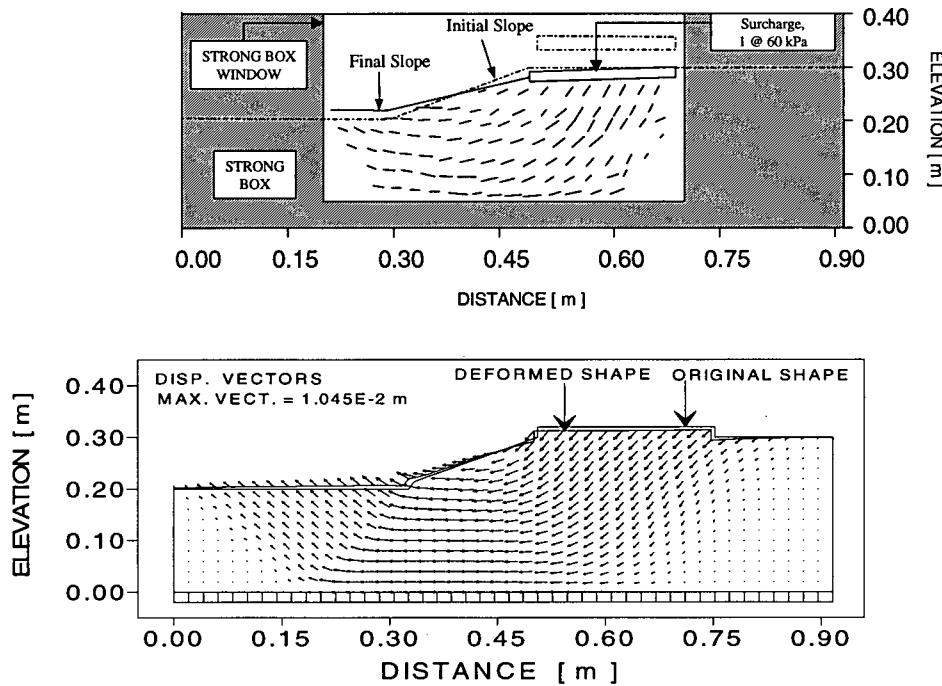


Figure 7.14 Undrained Analysis with allowance made for pore pressure dissipation between loading increments: Measured and predicted patterns of displacement following application of the first load (60 kPa) and after the first period of pore pressure dissipation.

7.7.3 Simulation of non-dilative undrained response of centrifuge model to loading

The effect of dilation will now be directly investigated through numerical analysis. To numerically promote a non-dilative response it will be recalled that the shear flow rule of the constitutive model relates the dilation ratio, $\Delta\epsilon_v^{ps}/\Delta\gamma^{ps}$, to the developed and constant volume friction angles, ϕ_d and ϕ_{cv} , respectively, as follows:

$$[4.17bis] \quad \frac{\Delta\epsilon_v^{ps}}{\Delta\gamma^{ps}} = \sin\psi_d = (\sin\phi_{cv} - \sin\phi_d)$$

If the maximum attainable value for the developed friction angle was equal to ϕ_{cv} , then the dilation ratio at that point would be zero and the model would not predict any dilation. By definition, the maximum possible value of ϕ_d is ϕ_f , and hence, reducing ϕ_f to ϕ_{cv} ($\phi_f = \phi_{cv}$) ensures a non-dilative response of the stress-strain model.

Therefore, the value of the friction angle at failure ϕ_f was assumed equal to ϕ_{cv} and the numerical analysis procedure explained in the previous section was used again to simulate the response of the centrifuge model under these conditions. Results from this analysis are compared with the measured pore pressures and displacements at the monitored points in the centrifuge test, in Table 7.5.

Table 7.5. Measured and predicted maximum values of displacements and peak pore pressures for undrained analysis assuming non-dilative response.

	LDT18 [mm]		LDT19 [mm]		TOE [mm]		PPT2 [kPa]		PPT3 [kPa]		PPT4 [kPa]	
LOAD INC.	Δq_1	Δq_2	Δq_1	Δq_2	Δq_2	Δq_1	Δq_2	Δq_1	Δq_2	Δq_1	Δq_2	
MEASURED	-4.3	-6.7	+2.7	+7.7	-40.7	60.0	66.4	128.0	149.3	103.7	107.2	
PREDICTED	-7.5	-15.0	+12.5	+33.0	-48.0	54.0	58.0	135.0	160.0	126.0	110.0	

Note: Displacements at LDT18 and LDT19 are vertical (positive upwards), and at the Toe, horizontal (positive towards the right). Δq_1 and Δq_2 indicate first and second loading increments, respectively.

In Table 7.5 it can be noted that the predicted values of both, pore pressures and displacements are greater than those measured in the centrifuge test. This was expected since during load application, undrained conditions rather than partially drained, as in the actual test, generally lead to a more severe condition. Furthermore, it is clear now that suppressing dilation effects in the “compression” region of the model, made possible the prediction of peak values of pore pressures in the range of those observed during performance of the centrifuge test. A comparison between the predicted non-dilative and dilative responses of element (32,7) is presented in Figure 7.15, in terms of stress paths. The response was essentially the same up to the point of dilation commencement. Afterwards, the stress paths clearly show that dilative behaviour causes the stress path to move up the strength envelope due to pore pressure drop while the non-dilative response induces contractive type of behaviour and generation of greater pore pressures.

The predicted displacements at LDT18 and LDT19 were about 2 to $2\frac{1}{2}$ times the measured values, and at the Toe, they were overestimated by a factor of 1.2. The predicted and measured patterns of displacement after the first load was applied are compared in Figure 7.16. Again, the predicted pattern is deep seated and consistent with the measured one.

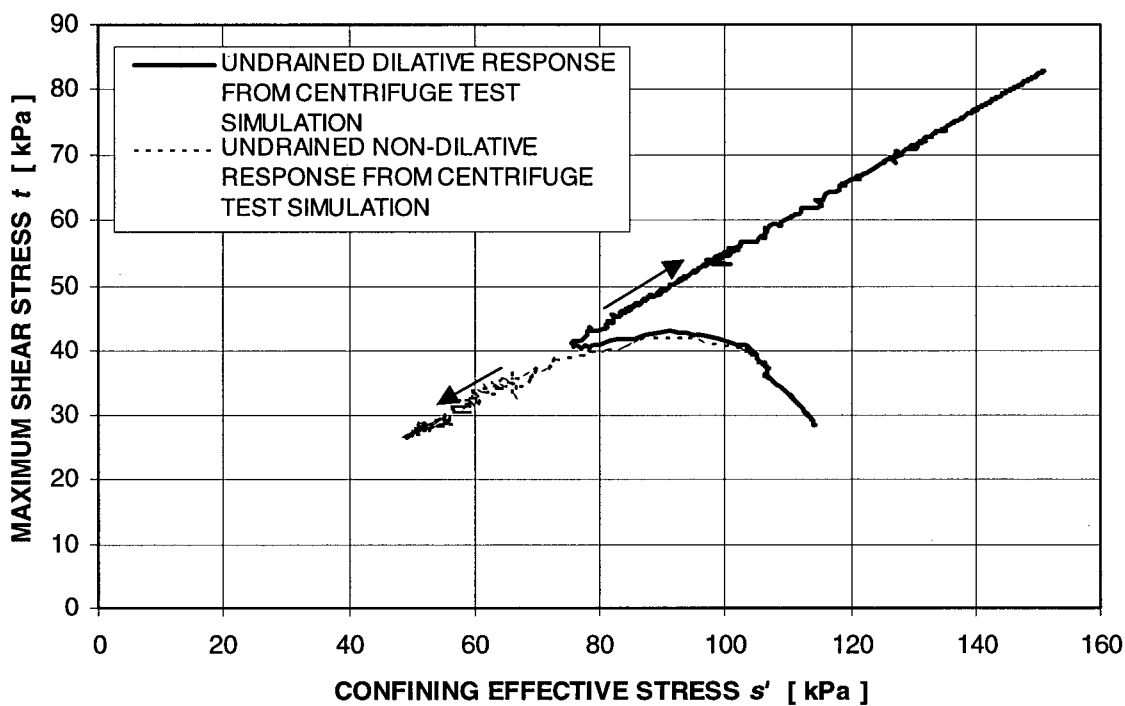


Figure 7.15 Comparison between non-dilative and dilative response of element (32,7) during simulation of the centrifuge test loading stage.

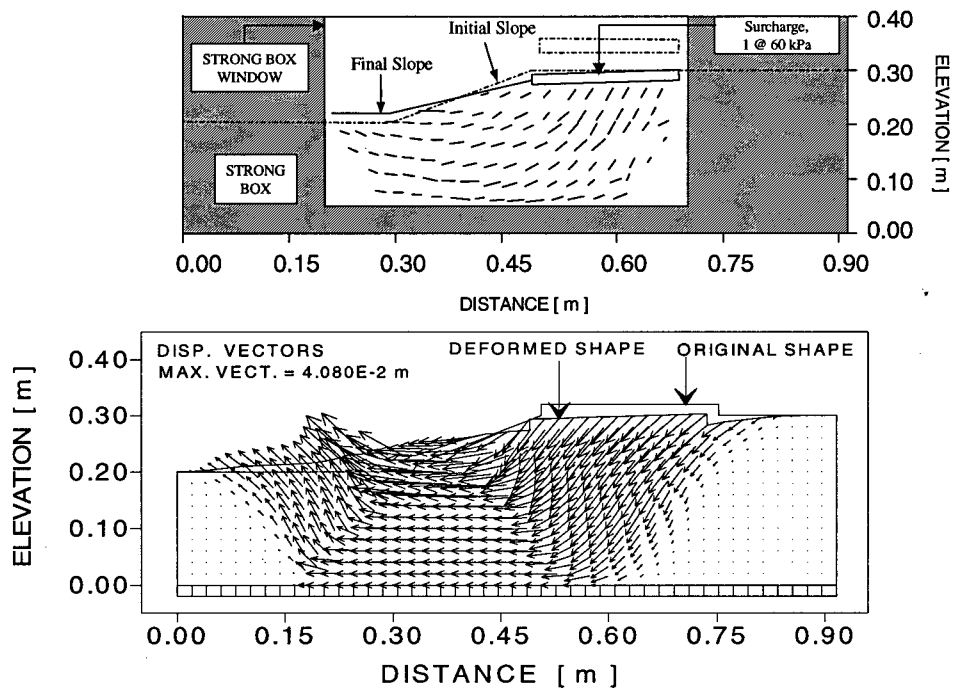


Figure 7.16 Undrained analysis assuming non-dilative response: Measured and predicted patterns of displacement after application of the first loading increment of 60 kPa.

7.7.4 Conclusions from undrained analyses

From the series of undrained analyses carried out to simulate the centrifuge model response to loading and discussed in Sections 7.7.1 to 7.7.3, the following conclusions can be drawn:

- Although undrained analyses could be seen as conservative in comparison with partially drained conditions, they can provide an upper bound to predicted response, as well as important insights and information about the problem under study.
- In the cases studied here so far, displacements either were over or underpredicted by about a factor of two.
- Despite the differences in predicted pore pressures at monitored points in the first three undrained analyses, the magnitude of predicted displacements did not vary in the same proportion as the pore pressures. Furthermore, the general pattern of displacements for all three cases was very similar.
- The predicted behaviour in an element that was extracted from the grid used to simulate the centrifuge model was remarkably consistent with the response predicted by an isolated single element under the same conditions of stress and loading.
- Results from the analysis carried out assuming non-dilative behaviour were consistent with the observed response in the actual centrifuge test. This is very important since if dilation cannot be relied upon, the response of a system comprised of sand would be worse than originally expected. Based on the laboratory data, the reasons for such non-dilative behaviour cannot be determined. However, the apparent non-dilative

response could be related to the differences in density of the sand or to the pore fluid used, i.e. $D_r = 29\%$ and oil in the centrifuge model; $D_r = 37\%$ and water in the laboratory specimens on which calibration of the constitutive model was based. In addition, this type of response can be caused by fluid coming from areas of contractive behaviour and flowing into areas of dilative behaviour. Nevertheless, the analysis in which flow effects were accounted for after load application did not reflect such response.

7.8 Coupled stress-flow analyses of the centrifuge model response to loading

Based on the model's calibration and findings from undrained analyses, a fully coupled stress-flow analysis approach was used to simulate the loading stage of the centrifuge model. The loading stage was described in detail while discussing the Centrifuge Test 1 (Section 7.1), and the response of the physical model to such loading presented in Figure 7.3. A simplified examination of the consolidation characteristics in the target layer was carried out to verify the type of response that could be expected during the loading stage. Assuming constant properties throughout the target layer, the coefficient of consolidation was computed to be $C_v \cong 4.2 \times 10^{-4} \text{ m}^2/\text{sec}$. For the time elapsed during placement of the loading plates, this C_v yielded a degree of consolidation of $U(\%) \cong 16\%$. Thus, an undrained type of response was anticipated during placement of the loading plates (application of loading).

Two different initial states of stress for analyzing the loading stage under partially drained conditions will be considered in this section. The first initial state was obtained from simulating the swing up stage (Section 7.5.2). The second state was obtained from assuming fully drained response during self-weight compression (Section 7.5.1). The purpose for considering these two initial conditions was to investigate the influence that the initial state of stress had in the results of the loading stage analysis.

7.8.1 Loading stage analysis from swing up simulation

Predicted and measured time-histories of pore pressures at the monitored points in the centrifuge test are compared in Figure 7.17a. As can be seen in this figure, although good agreement was achieved at PPT2, at PPT3 the peak values as well as rate of pore pressure dissipation were significantly underestimated. In contrast, at PPT4 the peaks of pore pressure as well as rate of pore pressure dissipation were considerably overpredicted. However, resemblance with the actual response can be observed. At PPT3, for example, a first peak was predicted, followed by a second peak that was significantly greater than the first one. This was precisely the pattern observed during the test at this point. At PPT4, the two predicted peak values of pore pressure did not differ by much, the second one being slightly greater than the first one. Again, this type of pattern was also observed in the actual test at this location. In addition, the rate of pore pressure dissipation at PPT3 was faster than it was at PPT4, as was also observed during the experiment.

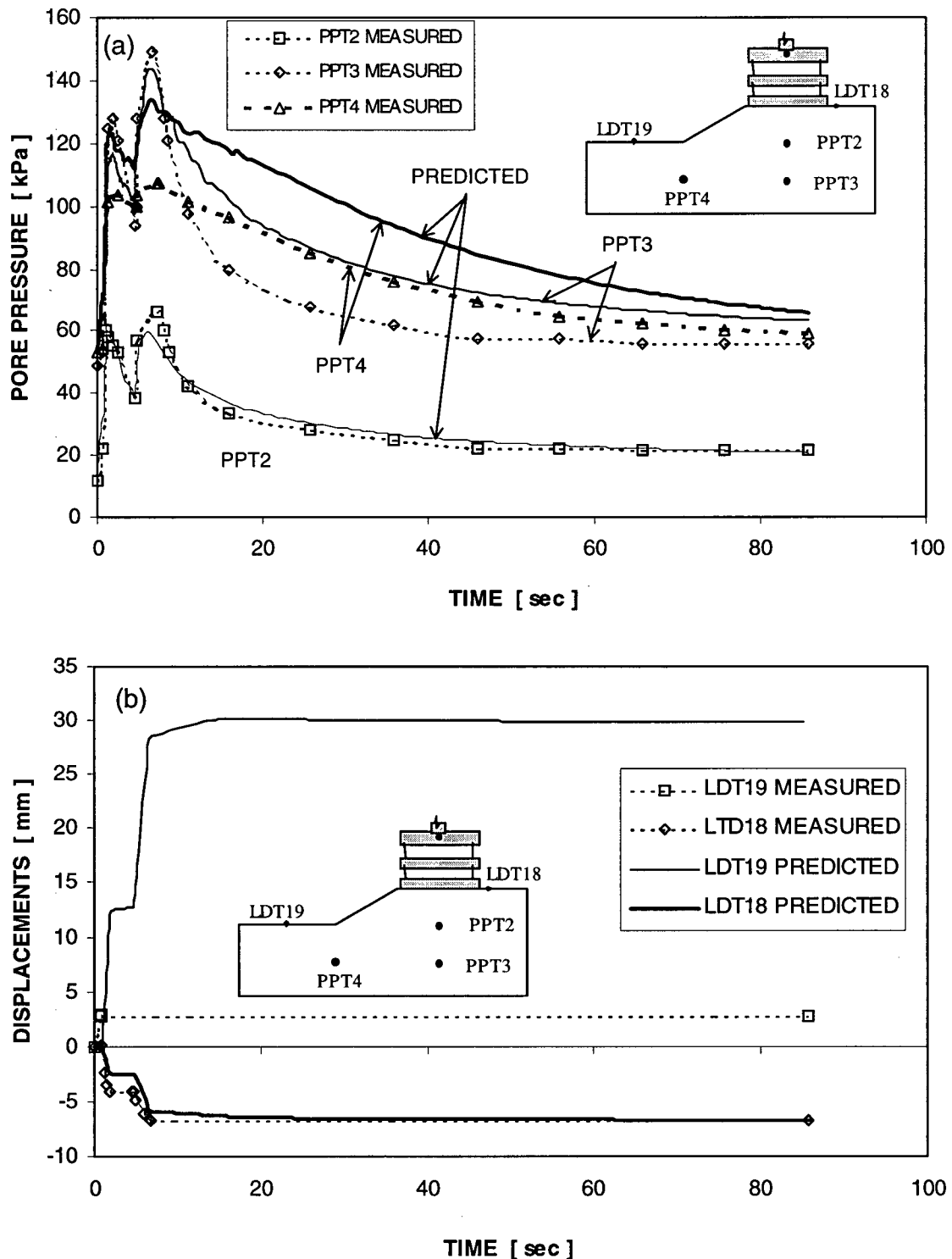


Figure 7.17 Comparison between predicted response of centrifuge model to loading by assuming partially drained conditions during self-weight compression, and observed behaviour. (a) Pore pressures. (b) Displacements.

In terms of displacements, a comparison between measured and predicted values is presented in Figure 7.17b and Table 7.6. The final predicted displacement at LDT18 was in excellent agreement with the observed value at this location, although the predicted time-history of displacement did not coincide with the measured one. The computed displacement at LDT18 resulting from application of the first loading increment was about half the observed value. However, while movement at this location continued to be predicted during the first pore pressure dissipation period, the measured displacement remained constant. The same pattern can be noted upon application of the second loading increment, although in this case the predicted increment of displacement was very similar to the measured value. This is apparently related to the predicted values of peak pore pressure and rates of dissipation, which were less than observed below the crest of the slope.

At the location of LDT19, the predicted displacements were significantly higher than observed. Nevertheless, since this transducer penetrated 5 to 10 mm during the course of the test (Phillips and Byrne, 1994), the values measured by LDT19 are not reliable. The predicted final displacement at the Toe of the slope was in very good agreement with the measured value, being overestimated by about 5%.

The predicted patterns of displacements after the first and second loads were applied are shown in Figure 7.18. Again, the predicted pattern is deep seated and consistent with the measured one.

Table 7.6. Measured and predicted maximum values of displacements and peak pore pressures for coupled stress-flow analysis from swing up simulation.

	LDT18 [mm]	LDT19 [mm]	TOE [mm]	PPT2 [kPa]	PPT3 [kPa]	PPT4 [kPa]					
LOAD INC.	Δq_1	Δq_2	Δq_1	Δq_2	Δq_1	Δq_2					
MEASURED	-4.3	-6.7	+2.7	+7.7	-40.7	60.0	66.4	128.0	149.3	103.7	107.2
				to +12.7							
PREDICTED	-2.6	-6.7	+12.8	+29.8	-42.8	63.0	63.0	108.0	141.0	125.0	132.0

Note: Displacements at LDT18 and LDT19 are vertical (positive upwards), and at the Toe, horizontal (positive towards the right). Δq_1 and Δq_2 indicate first and second loading increments, respectively.

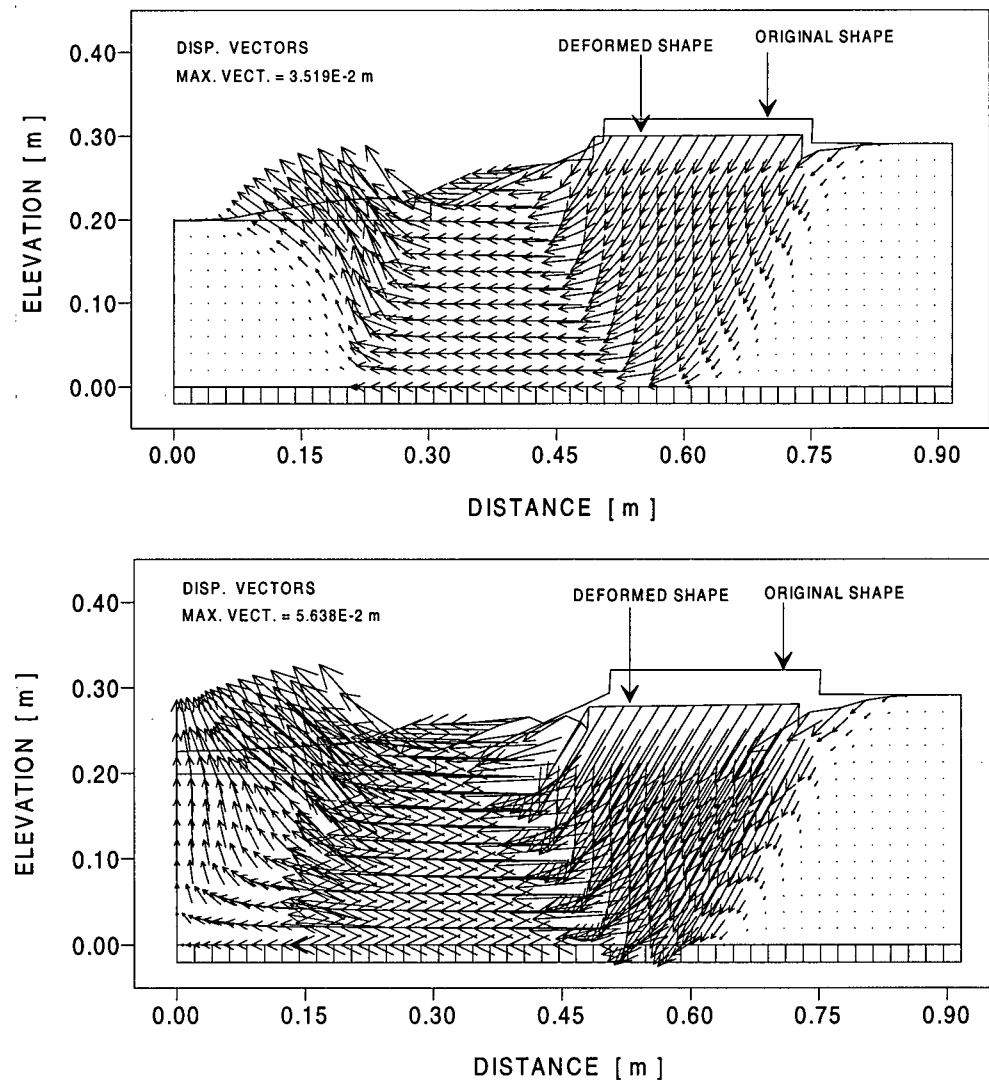


Figure 7.18 Predicted patterns of displacement for coupled stress-flow analysis from swing up simulation. (a) After application of first loading increment. (b) After application of second loading increment.

7.8.2 Loading stage analysis from assuming fully drained response during self-weight compression

A second coupled stress-flow analysis was carried out in which the initial conditions were obtained from assuming fully drained response during self-weight compression (Section 7.5.1). The model parameters used in this analysis were listed in Table 6.2. Predicted and measured time-histories of pore pressure at the monitored points in the centrifuge test are compared in Figure 7.19a. Good agreement in terms of both, magnitude and pattern can be noted. At PPT2 and PPT3, the peak values of pore pressures were slightly underestimated, 13% and 4%, respectively. In contrast, at PPT4 the peak values of pore pressure were slightly overpredicted (about 11%). Nevertheless, agreement with the observed response was good. At PPT3, for example, a first sharp peak was predicted, followed by a sharp drop of pore pressure. The pattern was repeated for the second loading increment but with a greater peak value. This was precisely the pattern observed during the test at this point. At PPT4, the two predicted peak values of pore pressure did not differ by much, being the second one slightly greater than the first one, and they were rather smooth than sharp. This was the type of pattern observed in the actual test at this location. In addition, the rate of pore pressure dissipation at PPT3 was faster than it was at PPT4, as was also observed during the experiment. Furthermore, the predicted pore pressure time-histories at PPT3 and PPT4 intersected each other at the same point in time, $t \approx 10$ sec, at which the corresponding measured time-histories also intersected. At PPT2, despite the difference in magnitude, the trace of measured and predicted curves was remarkably similar; see for example the shape of both curves during the first dissipation period as well as the shape of the second peak.

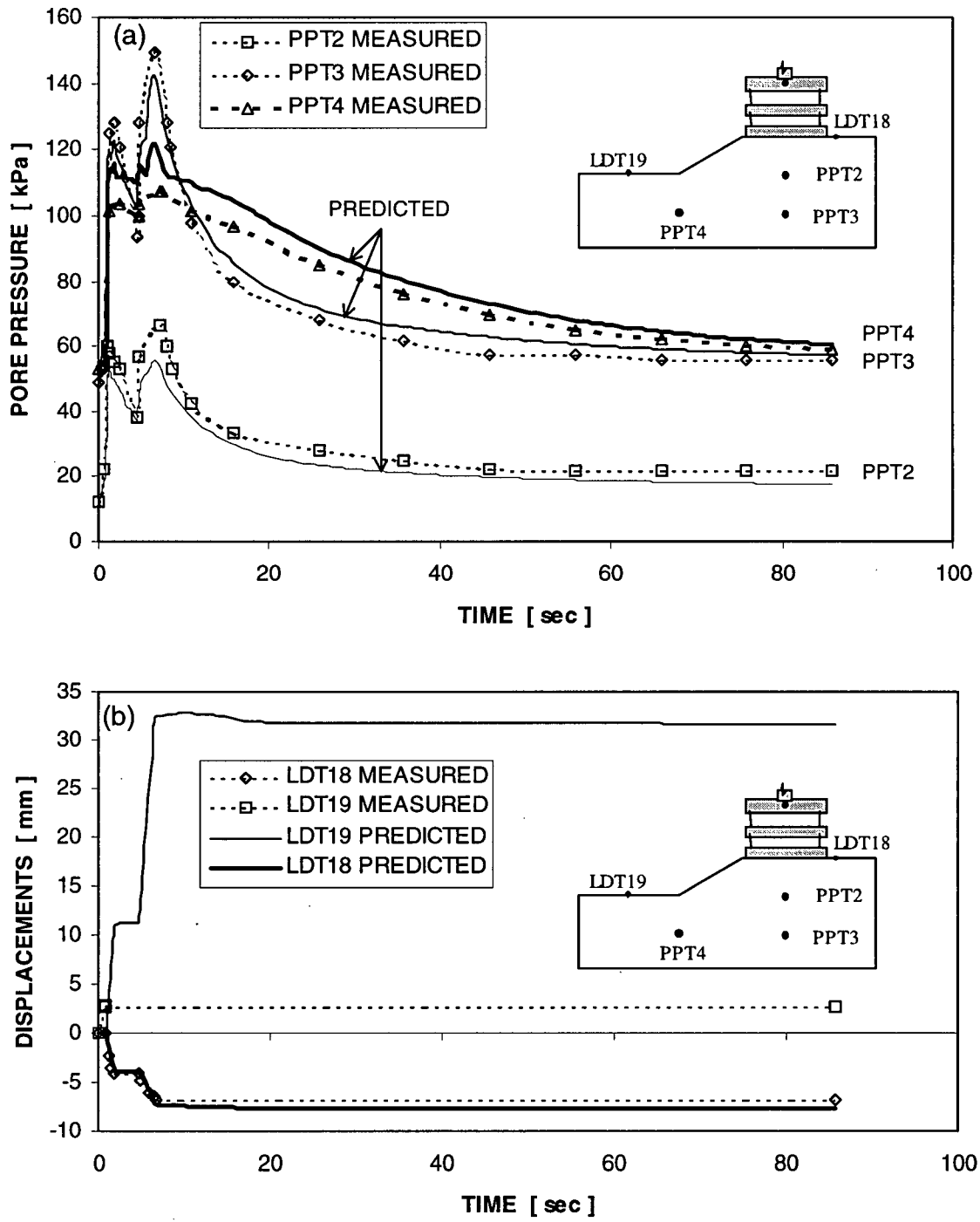


Figure 7.19 Comparison between predicted response of centrifuge model to loading by assuming fully drained conditions during self-weight compression, and observed behaviour. (a) Pore pressures. (b) Displacements.

In terms of displacements, a comparison between measured and predicted values is presented in Figure 7.19b and Table 7.7. The predicted time-history of displacement at LDT18 was in excellent agreement with the measured one, although the final predicted displacement at this location was slightly overestimated. At the location of LDT19, heave was overpredicted. However, since this transducer penetrated 5 to 10 mm during the course of the test (Phillips and Byrne, 1994), the values measured by LDT19 are not reliable. The predicted final displacement at the Toe of the slope was in very good agreement with the measured value, being underestimated by about 3%. The predicted patterns of displacements after the first and second loads were applied are shown in Figure 7.20. Again, the predicted pattern is deep seated and consistent with the measured one.

Table 7.7. Measured and predicted maximum values of displacements and peak pore pressures for coupled stress-flow analysis from assuming fully drained response during self-weight compression.

	LDT18 [mm]		LDT19 [mm]		TOE [mm]		PPT2 [kPa]		PPT3 [kPa]		PPT4 [kPa]	
LOAD INC.	Δq_1	Δq_2	Δq_1	Δq_2	Δq_2	Δq_1	Δq_2	Δq_1	Δq_2	Δq_1	Δq_2	
MEASURED	-4.3	-6.7	+2.7	+7.7	-40.7	60.0	66.4	128.0	149.3	103.7	107.2	
PREDICTED	-4.0	-7.8	+11.2	+31.9	-39.5	53.0	56.0	123.0	143.0	116.0	121.0	

Note: Displacements at LDT18 and LDT19 are vertical (positive upwards), and at the Toe, horizontal (positive towards the right). Δq_1 and Δq_2 indicate first and second loading increments, respectively.

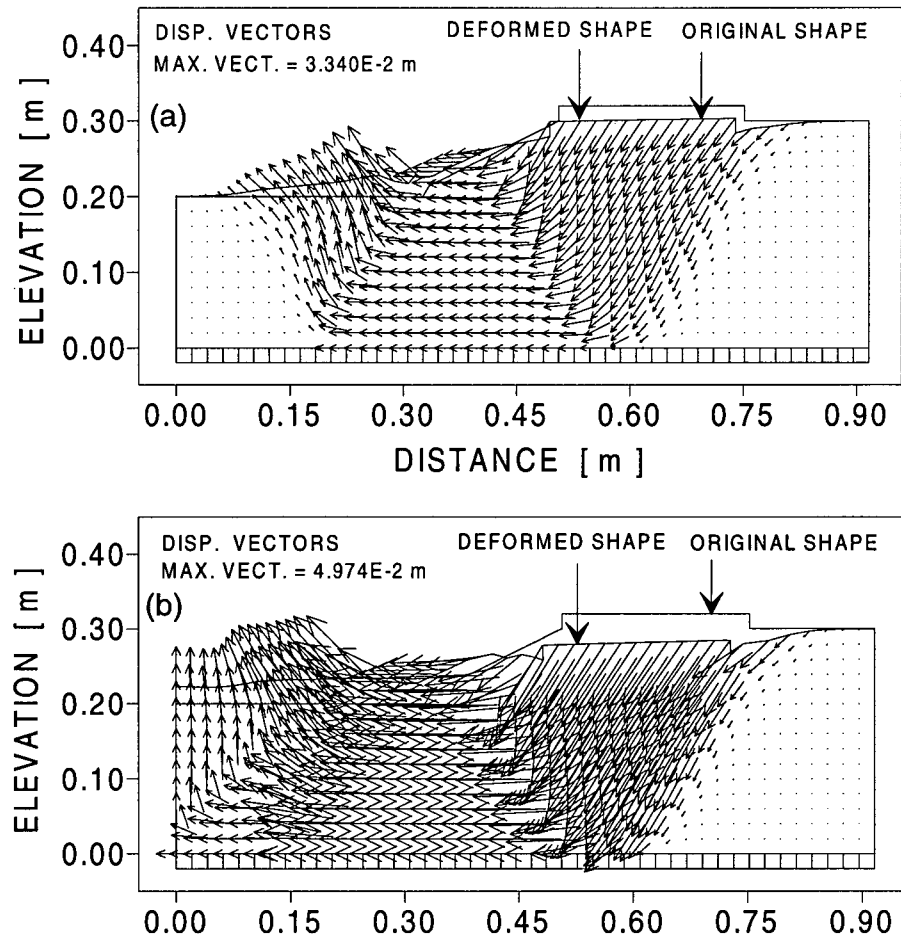


Figure 7.20 Predicted patterns of displacement for coupled stress-flow analysis from assuming fully drained response during self-weight compression. (a) After application of first loading increment. (b) After application of second loading increment.

7.8.3 Influence of the initial state of stress in the computed response of the centrifuge model to loading

From the results presented and discussed in the two previous sections, it can be seen that the initial state of stress had a strong influence in the computed responses of the centrifuge model to loading. For ease of discussion, the two initial conditions will be hereafter referred to as *PD* and *FD*. *PD* corresponds to the initial state of stress obtained by considering *Partially Drained* conditions during simulation of the swing up stage

(Section 7.5.2). *FD* corresponds to the initial state of stress obtained by assuming Fully Drained conditions during self-weight compression (Section 7.5.1).

Analysis of the loading stage from *PD* conditions yielded predicted time-histories of both, pore pressures and displacements that did not agree very closely with the observed ones. In addition, while the predicted peak values of pore pressure below the crest of the slope (compression region) were less than measured, beneath the Toe (extension region), the peak values were significantly overpredicted. Moreover, the predicted rates of pore pressure dissipation were slower than observed. Nevertheless, the characteristic response of the system as observed at the points where pore pressures and displacements were monitored, as well as general pattern of displacements, were reasonably well captured. Furthermore, the final values of predicted displacements at LDT18 and Toe of the slope were in very good agreement with the observed final displacements at these locations.

In contrast, analysis of the loading stage from *FD* conditions yielded predicted time-histories of both, pore pressures and displacements that agreed closely with the observed ones. In addition, while the peak values of pore pressure below the crest of the slope (compression region) were slightly underpredicted, beneath the Toe (extension region), the predicted peak values were slightly greater than observed. In terms of predicted rates of pore pressure dissipation, these showed good agreement with those observed. The final values of predicted displacements at LDT18 and Toe of the slope compared very favorably with the observed final displacements at these locations. Furthermore, the characteristic response of the system as observed at the points where

pore pressures and displacements were monitored, as well as the general pattern of displacements, were reasonably well captured.

As explained before, the initial state of stress could be an essential factor for correctly predicting the amount of excess pore pressure induced by undrained type of loading (see Figure 7.8). In addition, in Section 7.5.2 it was established that the state of stress obtained from *PD* conditions was significantly closer to the failure condition than that obtained from *FD* conditions (see Table 7.2). Furthermore, while *PD* conditions led to a state of stress beneath the Toe of the slope and characterized by element (16,7), in which $\sigma'_h < \sigma'_v$, the opposite state ($\sigma'_h > \sigma'_v$) was predicted for the same region from *FD* conditions. To illustrate the influence of these different states of stress in the predicted responses of the centrifuge model to loading, the computed stress paths for elements (32,7) and (16,7) in both coupled stress-flow analyses of the loading stage are compared in Figure 7.21.

In this figure, it can be clearly seen that the initial state of stress of element (32,7) as obtained from *PD* conditions was very close to the failure condition. Consequently, the prediction of the magnitude of peak pore pressure made at the location of PPT3 under the first loading increment was highly influenced by the initial state of stress. This provides an explanation as to why the peak value of pore pressure at PPT3 was significantly underpredicted when simulating loading from *PD* conditions and after the first surcharge was applied. In contrast, the initial state of stress in element (32,7) obtained from *FD* conditions was substantially away from the failure state, and this resulted in the prediction of a higher value of peak pore pressure and better agreement with observations. Upon application of the second surcharge, the initial responses to

loading in both analyses were very similar and thus the similarity in predicted peak values of pore pressures at PPT3. However, the initial state of stress from *PD* continued to influence the predicted response of the element to loading, and led to prediction of a slower rate of pore pressure dissipation.

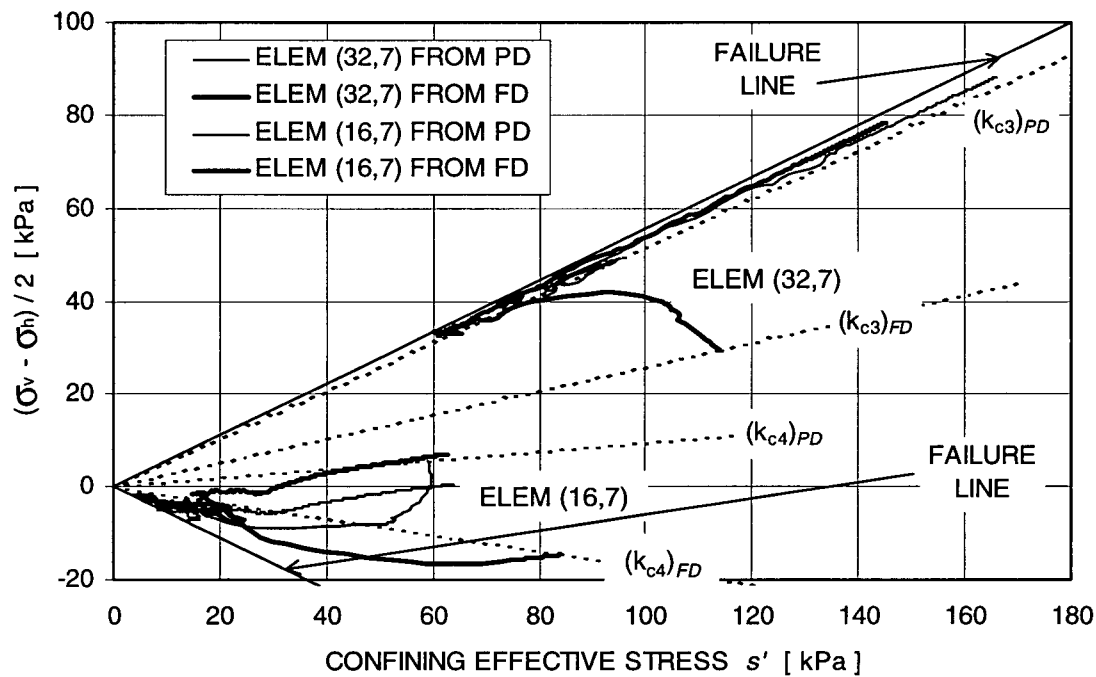


Figure 7.21 Comparison among stress paths of elements (32,7) and (16,7) as predicted from coupled stress-flow simulations of the centrifuge test loading stage that started from two different initial states of stress, namely *PD* and *FD*.

In the case of element (16,7), the initial state of stress from *PD* conditions was such that $\sigma'_h < \sigma'_v$. Upon application of the first loading increment, a stress reversal at this location was predicted, as can be noted in Figure 7.21. Consequently, the predicted peak value of pore pressure at PPT4 was large. This provides an explanation as to why the peak value of pore pressure at PPT4 was significantly overpredicted when simulating loading from *PD* conditions and after the first surcharge was applied. In contrast, the

initial state of stress in element (16,7) obtained from *FD* conditions was such that $\sigma'_h > \sigma'_v$, and thus, stress reversal at this location was not predicted upon application of the first surcharge. This resulted in the prediction of a lower value of peak pore pressure and better agreement with observations, although the peak pore pressure was overpredicted by about 11%. Upon application of the second surcharge, the shapes of the stress path of element (16,7) in both analyses were very similar, but clearly showed the influence that the different states of stress had in the response of the element.

Despite the differences discussed above, the overall patterns of displacement obtained through both analyses were essentially the same and resembled the observed failure mechanism. This might have been caused by the constraints imposed by the boundaries of the modelled system. Had the boundaries been farther from the slope, it is possible that both analyses would have yielded dissimilar general patterns of displacement. Effects induced by the location of boundaries in the response of the system were not investigated, but as it will be shown in Section 7.8.4, the boundary conditions can significantly influence the predicted response.

7.8.4 Effects of scaling centrifuge model from 50g to 1g and element size of the grid

Effects of scaling the centrifuge model from 50 g to 1 g were investigated by using a grid that represented a 5 m high embankment resting on a 10 m foundation layer under an acceleration field of 1 g. In addition, grid dependence of predicted response was studied by discretizing the centrifuge model with a grid that comprised elements four times smaller than those used in the previous simulations. Coupled stress-flow analyses were then carried out. In both cases, the predicted responses were essentially identical to the

one presented and discussed in Section 7.8.2. These two additional analyses provided more evidence that supported the validity of the numerical procedure used.

7.8.5 Effects of friction on the bottom boundary of the centrifuge model

Although friction on all boundaries of the centrifuge model could influence the response of the system, effects of friction at the bottom boundary were considered the most relevant to the problem under study. To investigate such effects, an interface element was used on the bottom boundary of the numerical model. Various values of friction on the interface were specified: 1° , 2° , 3° , 5° , 10° and 15° . An additional case in which the nodes of the bottom boundary were fixed in both horizontal and vertical directions was also considered. Results of these analyses are presented in terms of pore pressure time-histories at the monitored points and general pattern of displacements in Figures 7.22 to 7.28. In these figures, it can be noted that friction effects became evident even for a friction angle as small as 2° (note reduction on predicted peak values of pore pressure upon application of the second loading increment). As friction was increased to 5° , 10° and 15° , a very significant change in the failure mechanism was predicted. In addition, the pattern of predicted pore pressure time-histories also changed in a drastic manner. Liquefaction susceptibility of the embankment to the first loading increment decreased rapidly as the specified value of friction at the boundary was increased. According to the analyses performed here, a friction angle of about 5° at the interface would prevent the embankment from suffering significant displacements under the first load of 60 kPa. However, upon application of the second surcharge, the sand beneath the slope was

predicted to liquefy and the embankment suffered significant movements. The failure surface is well above the base in this case.

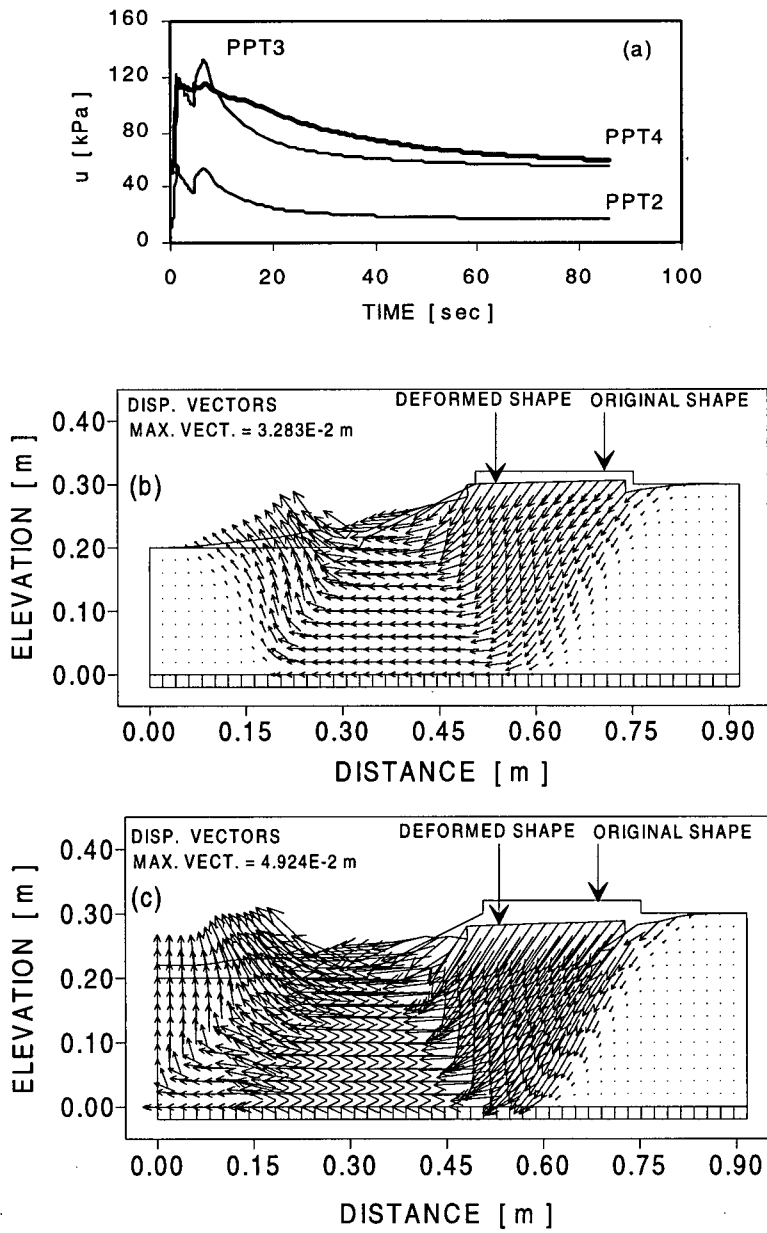


Figure 7.22 Predicted response of centrifuge model to loading for the case in which the angle of friction at the bottom boundary was specified as 1° . (a) Pore pressures. (b) Pattern of displacements after application of the first loading increment. (c) Pattern of displacements after application of the second loading increment.

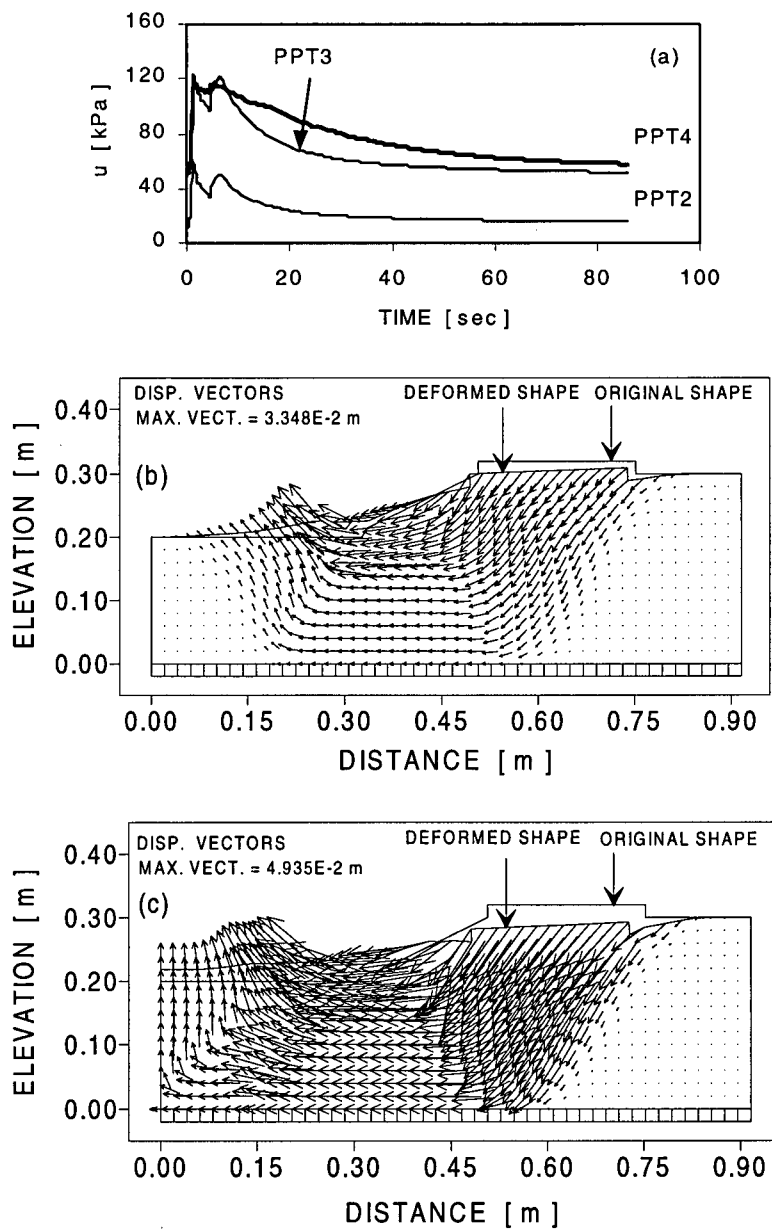


Figure 7.23 Predicted response of centrifuge model to loading for the case in which the angle of friction at the bottom boundary was specified as 2° . (a) Pore pressures. (b) Pattern of displacements after application of the first loading increment. (c) Pattern of displacements after application of the second loading increment.

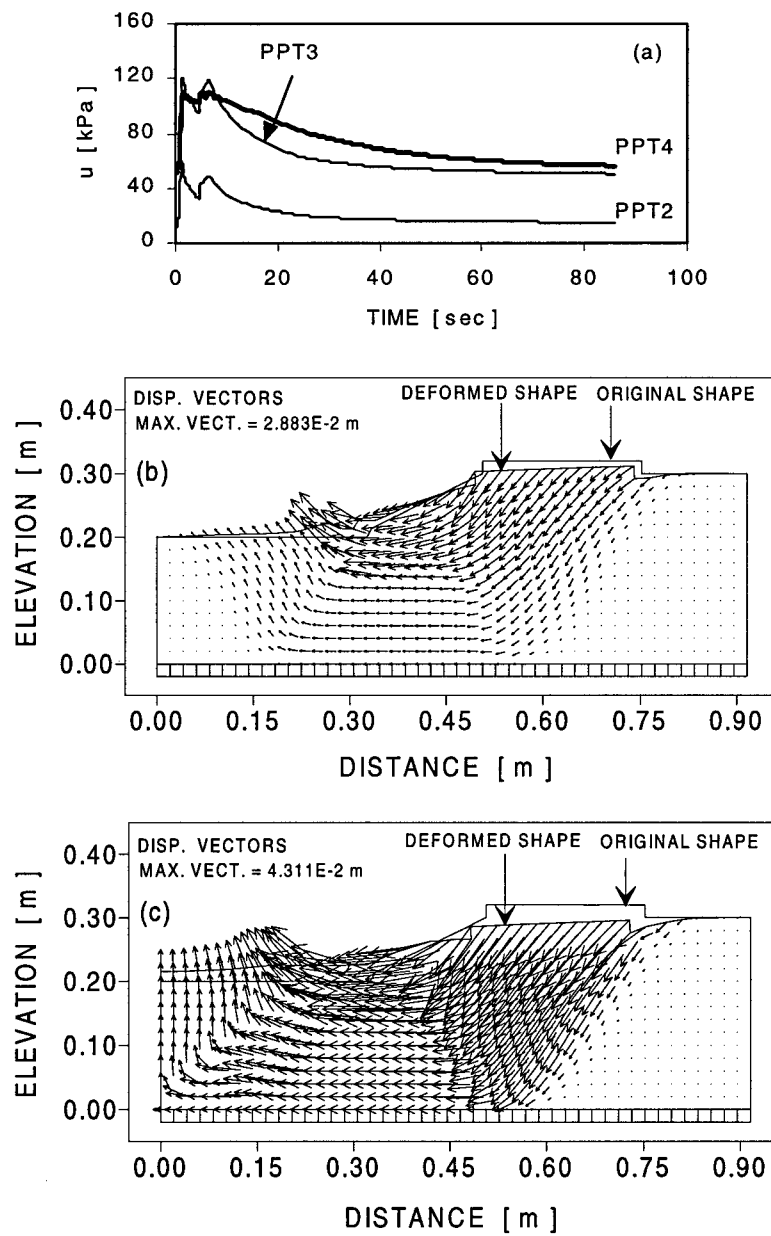


Figure 7.24 Predicted response of centrifuge model to loading for the case in which the angle of friction at the bottom boundary was specified as 3° . (a) Pore pressures. (b) Pattern of displacements after application of the first loading increment. (c) Pattern of displacements after application of the second loading increment.

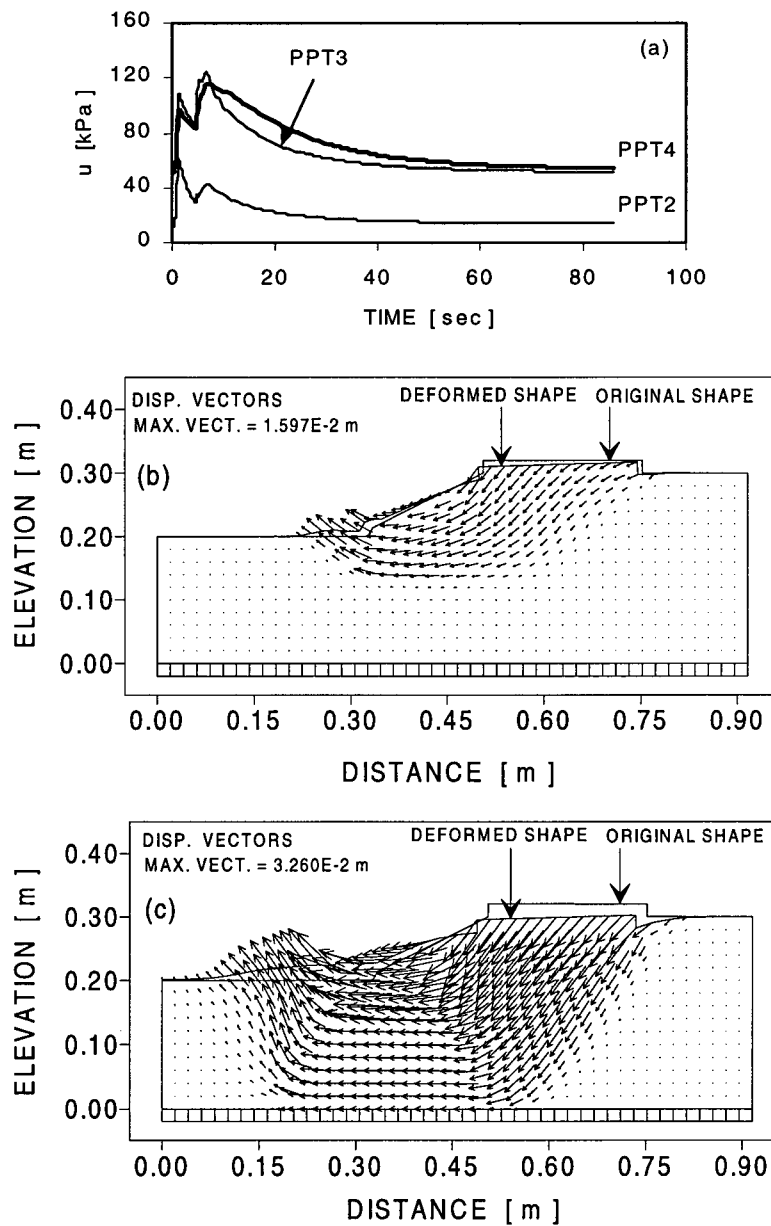


Figure 7.25 Predicted response of centrifuge model to loading for the case in which the angle of friction at the bottom boundary was specified as 5° . (a) Pore pressures. (b) Pattern of displacements after application of the first loading increment. (c) Pattern of displacements after application of the second loading increment.

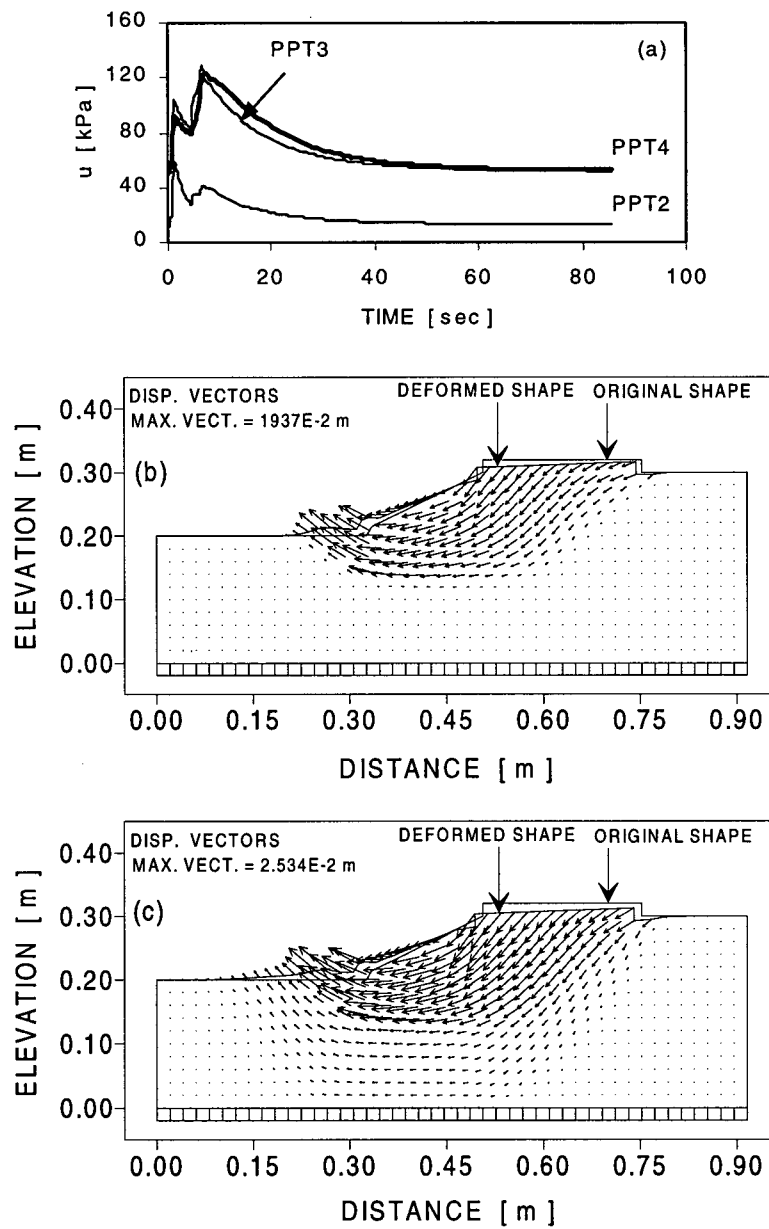


Figure 7.26 Predicted response of centrifuge model to loading for the case in which the angle of friction at the bottom boundary was specified as 10° . (a) Pore pressures. (b) Pattern of displacements after application of the first loading increment. (c) Pattern of displacements after application of the second loading increment.

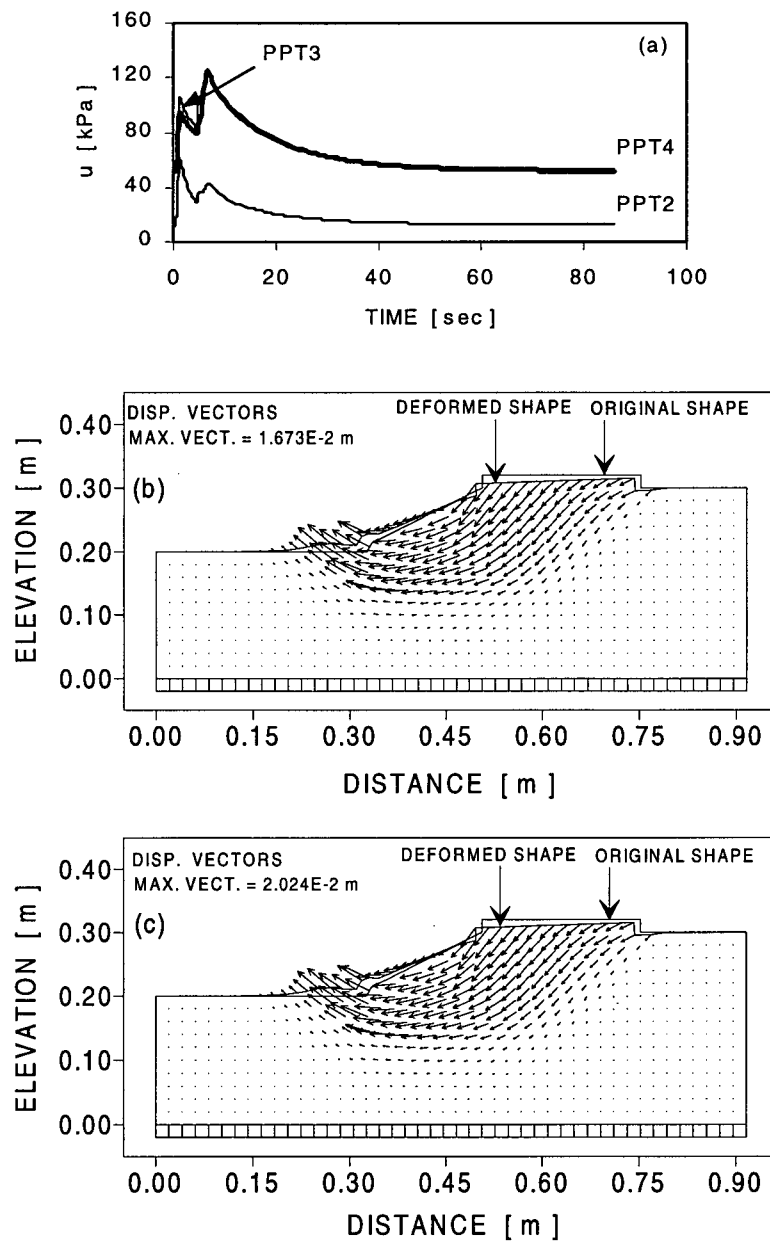


Figure 7.27 Predicted response of centrifuge model to loading for the case in which the angle of friction at the bottom boundary was specified as 15° . (a) Pore pressures. (b) Pattern of displacements after application of the first loading increment. (c) Pattern of displacements after application of the second loading increment.

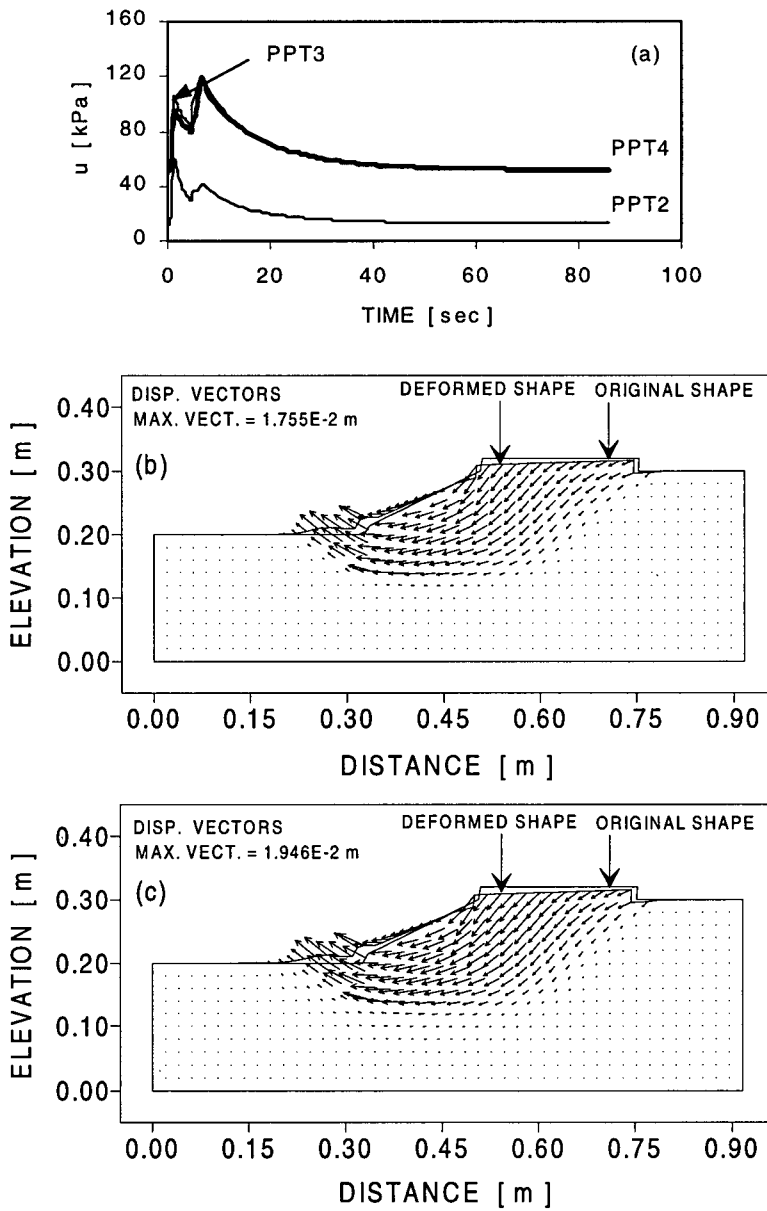


Figure 7.28 Predicted response of centrifuge model to loading for the case in which the nodes at the bottom boundary were specified as fixed. (a) Pore pressures. (b) Pattern of displacements after application of the first loading increment. (c) Pattern of displacements after application of the second loading increment.

7.8.6 Conclusions from coupled stress-flow analyses

From the series of coupled stress-flow analyses carried out to simulate the centrifuge model and discussed in Sections 7.5.2 (swing up stage), and 7.8.1 to 7.8.5 (loading stage), the following conclusions can be drawn:

Swing up stage:

- The characteristic response of the physical model during the swing up stage was captured in essence by the numerical simulation, although agreement between specific predicted and observed values of pore pressures and displacements was not very close. Insufficient data for properly calibrating the model at low confining stresses seemed to be the reason for such lack of agreement.
- The initial state of stress before loading strongly influenced the predicted response of the system to subsequent application of loading.
- The initial state of stress due to self-weight compression of the sand model appeared to be better estimated by assuming fully drained conditions during the compression process than by considering partial drainage during the swing up stage.
- Further study on swing up type of problems is necessary and recommended in order to determine the suitability of the constitutive model and numerical procedure for this kind of problems.

Loading stage:

- A reasonably successful coupled stress-flow analysis of the loading stage was achieved by assuming fully drained conditions to predict the initial state of stress, and by scaling the value of permeability from a relative density of 40%, to a $D_r = 29\%$.

- Drainage conditions during load application were shown to be important in predicting the centrifuge model response to loading. Consideration of partial drainage in analysis of the loading stage led to better agreement with the observed response and less conservative predictions than those yielded by undrained analysis.
- The constitutive model and the analysis procedure used here were shown adequate for capturing liquefaction (induced by rapid monotonic loading) under the toe of the centrifuge embankment, as observed in the actual test. Hence, both the constitutive model and the analysis procedure are considered suitable for carrying out static liquefaction analysis of this type.
- The effects induced by friction at the bottom boundary of the centrifuge model were shown to be very important in predicting the response of the system to loading.
- Results from the analyses performed in this study indicated that frictionless boundaries were the most appropriate for analyzing the centrifuge experiment discussed here.

7.9 Summary

Numerical simulations of a centrifuge test in which liquefaction was triggered by rapid monotonic loading have been presented and discussed in this chapter. The centrifuge test was numerically modelled according to the construction sequence and conditions, the increase in acceleration field from 1 g to 50 g (swing up stage), and the final loading stage. Fully drained and partially drained conditions were considered in the analysis of the swing up stage, while undrained and partially drained conditions were considered in the analysis of the loading stage.

Results from the numerical analysis of the swing up stage that was carried out assuming partially drained conditions were in good agreement with the pattern of behaviour observed during this stage of the test. However, some discrepancies were found between the magnitude of measured and predicted pore water pressures and displacements. Such discrepancies could be due to the difference in range of stress levels for which the model was calibrated and the range in which the stress levels varied during the actual swing up stage, e.g., at mid-depth of the foundation layer the vertical effective stress, σ'_v , ranged between 0.9 and 2.8 kPa at 1 g, but between 45 to 140 kPa under 50 g. In contrast, the constitutive model was calibrated for stress levels ranging between 50 to 200 kPa, since experimental data of Syncrude sand at lower levels of stress was not available. Further study of problems involving a wide range of stress levels is necessary to establish the applicability of the constitutive model to this type of studies, i.e., was lack of accuracy in predicted response due to limitations of the constitutive model, or to insufficient data for calibrating the model according to the actual range of stress levels?

The loading stage of the centrifuge test was numerically modelled under undrained and partially drained conditions. Results from these analyses showed that the constitutive model was capable of reproducing Syncrude sand response under compressive loading as observed in triaxial tests, but that such response did not agree with the observed behaviour in the centrifuge model within the region of compressive loading. However, it was found that good agreement between measured and predicted response could be achieved by assuming a non-dilative type of behaviour of the material if loaded in compression. In contrast, the observed behaviour in the region of the centrifuge model in which liquefaction was triggered (region under extension type of

loading) was reasonably well captured by the model independently of the type of response assumed in the compression region. The discrepancies between the responses measured in laboratory tests and in the centrifuge model under compressive loading may be related to the differences in type of pore fluid and relative densities, i.e., water and $D_r \approx 37\%$ in triaxial tests; oil and $D_r \approx 29\%$ in the centrifuge model.

In addition, effects of friction in the bottom boundary of the physical model were numerically simulated by using a friction interface element at such location. Results of this study showed that friction effects in such boundary could significantly influence the predicted response of the centrifuge model to loading.

The numerical procedure and constitutive model used for simulating the centrifuge test were shown capable of capturing the observed response of the physical model within a reasonable range of accuracy, particularly in the region in which liquefaction was triggered as consequence of rapid loading. Hence, the numerical procedure and constitutive model will be applied in Chapter 8 for analyzing the CANLEX field event but using model parameters according to the in-situ conditions, as discussed in Section 6.2.

CHAPTER 8

ANALYSIS OF CANLEX FIELD EVENT

8.1 Liquefaction event

The liquefaction event was carried out at the Syncrude site, near Fort McMurray, Alberta.

The purpose of this full-scale event was to statically trigger a liquefaction flow slide by rapidly loading a loose, saturated sand deposit. This involved the construction of a test embankment over the loose layer. The event is described in detail by Byrne et al. (1995*b*), but a summary will be given here and is illustrated in Figure 8.1.

An abandoned borrow pit at the Syncrude site, J-Pit, was used to carry out the field event. The foundation sand layer was first placed hydraulically into standing water inside J-Pit and up to Elevation 318m. This sand was referred to as beach below water sand (BBW-sand). A level platform was then formed at Elevation 321m by placing tailings sand above the water. This platform was termed beach above water sand (BAW-sand). A clay dyke 8 m high with sideslopes of 2.5:1 (horizontal to vertical) was subsequently constructed over the tailings. Construction was slow so as to allow full drainage of the sand to occur. A 10 m high compacted sand cell that served as containment structure was also constructed to form an enclosure. Rapid loading was brought about by pumping tailings (contained sand) behind the clay dyke.

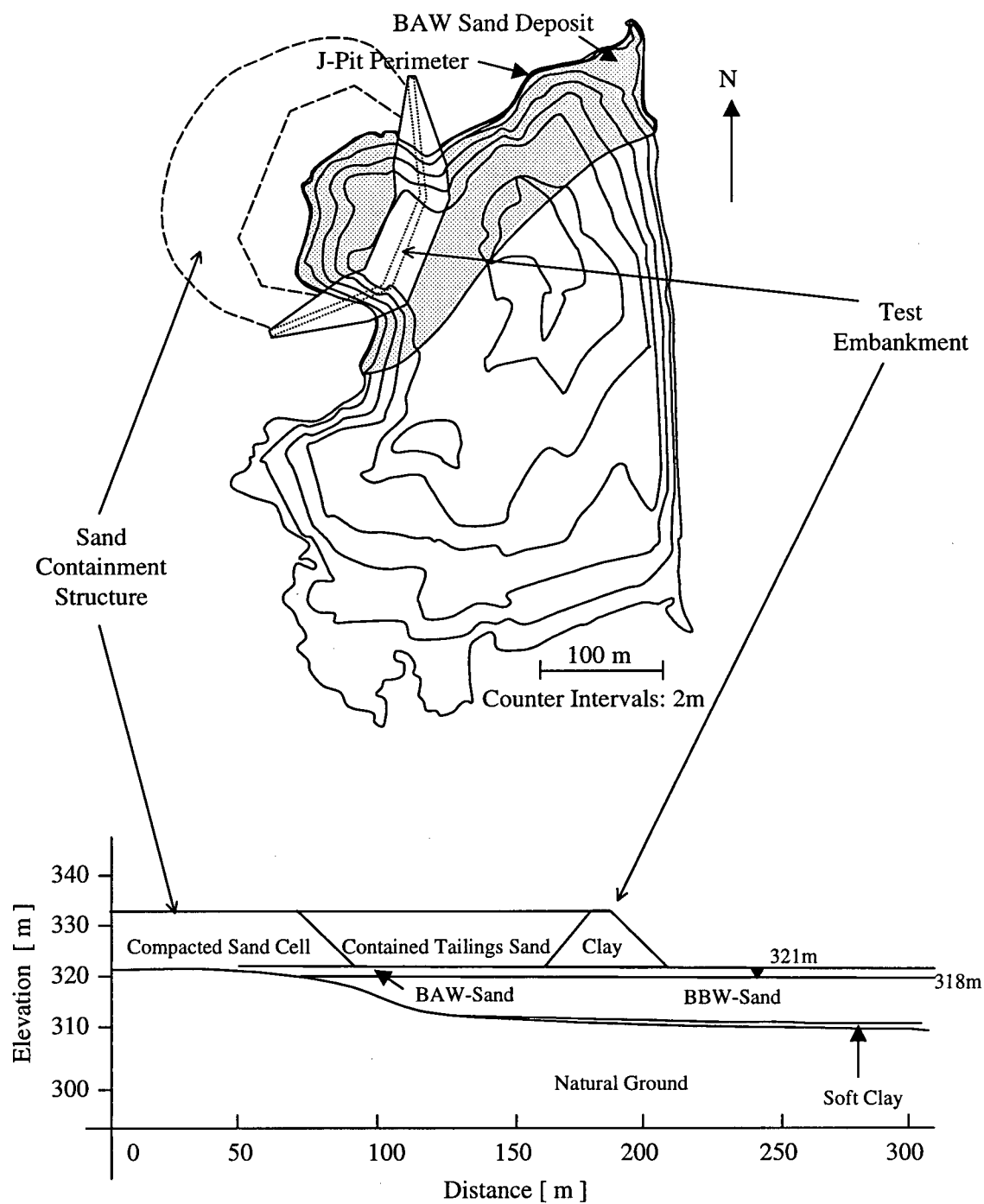


Figure 8.1 Plan and cross-sectional views of liquefaction event site.

The site was characterized and instrumented as discussed by Byrne et al. (1995b). The characterization involved in-situ testing (Seismic Cone Penetration Test, Standard Penetration Test with energy measurements, Self-boring Pressuremeter Testing and Geophysical Logging), undisturbed sampling using in-situ ground freezing, and laboratory testing of the samples. The target sand layer was found to be very loose with an average $(N_1)_{60} = 3.4$, and average values of the normalized cone tip resistance and shear wave velocity of $(q_{c1})_{ave} = 2.35 \text{ MPa}$ and $(V_{s1}) = 127 \text{ m/s}$, respectively (Hofmann et al., 1996). Laboratory testing of undisturbed and reconstituted samples showed this very loose material to be strain softening when loaded under undrained simple shear and extension conditions, but strain hardening when loaded under undrained compression conditions.

Five lines of instrumentation under the test embankment, and extending to about 30 m beyond the toe of the dyke, were originally planned. The instrumentation comprised piezometers, tilt meters and settlement gauges. However, piezometers were installed only in four lines as described by Hofmann et al. (1996) and shown in Figure 8.2. The tilt meters were installed in between piezometric instrumentation lines and the settlement gauges, adjacent to instrumentation Lines 1 and 2. In addition, a remote optical survey system was used to monitor surface movements.

The field event took place from September 18 to September 20, 1995. Water and tailings were pumped behind the clay embankment during this period. The water level was raised within 12 hours after the loading process commenced, to a maximum height of 6 m. The full tailings sand load was completed after approximately 37 hours of pumping tailings behind the clay dyke, to a maximum height of 7 m (Natarajan et al. 1996).

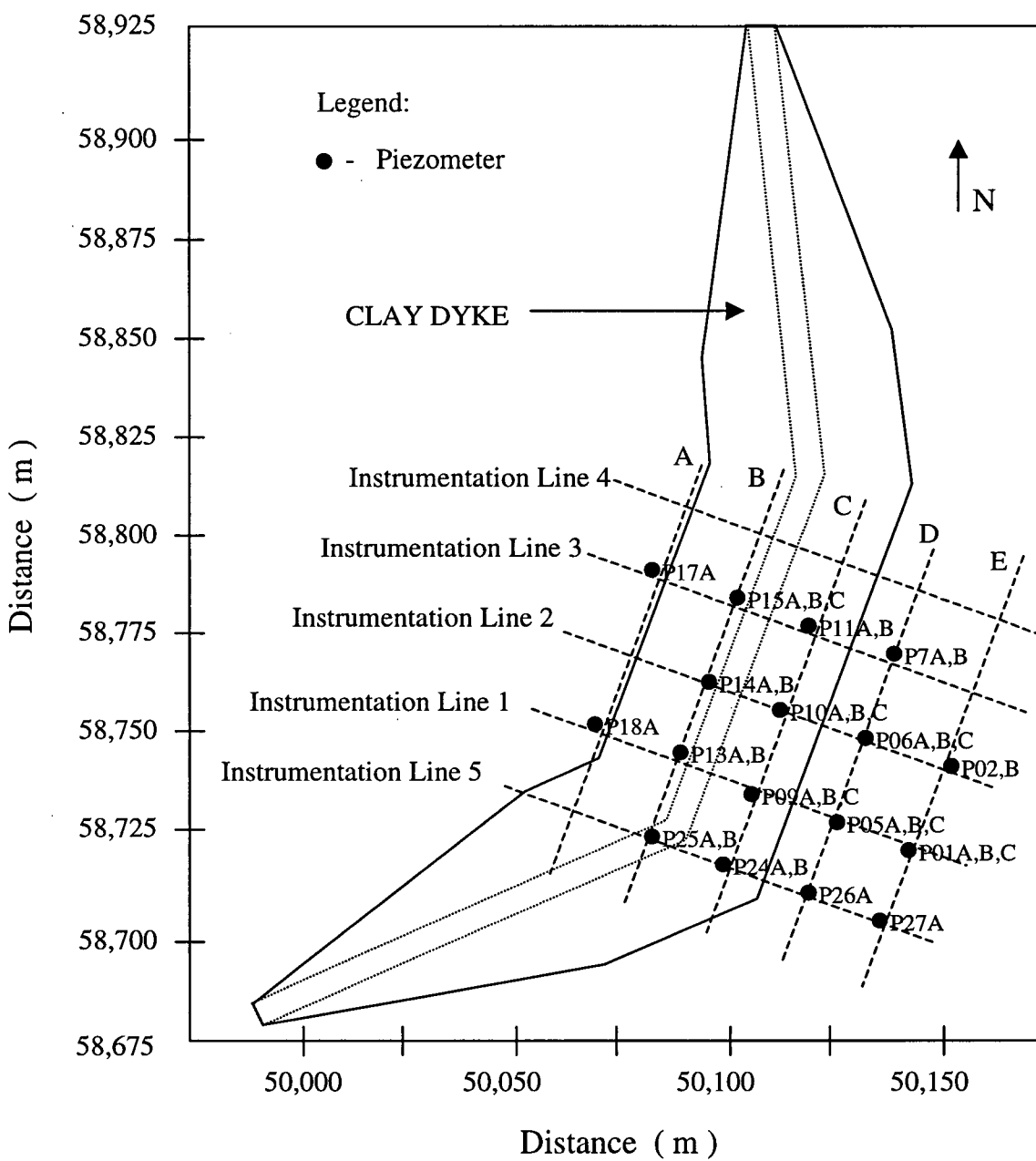


Figure 8.2 Plan view of instrumentation lines through embankment (after Natarajan et al., 1996).

As result of rapid loading, the Toe of the clay embankment experienced a maximum displacement of 0.054 m and the average movement of the dyke was 0.020 m (Natarajan et al., 1996). Hence, displacements due to loading were small. These

movements were measured by the survey system. Since deformations of the target layer were within the resolution of the tilt meters, it was not possible to construct displacement profiles in the foundation layer (Hofmann et al., 1996). In terms of pore pressure, the highest increase in piezometric head, 6.7 m, was measured at mid depth of the target layer by piezometer P18A. This piezometer was located 5 m below the upstream Toe of the clay dyke. Beneath the crest of the dam, the average increase in piezometric head was 3.5 m (Hofmann et al., 1996). It is evident that these excess pore pressures were not sufficient to trigger liquefaction in the foundation layer underneath the dyke and beyond its Toe. The embankment response to rapid loading in terms of time-histories of piezometric head along Sections A, B, C and D (Figure 8.2) is presented in Figure 8.3. As can be noted in this figure, higher values of excess pore pressure were in general registered by piezometers along Lines 1 and 5. Hofmann et al. (1996) explained such higher values as result of the looser state that sand in the foundation layer had towards the south end of the embankment.

8.2 Analysis of field event

The field event was modelled in the analysis by simulating the construction and loading conditions. It was assumed that all materials behaved in a fully drained manner during placement, except the contained tailings sand (Figure 8.1), which was assumed to behave as a heavy fluid. The clay dyke and compacted sand cell were modelled as elastic-perfectly-plastic materials and their parameters based on Duncan et al. (1980) and Byrne et al. (1987). These parameters are listed in Table 8.1.

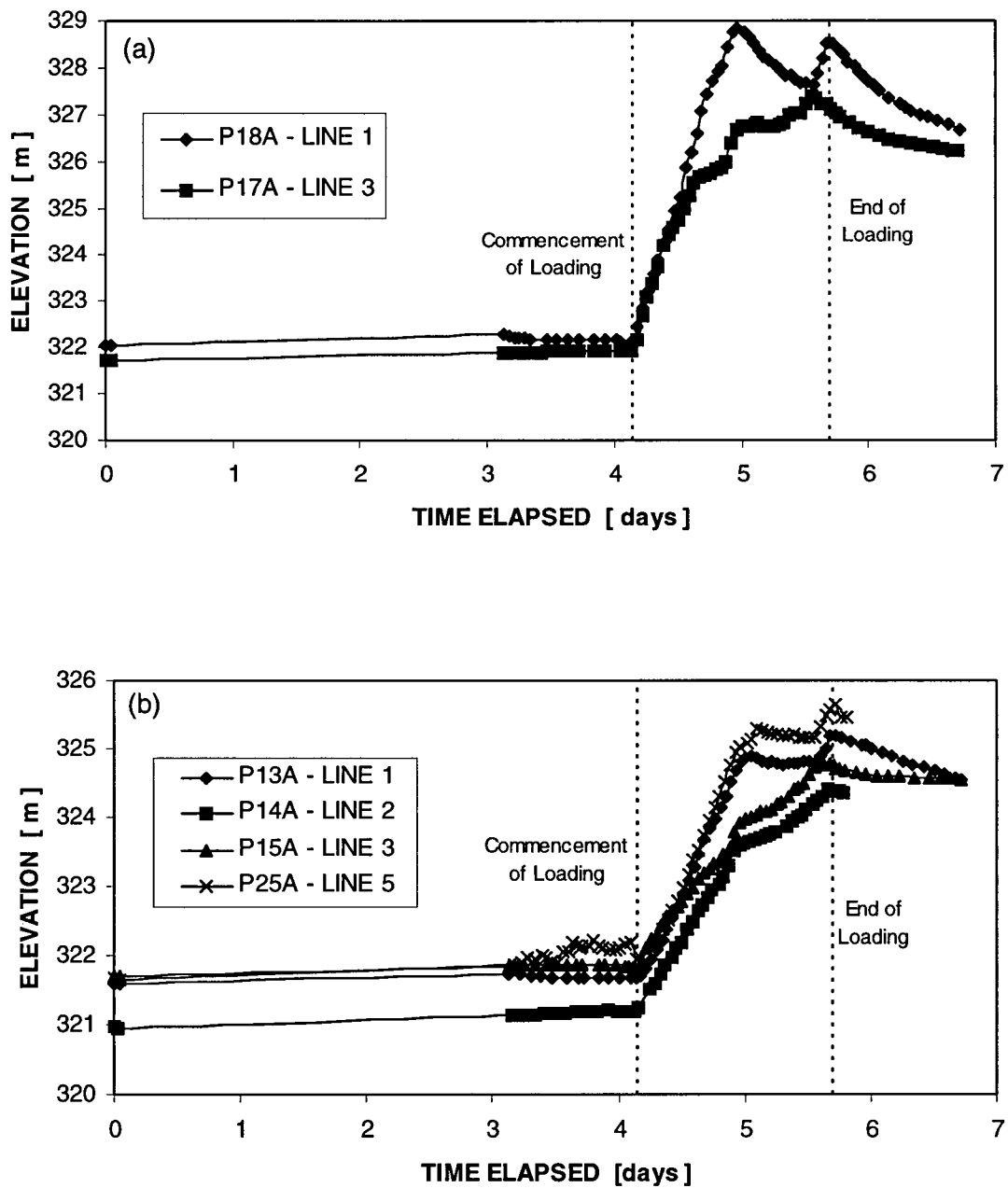


Figure 8.3 Pore pressure response to embankment loading in terms of piezometric heads along Lines 1, 2, 3 and 5 (after Natarajan et al., 1996). (a) Section A. (b) Section B. (c) Section C. (d) Section D. See Figure 8.2 for location of lines and sections.

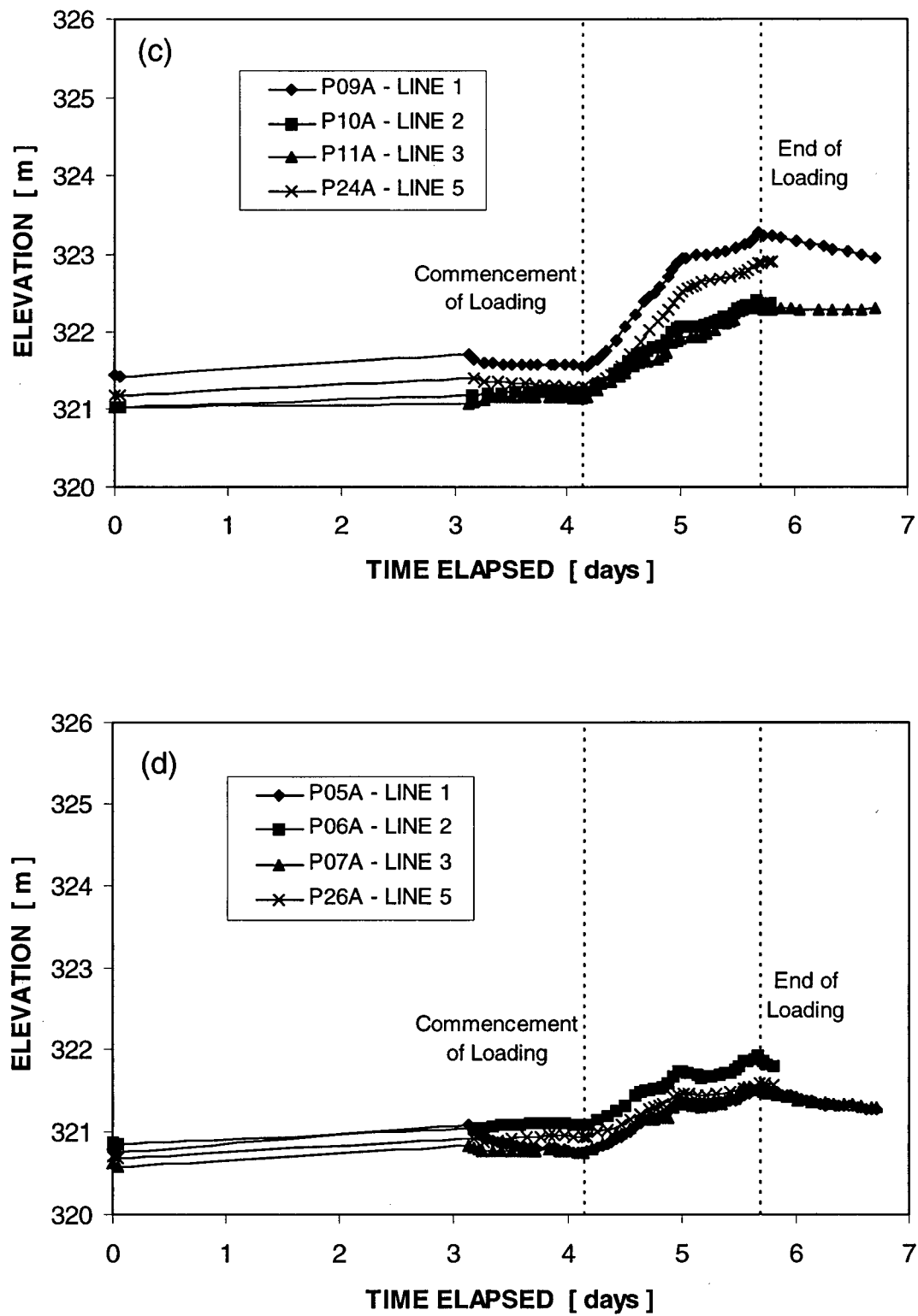


Figure 8.3 Continued.

Table 8.1. Typical material parameters used for the earth-structures at the field event site.

Material	B ⁺ [kPa]	G ⁺ [kPa]	c ⁺ [kPa]	ϕ ⁺ [°]	k ⁺⁺ [m/sec]	ρ ⁺ [T/m ³]
Clay Dyke	30000	30000	30	0	1×10^{-8}	1.5
Sand Cell	30000	30000	0	36	8×10^{-6}	2.0
Contained	10000	100	2	0	1×10^{-4}	1.7
Tailings Sand						
Soft Clay	10000	2000	10	0	1×10^{-11}	1.1

Note: B and G are elastic bulk and shear moduli, respectively; c, is the cohesion; ϕ, the friction angle; k, the hydraulic conductivity; and ρ, the dry density.

⁺ Duncan et al. (1980) and Byrne et al. (1987).

⁺⁺ Terzaghi and Peck, 1967.

The parameters for the stress-strain model used to simulate the response of the foundation sand were obtained by back analysis of UBC element test data from Vaid et al. (1995b and 1996). A list of these parameters was presented in Table 6.4. UBC tests were chosen over C-CORE tests for calibrating the stress-strain model because they were carried out on water pluviated specimens and hence, they were considered to resemble the characteristics of the field foundation layer more closely.

The boundary conditions on the numerical model were as follows: zero horizontal displacements on the vertical boundaries at x = -30 and 300 m (Figure 8.1), and zero horizontal and vertical displacements on the bottom boundary (natural ground surface, Figure 8.1). The water table was horizontal and coincided with the surface of the target layer (BBW-Sand) before the load was applied. After loading, the water level on the upstream side of the embankment was assumed to coincide with Elevation 327 m (maximum water height of 6 m, Natarajan et al. 1996). On the downstream side of the dyke, the water level was assumed to coincide with the surface of the sand layer (Elevation 321 m).

The rapid placement of the contained sand comprised the “loading”. Under this loading, two different assumptions were made regarding the drainage conditions of the target sand (foundation sand): 1) partially drained (coupled stress-flow), and 2) undrained conditions. These assumptions led to two separate analyses and allowed investigation of the effects that rate of loading would induce in the embankment response to such loading.

8.2.1 Initial state of stress in the foundation layer

Based on findings from modelling the centrifuge experiment (Sections 7.5 and 7.8.3), the initial state of stress in the foundation layer of the field event was obtained by assuming a fully drained response of the tailings sand during its placement. The numerical procedure used for this stage of analysis was essentially the same as that utilized for simulating the centrifuge model construction (Section 7.4). However, in this case the water table was located as discussed in the previous section and deposition of tailings sand was simulated by gradually placing 10 lifts of 1 m each. After gradual placement of each lift, the numerical model was brought to equilibrium. The initial state of stress attained at the end of the analysis was characterized in the same manner as for analyzing the centrifuge experiment. The ratio $1/k_c = \sigma'_v / \sigma'_h$ obtained in the foundation layer was 0.56 for the region in which the bottom boundary was approximately horizontal (natural ground, $x > 125$ m in Figure 8.1). For the region in which the bottom boundary was inclined ($x < 125$ m), the ratio $1/k_c$ was slightly greater ($1/k_c = 0.61$) as result of higher horizontal stresses induced by the slope of the natural ground in this zone.

8.2.2 Numerical simulation of Clay Embankment and Compacted Sand Cell construction

The construction of both, clay embankment and compacted cell sand was numerically simulated by progressively placing 8 lifts of 1 m each. Lifts of each material were placed simultaneously and gradually in their corresponding location. After placement of each lift, the numerical model was brought to equilibrium. Since in the field the construction of both structures was carried out slowly enough as to allow dissipation of excess pore pressures in the target layer, a fully drained response of the foundation sand was assumed for numerical simulation.

The final configuration of the numerical system after construction of these structures is shown in Figure 8.4. The direction of the major and minor principal stresses in the region where the clay embankment was located is presented in Figure 8.5. It can be noted in this figure that the direction of the principal stresses, originally coinciding with the vertical and horizontal orientations, changed as a consequence of building the clay dyke.

8.2.3 Numerical simulation of CANLEX Embankment and Foundation Layer response to loading under partially drained conditions

Loading of the field embankment was commenced at 17:15 hours on September 18, 1995, and concluded at 06:30 hours on September 20, 1995. Hence, the rate of loading in the field was approximately 19 cm/hr. Using the same rate of loading in the numerical simulation and a coupled stress-flow approach, loading under partially drained conditions

was modelled. This approach allowed accounting for pore pressure generation and dissipation during and after load application.

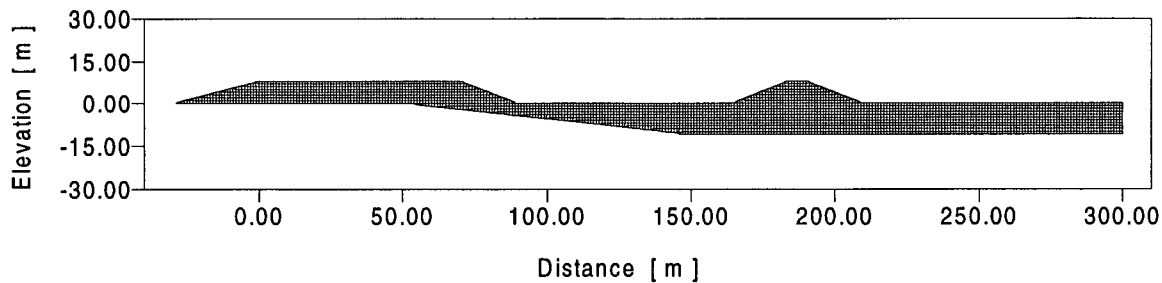


Figure 8.4 Configuration of the numerical system after construction of clay dyke and sand cell.

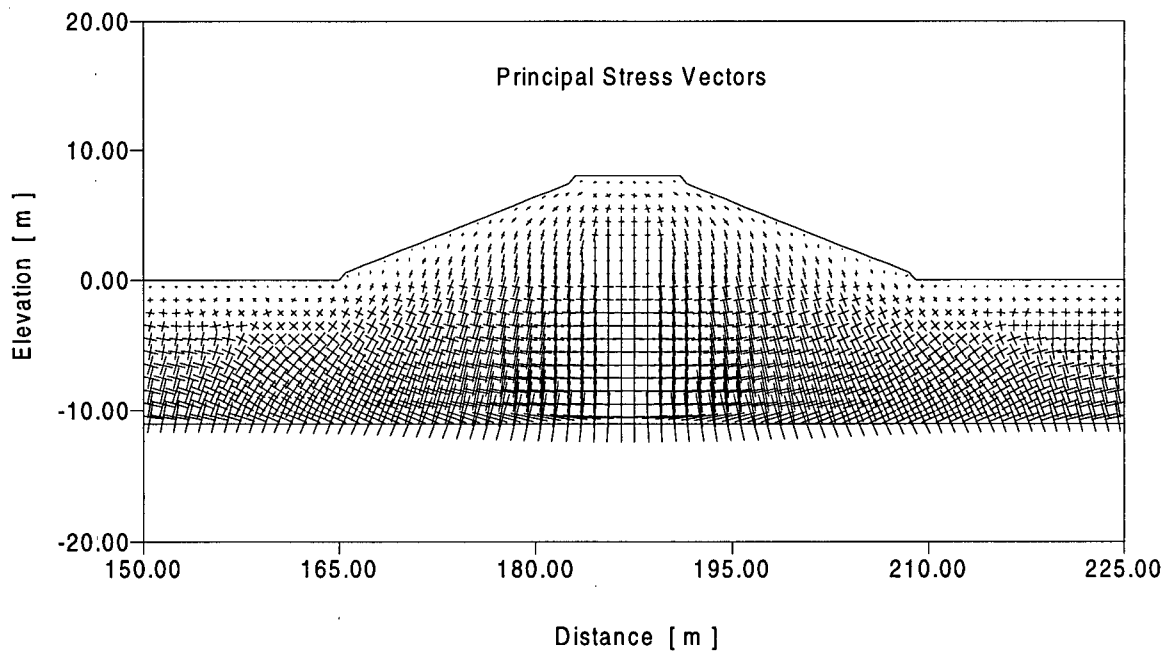


Figure 8.5 Direction of major and minor principal stresses in the region where the clay embankment was located immediately after construction.

Seven lifts of 1 m each were placed gradually to simulate the pumping of tailings sand behind the clay embankment. Placement of each lift was carried out in 319 minutes of flow-time (approximately 19 cm/hr). Once the contained sand (heavy fluid) was placed rapidly (37 hours), its surface became a drainage boundary with pore pressure equal to zero. The surface of the tailings downstream of the toe was also specified as a drainage boundary with pore pressure equal to zero. The vertical boundaries at $x = -30$ and 300 m (Figure 8.4), as well as the bottom boundary (natural ground surface), were considered impermeable. Seepage flow into all the zones within the boundaries was considered. The hydraulic conductivity of the foundation sand was based on field experience at the Syncrude site (Tan, 1995), which indicated that the horizontal hydraulic conductivity was 15 times greater than the vertical. The values used for the analysis were: $k_x = 7.5 \times 10^{-6}$ m / sec and $k_y = 5.0 \times 10^{-7}$ m / sec. The hydraulic conductivity of the clay dyke was assumed to be $k = 1.0 \times 10^{-8}$ m / sec (Terzaghi and Peck, 1967), while the contained sand (heavy fluid), was considered to have a hydraulic conductivity $k = 1.0 \times 10^{-4}$ m / sec (Terzaghi and Peck, 1967).

A comparison between predicted and measured time-histories of excess pore pressures in Sections B, C and D (Figure 8.2) during and immediately after loading the test embankment is presented in Figure 8.6. The predicted response of pore pressures agreed very well with observations during the first 21 hours of loading; afterwards, the pore pressures were overpredicted. However, it is evident that after the first 21 hours of loading the observed pattern of pore pressures changed its trend, while the predicted pattern did not change. Hofmann et al. (1996) suggested that the observed change in pattern of pore pressures was the result of applying the full water load in 12 hours, while

the full tailings sand load was accomplished in approximately 36 hours. Due to the characteristics of the program used to carry out the analysis (FLAC), it was not possible to exactly replicate such loading conditions in a simple manner. In the numerical modelling, the levels of water and tailings sand were raised at the same rate. Therefore, small differences between predicted and observed values were expected.

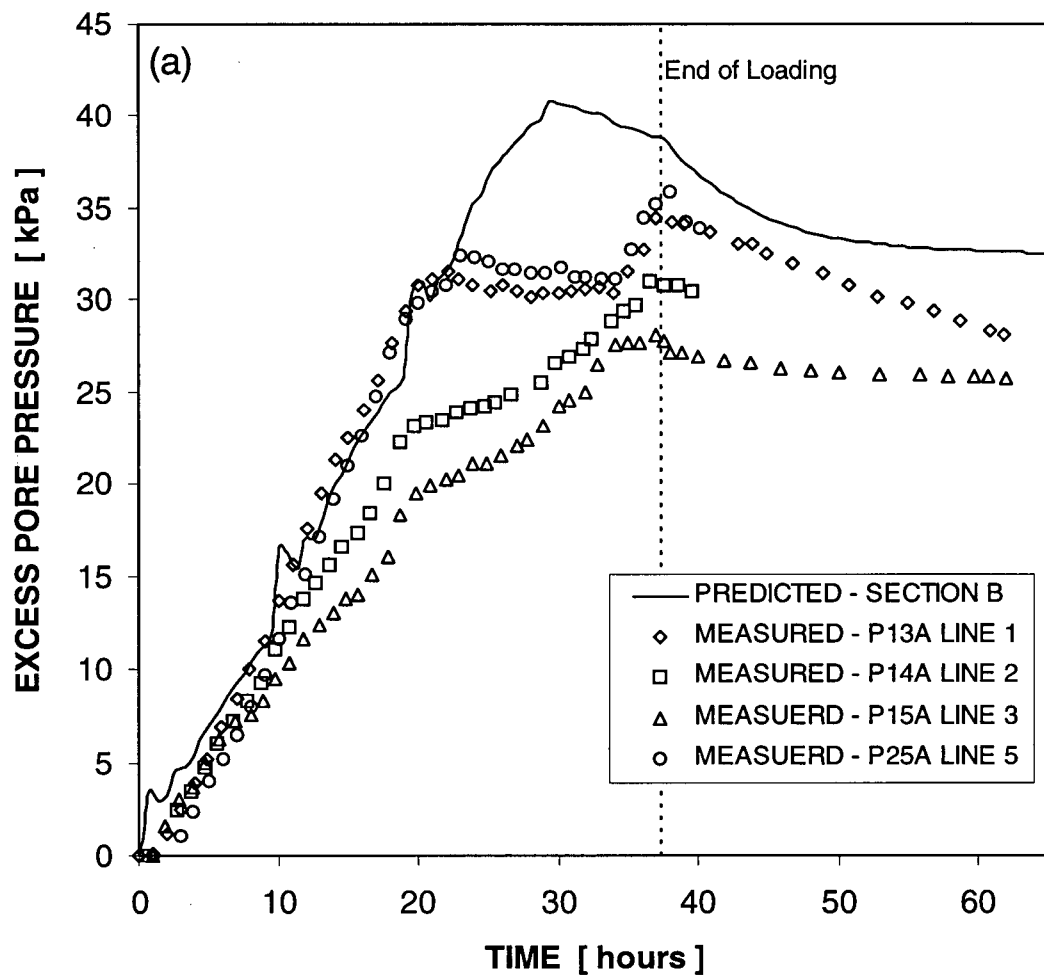


Figure 8.6 Comparison between predicted and measured time-histories of excess pore pressures during and immediately after loading the test embankment. (a) Section B. (b) Section C. (c) Section D. The location of Sections B, C and D can be found in Fig. 8.2.

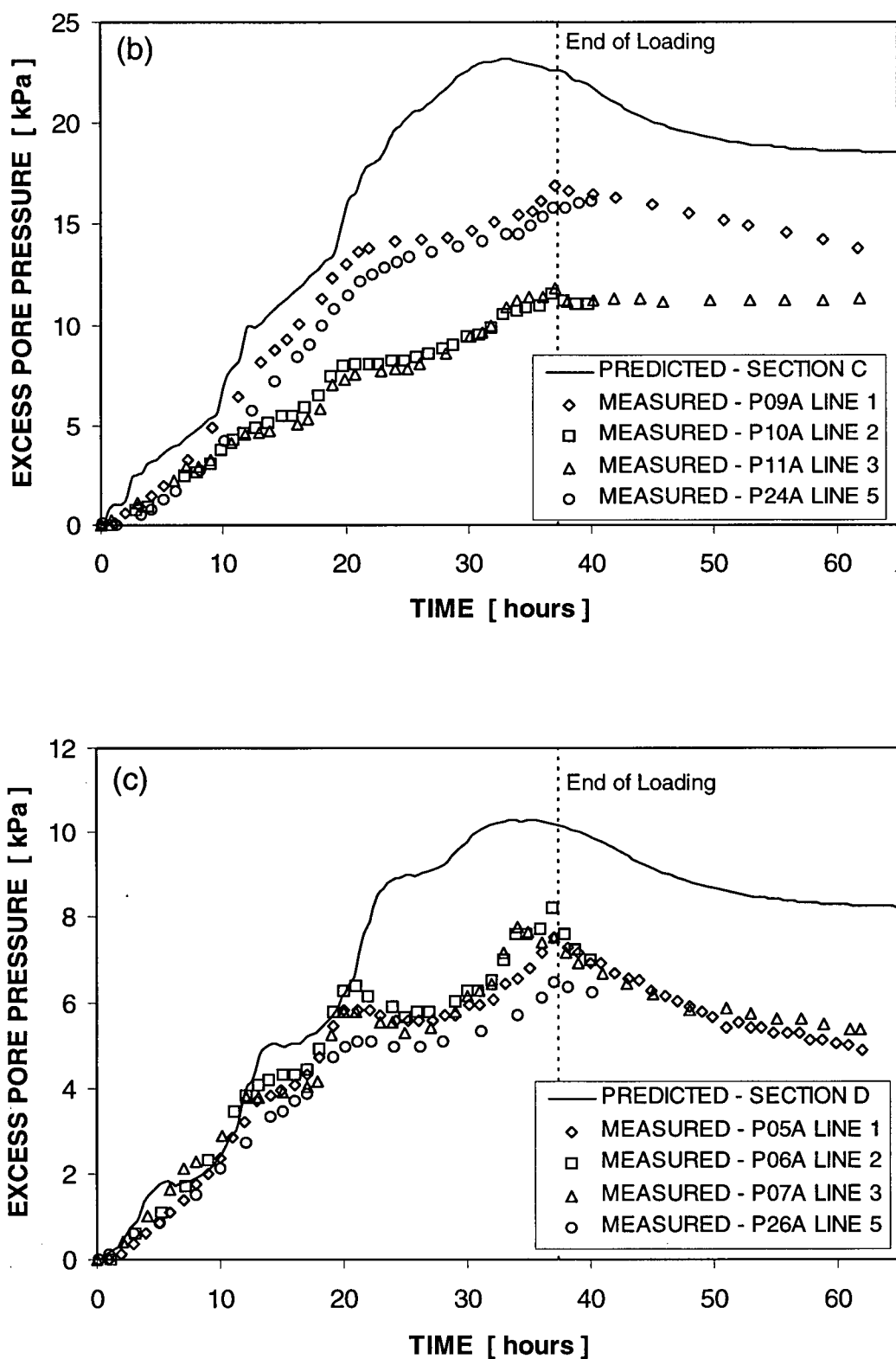


Figure 8.6 Continued.

The predicted pattern of displacements is shown in Figure 8.7. It can be observed that displacements in the order of 3 cm were predicted to the full depth on the upstream side of the embankment, dropping rapidly with depth under the downstream slope of the dyke. Beyond the Toe of the clay embankment, the predicted movements were small. The maximum displacement of the dyke was predicted in the toe area and had a magnitude of about 1.3 cm. This value compares well with the average observed displacement of 2 cm.

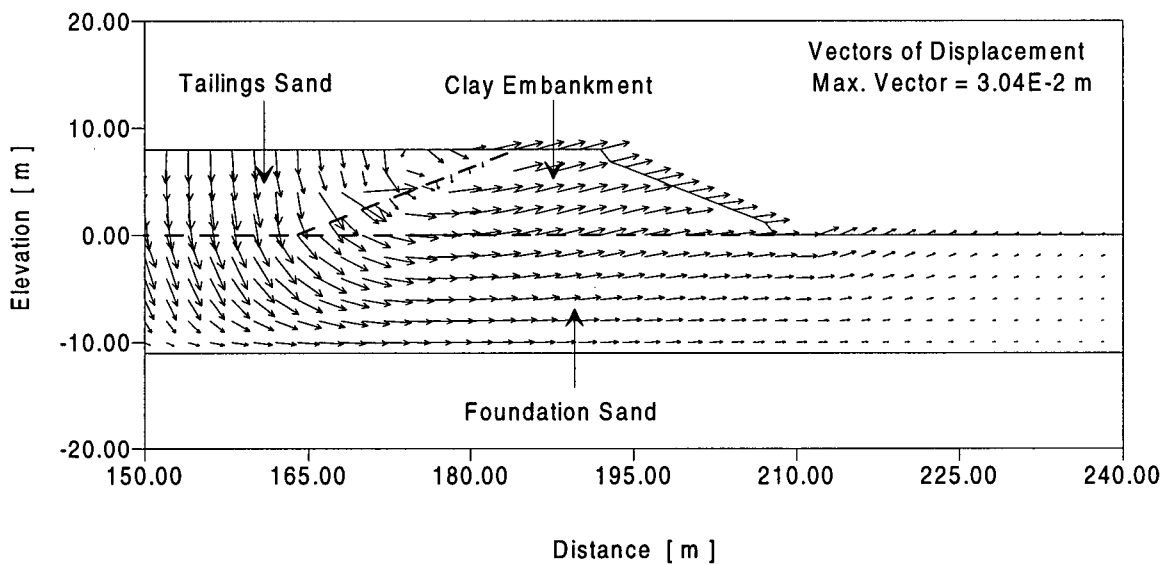


Figure 8.7 Pattern of displacements predicted under partially drained conditions.

Contours of predicted total pore water pressure after the steady state seepage condition was reached are presented in Figure 8.8. The contours showed an almost hydrostatic distribution of pore pressures beneath the applied load and beyond the downstream slope of the embankment. In turn, this suggests that under the applied loading, the foundation layer had a high capacity for dissipating excess pore pressure; i.e.

either the hydraulic conductivity of the foundation layer was too high, the rate of loading was not fast enough, the magnitude of the applied load was not large enough, or a combination of these factors.

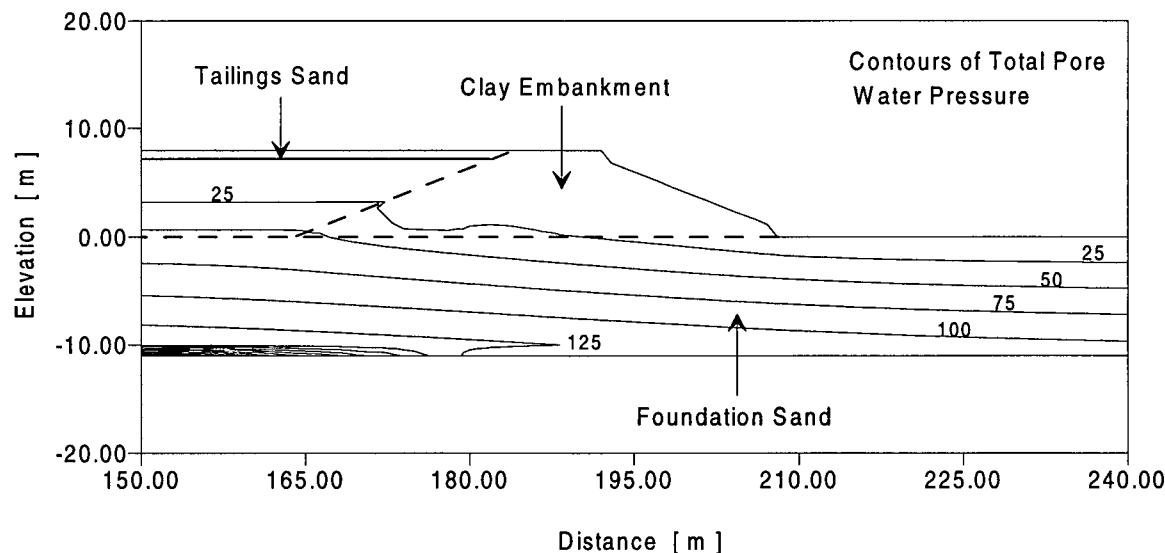


Figure 8.8 Contours of predicted total pore water pressure after the steady state seepage condition was reached.

Another essential factor influencing the response of the embankment to loading was the direction of loading. Laboratory testing showed that under undrained conditions and if loaded in compression mode, the foundation sand exhibited a dilative type of response and had an average normalized undrained strength ratio, (s_{ur}/s_o), of about 0.3. In contrast, when loaded in extension mode, the response was contractive and had an average $s_{ur}/s_o \approx 0.06$. As can be seen from the orientation of the principal stresses shown in Figure 8.9, only a small region near the Toe of the embankment was subjected to extension mode of loading and hence, the foundation layer could have not responded in a strain softening manner.

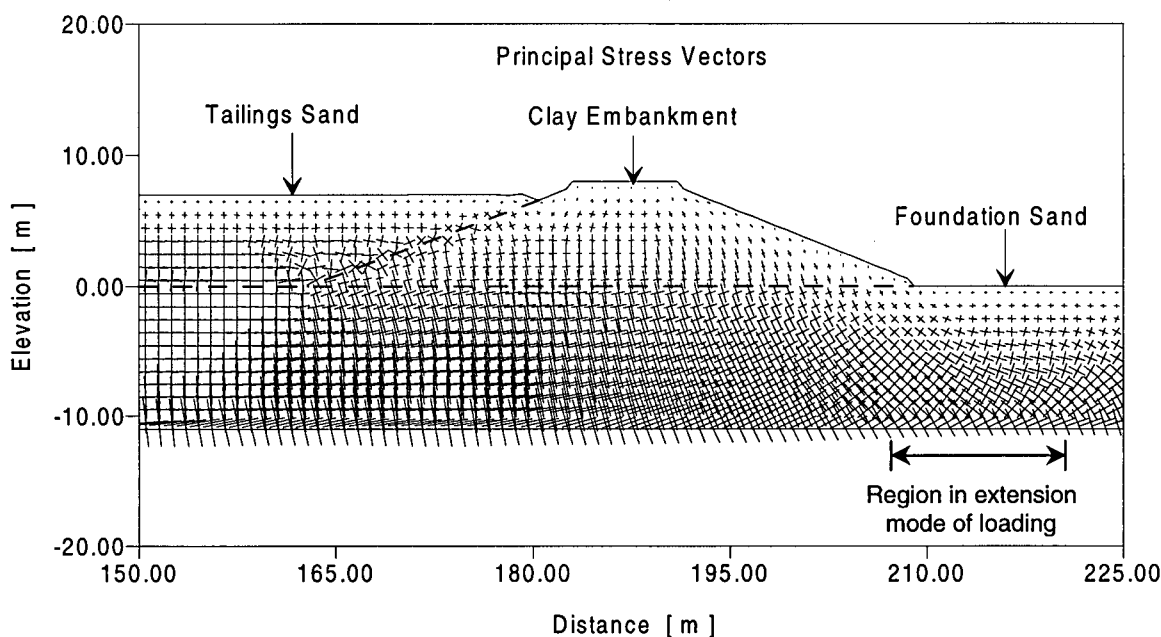


Figure 8.9 Orientation of principal stresses after pumping tailings sand behind the clay dyke under partially drained conditions.

The observed response of the test embankment and foundation layer to loading seemed to be reasonably well captured by the numerical simulation discussed above. Both the observed and predicted responses indicated that the pore pressures induced by pumping tailings behind the dyke were rather low and unlikely to trigger liquefaction in the foundation layer. However, the aim of CANLEX field event was to statically trigger a liquefaction flow slide and this did not occur in the field. In an attempt to establish the factors that prevented the occurrence of such failure, numerical simulations of the field event were carried out assuming different loading conditions; i.e., loading under undrained conditions and applying a larger load. In addition, the implications of using the state-of-the-practice approach in which the s_u/s_o is considered independent of the direction of loading will be investigated. Results from these numerical analyses will be presented in the sections to follow.

8.2.4 Numerical simulation of CANLEX Embankment and Foundation Layer response to loading under undrained conditions

Assuming an undrained response of the foundation sand allowed investigating the influence that the hydraulic conductivity of the target layer and the rate of loading had in the test embankment response to loading. To avoid shocking the system by applying a large load instantaneously, loading was brought about using the same type of numerical procedure explained in Section 8.2.3. However, for the case currently under discussion, loading was simulated by placing the 7 lifts of tailings sand under undrained conditions. After placement of each lift, the numerical system was brought to equilibrium. The procedure was repeated until the seventh lift was placed.

The predicted pattern of displacements is shown in Figure 8.10. It can be observed in this figure that displacements in the order of 7 cm were predicted to the full depth on the upstream side of the embankment, dropping with depth under the downstream slope of the dyke. Beyond the Toe of the clay embankment, the predicted movements were small. In contrast with the previous analysis, the dyke was predicted to move uniformly about 2.6 cm in the horizontal direction. Preventing the effects of drainage on dissipation of excess pore pressure led to predict displacements of about double the values predicted for partially drained conditions.

Contours of predicted total pore water pressure after the state of equilibrium was reached under undrained conditions are presented in Figure 8.11. The contours indicated large pore pressures beneath the applied load, but beyond the downstream slope, the effects of the load on pore pressure were not significant. Lack of excess pore pressure

beyond the Toe of the embankment is the likely reason for the small displacements in this region.

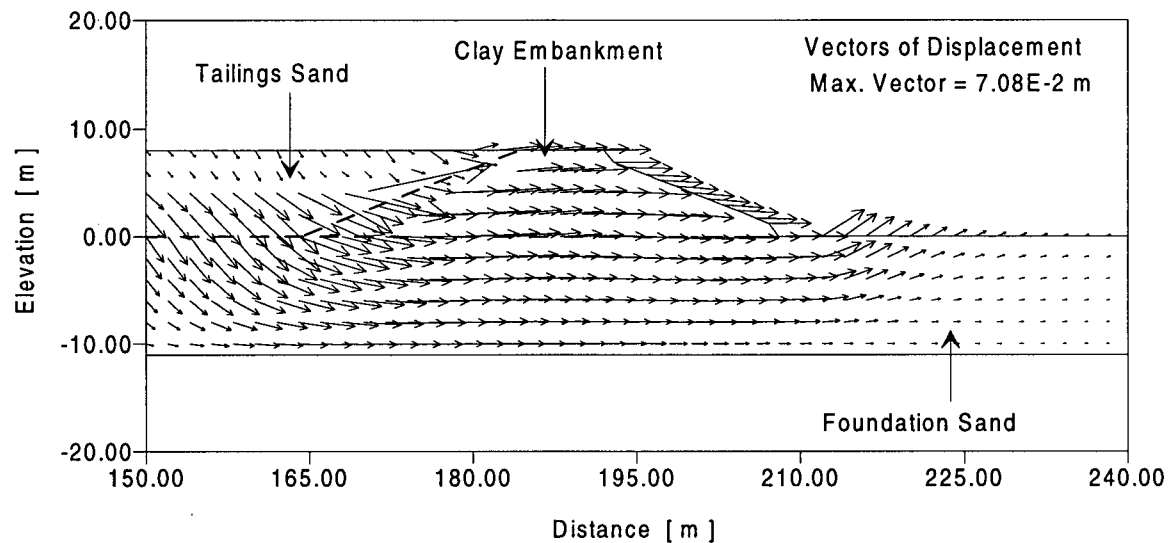


Figure 8.10 Pattern of displacements predicted under undrained conditions.

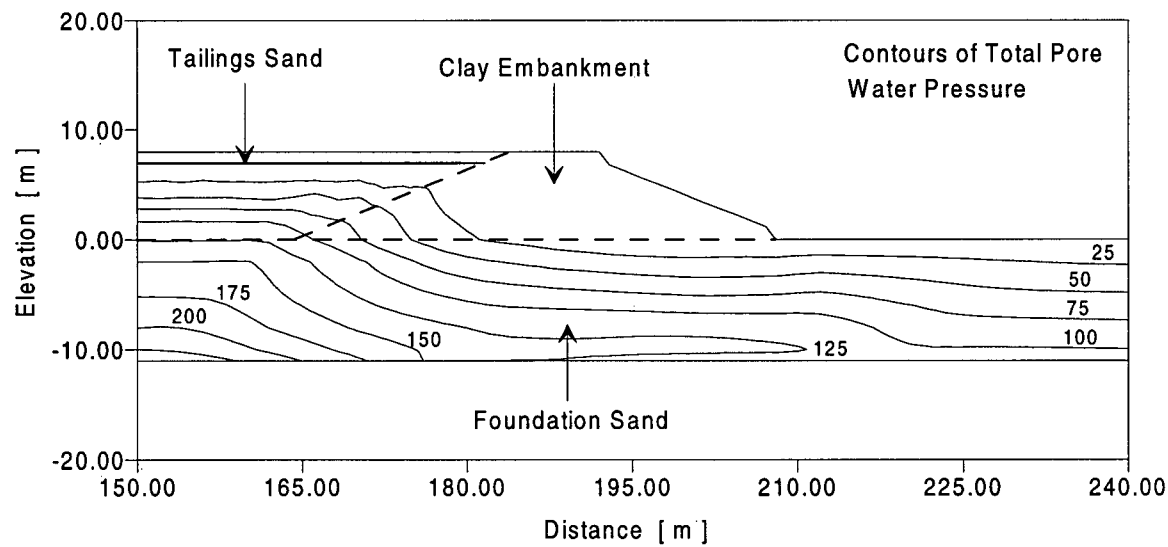


Figure 8.11 Contours of predicted total pore water pressure after the state of equilibrium under undrained conditions was reached.

From the results presented above, it can be seen that both, rate of loading and drainage conditions influenced the predicted response of the system to loading. However, liquefaction in the target sand was not triggered under the analyzed loading conditions. Furthermore, Figure 8.12 shows the predicted stress paths in an element located at mid depth of the foundation layer and 10 m downstream from the Toe, under both partially drained and undrained conditions. Such location corresponds to Section D, shown in Figure 8.2, but 5 m below the ground surface. At this location, the target layer was loaded in extension mode. As it can be noted in Figure 8.12, the applied load was not large enough to induce stresses in the foundation sand that would reach the undrained peak strength of the soil.

8.2.5 Hypothetical case in which the height of the embankment would have been 16m

A hypothetical case in which the height of the embankment would have been 16 m instead of 8 m will be presented in this section. For ease of analysis, the clay dyke, sand cell and tailings sand were scaled to 16 m of height by doubling the density of the materials comprising these structures, while their geometry was not changed. The initial state of stress under these new conditions was determined following the same procedure used to simulate the construction process in Section 8.2.2. Loading was applied under undrained conditions and the numerical procedure utilized for simulating the pumping of tailings sand behind the dyke was the same as that used in Section 8.2.4.

The predicted stress path at mid depth of the foundation layer and 10 m downstream from the Toe is presented in Figure 8.13. The stress path shown in the figure

indicates that in this region and under the analyzed loading condition, the foundation layer would have exhibited a strain softening type of behaviour.

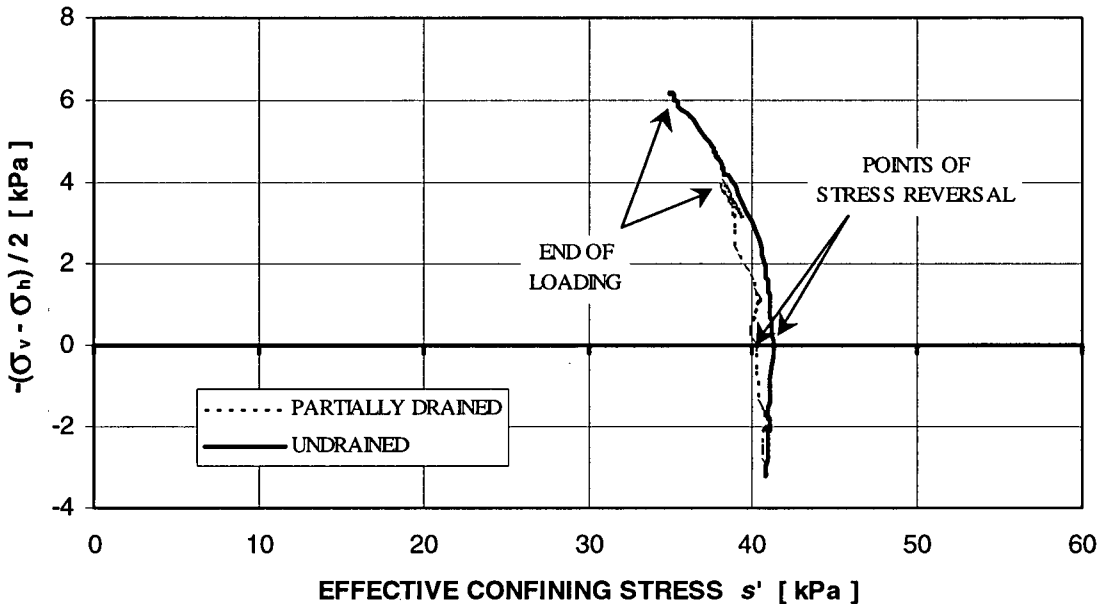


Figure 8.12 Predicted response at mid depth of the foundation layer in Section D (see Fig. 8.2).

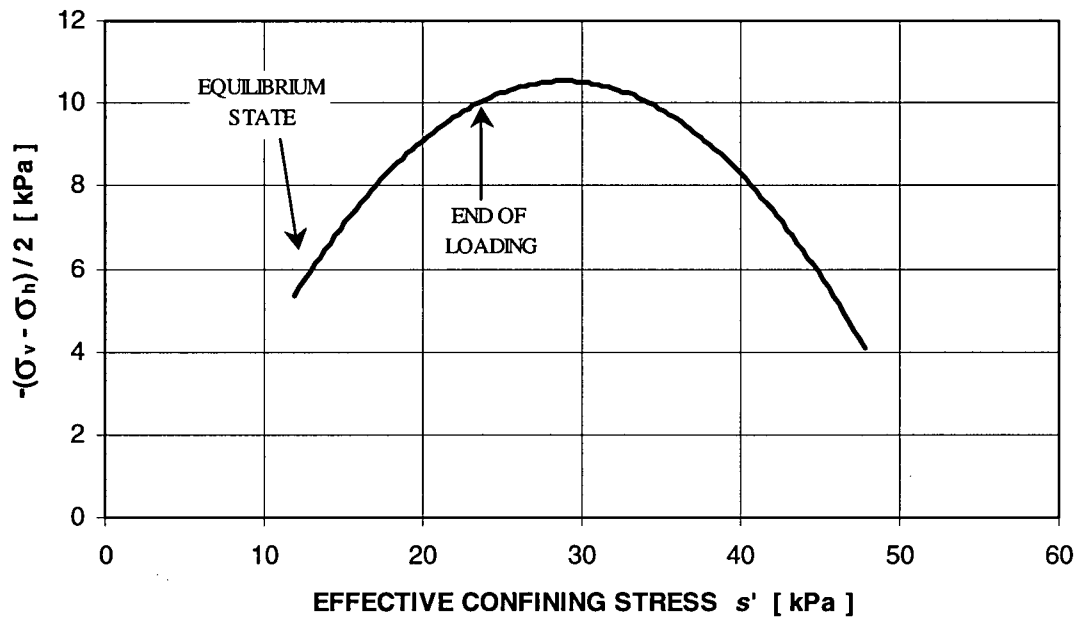


Figure 8.13 Predicted undrained response at mid depth of the foundation layer in Section D (see Fig. 8.2), had the embankment height been 16 m in stead of 8 m.

The predicted pattern of displacements is shown in Figure 8.14. Significant displacements under the dyke and beyond the Toe were predicted with values in excess of 1.0 m in the toe area. The pattern of displacements was deep seated and typical of a liquefaction failure.

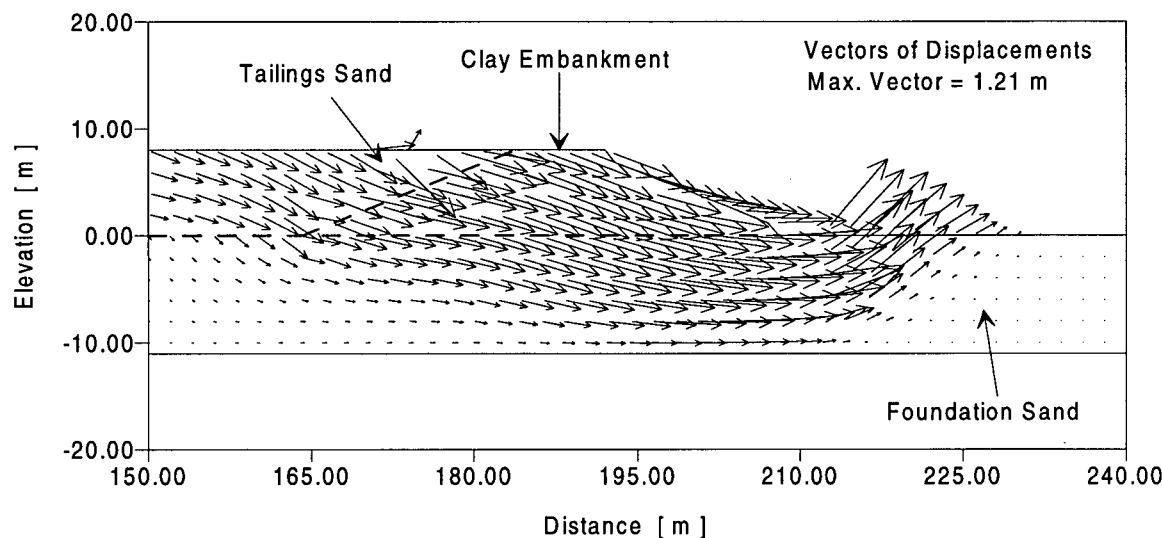


Figure 8.14 Predicted pattern of displacements, had the embankment height been 16 m instead of 8 m and loaded under undrained conditions.

The predicted contours of total pore water pressure are shown in Figure 8.15. High pore pressures were now predicted in the toe area indicating, a link between high values of predicted pore pressure and large displacements beyond the toe.

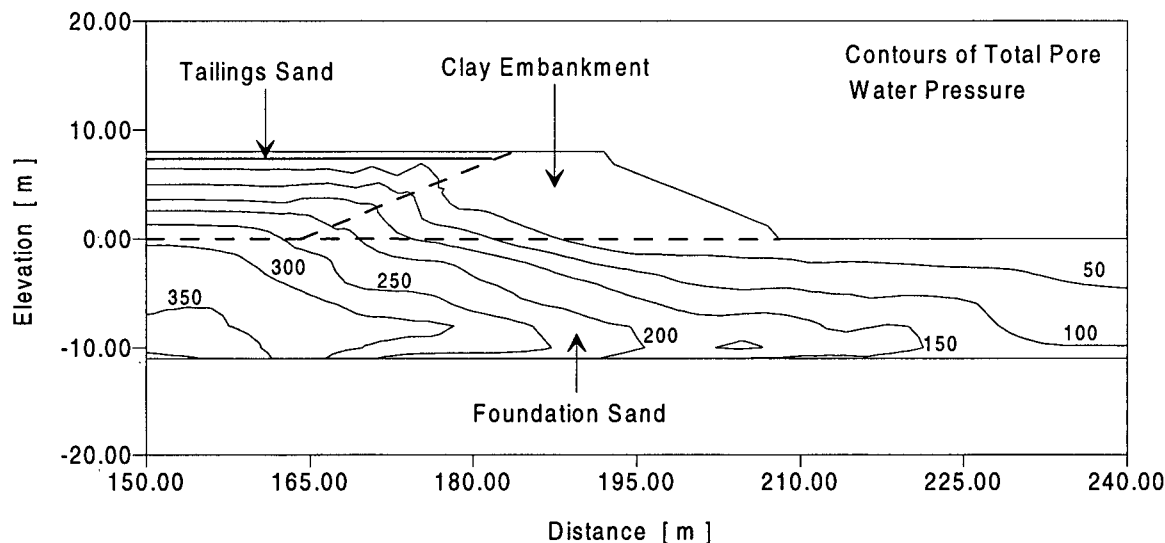


Figure 8.15 Predicted contours of total pore water pressure, had the embankment height been 16 m instead of 8 m and loaded under undrained conditions.

Results from this analysis showed that had the embankment height been 16 m instead of 8 m, then rapid undrained loading would have triggered a static liquefaction failure.

8.3 Implications of using the state-of-the-practice approach for liquefaction analysis

The current practice in engineering for carrying out liquefaction analysis is to use a normalized strength ratio s_{ur}/s_o based on penetration resistance and field experience, and to neglect direction of loading as well as partial drainage effects. Some implications that this approach has in predicting the response of a system to loading will be discussed in this section.

It will be recalled that in Section 4.3.3 the plastic shear anisotropy factor, F , was introduced into the constitutive model to account for direction of loading effects. By making F equals unity, the response predicted by the stress-strain model becomes independent of direction of loading and the predicted normalized undrained strength

ratio, s_{ur}/s_o , becomes then constant. Therefore, the constitutive model can be easily used to carry out analysis with specific and constant values of the ratio s_{ur}/s_o .

Based on laboratory data (Vaid et al. 1996), a normalized undrained strength ratio of 0.06, which corresponded to the extension mode of loading, was selected for analyzing the CANLEX embankment under undrained conditions and constant s_{ur}/s_o .

The predicted pattern of displacements and contours of total pore water pressure are presented in Figure 8.16. As can be seen in Figure 8.16a, a liquefaction failure was now predicted, with displacement in excess of 3.0 m in the Toe area. In terms of pore pressures, these were high in the Toe region as can be noted in Figure 8.16b. Note also that in comparison with the case in which the height of the dyke was assumed to be 16 m, the predicted displacements were now larger and the failure surface higher.

As shown by the results of this analysis, neglecting the effects that direction of loading has in the undrained strength of the soil could be unduly conservative. When a variable s_{ur}/s_o based on laboratory test data was accounted for in analysis for both, partially drained and undrained conditions (Sections 8.2.3 and 8.2.4), a liquefaction failure was not predicted. Because the strength in the compression zone, upstream of the crest of the dyke, was so high, the stresses in the potential strain softening zone in the Toe region never rose to their peak value. Hence, the foundation sand did not strain soften and a liquefaction failure did not developed. However, by assuming a constant s_{ur}/s_o that corresponded to the extension mode of loading, the variation of s_{ur}/s_o with direction of loading was neglected. This in turn led to predict the occurrence of a liquefaction failure under undrained conditions.

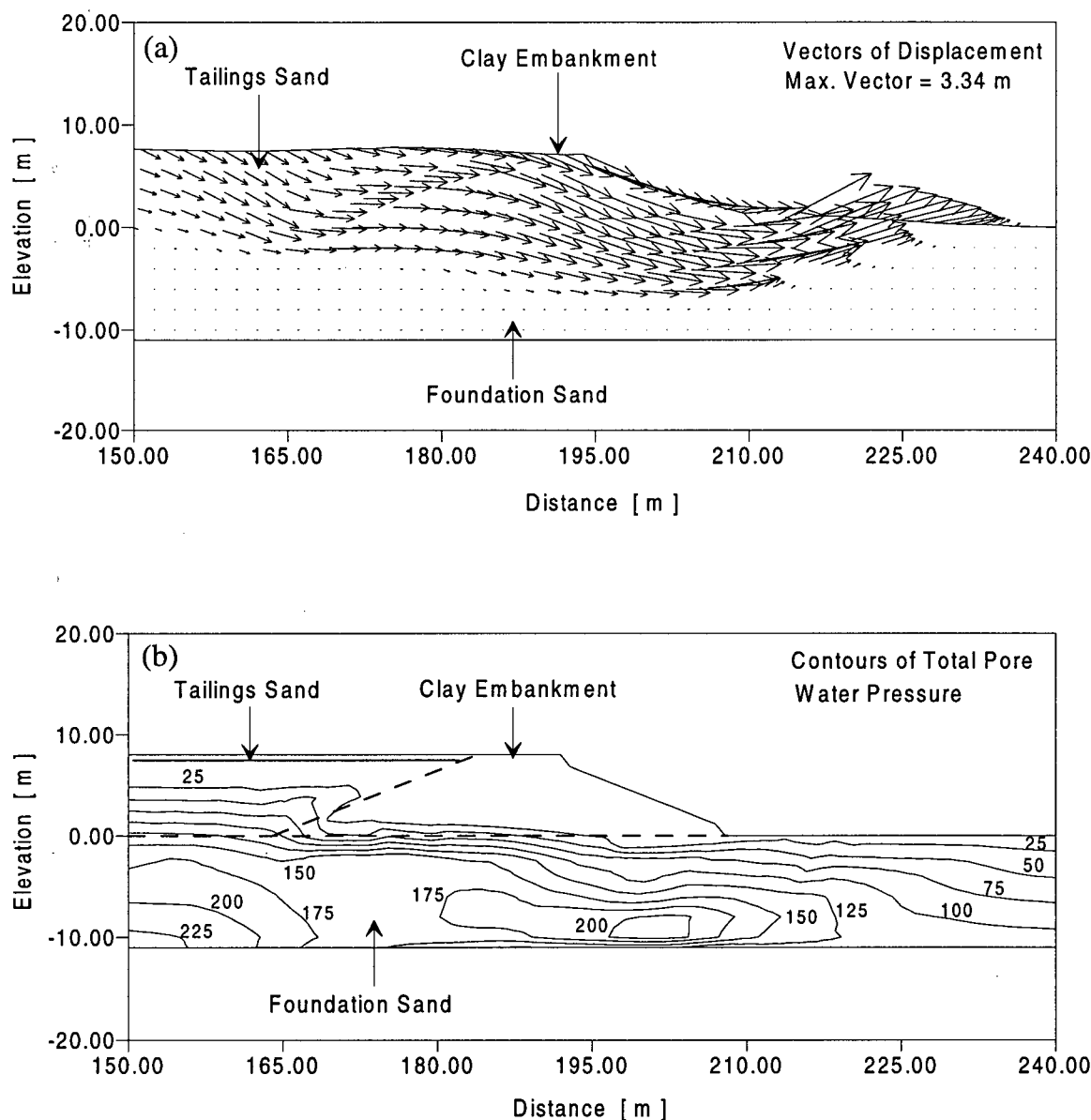


Figure 8.16 Results from undrained analysis of CANLEX field event carried out assuming a s_{ur}/s_o ratio constant (independent of direction of loading) and equal to 0.06. (a) Pattern of displacements. (b) Contours of total pore water pressure.

A second analysis assuming s_{ur}/s_o constant and equal to 0.06 was carried out, but accounting for partially drained as opposed to undrained conditions. The predicted pattern of displacements and contours of total pore water pressure are presented in Figure

8.17. As can be seen in this figure, a liquefaction failure was not predicted, the computed displacements were small and the excess pore pressures in the Toe region were low.

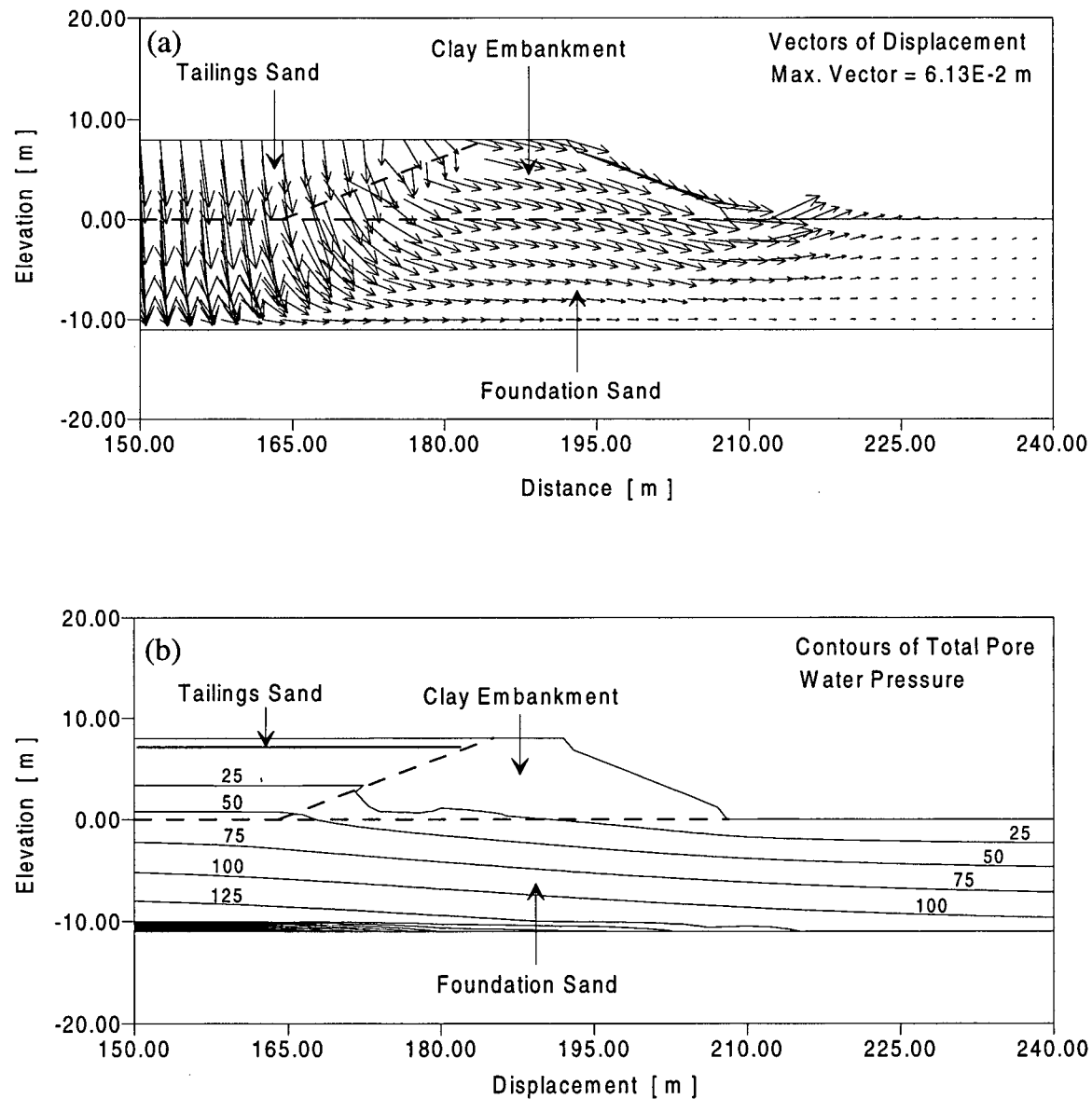


Figure 8.17 Results from partially drained analysis of CANLEX field event carried out assuming a s_{ur}/s_o ratio constant (independent of direction of loading) and equal to 0.06. (a) Pattern of displacements. (b) Contours of total pore water pressure.

Therefore, it can be seen from the observed response in the field event and results of the analyses presented here that the state-of-the-practice approach implies assumptions that may be unduly conservative when designing against a static liquefaction failure.

8.4 Conclusions from CANLEX Field Event analysis

From the analyses carried out to simulate the CANLEX field event and discussed in Sections 8.2 and 8.3, the following conclusions can be drawn:

- The elastic-plastic stress-strain model and the numerical procedure used in these analyses were appropriate for simulating CANLEX field event.
- The numerical simulation of CANLEX field event carried out under partially drained conditions captured the observed response reasonably well.
- Neglecting the effects of partial drainage (undrained conditions) in the analysis led to predict displacements that were twice the values predicted under partially drained conditions.
- Both rate of loading and drainage conditions were shown to significantly influence the predicted response of the test embankment to loading.
- The reason for small displacements beyond the Toe of the embankment was the lack of excess pore water pressure generated in this region.
- Excess pore water pressures did not rise sufficiently to induce liquefaction in the foundation sand because the applied load was not large enough and was not applied quickly enough.
- Analysis showed that had the embankment been 16 m high instead of 8 m, then rapid undrained loading would have triggered a static liquefaction failure.

- The variation of the strength with direction of loading was shown to be an essential factor controlling whether stability of the test embankment was predicted or not.
- The state-of-the-practice approach, in which direction of loading and partial drainage effects are neglected, may be unduly conservative because: (i) the variation of strength with loading direction is significant; (ii) the strength in compression zones may be much higher than assumed; and (iii) drainage can lead to significantly increased strength.

CHAPTER 9

SUMMARY, FINDINGS AND FURTHER STUDIES

9.1 Summary and findings

Due to static liquefaction, catastrophic consequences including loss of life, deterioration of the environment and severe damage or even destruction of structures and facilities, have been observed on numerous occasions. For these reasons, reliable methods for predicting these phenomena are important. Although, various analytical methods have been developed to fulfill this need, only a few of them are suitable for carrying out adequate static liquefaction analysis. Methods that are simple enough for use in engineering practice and at the same time account for the main features of sand behaviour regarding liquefaction phenomena, are not available. Therefore, the first objective of this dissertation was to develop a relatively simple constitutive model for analyzing sand static liquefaction. Towards this goal, sand behaviour as observed from laboratory tests was analyzed in Chapter 2, to establish the most important issues to be considered in liquefaction analysis. The main features of sand behaviour were identified and interpreted within an elastic-plastic framework in Chapter 3. Based on physics fundamentals, rather than curve fitting techniques, and incremental elastic-plastic theory,

a constitutive model capable of capturing sand characteristic behaviour was presented in Chapter 4.

The proposed constitutive model was incorporated into a commercially available computer program, FLAC (Cundall, 1995). The code uses the finite difference method and satisfies dynamic equilibrium using a step-by-step explicit time domain procedure. This program allows solving boundary value problems accounting for groundwater flow and large deformations. The numerical implementation of the model, the different types of analysis regarding drainage conditions and the modelling of the single element behaviour were discussed in Chapter 5.

For practical purposes, the ease with which a constitutive model is calibrated for modelling the behaviour of a specific soil is very important. Hence, only data from conventional laboratory tests was used for calibrating the proposed model, as discussed in Chapter 6. This approach is limited since stress paths other than those used to calibrate the model are not specifically taken into account. However, the model was shown to capture reasonably well the drained and undrained characteristic response of Syncrude sand as observed from laboratory element tests over a range of confining stresses, and two stress paths not specifically considered in the model's calibration, i.e., undrained plane strain and undrained triaxial extension that included a state of stress reversal. The element tests utilized for calibrating the model included triaxial compression and extension, as well as simple shear tests, performed on specimens reconstituted by air and water pluviation. Two sets of model parameters were used to capture the characteristic response of Syncrude sand: one for air pluviated specimens, and another for samples that were reconstituted by water pluviation. The reason for this differentiation was to account

for the two deposition methods used to build the CANLEX centrifuge model (air pluviation) and prototype (water pluviation). Since the response of sand to first time loading is strongly influenced by the environment in which the sand grains are deposited (Vaid et al., 1995a), it was considered important to take such conditions into account.

The calibrated constitutive model was used for modelling one of the CANLEX centrifuge tests. Test 1 (Phillips and Byrne, 1994) was chosen for analysis because it resembled the CANLEX field event most closely. The centrifuge embankment was modelled as a collection of elements, the response of which to loading was based on the single element behaviour. The centrifuge experiment was numerically simulated following the *construction process*; the building up of stress during “swing up” under fully drained and partially drained conditions, which in turn yielded two different initial states of stress; and the *loading stage* under both, undrained and partially drained conditions. The latter stage was modelled starting from the two different initial states of stress, i.e.: (i) the one predicted under an acceleration field of 50 g by assuming a fully drained response of the tailings sand, and (ii) the one obtained from the “swing up” stage simulation under partially drained conditions. In addition, effects of friction at the bottom boundary of the centrifuge model were investigated by using an interface element at this location and specifying different values of friction. The results from the analyses performed were presented and discussed in Chapter 7. The main findings from the numerical simulations of the centrifuge test were as follows:

- The proposed constitutive model and numerical procedure used to simulate the centrifuge experiment were shown to be adequate for carrying out analysis of sand liquefaction, triggered by rapid monotonic (static) loading, in centrifuge models.

However, it was found that the type of response measured in undrained triaxial compression tests and predicted by the model under such conditions did not agree with the type of response observed in the centrifuge model within the region of compressive loading. Possible explanations for such discrepancy will be discussed in a later point. In contrast, the observed response in the region of the centrifuge model in which liquefaction was triggered (region under extension type of loading) was reasonably well captured by the model. The latter achievement was possible because the model directly accounts for effects induced by direction of loading and states of stress reversal. Had such effects been neglected by the proposed constitutive model, it would have failed to predict liquefaction in this region. Models that assume isotropic expansion of the elastic region and/or do not account for effects induced by direction of loading cannot directly predict this type of response.

- The initial state of stress before load application was shown to strongly influence the predicted response of the centrifuge model to subsequent loading.
- The initial state of stress due to self-weight compression of the sand model appeared to be better estimated by assuming fully drained conditions during the consolidation process than by considering partial drainage during the swing up stage. However, due to the simplistic approach followed to overcome the lack of data for properly calibrating the model at very low stress levels and relative densities, a definite conclusion in this respect was not drawn. Further study of problems involving a wide range of stress levels is necessary to establish the applicability of the constitutive model to this type of problems, i.e., was lack of accuracy in predicted response due to

limitations of the constitutive model, or to insufficient data for calibrating the model according to the actual range of stress levels?

- The response of the centrifuge model to loading in terms of both pore pressures and displacements, was reasonably well captured by assuming a non-dilative behaviour of the tailings sand and following a coupled stress-flow approach in which partial drainage during and after application of loading was considered. Nevertheless, the analysis carried out under undrained conditions was found to provide an upper bound to predicted response, i.e., the most unfavorable condition that was predicted, and important insights about the problem.
- Results from the analyses carried out assuming a non-dilative behaviour of the tailings sand were consistent with the observed response in the actual centrifuge test. This is considered a very important issue since if dilation cannot be relied upon, the response of a system comprised of sand could be worse than originally expected. The reasons for such non-dilative behaviour were not determined. Nonetheless, these could be related to the state of density that could have been looser in the centrifuge embankment than in the laboratory specimens on which calibration of the constitutive model was based. In addition, using oil as a fluid in the centrifuge model, as opposed to water for laboratory testing, could have caused the friction angle at failure to decrease. This in turn would translate into a lesser tendency of the sand to dilate and larger induced displacements.
- Friction effects at the bottom boundary of the centrifuge model were shown to be very important in predicting the response of the system to loading.

The final goal of this dissertation was to numerically simulate the full-scale CANLEX field event in which a liquefaction flow slide triggered by rapid monotonic loading was attempted. The field event was modelled in the analysis by simulating the construction process and loading conditions. Both, CANLEX field event and numerical simulations of the event under partially drained and undrained conditions were described and explained in Chapter 8. In addition, an investigation for determining the factors that prevented the occurrence of a liquefaction failure in the field was carried out through numerical analysis. Furthermore, the state-of-the-practice approach for liquefaction analysis was used to predict the CANLEX field event and the implications of such procedure were discussed. The following were the main findings yielded by this endeavour:

- The response of the CANLEX embankment to loading as observed in the field was reasonably well captured by a numerical simulation in which the drainage conditions and loading rate were accounted for together with the proposed stress-strain model. Neglecting the effects of partial drainage (undrained conditions) led to predicted displacements that were twice the values predicted under partially drained conditions. However, a liquefaction flow slide was not predicted in either case, which was in agreement with field observations.
- Results from the analyses carried out to investigate possible reasons for not triggering a liquefaction flow slide in the field showed that the applied load was not large and fast enough. Had the embankment been 16 m high instead of 8 m, then rapid undrained loading would have triggered a static liquefaction failure.
- The variation of the strength with direction of loading and drainage effects was shown to be an essential factor controlling whether stability of the test embankment

was predicted or not. The state-of-the-practice approaches of analysis in which both effects are commonly neglected, and/or results from moist tamped samples are used, may be unduly conservative.

9.2 Further research

During the course of this research, some important problems were identified as topics in which further study is needed. In regard to the constitutive model presented here, this was developed to carry out the analysis of the CANLEX static liquefaction problem, i.e. liquefaction triggered by rapid monotonic loading. Thus, the cyclic behaviour of sand was not strictly simulated by the model, but only in a simplified manner. Since sand does not respond as a purely elastic material when the unload-reload loops are large, the elastic region of the proposed model needs to be reduced or furthermore, shrunk to a point in which case the entire response would be considered elastic-plastic. In addition, as discussed in Chapter 2, the unload-reload loops tend to close as cyclic irrecoverable (“plastic”) strains accumulate and hence, a hardening function that would allow capturing this effect is needed to complete the model. Both tasks could be implemented within the framework of the proposed constitutive model, but were left for future development since these were not essential to the CANLEX problem.

The effect of relative density in the stress-strain model response could be considered explicitly by making the stiffness moduli dependent on void ratio. In regard to this, several relationships between elastic moduli and void ratio can be found in the literature. Nonetheless, there is little knowledge regarding plastic parameters. This is considered an important area for further study since the “*cyclic-strain hardening*”

(unload-reload loops tendency to close as cyclic strains accumulate) response of sand observed during cyclic loading might be directly related to the change in the plastic moduli with void ratio.

It was pointed out in Chapter 6 that the effect of rotation of principal stresses appeared not to be fully accounted for by the constitutive model, as such rotation was observed in simple shear tests. Data from tests in which *pure* rotation of principal stresses occur, i.e. the mean stress s' and maximum shear stress t remain constant, must be analyzed and captured by the model to verify the adequacy of this part of the constitutive formulation. Further improvement of the model with this respect might be necessary.

It was emphasized in Chapter 7 that considering the limitations faced in modelling the swing up stage of the centrifuge experiment, both constitutive model and analysis procedure appeared appropriate for capturing the essence of the problem. The lack of accuracy in predicted response of the model to swing up was regarded as due to insufficient data for properly calibrating the stress-strain model at very low stress levels. Further study on this type of problems is necessary and recommended in order to verify the suitability of the constitutive model and numerical procedure for this kind of analysis.

The problem studied here was very interesting and challenging. Engineers usually design structures that would not fail under the action of loading. The case of the CANLEX embankment was the reverse, i.e. to design a structure that would fail upon application of rapid monotonic loading.

The CANLEX field event showed that despite how well the soil characteristics in a site could be known, the fundamental behaviour of soils must be understood and

considered into analysis in order to achieve meaningful results from numerical simulations.

BIBLIOGRAPHY

- Arthur, J.R.F., Chua, K.S., Dunstan, T., and Rodriguez, J.I. (1980). Principal stress rotation: a missing parameter, *Journal of Geotechnical Engineering Division, ASCE*, Vol. 106, GT. 4, pp. 419-433.
- Arthur, J.R.F., Bekenstein, S., Germaine, J.T., and Ladd, C.C. (1981). Stress path tests with controlled rotation of principal stress directions, *Laboratory Shear Strength of Soil, ASTM, STP 740*, pp. 516-540.
- Arulanandan, K., and Scott, R.F., Editors. (1994). VELACS Project. In Proc. of the International Conference on the verification of numerical procedures for the analysis of soil liquefaction problems, University of California, Davis, California, USA. October 17-20, 1993, Vols. 1-2.
- Bardet, J.P. (1986). Bounding surface plasticity model for sands, *Journal of the Geotechnical Engineering Division, ASCE*, Vol. 112, No. 11, November, pp. 1198-1217.
- Bazant, Z.P., and Krizek, R.J. (1976). Endochronic constitutive law for liquefaction of sand, *Journal of the Engineering Mechanics Division, ASCE*, Vol. 102, No, EM2, April, pp. 225-238.
- Bazant, Z.P. Ansal, A.M., and Krizek, R.J. (1982). Endochronic models for soils, *Soil Mechanics-Transient and Cyclic Loads*, Editors: G.N. Pande and O.C. Zienkiewicks, John Wiley and Sons, Ltd., New York, N.Y., pp. 419-438.
- Bishop, A.W. (1966). The strength of soils as engineering materials. *Géotechnique*, Vol. 16, No. 2, pp.91-130.
- Byrne, P.M. (1998). Personal communication.
- Byrne, P.M. (1996). Liquefaction case histories: Can we predict response? In Symposium on Recent Developments in Seismic Liquefaction Assessment, April12, 1996, Waterfront Hotel, Vancouver, B.C., Canada. Sponsored by Conetec.
- Byrne, P.M. (1991). A model for predicting liquefaction induced displacements due to seismic loading. In Proc. of the 2nd International Conference on Recent Advances in Geotechnical Earthquake Engineering and Soil Dynamics, March 11-15, St. Louis, Missouiri, Vol. 2, paper 7.14, pp. 1027-1035.

- Byrne, P.M., Cheung, H., and Yan, L. (1987). Soil parameters for deformation analysis of sand masses, Canadian Geotechnical Journal 24(3), 366-376.
- Byrne, P.M., Vaid, Y., and Stuckert, B. (1982). Model tests on earthquake stability of tailings slopes, ASCE National Convention, Specialty Session No. 67 on Physical Modeling of Soil, Dynamic Problems, Las Vegas, Nevada, April.
- Byrne, P.M., Debasis, R., Campanella, R., and Hughes, J. (1995a). Predicting liquefaction response of granular soils from self-boring pressuremeter tests. In Static and dynamic properties of gravelly soils, ASCE National Convention, San Diego, Calif., 23-27 Oct. Edited by M.D. Evans and R.J. Fragaszy. Geotechnical Special Publication 56, pp. 122-135.
- Byrne, P.M., Robertson, P.K., Plewes, H.D., List, B., and Tan, S. (1995b). Liquefaction event planning. In Proc., 48th Canadian Geotechnical Conference, Vancouver, B.C., 25-27 Sept., Vol. 1, pp. 341-352.
- Byrne, P.M., Puebla, H., Chan, D.H., Soroush, A., Morgenstern, N.R., Cathro, D.C., Gu, W.H., Phillips, R., Robertson, P.K., Hofmann, B.A., Wride (Fear), C.E., Sego, D.C., Plewes, H.P., List, B.R., and Tan, S. (1998). CANLEX Full-Scale experiment and modelling. Submitted to the Canadian Geotechnical Journal.
- Carter, J.P., Booker, J.R., and Wroth, C.P. (1982). A critical state soil model for cyclic loading, Soil Mechanics-Transient and Cyclic Loads, Editors: G.N. Pande and O.C. Zienkiewicks, John Wiley and Sons, Ltd., New York, N.Y., pp. 219-252.
- Casagrande, A. (1975). Liquefaction and cyclic deformation of sands, a critical review. In Proceedings of 5th Pan American Conference on Soil Mechanics and Foundation Engineering, Buenos Aires, Argentina, 1975, Vol. 5, pp. 79-133.
- Castro, G. (1969). Liquefaction of Sands, Ph.D. Thesis, Harvard Soil Mechanics Series, No. 81, Harvard University, Cambridge, Mass.
- Castro, G., Poulos, S.J., and Leathers, F.D. (1985). Re-examination of slide of Lower San Fernando dam, Journal of Geotechnical Engineering Division, ASCE, Vol. 111, No. 9, September, pp. 1093-1107.
- Cundall, P. (1995). FLAC User's Manual, version 3.3. ITASCA Consulting Group Inc., Minneapolis, U.S.A.
- Dafalias, Y.F., and Herrmann, L.R. (1982). Bounding surface formulation of soil plasticity, Soil Mechanics – Transient and Cyclic Loads, Editors: G.N. Pande and O.C. Zienkiewicks, John Wiley and Sons, Ltd., New York, N.Y., pp. 253-282.

- Dafalias, Y.F., and Herrmann, L.R. (1980). A bounding surface soil plasticity model. In Proceedings of the International Symposium on Soils Under Cyclic and Transient Loading, G.N. Pande and O.C. Zienkiewicks, eds., A.A. Balkema, Rotterdam, Vol. 1:2, pp. 335-345.
- Drucker, D.C., and Prager, W. (1952). Soil mechanics and plastic analysis or limit design, Quarterly of Applied Mathematics, 10, p. 157.
- Drucker, D.C., Gibson, E., and Henkel, D.J. (1955). Soil mechanics and work hardening theories of plasticity, ASCE, Transactions, Paper No. 2864, pp. 338-346.
- Duncan, J.M., and Chang, C.Y. (1970). Nonlinear analysis of stress and strain in soils, Journal of the Soil Mechanics and Foundations Division, ASCE, 96(SM5): 1629-1653.
- Duncan, J.M., Byrne, P.M., Wong, K.S., and Marby, P. (1980). Strength, stress-strain and bulk modulus parameters for finite element analyses of stresses and movements in soil masses. University of California, Berkeley, Report UCB/GT/80-01.
- Eliadorani, A. (1999). Forthcoming Ph.D. Thesis, University of British Columbia, Vancouver, Canada.
- El-Sohby, M.A., and Andrawes, K.Z. (1973). Experimental examination of sand anisotropy. In Proc. of 8th International Conference on Soil Mechanics and Foundation Engineering, Moscow, Vol. 1, pp. 103-109.
- Finn, W.L.D. (1981). Liquefaction potential: developments since 1976. In Proc. of the 1st International Conference on Recent Advances in Geotechnical Earthquake Engineering and Soil Dynamics, April 26-May 3, St. Louis, Missouri, Vol. 2, pp. 655-681.
- Finn, W.D.L., Pickering, D.J., and Bransby, P.L. (1971a). Sand liquefaction in triaxial and simple shear tests, Journal of Soil Mechanics and Foundations Division, ASCE, Vol. 97, No. SM4, April, pp. 639-659.
- Finn, W.D.L., Emry, J.J., and Gupta, Y.P. (1971b). Liquefaction of large samples of saturated sand on a shaking table. In Proc. 1st Canadian Conference on Earthquake Engineering, Vancouver, B.C., May, pp. 97-110.
- Finn, W.D.L., Emry, J.J., and Gupta, Y.P. (1970). A shake table study of the liquefaction of saturated sands during earthquakes. In Proc. 3rd European Symposium on Earthquake Engineering, Vancouver, B.C., May, pp. 253-262.

- Hardin, B.O. (1978). The nature of stress-strain behaviour of soils. In Proc. Special Conference on Earthquake Engineering and Soil Dynamics, ASCE, Pasadena, Vol. 1, pp. 3-90.
- Hardin, B.O., and Drenich, V.D. (1972). Shear modulus and damping in soils, design equations and curves, Journal of the Soil Mechanics and Foundations Division, ASCE, **89**(SM7): 667-692.
- Hill, R. (1950). The Mathematical Theory of Plasticity, Clarendon Press, Oxford, England.
- Hofmann, B.A., Robertson, P.K., Grapell, C., Cyre, C., and Lefebvre, M. (1996). CANLEX Phase III – Full Scale Liquefaction Tests: Instrumentation and Construction, 49th Canadian Geotechnical Conference, St. Johns, Newfoundland, Sept. 23-25, pp. 587-595.
- Ishihara, K. (1993). Liquefaction and flow failure during earthquakes. The 33rd Rankine Lecture, Géotechnique 43, No. 3, pp. 351-415.
- Ishihara, K. (1984). Post-earthquake failure of a tailings dam due to liquefaction of the pond deposit. In Proc. of the International Conference on Case Histories in Geotechnical Engineering, Vol. 3. pp. 1129-1143, May 6-11, University of Missouri, Rolla, Missouri.
- Ishihara, K., and Towhata, I. (1983). Cyclic behaviour of sand during rotation of principal stress axes, Mechanics of Granular Materials: New Models and Constitutive Relations, J.T. Jenkins and M. Satake, Editors, Elsevier Science Publishers B.V., Amsterdam.
- Ishihara, K., and Okada, S. (1978). Effects of stress history on cyclic behaviour of sand, Soils and Foundations, Vol. 18, No. 4, pp. 31-45.
- Ishihara, K., and Li, S.I. (1972). Liquefaction of saturated sand in triaxial torsion shear test, Soils and Foundations, Vol. 12, No. 3, June, pp. 19-39.
- Ishihara, K., Tatsuoka, F. and Susumu, Y. (1975). Undrained deformation and liquefaction of sand under cyclic stresses, Soils and Foundations, 15, 29-44.
- Iwasaki, T., and Tatsuoka, F. (1977). Effects of grain size and grading on dynamic shear moduli of sand, Soils and Foundations, 17(3), 19-35.
- Jaky, J. (1944). A nyugalmi nyomas tenyezoje (The coefficient of earth pressure at rest), Magyar Mernok es Epitesz-Egylet Kozlonye (J. of the Union of Hungarian Engineers and Architects), pp. 355-38.

- Jefferies, M. (1997). Plastic work and isotropic softening in unloading. *Géotechnique*, Vol. 47, No. 5, pp. 1037-1042.
- Jitno, H., and Byrne, P.M. (1995). Predicted and observed response of Mochikoshi tailings dam. In Proc. of the 1st International Conference on Earthquake Geotechnical Engineering, IS-Tokyo 95, Kenji Ishihara (Ed.), Vol.2, pp. 1085-1090.
- Koiter, W.T. (1953). Stress-Strain relations, uniqueness, and variational theorems for elastic-plastic materials with a singular yield surface, *Quarterly of Applied Mathematics*, 11, pp. 350-354.
- Kondner, R.L., and Zelasko, J.S. (1963). A hyperbolic stress-strain formulation for sands. In Proc. 2nd Pan-American Conference on Soil Mechanics and Foundation Engineering, Brazil, Vol. 1, pp. 289-324.
- Lade, P. (1977). Elasto-Plastic stress-strain theory for cohesionless soil with curved yield surfaces, *Int. J. Solids Structures*, Vol. 13, pp. 1019-1035.
- Lade, P., and Nelson, R.B. (1987). Modelling the elastic behaviour of granular materials, *International Journal for Numerical and Analytical Methods in Geomechanics*, Vol. 11, pp. 521-542.
- Lade, P., and Boonyachut, S. (1982). Large stress reversals in triaxial tests on sand. In Proc. of IV International Conference on Numerical Methods in Geomechanics, Edmonton, Canada, Vol. 1, pp. 171-182.
- Lade, P., and Duncan, J.M. (1975). Elastoplastic stress-strain theory for cohesionless soil, *Journal of the Geotechnical Engineering Division, ASCE*, Vol. 101, No. GT 10, October, pp. 1037-1053.
- Martin, G.R., Finn, W.D.L., and Seed, H.B. (1975). Fundamentals of liquefaction under cyclic loading, *Journal of the Geotechnical Engineering Division, ASCE*, Vol. 104, GT5, pp. 423-438.
- Matsuoka, H. (1974). A microscopic study on shear mechanism of granular materials, *Soils and Foundations*, Vol. 14, No. 1, pp. 29-43.
- Matsuoka, H., and Sakakibara, K. (1987). A constitutive model for sands and clays evaluating principal stress rotation, *Soils and Foundations*, Vol. 27, No. 4, Dec, pp. 73-88.
- Matsuoka, H., and Nakai, T. (1977). Stress-strain relationship of soil based on the SMP. In Proc. 9th International Conference on Soil Mechanics and Foundation Engineering, Specialty Session 9, 1977, pp. 153-162.

- Molenkamp, F. (1988). A simple model for isotropic non-linear elasticity of frictional materials, International Journal of Numerical and Analytical Methods in Geomechanics, 12, pp. 467-475.
- Mroz, Z. (1967). On the description of anisotropic workhardening, Journal of the Mechanics and Physics of Solids, Vol. 15, pp. 163-175.
- Natarajan, S., Hofmann, B.A., Lefebvre, M.E., and Robertson, P.K. (1996). CANLEX Phase III – Liquefaction Event: Performance Report (Response to Embankment Loading), University of Alberta, February.
- Negussey, D. (1984). An experimental study on the small strain response of sand. Ph.D. Thesis, University of British Columbia, Vancouver, B.C., Canada.
- Negussey, D., and Vaid, Y.P. (1990). Stress dilatancy of sand at small stress ratio states. Soils and Foundations, Vol. 30, No. 1, pp. 155-166.
- NRC – National Research Council. (1985). Liquefaction of soils during earthquakes, Report No. CETS-EE-001, National Academic Press, Washington, D.C.
- O'Rourke, T.D., and Hamada, W. (1992). Case Studies of Liquefaction and Lifeline Performance During Past Earthquakes, Vol. 2: United States Case Studies, Technical Report NCEER-92-0002, February 17, 1992.
- Park, C., and Tatsuoka, F. (1994). Anisotropic strength and deformation of sands in plane strain. In Proc. of XIII International Conference on Soil Mechanics and Foundation Engineering, New Delhi, India, Vol. 1, pp. 1-4.
- Peacock, W.H., and Seed, H.B. (1968). Sand liquefaction under cyclic loading simple shear conditions, Journal of Soil Mechanics and Foundations Division, ASCE, Vol. 94, No. SM3, May, pp. 689-708.
- Phillips, R., and Byrne, P.M. (1994). CANLEX, Phase II, Activity II-6D – Test 1, Centrifuge Testing, C-CORE Contract Report No. 93-C18.
- Phillips, R., and Byrne, P.M. (1993). CANLEX, Phase I, Activity 8e-Stage 1, Centrifuge Testing, C-CORE Contract Report No. 93-C14.
- Poorooshasp, H.B., Holubec, I., and Sherbourne, A.N. (1967). Yielding and flow of sand in triaxial compression: Parts II and III, Canadian Geotechnical Journal 4(4), 376-397.
- Poorooshasp, H.B., Holubec, I., and Sherbourne, A.N. (1966). Yielding and flow of sand in triaxial compression: Parts I, Canadian Geotechnical Journal 3(4), 179-190.

- Poulos, S.J. (1981). The steady state of deformation, Journal of the Geotechnical Engineering Division, ASCE, Vol. 107, No. GT5, 1981, pp. 553-562.
- Prager, W. (1955). The theory of plasticity: A survey on recent achievement. In Proceedings Inst. Mech. Eng., London, Vol. 169, pp. 41-57.
- Prevost, J., and Hoeg, K. (1975). Effective stress-strain-strength model for soils, Journal of the Geotechnical Engineering Division, ASCE, Vol. 101, No. GT3, March, pp. 259-278.
- Puebla, H., and Byrne, P.M. (1996). Static liquefaction case history: Analysis and field observations. In Proc. of XIV International Conference on Soil Mechanics and Foundation Engineering, Hamburg, Germany, Sept. 6-12, Vol. 1, pp. 177-180.
- Puebla, H., Byrne, P.M., and Phillips, R. (1997). Analysis of CANLEX liquefaction embankments: Prototype and centrifuge models, Canadian Geotechnical Journal, Vol. 34, No. 5, pp. 641-657.
- Robertson, P.K., and Wride, C.E. (Fear) (1997). CANLEX Final Summary Data Review Report, Department of Civil and Environmental Engineering, University of Alberta, Edmonton, December.
- Robertson, P.K., and Fear, C.E. (1995). Liquefaction of sand and its evaluation. In Proc. of the 1st International Conference on Earthquake Geotechnical Engineering, IS Tokyo 95, Keynote Lecture.
- Robertson, P.K., Campanella, R.G., and Wightman, A. (1983). SPT – CPT correlations. Journal of the Geotechnical Division, ASCE, **109**:1449-1459.
- Roscoe, K.H., and Burland, J.B. (1968). On the generalized stress-strain behaviour of wet clay, Engineering Plasticity, J. Heyman and F. Leckie, eds., Cambridge University Press, Cambridge, England, pp. 535-609.
- Rowe, P.W. (1971). Theoretical meaning and observed values of deformation parameters for soil. In Proc. Roscoe Memorial Symposium Stress-Strain Behaviour of Soils, pp. 143-194.
- Rowe, P.W. (1962). The stress-strain dilatancy relation for static equilibrium of an assembly of particles in contact. In Proc. of the Royal Society of London, Mathematical and Physical Sciences, Series A, **269**:500-527.
- Roy, D. (1997). Mechanical properties of granular deposits from self-boring pressuremeter tests. Ph.D. Thesis, University of British Columbia, Vancouver, B.C., Canada.

- Schofield, A.N. (1980). Cambridge Geotechnical Centrifuge operations, 20th Rankine Lecture. *Géotechnique*, Vol. 30, No. 3, pp. 227-268.
- Schofield, A.N., and Wroth, C.P. (1968). Critical State Soil Mechanics, McGraw-Hill, Inc., London, England.
- Seed, H.B. (1984). The role of case studies in the evaluation of soil liquefaction potential. In Proc. of the International Conference on Case Histories in Geotechnical Engineering, Vol. 4. pp. 1681-1691, May 6-11, University of Missouri, Rolla, Missouri.
- Seed, H.B. (1979a). Considerations in the earthquake resistant design of earth and rockfill dams. *Géotechnique*, Vol. 29, No. 3.
- Seed, H.B. (1979b). Soil liquefaction and cyclic mobility evaluation for level ground during earthquakes, *Journal of Geotechnical Engineering Division, ASCE*, Vol. 105, No. GT2, pp. 201-255.
- Seed, H.B., and Lee, K.L. (1966). Liquefaction of saturated sands during cyclic loading, *Journal of Soil Mechanics and Foundations Division, ASCE*, Vol. 92, No. SM6.
- Seed, H.B., Lee, K.L., Idriss, I.M., and Makdisi, F.I. (1973). Analysis of the slides in the San Fernando dams during the earthquake of February 9, 1971, Report No. EERC 73-2, University of California, Berkeley, Calif., NTIS No. PB 223 402, 1973.
- Steedman, R.S. (1986). Embedded Structure on sand foundation. Data Report of Centrifuge Model Tests, RSS110 and RSS111, Engineering Department, Cambridge University, Cambridge, England.
- Tan, S. (1995). Personal communication.
- Tatsuoka, F., and Ishihara, K. (1974). Yielding of sand in triaxial compression, *Soils and Foundations*, 14, pp. 63-76.
- Taylor, D.W. (1948). Fundamentals of soil mechanics. J. Wiley and Sons, New York.
- Terzaghi, K., and Peck, R.B. (1967). Soil Mechanics in Engineering Practice, Second edition, John Wiley and Sons, Inc.
- Vaid, Y.P. (1999). Personal communication.
- Vaid, Y.P. (1998). Fundamental factors affecting liquefaction susceptibility of sands, Keynote Lecture. International Workshop on the Physics and Mechanics of Liquefaction, John Hopkins University, Baltimore, U.S.A., September 10 – 11.

- Vaid, Y.P., and Chern, J.C. (1985). Cyclic and monotonic undrained response of saturated sands, in Advances in the Art of Testing Soils Under Cyclic Conditions, ASCE Convention, Detroit, Mich., 1985. Vithosla (Ed.), pp. 120-147.
- Vaid, Y.P., and Chern, J.C. (1983). Effect of static shear on resistance to liquefaction, Soils and Foundations, 23-1, pp. 47-60.
- Vaid, Y.P., Byrne, P.M., and Hughes, J.M.O. (1981). Dilation angle and liquefaction potential. In Proc. International Conference on Recent Advances in Geotechnical Engineering and Soil Dynamics, St. Louis, Mo., April 26-May 3, 1981, Vol. 1, pp. 161-165.
- Vaid, Y.P., Sivathayalan, S., Eliadorani, A., and Uthayakumar, M. (1996). Laboratory testing at UBC. CANLEX Report, Department of Civil Engineering, University of British Columbia, B.C., Canada.
- Vaid, Y.P., Uthayakumar, M., Sivathayalan, S., Robertson, P.K., and Hofmann, B. (1995a). Laboratory testing of Syncrude sand. In Proceedings, 48th Canadian Geotechnical Conference, Vancouver, B.C., 25-27 Sept. 1995, Vol. 1, pp. 223-232.
- Vaid, Y.P., Sivathayalan, S., Uthayakumar, M., and Eliadorani, A. (1995b). Liquefaction potential of reconstituted Syncrude sand. In Proceedings, 48th Canadian Geotechnical Conference, Vancouver, B.C., 25-27 Sept. 1995, Vol. 1, pp. 319-329.
- Valanis, K.C. (1971). A theory of viscoplasticity without a yield surface, I, II, Arch. Mech. Stosowanej, 23, 4 Warszawa, pp. 517-551.
- Valanis, K.C., and Read, H.E. (1982). A new endochronic plasticity model for soils, Soil Mechanics-Temporary and Cyclic Loads, Editors: G.N. Pande and O.C. Zienkiewicks, John Wiley and Sons, Ltd., New York, N.Y., pp. 375-417.
- Vermeer, P.A. (1980). Formulation and analysis of sand deformation problems. Report 195 of the Geotechnical Laboratory, 142p. Delft University of Technology.
- Vermeer, P.A. (1978). A double hardening model for sand. Géotechnique, Vol. 28, No. 4, pp. 413-433.
- Yoshimi, Y., Richart, F.E., Prakash, S., Balkan, D.D., and Ilychev, V.A. (1977). Soil dynamics and its application to foundation engineering. In Proc. 9th International Conference on Soil Mechanics and Foundation Engineering, Tokyo, Japan, Vol. 2, pp. 605-650.

- Yu, P., and Richart, F.E. Jr. (1984). Stress ratio effects on shear modulus of dry sands, Journal of Geotechnical Engineering Division, ASCE, Vol. 110, pp. 331-345.

APPENDIX A

DERIVATION OF SHEAR FLOW RULE

The flow rule expressed in Equation 4.16 can be derived from energy considerations as follows: If an element under stresses s' and t is subjected to probing increments $\Delta s'$ and Δt , then the energy input ΔE , for plane strain conditions is:

$$[A.1] \quad \Delta E = \sigma'_1 \Delta \varepsilon_1 + \sigma'_3 \Delta \varepsilon_3$$

Assuming that $\Delta \varepsilon_2^e = \Delta \varepsilon_2^p = 0$, the dissipated energy ΔE^D can be written as:

$$[A.2] \quad \Delta E^D = \sigma'_1 \Delta \varepsilon_1^{ps} + \sigma'_3 \Delta \varepsilon_3^{ps}$$

Rewriting,

$$\sigma'_1 \Delta \varepsilon_1^{ps} + \sigma'_3 \Delta \varepsilon_3^{ps} = \frac{\sigma'_1 + \sigma'_3}{2} (\Delta \varepsilon_1^{ps} + \Delta \varepsilon_3^{ps}) + \frac{\sigma'_1 - \sigma'_3}{2} (\Delta \varepsilon_1^{ps} - \Delta \varepsilon_3^{ps})$$

$$[A.3] \quad \Delta E^D = s' \Delta \varepsilon_v^{ps} + t \Delta \gamma^{ps}$$

At the critical state the element strains under constant volume and therefore, the energy dissipated is:

$$[A.4] \quad \Delta E^D = t \Delta \gamma^{ps} = s' \sin \phi_{cv} \Delta \gamma^{ps}$$

where ϕ_{cv} is the constant volume friction angle, and $t/s' = \sin \phi_{cv}$.

Assuming that the plastic energy ΔE^P is always $s' \sin \phi_{cv} \Delta \gamma^{ps}$, as per CAMCLAY model (Schofield and Wroth 1968), then from Equations A.3 and A.4:

$$[A.5] \quad s' \Delta \varepsilon_v^{ps} + t \Delta \gamma^{ps} = s' \sin \phi_{cv} \Delta \gamma^{ps}$$

Therefore:

$$[A.6] \quad \Delta \varepsilon_v^{ps} = \left(\sin \phi_{cv} - \frac{t}{s'} \right) \Delta \gamma^{ps}$$

Hence, the flow rule expressed in Equation 4.16 can be derived from energy considerations assuming that $\Delta \varepsilon_2^e = \Delta \varepsilon_2^P = 0$.

APPENDIX B

CONSTITUTITVE MODEL IMPLEMENTATION

In this appendix, a detailed description of the constitutive model implementation is presented together with the expressions to evaluate the parameter λ and the plastic strain increments related to each yield surface. All the stresses to which reference will be made in this appendix are effective stresses, but the symbol “ ‘ ” generally used to differentiate effective from total stresses will be omitted for ease of presentation.

As discussed in Chapter 4, the model is a double hardening model that comprises two main plastic parts: (i) the plastic shear or cone mechanism, and (ii) the plastic volumetric or cap mechanism. In addition, a tensile failure criterion is used to complete the model. The failure envelope is defined by a Mohr-Coulomb criterion (shear) with tension cutoff (tensile). The shear or cone flow rule is non-associative, while both volumetric or cap and tensile flow rules are associative. The implementation is based on that of FLAC’s Double-Yield model, Cundall (1995).

B.1 Plane strain formulation

B.1.1 Incremental elastic law

The model is implemented in terms of principal stresses σ_1 , σ_2 and σ_3 , one of them being the out-of-plane stress, σ_{zz} . From the stress tensor components σ_{ij} , the principal stresses and principal directions are evaluated. Since the shear yield and tensile failure functions are expressed in terms of major and minor principal stresses, these are ordered as follows:

$$[B.1] \quad \sigma_1 \leq \sigma_2 \leq \sigma_3$$

This order is due to the sign convention used in FLAC, which specifies compressive stresses as negative. In accordance with plasticity theory, the principal strain increments, $\Delta\epsilon_1$, $\Delta\epsilon_2$ and $\Delta\epsilon_3$, are the sum of their elastic and plastic components:

$$[B.2] \quad \Delta\epsilon_i = \Delta\epsilon_i^e + \Delta\epsilon_i^p$$

where $i = 1$ to 3 , and the superscripts “e” and “p” refer to the elastic and plastic components, respectively. Compressive strains are considered negative. Furthermore, the plastic contribution of each yield surface, i.e. shear, volumetric and tensile, are added to form the plastic strain increment as follows:

$$[B.3] \quad \Delta\epsilon_i^p = \Delta\epsilon_i^{ps} + \Delta\epsilon_i^{pc} + \Delta\epsilon_i^{pt}$$

where the superscripts “ps”, “pc”, and “pt” stand for plastic shear, plastic cap and plastic tensile strain, respectively.

The incremental expression of Hooke’s law in terms of principal stresses and strains has the form:

$$[B.4] \quad \begin{aligned} \Delta\sigma_1 &= \alpha_1 \Delta\epsilon_1^e + \alpha_2 (\Delta\epsilon_2^e + \Delta\epsilon_3^e) \\ \Delta\sigma_2 &= \alpha_1 \Delta\epsilon_2^e + \alpha_2 (\Delta\epsilon_1^e + \Delta\epsilon_3^e) \\ \Delta\sigma_3 &= \alpha_1 \Delta\epsilon_3^e + \alpha_2 (\Delta\epsilon_1^e + \Delta\epsilon_2^e) \end{aligned}$$

where:

$$[B.5] \quad \alpha_1 = B^e + \frac{4G^e}{3}$$

$$[B.6] \quad \alpha_2 = B^e - \frac{2G^e}{3}$$

$$[B.7] \quad G^e = k_G^e P_A \left(\frac{s'}{P_A} \right)^{me}$$

$$[B.8] \quad B^e = \frac{2G^e(1+\nu)}{3(1-2\nu)}$$

and G^e , B^e are the elastic shear and bulk moduli, respectively; k_G^e , elastic shear modulus number; P_A , the atmospheric pressure; me , the elastic shear modulus exponent; s' , the effective mean stress = $(\sigma_1 + \sigma_3)/2$; and ν , the Poisson's ratio.

B.1.2 Yield and potential functions

The shear, volumetric or cap, and tensile yield functions, referred to here as f^s , f^c and f^t , respectively, are defined as:

$$[B.9] \quad f^s = \sigma_1 - \sigma_3 N_{\phi_d} + 2c\sqrt{N_{\phi_d}} = 0$$

$$[B.10] \quad f^c = -\frac{1}{3}[\sigma_1^2 + \sigma_2^2 + \sigma_3^2] + (\sigma^c)^2 = 0$$

$$[B.11] \quad f^t = \sigma' - \sigma_3 = 0$$

where

$$[B.12] \quad N_{\phi_d} = \frac{(1 + \sin \phi_d)}{(1 - \sin \phi_d)}$$

and ϕ_d is the developed friction angle; c , the cohesion, usually equal to zero for sands; σ^t , the tensile strength, usually equal to zero for sands; and σ^c , the cap pressure, equal to the maximum radius attained by the spherical cap.

The potential functions are:

$$[B.13] \quad g^s = \sigma_1 - \sigma_3 N_{\psi_d} = 0 \Rightarrow \text{Non-Associative flow rule}$$

$$[B.14] \quad g^c = f^c \Rightarrow \text{Associative flow rule}$$

$$[B.15] \quad g^t = f^t \Rightarrow \text{Associative flow rule}$$

where

$$[B.16] \quad N_{\psi_d} = \frac{(1 + \sin \psi_d)}{(1 - \sin \psi_d)}$$

and ψ_d is the developed dilation angle.

B.1.3 Hardening/Softening parameters

Since the tensile yield surface does not harden or soften in this model, only two hardening parameters are used: one corresponding to the shear or cone yield surface, γ^{ps} , and another one corresponding to the volumetric or cap yield locus, ε_v^{pc} . Their incremental forms are:

$$[B.17] \quad \Delta \gamma^{ps} = |\Delta \varepsilon_1^{ps} - \Delta \varepsilon_3^{ps}|$$

$$[B.18] \quad \Delta \varepsilon_v^{pc} = (\Delta \varepsilon_1^{pc} + \Delta \varepsilon_2^{pc} + \Delta \varepsilon_3^{pc})$$

where $\Delta \gamma^{ps}$ is *plastic cone* shear strain increment; $\Delta \varepsilon_1^{ps}$ and $\Delta \varepsilon_3^{ps}$ are the *plastic cone* major and minor principal strain increments, respectively; the absolute value in Equation B.17 is introduced to ensure that $\Delta \gamma^{ps} > 0$ and thus, guarantee hardening of the *shear yield*

surface; $\Delta\varepsilon_v^{pc}$ is the *plastic cap* volumetric strain increment; and $\Delta\varepsilon_1^{pc}$, $\Delta\varepsilon_2^{pc}$ and $\Delta\varepsilon_3^{pc}$ are the *plastic cap* major, intermediate and minor principal strain increments, respectively.

These hardening parameters are used to determine the new values of developed stress ratio, η_d , the *sine* of developed dilation angle, $\sin\psi_d$, and the cap pressure, σ^c , as follows:

$$[B.19] \quad \Delta\eta_d = G^* \Delta\gamma^{ps}$$

where

$$[B.20] \quad G^* = k_G^p \left(\frac{s'}{P_A} \right)^{np-1} \left[1 - \left(\frac{\eta_d}{\eta_f} \right) R_F \right]^2$$

and $\Delta\eta_d$ is the developed stress ratio increment; G^* , the normalized tangent plastic shear modulus; k_G^p , the plastic shear modulus number; np , the plastic shear modulus exponent; η_f , the stress ratio at failure, equal to $\sin\phi_f$; ϕ_f , the friction angle at failure; and R_F , the failure ratio. Therefore, the new η_d is:

$$[B.21] \quad \eta_d^{new} = \eta_d^{old} + \Delta\eta_d = \sin\phi_d^{new}$$

The new value of $\sin\psi_d$, is given by:

$$[B.22] \quad \sin\psi_d^{new} = (\sin\phi_{cv} - \sin\phi_d^{new})$$

The cap pressure is updated by:

$$[B.23] \quad (\sigma^c)^{new} = (\sigma^c)^{old} + \Delta\sigma^c$$

where

$$[B.24] \quad \Delta\sigma^c = -B^p \Delta\varepsilon_v^{pc}$$

and B^p is the plastic bulk modulus given by:

$$[B.25] \quad B^p = k_B^p P_A \left(\frac{s'}{P_A} \right)^{mp}$$

where k_B^p is the plastic bulk modulus number; mp , the plastic bulk modulus exponent; and the negative sign in Equation B.24 is due to FLAC's sign convention in which compressive strains are negative.

B.1.4 Plastic corrections

To establish whether the failure criteria are violated or not, an elastic guess σ_i^I is determined by adding the old values of the stress, σ_i^{old} , to the stress increments obtained by assuming the total strain increments, $\Delta\epsilon_i$, as elastic:

$$[B.26] \quad \begin{aligned} \sigma_1^I &= \sigma_1^{old} + \alpha_1 \Delta\epsilon_1 + \alpha_2 (\Delta\epsilon_2 + \Delta\epsilon_3) \\ \sigma_2^I &= \sigma_2^{old} + \alpha_1 \Delta\epsilon_2 + \alpha_2 (\Delta\epsilon_1 + \Delta\epsilon_3) \\ \sigma_3^I &= \sigma_3^{old} + \alpha_1 \Delta\epsilon_3 + \alpha_2 (\Delta\epsilon_1 + \Delta\epsilon_2) \end{aligned}$$

The yield functions are then evaluated for the values of the elastic guesses σ_i^I . If σ_i^I fell outside the elastic region, i.e. $f_j(\sigma_i^I) < 0$, plastic corrections would then be needed.

In general, eight scenarios are possible:

- | | | |
|--|---------------|------------------------------------|
| 1) $f^s(\sigma_i^I) < 0$ | \Rightarrow | Shear yielding |
| 2) $f^c(\sigma_i^I) < 0$ | \Rightarrow | Volumetric yielding |
| 3) $f^t(\sigma_i^I) < 0$ | \Rightarrow | Tensile yielding |
| 4) $f^s(\sigma_i^I) < 0$ and $f^c(\sigma_i^I) < 0$ | \Rightarrow | Shear and Volumetric yielding |
| 5) $f^s(\sigma_i^I) < 0$ and $f^t(\sigma_i^I) < 0$ | \Rightarrow | Shear and Tensile yielding |
| 6) $f^c(\sigma_i^I) < 0$ and $f^t(\sigma_i^I) < 0$ | \Rightarrow | Volumetric and Tensile yielding |
| 7) $f^s(\sigma_i^I) < 0$; $f^c(\sigma_i^I) < 0$ and $f^t(\sigma_i^I) < 0$ | \Rightarrow | Shear, Volume and Tensile yielding |

$$8) \quad f^s(\sigma_i^I) > 0; f^c(\sigma_i^I) > 0 \text{ and } f^t(\sigma_i^I) > 0 \quad \Rightarrow \quad \text{No yielding} \therefore \text{Elastic response}$$

In case of yielding, the plastic strain increments are determined from the corresponding flow rules as follows:

Shear Yielding:

$$\text{If } f^s(\sigma_i^I) < 0 \quad \Rightarrow \quad \Delta\epsilon_i^{ps} = \lambda^s \frac{\partial g^s}{\partial \sigma_i}, \text{ and hence}$$

$$\begin{aligned} \Delta\epsilon_1^{ps} &= \lambda^s \\ [\text{B.27}] \quad \Delta\epsilon_2^{ps} &= 0 \\ \Delta\epsilon_3^{ps} &= -\lambda^s N_{\psi_d} \end{aligned}$$

Volumetric Yielding:

$$\text{If } f^c(\sigma_i^I) < 0 \quad \Rightarrow \quad \Delta\epsilon_i^{pc} = \lambda^c \frac{\partial g^c}{\partial \sigma_i}, \text{ and hence}$$

$$\begin{aligned} \Delta\epsilon_1^{pc} &= -\frac{2}{3}\sigma_1\lambda^c \\ [\text{B.28}] \quad \Delta\epsilon_2^{pc} &= -\frac{2}{3}\sigma_2\lambda^c \\ \Delta\epsilon_3^{pc} &= -\frac{2}{3}\sigma_3\lambda^c \end{aligned}$$

Tensile Yielding:

$$\text{If } f^t(\sigma_i^I) < 0 \quad \Rightarrow \quad \Delta\epsilon_i^{pt} = \lambda^t \frac{\partial g^t}{\partial \sigma_i}, \text{ and hence}$$

$$\begin{aligned} \Delta\epsilon_1^{pt} &= 0 \\ [\text{B.29}] \quad \Delta\epsilon_2^{pt} &= 0 \\ \Delta\epsilon_3^{pt} &= -\lambda^t \end{aligned}$$

From Equation B.3, the total plastic strain increments are given by:

$$\begin{aligned}
 [B.30] \quad \Delta\varepsilon_1^p &= \lambda^s - \frac{2}{3}\sigma_1\lambda^c \\
 \Delta\varepsilon_2^p &= -\frac{2}{3}\sigma_2\lambda^c \\
 \Delta\varepsilon_3^p &= -\lambda^s N_{\psi_d} - \frac{2}{3}\sigma_3\lambda^c - \lambda^t
 \end{aligned}$$

The new values of the principal stresses, σ_i^{new} , corrected due to plasticity can then be evaluated as follows:

$$\begin{aligned}
 [B.31] \quad \sigma_1^{new} &= \sigma_1^I - [\alpha_1 \Delta\varepsilon_1^p + \alpha_2 (\Delta\varepsilon_2^p + \Delta\varepsilon_3^p)] \\
 \sigma_2^{new} &= \sigma_2^I - [\alpha_1 \Delta\varepsilon_2^p + \alpha_2 (\Delta\varepsilon_1^p + \Delta\varepsilon_3^p)] \\
 \sigma_3^{new} &= \sigma_3^I - [\alpha_1 \Delta\varepsilon_3^p + \alpha_2 (\Delta\varepsilon_1^p + \Delta\varepsilon_2^p)]
 \end{aligned}$$

Substitution of Equation B.30 in Equation B.31 yields:

$$\begin{aligned}
 [B.32] \quad \sigma_1^{new} &= \sigma_1^I - A_{12}\lambda^s + S_1\lambda^c + \alpha_2\lambda^t \\
 \sigma_2^{new} &= \sigma_2^I - A_{22}\lambda^s + S_2\lambda^c + \alpha_2\lambda^t \\
 \sigma_3^{new} &= \sigma_3^I - A_{21}\lambda^s + S_3\lambda^c + \alpha_1\lambda^t
 \end{aligned}$$

where

$$[B.33] \quad A_{12} = (\alpha_1 - \alpha_2 N_{\psi_d})$$

$$[B.34] \quad A_{22} = (\alpha_2 - \alpha_2 N_{\psi_d})$$

$$[B.35] \quad A_{21} = (\alpha_2 - \alpha_1 N_{\psi_d})$$

$$[B.36] \quad S_1 = \frac{2}{3}[\alpha_1\sigma_1 + \alpha_2(\sigma_2 + \sigma_3)]$$

$$[B.37] \quad S_2 = \frac{2}{3}[\alpha_1\sigma_2 + \alpha_2(\sigma_1 + \sigma_3)]$$

$$[B.38] \quad S_3 = \frac{2}{3}[\alpha_1\sigma_3 + \alpha_2(\sigma_1 + \sigma_2)]$$

To carry out the stress corrections due to plasticity, the parameters λ^s , λ^c and λ^t must be known. Since in compliance with the consistency condition the new stresses σ_i^{new} lie on the yield loci, the yield functions for which yield conditions are exceeded must be satisfied by σ_i^{new} . Therefore, the parameters λ_j can be obtained by solving the system of simultaneous equations given by $f_j(\sigma_i^{new}) = 0$, in which the subscript “ j ” refers to the modes of yielding, and $\lambda_i = 0$, in which the subscript “ i ” indicates the yielding conditions that were not exceeded.

B.1.4.1 Shear and volumetric yield conditions

In this case, both *shear* and *volumetric yielding* occur but the tensile criterion is not violated. Hence, substitution of $\lambda^t = 0$ and B.32 into Equations B.9, i.e. $f^s(\sigma_i^{new}) = 0$, and B.10, i.e. $f^c(\sigma_i^{new}) = 0$, and solving for λ^s and λ^c , yields:

$$[B.39] \quad \lambda^c = \frac{f^s(\sigma_i^t) + (A_{21}N_{\phi_d} - A_{12})\lambda^s}{(S_3N_{\phi_d} - S_1)}$$

and

$$[B.40] \quad \lambda^s = \frac{-B_2 \pm \sqrt{B_2^2 - 4B_1B_3}}{2B_1}$$

where

$$\begin{aligned}
 B_1 &= \left[AA + \frac{AS(A_{21}N_{\phi_d} - A_{12})}{(S_3N_{\phi_d} - S_1)} + \frac{SS(A_{21}N_{\phi_d} - A_{12})^2}{(S_3N_{\phi_d} - S_1)^2} \right] \\
 [B.41] \quad B_2 &= \left[Asi + \frac{AS \cdot f^s(\sigma_i^I) + Ssi(A_{21}N_{\phi_d} - A_{12})}{(S_3N_{\phi_d} - S_1)} + \frac{2SS \cdot f^s(\sigma_i^I)(A_{21}N_{\phi_d} - A_{12})}{(S_3N_{\phi_d} - S_1)^2} \right] \\
 B_3 &= \left[f^c(\sigma_i^I) + \frac{Ssi \cdot f^s(\sigma_i^I)}{(S_3N_{\phi_d} - S_1)} + \frac{SS(f^s(\sigma_i^I))^2}{(S_3N_{\phi_d} - S_1)^2} \right] \\
 [B.42] \quad AA &= -\frac{(A_{12}^2 + A_{22}^2 + A_{21}^2)}{3} \\
 [B.43] \quad SS &= -\frac{(S_1^2 + S_2^2 + S_3^2)}{3} \\
 [B.44] \quad Asi &= \frac{2(A_{12}\sigma_1^I + A_{22}\sigma_2^I + A_{21}\sigma_3^I)}{3} \\
 [B.45] \quad Ssi &= -\frac{2(S_1\sigma_1^I + S_2\sigma_2^I + S_3\sigma_3^I)}{3} \\
 [B.46] \quad AS &= \frac{2(A_{12}S_1 + A_{22}S_2 + A_{21}S_3)}{3}
 \end{aligned}$$

and λ^s is the root with smallest absolute value.

B.1.4.2 Shear yield conditions only

If only *shear yielding* occurs, then $\lambda^t, \lambda^c = 0$ and solving Equation B.9, i.e. $f^s(\sigma_i^{new}) = 0$, λ^s is given by:

$$[B.47] \quad \lambda^s = \frac{f^s(\sigma'_i)}{(A_{12} - A_{21}N_{\phi_d})}$$

B.1.4.3 Volumetric yield conditions only

If only *volumetric yielding* occurs, then $\lambda^t, \lambda^c = 0$ and solving Equation B.10, i.e. $f^c(\sigma_i^{new}) = 0$, λ^c is given by:

$$[B.48] \quad \lambda_c = \frac{-Ssi \pm \sqrt{Ssi^2 - 4SS \cdot f^c(\sigma'_i)}}{2SS}$$

where λ^c is the root with smallest absolute value.

B.1.4.4 Shear, Volumetric and Tensile yield conditions

In this case, *shear*, *volumetric* and *tensile yielding* occur simultaneously. Hence, substitution of B.32 into Equations B.9, i.e. $f^s(\sigma_i^{new}) = 0$, and B.10, i.e. $f^c(\sigma_i^{new}) = 0$, and B.11, i.e. $f^t(\sigma_i^{new}) = 0$, and solving for λ^s, λ^c and λ^t , yields:

$$[B.49] \quad \lambda^s = \frac{-C_2 \pm \sqrt{C_2^2 - 4C_1C_3}}{2C_1}$$

$$[B.50] \quad \lambda^c = \frac{-(F_7\lambda^s + F_9)}{F_8}$$

$$[B.51] \quad \lambda^t = \frac{f^t(\sigma'_i) + A_{21}\lambda^s - S_3\lambda^c}{\alpha_1}$$

where

$$\begin{aligned}
 [B.52] \quad C_1 &= \left[F_1 - \frac{F_3 F_7}{F_8} + \frac{F_2 F_7^2}{F_8^2} \right] \\
 C_2 &= \left[F_4 - \frac{(F_3 F_9 + F_5 F_7)}{F_8} + \frac{2 F_2 F_7 F_9}{F_8^2} \right] \\
 C_3 &= \left[F_6 - \frac{F_5 F_9}{F_8} + \frac{F_2 F_9^2}{F_8^2} \right]
 \end{aligned}$$

$$[B.53] \quad F_1 = \left[AA + \frac{AAst \cdot A_{21}}{\alpha_1} + \frac{AAt \cdot A_{21}^2}{\alpha_1^2} \right]$$

$$[B.54] \quad F_2 = \left[SS - \frac{SAct \cdot S_3}{\alpha_1} + \frac{AAAt \cdot S_3^2}{\alpha_1^2} \right]$$

$$[B.55] \quad F_3 = \left[AS + \frac{SAct \cdot A_{21} - AAst \cdot S_3}{\alpha_1} - \frac{2AAAt \cdot A_{21} \cdot S_3}{\alpha_1^2} \right]$$

$$[B.56] \quad F_4 = \left[Asi + \frac{Asit \cdot A_{21} + AAst \cdot f'(\sigma_i^I)}{\alpha_1} + \frac{2AAAt \cdot A_{21} \cdot f'(\sigma_i^I)}{\alpha_1^2} \right]$$

$$[B.57] \quad F_5 = \left[Ssi + \frac{SAct \cdot f'(\sigma_i^I) - Asit \cdot S_3}{\alpha_1} - \frac{2AAAt \cdot S_3 \cdot f'(\sigma_i^I)}{\alpha_1^2} \right]$$

$$[B.58] \quad F_6 = \left[f^c(\sigma_i^I) + \frac{Asit \cdot f'(\sigma_i^I)}{\alpha_1} + \frac{AAAt \cdot \{f'(\sigma_i^I)\}^2}{\alpha_1^2} \right]$$

$$[B.59] \quad F_7 = \left[(A_{21} N_{\phi_d} - A_{12}) + \frac{(\alpha_2 - \alpha_1 N_{\phi_d}) A_{21}}{\alpha_1} \right]$$

$$[B.60] \quad F_8 = \left[(S_1 - S_3 N_{\phi_d}) - \frac{(\alpha_2 - \alpha_1 N_{\phi_d}) S_3}{\alpha_1} \right]$$

$$[B.61] \quad F_9 = \left[f^s(\sigma_i^I) + \frac{(\alpha_2 - \alpha_1 N_{\phi_d}) \cdot f'(\sigma_i^I)}{\alpha_1} \right]$$

$$[B.62] \quad AAAt = -\frac{(2\alpha_2^2 + \alpha_1^2)}{3}$$

$$[B.63] \quad Asit = -\frac{2[(\sigma'_1 + \sigma'_2)\alpha_2 + \sigma'_3\alpha_1]}{3}$$

$$[B.64] \quad AAst = \frac{2[(A_{12} + A_{22})\alpha_2 + A_{21}\alpha_1]}{3}$$

$$[B.65] \quad SAct = -\frac{2[(S_1 + S_2)\alpha_2 + S_3\alpha_1]}{3}$$

and λ^s is the root with smallest absolute value.

B.1.4.5 Volumetric and tensile yield conditions

In this case, both *volumetric* and *tensile yielding* occur but the shear criterion is not violated. Hence, substitution of $\lambda^s = 0$ and B.32 into Equations B.10, i.e. $f^c(\sigma_i^{new}) = 0$, and B.11, i.e. $f^t(\sigma_i^{new}) = 0$, and solving for λ^c and λ^t , yields:

$$[B.66] \quad \lambda^t = \frac{f^t(\sigma_i^t) - S_3\lambda^c}{\alpha_1}$$

$$[B.67] \quad \lambda^c = \frac{-F_5 \pm \sqrt{F_5^2 - 4F_2F_6}}{2F_2}$$

B.1.4.6 Tensile yield conditions only

If only *tensile yielding* occurs, then $\lambda^s, \lambda^c = 0$ and solving Equation B.11, i.e. $f^t(\sigma_i^{new}) = 0$, λ^t is given by:

$$[B.68] \quad \lambda^t = \frac{f^t(\sigma_i^t)}{\alpha_1}$$

B.1.4.7 Shear and tensile yield conditions

The case of shear and tensile yield is treated as either shear yielding only, or as tensile yielding only, depending on the location of the stress point σ_i^t respect to the bisectrix of the angle formed by f^s and f^t in the $\sigma_1 : \sigma_3$ plane. The expressions to obtain λ^s or λ^t are the same as those given by Equations B.47 or B.68, respectively, and the procedure followed is identical to that used in FLAC's Mohr-Coulomb model (Cundall, 1995), for this specific case.

B.2 Axi-symmetric formulation

As discussed in Chapters 4 and 5, although many problems in geotechnical engineering are analyzed assuming plane strain conditions, e.g. slopes, dams, etc., plane strain data for calibrating constitutive models are not usually available. Hence, it was considered important to also formulate the model for axi-symmetric conditions, like those typical of triaxial and uniaxial consolidation laboratory tests. In such tests, two of the principal stresses are equal, e.g. $\sigma_2 = \sigma_3$ in triaxial compression, or $\sigma_1 = \sigma_2$ in triaxial extension. Due to the characteristics of the model, which assumes yield loci and failure surface to be of the Mohr-Coulomb type, when two of the principal stresses are equal, the stress point moves along a corner of the Mohr-Coulomb pyramid (Figure 4.4). The corners are defined by the intersection of the two current yield surfaces and thus, by symmetry, each of these surfaces contributes to take the load in the same proportion. Koiter (1953) discussed the manner in which corner points should be treated from the elastic-plastic viewpoint. In accordance with Koiter, the problem can be approached by defining yield and potential functions for each yield surface converging at a given point of a corner, and

adding the contribution of each of them. Therefore, yield and potential functions for each side of the Mohr-Coulomb pyramid, as well as for the tension cutoffs and cap were defined in terms of principal stresses, as follows:

The yield functions are:

$$[B.69] \quad f_{1,3}^s = [\sigma_1 - \sigma_3 N_{\phi_d} + 2c\sqrt{N_{\phi_d}}]_{1,3} = 0$$

$$[B.70] \quad f_{1,2}^s = [\sigma_1 - \sigma_2 N_{\phi_d} + 2c\sqrt{N_{\phi_d}}]_{1,2} = 0$$

$$[B.71] \quad f_{2,3}^s = [\sigma_2 - \sigma_3 N_{\phi_d} + 2c\sqrt{N_{\phi_d}}]_{2,3} = 0$$

$$[B.72] \quad f^c = -\frac{1}{3}[\sigma_1^2 + \sigma_2^2 + \sigma_3^2] + (\sigma^c)^2 = 0$$

$$[B.73] \quad f_{1,3}^t = (\sigma^t)_{1,3} - \sigma_3 = 0$$

$$[B.74] \quad f_{1,2}^t = (\sigma^t)_{1,2} - \sigma_2 = 0$$

$$[B.75] \quad f_{2,3}^t = (\sigma^t)_{2,3} - \sigma_3 = 0$$

where the subscripts “1,3”, “1,2”, and “2,3” indicate the pair of stresses $\sigma_1:\sigma_3$, $\sigma_1:\sigma_2$, or $\sigma_2:\sigma_3$, respectively, in which the yield functions depend on as well as the N_{ϕ_d} and N_{ψ_d} factors.

The potential functions are:

$$[B.76] \quad g_{1,3}^s = [\sigma_1 - \sigma_3 N_{\psi_d}]_{1,3} = 0$$

$$[B.77] \quad g_{1,2}^s = [\sigma_1 - \sigma_2 N_{\psi_d}]_{1,2} = 0$$

$$[B.78] \quad g_{2,3}^s = [\sigma_2 - \sigma_3 N_{\psi_d}]_{2,3} = 0$$

$$[B.79] \quad g^c = f^c$$

$$[B.80] \quad g_{1,3}^t = f_{1,3}^t$$

$$[B.81] \quad g_{1,2}^t = f_{1,2}^t$$

$$[B.82] \quad g_{2,3}^t = f_{2,3}^t$$

B.2.1 Loading with vertical compression under axi-symmetric conditions

Under axi-symmetric conditions and loading with vertical compression, $\sigma_2 = \sigma_3$ and hence, $f^c_{1,3} = f^c_{1,2}$; $f^s_{1,3} = f^s_{1,2}$; $g^s_{1,3} = g^s_{1,2}$; and $g^t_{1,3} = g^t_{1,2}$. In addition, since the material response is assumed isotropic under constant direction of loading, then $\lambda^s_{1,3} = \lambda^s_{1,2} = \lambda^s$ and $\lambda^t_{1,3} = \lambda^t_{1,2} = \lambda^t$. Therefore, in case of yielding the plastic strain increments are determined from the corresponding flow rules as follows:

Shear Yielding:

$$\text{If } f^s(\sigma_i^I) < 0 \Rightarrow \Delta\epsilon_i^{ps} = \lambda^s \left[\frac{\partial g_{1,3}^s}{\partial \sigma_i} + \frac{\partial g_{1,2}^s}{\partial \sigma_i} \right], \text{ and hence}$$

$$[B.83] \quad \begin{aligned} \Delta\epsilon_1^{ps} &= 2\lambda^s \\ \Delta\epsilon_2^{ps} &= -\lambda^s N_{\psi_d} \\ \Delta\epsilon_3^{ps} &= -\lambda^s N_{\psi_d} \end{aligned}$$

Volumetric Yielding:

$$\text{If } f^c(\sigma_i^I) < 0 \Rightarrow \Delta\epsilon_i^{pc} = \lambda^c \frac{\partial g^c}{\partial \sigma_i}, \text{ and hence}$$

$$[B.84] \quad \begin{aligned} \Delta\epsilon_1^{pc} &= -\frac{2}{3}\sigma_1\lambda^c \\ \Delta\epsilon_2^{pc} &= -\frac{2}{3}\sigma_2\lambda^c \\ \Delta\epsilon_3^{pc} &= -\frac{2}{3}\sigma_3\lambda^c \end{aligned}$$

Tensile Yielding:

$$\text{If } f^t(\sigma_i^t) < 0 \Rightarrow \Delta\epsilon_i^{pt} = \lambda^t \left[\frac{\partial g_{1,3}^t}{\partial \sigma_i} + \frac{\partial g_{1,2}^t}{\partial \sigma_i} \right], \text{ and hence}$$

$$\begin{aligned} \Delta\epsilon_1^{pt} &= 0 \\ \Delta\epsilon_2^{pt} &= -\lambda^t \\ \Delta\epsilon_3^{pt} &= -\lambda^t \end{aligned} \quad [\text{B.85}]$$

From Equation B.3, the total plastic strain increments are given by:

$$\begin{aligned} \Delta\epsilon_1^p &= 2\lambda^s - \frac{2}{3}\sigma_1\lambda^c \\ \Delta\epsilon_2^p &= -\lambda^s N_{\psi_d} - \frac{2}{3}\sigma_2\lambda^c - \lambda^t = \Delta\epsilon_3^p \\ \Delta\epsilon_3^p &= -\lambda^s N_{\psi_d} - \frac{2}{3}\sigma_3\lambda^c - \lambda^t = \Delta\epsilon_2^p \end{aligned} \quad [\text{B.86}]$$

The new values of the principal stresses, σ_i^{new} , corrected due to plasticity can then be evaluated by substitution of Equation B.86 in Equation B.31. Following the same procedure as for the plane strain formulation, the parameters λ_j corresponding to each mode of failure can be derived by solving the system of simultaneous equations given by $f_j(\sigma_i^{new}) = 0$. The derivation of these parameters is straightforward and it is left to the reader.

B.2.2 Loading with vertical extension under axi-symmetric conditions

Under axi-symmetric conditions and loading with vertical extension, $\sigma_1 = \sigma_2$ and hence, $f^s_{1,3} = f^s_{2,3}$; $f^t_{1,3} = f^t_{2,3}$; $g^s_{1,3} = g^s_{2,3}$; and $g^t_{1,3} = g^t_{2,3}$. In addition, since the material response is assumed isotropic under constant direction of loading, then $\lambda^s_{1,3} = \lambda^s_{2,3} = \lambda^s$ and $\lambda^t_{1,3} = \lambda^t_{2,3} = \lambda^t$. Therefore, in case of yielding the plastic strain increments are determined from the corresponding flow rules as follows:

Shear Yielding:

If $f^s(\sigma_i^I) < 0 \Rightarrow \Delta\epsilon_i^{ps} = \lambda^s \left[\frac{\partial g_{1,3}^s}{\partial \sigma_i} + \frac{\partial g_{2,3}^s}{\partial \sigma_i} \right]$, and hence

$$\begin{aligned} \Delta\epsilon_1^{ps} &= \lambda^s \\ [B.87] \quad \Delta\epsilon_2^{ps} &= \lambda^s \\ \Delta\epsilon_3^{ps} &= -2\lambda^s N_{\psi_d} \end{aligned}$$

Volumetric Yielding:

If $f^c(\sigma_i^I) < 0 \Rightarrow \Delta\epsilon_i^{pc} = \lambda^c \frac{\partial g^c}{\partial \sigma_i}$, and hence

$$\begin{aligned} \Delta\epsilon_1^{pc} &= -\frac{2}{3}\sigma_1\lambda^c \\ [B.88] \quad \Delta\epsilon_2^{pc} &= -\frac{2}{3}\sigma_2\lambda^c \\ \Delta\epsilon_3^{pc} &= -\frac{2}{3}\sigma_3\lambda^c \end{aligned}$$

Tensile Yielding:

If $f^t(\sigma_i^I) < 0 \Rightarrow \Delta\epsilon_i^{pt} = \lambda^t \left[\frac{\partial g_{1,3}^t}{\partial \sigma_i} + \frac{\partial g_{2,3}^t}{\partial \sigma_i} \right]$, and hence

$$\begin{aligned} \Delta\epsilon_1^{pt} &= 0 \\ [B.89] \quad \Delta\epsilon_2^{pt} &= 0 \\ \Delta\epsilon_3^{pt} &= -2\lambda^t \end{aligned}$$

From Equation B.3, the total plastic strain increments are given by:

$$\begin{aligned} \Delta\epsilon_1^p &= \lambda^s - \frac{2}{3}\sigma_1\lambda^c \\ [B.90] \quad \Delta\epsilon_2^p &= \lambda^s - \frac{2}{3}\sigma_2\lambda^c = \Delta\epsilon_1^p \\ \Delta\epsilon_3^p &= -2\lambda^s N_{\psi_d} - \frac{2}{3}\sigma_3\lambda^c - 2\lambda^t \end{aligned}$$

The new values of the principal stresses, σ_i^{new} , corrected due to plasticity can then be evaluated by substitution of Equation B.90 in Equation B.31. Following the same procedure as for the plane strain formulation, the parameters λ_j corresponding to each mode of failure can be derived by solving the system of simultaneous equations given by $f_j(\sigma_i^{new}) = 0$. The derivation of these parameters is straightforward and it is left to the reader.

B.2.3 Shear hardening parameter under axi-symmetric conditions

To comply with the plastic shear mechanism flow rule of the model the hardening parameter must be derived for axi-symmetric conditions and in terms of the stress parameters s and t , from energy considerations. The plastic energy dissipated during yielding can be written in incremental form as follows:

$$[B.91] \quad \Delta E^p = \sigma_1 \Delta \varepsilon_1^{ps} + \sigma_2 \Delta \varepsilon_2^{ps} + \sigma_3 \Delta \varepsilon_3^{ps} = s \cdot \Delta \varepsilon_v^{ps} + t \cdot \Delta \gamma^{ps}$$

For the case of vertical compression, $\sigma_2 = \sigma_3$ and $\Delta \varepsilon_2^{ps} = \Delta \varepsilon_3^{ps}$. Substitution of $s = (\sigma_1 + \sigma_3)/2$; $t = (\sigma_1 - \sigma_3)/2$; and $\Delta \varepsilon_v^{ps} = (\Delta \varepsilon_1^{ps} + \Delta \varepsilon_2^{ps} + \Delta \varepsilon_3^{ps})$ in Equation B.91 gives:

$$[B.92] \quad \Delta E^p = \sigma_1 \Delta \varepsilon_1^{ps} + 2\sigma_3 \Delta \varepsilon_3^{ps} = \left(\frac{\sigma_1 + \sigma_3}{2} \right) \cdot (\Delta \varepsilon_1^{ps} + 2\Delta \varepsilon_3^{ps}) + \left(\frac{\sigma_1 - \sigma_3}{2} \right) \cdot \Delta \gamma_{vc}^{ps}$$

and simplifying:

$$[B.93] \quad \Delta \gamma_{vc}^{ps} = (\Delta \varepsilon_1^{ps} - 2\Delta \varepsilon_3^{ps})$$

where the subscript vc indicates vertical compression under axi-symmetric conditions.

For the case of vertical extension, $\sigma_1 = \sigma_2$ and $\Delta \varepsilon_1^{ps} = \Delta \varepsilon_2^{ps}$. Substitution of $s = (\sigma_1 + \sigma_3)/2$; $t = (\sigma_1 - \sigma_3)/2$; and $\Delta \varepsilon_v^{ps} = (\Delta \varepsilon_1^{ps} + \Delta \varepsilon_2^{ps} + \Delta \varepsilon_3^{ps})$ in Equation B.91 gives:

$$[B.94] \quad \Delta E^p = 2\sigma_1 \Delta \varepsilon_1^{ps} + \sigma_3 \Delta \varepsilon_3^{ps} = \left(\frac{\sigma_1 + \sigma_3}{2} \right) \cdot (2\Delta \varepsilon_1^{ps} + \Delta \varepsilon_3^{ps}) + \left(\frac{\sigma_1 - \sigma_3}{2} \right) \cdot \Delta \gamma_{ve}^{ps}$$

and simplifying:

$$[B.95] \quad \Delta \gamma_{ve}^{ps} = (2\Delta \varepsilon_1^{ps} - \Delta \varepsilon_3^{ps})$$

where the subscript ve indicates vertical extension under axi-symmetric conditions.

Although the plastic shear strain increments for vertical compression and vertical extension are apparently different, substitution of Equations B.83 and B.87 into B.93 and B.95, respectively, gives:

$$[B.96] \quad \Delta \gamma_{vc}^{ps} = 2\lambda^s (1 + N_{\psi_d})$$

and

$$[B.97] \quad \Delta \gamma_{ve}^{ps} = 2\lambda^s (1 + N_{\psi_d})$$

Equations B.96 and B.97 are identical and they yield twice the value of the shear hardening parameter for plane strain conditions (Equation B.17):

$$[B.98] \quad \Delta \gamma^{ps} = |\Delta \varepsilon_1^{ps} - \Delta \varepsilon_3^{ps}| = |\lambda^s (1 + N_{\psi_d})|$$

Since under axi-symmetric conditions the shear stress is taken simultaneously by both yielding planes (Mohr-Coulomb pyramid corner), for an isotropic material each yielding plane contributes with half the strength and strain. Therefore, the hardening parameter to which the shear hardening rule responds must be half the plastic shear strain increment yielded by Equation B.96 or B.97, and it is given by Equation B.98.